Investigating temperature-dependent differences in human coronavirus OC43 replication and Type I interferon signalling in human cells

Tukur Baba Abdullahi

A thesis submitted for the degree of Doctor of Philosophy in Molecular Medicine

School of Life Sciences

University of Essex

October 2025

Abstract

Human coronaviruses (HCoVs) are widespread respiratory pathogens that generally cause mild upper respiratory tract (URT) infections, unlike epidemic coronaviruses such as SARS-CoV, MERS-CoV and SARS-CoV-2, which more often replicate in the lower respiratory tract (LRT) and cause severe disease. A physiological temperature gradient exists in the airway, with 33 °C in the URT and 37 °C in the LRT. I tested whether HCoV-OC43 confinement to the URT reflects temperature-dependent regulation of type I interferon. I combined multi-cycle growth assays across human cell infection models, transcriptomics in primary nasal epithelial cells, stimulation of pattern-recognition receptors, IFNα pretreatment and JAK/STAT inhibition, and targeted knockouts. Across multiple cell types, HCoV-OC43 replicated more efficiently at 33 °C than at 37 °C. Replication was sensitive to IFNα at both temperatures, yet induction of interferon-stimulated genes was reduced at 33 °C, resulting in a weaker antiviral state. Cytokine profiling following stimuli revealed that secretion of cytokines was generally stronger at 33 °C. PRR stimulation revealed temperature sensitivity of RIG-I signalling, with stronger ISG induction and MAPK or STAT phosphorylation at 37 °C and attenuated responses at 33 °C. In contrast, MDA5/TLR3 pathways and direct IFNAR signalling were relatively stable across temperatures. In A549 knockouts, loss of *RIG-I, MDA5*, or *MAVS* increased replication, however, only MAVS deficiency attenuated the temperature-dependent replication difference, indicating that MAVS is a major contributor to antiviral restriction at 37 °C while additional temperature-sensitive mechanisms remain operative. These data support a dual mechanism for HCoV-OC43 upper-airway tropism, where cooler temperatures promote replication and attenuate MAVS-linked antiviral programs. While MAVS emerges as a critical adaptor in this process, further research is needed to define its interplay with downstream effectors and to assess how such temperature-sensitive innate responses shape coronavirus tissue tropism more broadly.

Statement of originality

I confirm that this is my own work and that I have fully acknowledged all materials and sources used in its preparation. No portion of the work described has been submitted in support of an application for another degree or qualification at this or any other university or learning institution. All research presented in this thesis was carried out by the author at the University of Essex.

Acknowledgements.

In the name of Allah (SWT), the Most Gracious, the Most Merciful.

First and foremost, I thank God Almighty for sustaining me with strength, patience, and spiritual guidance throughout this journey.

I am deeply grateful to my principal supervisor, Dr Efstathios Giotis, for his extraordinary patience, expert insight, and unwavering confidence in my work. Your encouragement and trust have been the cornerstone of this thesis. I also wish to thank my second supervisor, Professor Nelson Fernandez, for his fatherly advice, sage guidance, and steadfast support. The lessons I have learned from you both extend far beyond the laboratory and will stay with me always.

I would like to acknowledge my panel chair, Dr Ralf Zwacka, for his valuable oversight and constructive feedback during my progress reviews. I also thank Dr Greg Brooke for his generous assistance with critical laboratory techniques; your willingness to share expertise significantly advanced the quality of my experiments.

My gratitude extends to the Petroleum Development Trust Fund (PTDF) for their generous sponsorship, which made this research possible.

Heartfelt thanks go to everyone in the Giotis Lab, in particular, Riaz, Tiffany, and Dami. We began this journey side by side, from brainstorming sessions and shared frustrations over countless cups of coffee, to the milestones we have reached today. The time spent with you, both inside and outside the lab, has been enriching. Thank you for your camaraderie and support.

To my friends Kimia, Cait, Rushba, Aygun, Farid, Emi, and many others: thank you for the laughter, the meals out, and the moments of relaxation that kept me grounded. Your friendship has been a vital source of joy and balance.

I am profoundly grateful to my parents for their constant prayers, emotional and financial support, and wise advice throughout this journey. Your visits and unwavering belief in me have been a source of strength.

Lastly, my deepest gratitude is reserved for my wife, Maryam. Your endless love, patience, and understanding have been my anchor. Your sacrifices and unwavering support made this achievement possible. May Allah (SWT) reward you abundantly.

List of contents

List of abbreviations:

9-O-Ac-Sia	9-O-acetylated-sialic Acid
ACE2	Angiotensin-Converting Enzyme 2
APS	Ammonium Persulfate
BCA	Bicinchoninic Acid
BSA	Bovine Serum Albumin
cDNA	Complementary DNA
CMC	Carboxymethyl Cellulose
CM	Conditioned Medium
COVID-19	Coronavirus Disease 2019
CPE	Cytopathic Effect
DAPI	4′,6-Diamidino-2-Phenylindole
DC	Dendritic Cell
DMSO	Dimethyl Sulfoxide
DMEM	Dulbecco's Modified Eagle Medium
E	Enveloped Protein
E. coli	*Escherichia coli*
EDTA	Ethylenediaminetetraacetic Acid
ECL	Enhanced Chemiluminescence
ER	Endoplasmic Reticulum
ETC	Electron Transport Chain

FBS	Fetal Bovine Serum
FFU	Focus-Forming Unit
GAPDH	Glyceraldehyde-3-Phosphate Dehydrogenase
GO	Gene Ontology
GSEA	Gene Set Enrichment Analysis
HCoV	Human Coronavirus
HE	Hemagglutinin-Esterase
HKG	Housekeeping gene
HRP	Horseradish Peroxidase
IFIT	Interferon-induced protein with tetratricopeptide repeats
IFN	Interferon
IFNAR1/2	Interferon-α/β Receptor 1 and 2
IFNGR1/2	Interferon-γ Receptor 1 and 2
IFNLR1	Interferon-λ Receptor 1
IL	Interleukin
IL10R2	Interleukin-10 Receptor 2
IRF	Interferon Regulatory Factor
ISG	Interferon-Stimulated Gene
ISGF3	Interferon-Stimulated Gene Factor 3
ISRE	IFN-Stimulated Response Element

JAK	Janus Kinase
kDa	Kilodalton
kb	Kilobase
LB	Luria Broth
MAVS	Mitochondrial Antiviral Signalling Protein
MEM	Minimum Essential Medium
mAb	Monoclonal Antibody
MERS	Middle East Respiratory Syndrome
mg	Milligram
mL	Millilitre
MOI	Multiplicity of Infection
mRNA	Messenger Ribonucleic Acid
NF-κB	Nuclear Factor-kappa B
NGS	Next-Generation Sequencing
NSPs	Non-Structural Proteins
ORF	Open Reading Frame
PBS	Phosphate-Buffered Saline
PBST	Phosphate-Buffered Saline + 0.1% Tween-20
PFU	Plaque-Forming Unit
PFA	Paraformaldehyde

PLP	Papain-like protease
Poly I:C	Polyinosinic: polycytidylic acid
PRR	Pattern Recognition Receptor
qPCR	Quantitative Polymerase Chain Reaction
qRT-PCR	Quantitative Reverse Transcription PCR
RBD	Receptor-Binding Domain
RIG-I	Retinoic Acid-Inducible Gene I
RLR	RIG-I-Like Receptor
RNA	Ribonucleic Acid
RNA-seq	RNA Sequencing
RT-PCR	Reverse Transcription PCR
rpm	Revolutions per Minute
SARS-CoV-2	Severe Acute Respiratory Syndrome Coronavirus 2
SDS	Sodium Dodecyl Sulphate
SDS-PAGE	Sodium Dodecyl Sulphate–Polyacrylamide Gel Electrophoresis
SOCS	Suppressor of cytokine signalling
STAT	Signal Transducer and Activator of Transcription
TBK1	TANK-Binding Kinase 1
$TCID_{50}$	Tissue Culture Infectious Dose 50%

TEMED	N,N,N′,N′-Tetramethyl ethylenediamine
TLR	Toll-Like Receptor
TNF-α	Tumour Necrosis Factor-alpha
TRIzol	Phenol/guanidine isothiocyanate reagent for RNA isolation
TYK2	Tyrosine Kinase 2
µg	Microgram
µL	Microliter
°C	Degrees Celsius
%	Percent

List of figures and tables

Figures:

Tables:

Chapter 1 Introduction

1.1 Background of study

The first line of cellular defence against pathogen infection is innate immunity, working together with physical and biological barriers. The innate immune system is activated when pathogen-associated molecular patterns (PAMPs) and damage-associated molecular patterns (DAMPs) are recognised by Pattern Recognition Receptors (PRRs). When PRRs are activated, they rapidly activate multiple host defence programmes to protect against harmful invaders, including viruses. As a result, pathogens have evolved strategies to subvert innate immunity and evade detection. Such pathogen-driven imbalances in innate immune responses are frequently associated with the development of disease.

Viruses are obligate intracellular pathogens with genomes made of either DNA or RNA, each capable of being single- or double-stranded. Most RNA viruses replicate using viral RNA-dependent RNA polymerases that lack strong proofreading, which increases mutation rates and aids adaptation (Duffy, 2018; Peck and Lauring, 2018). Retroviruses encode a reverse transcriptase that copies their RNA genome into DNA via an RNA-DNA intermediate (Ilina *et al.*, 2021). By contrast, viroids are small, non-coding RNA pathogens that do not use reverse transcription; instead, nuclear-replicating viroids hijack host DNA-dependent RNA polymerase II to copy RNA templates in a rolling-circle process, and chloroplast-replicating viroids use plastid RNA polymerases for an analogous RNA-to-RNA replication cycle (Mudiyanselage *et al.*, 2022; Zhang *et al.*, 2024). Many known defence mechanisms can prevent or lessen the severity of a viral infection. Viruses and their hosts engage in antagonistic interactions over long periods, which is thought to have resulted in the development and refinement of immune systems that can distinguish between "self" and "non-self" and eliminate "non-self"; the

genomes of the host encode several complex systems known to mediate antiviral functions (Takahashi *et al.*, 2021).

Coronaviruses have developed a wide array of strategies to avoid host antiviral immunity. Although coronaviruses are now widely recognised in veterinary medicine as highly virulent pathogens, in the past, they have been treated in humans as mild infectious agents that cause a seasonal cold and mild respiratory illness. However, since the first outbreak of SARS-CoV in 2003, some zoonotic coronavirus strains, such as severe acute respiratory syndrome-associated coronavirus (SARS-CoV), Middle East respiratory syndrome coronavirus (MERS-CoV), and the recently emerged SARS-CoV-2, have caused repeated outbreaks, infecting humans, threatening human health and causing a public health and global economic crisis. These coronaviruses disrupt the host defence system by impairing antiviral innate immune responses via multiple viral inhibitory mechanisms, resulting in viral transmission and adaptation to the human host (Kasuga *et al.*, 2021). Research into the SARS-CoV-2 pandemic has reignited interest in human coronaviruses that cause the common cold, notably as biosafety level (BSL) 2 surrogates for research into SARS-CoV-2, which must be undertaken at a BSL-3 level (Bracci *et al.*, 2020; Fausto *et al.*, 2023).

It is common knowledge that coronaviruses are widespread and can cause disease in humans and other animals. In 1937, a coronavirus was identified for the first time as the infectious agent responsible for bronchitis in birds (Wang *et al.*, 2015). A few coronaviruses known to infect humans were identified during research conducted on the common cold. The progression of events leading up to the discovery of seasonal human coronaviruses (HCoVs) is detailed in Table 1.

Table 1.1 Overview of the major features of the seasonal Coronaviruses.

Disease	229E	NL-63	OC-43	HKU-1
Disease Causing Pathogen	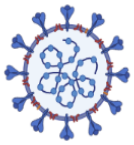 229E	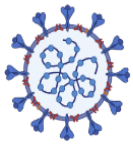 NL-63	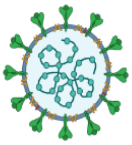 OC-43	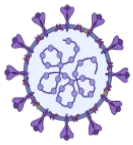 HKU-1
Genera	α-Covs	α-Covs	β-Covs	β-Covs
Origin	Bats	Bats, Palm civets	Bats, Cattle	Bats, Mice
Incubation Time	2 - 4 days	2 - 4 days	2 - 4 days	2 - 4 days
Discovery Year/Country	1962/United States	2004/ Netherlands	1967/United States	2005/Hong Kong
Receptors	APN	ACE2	9-O-Acetylated sialic acid	9-O-Acetylated sialic acid
Proteases	TMPRSS2, Cathepsin	TMPRSS2, Clathrin	?, Caveolin -1-dependent endocytosis	?, Surface TMPRSS2 Endosomal cathepsins
Reference	Pillaiyar *et al.*, 2020 Tyrrell *et al.*, 1965 Monto *et al.*, 2014	Van Der Hoek *et al.*, 2004 Fouchier *et al.*, 2004	McIntosh *et al.*, 1967 Pillaiyar *et al.*, 2020	Woo *et al.*, 2005 Pillaiyar *et al.*, 2020

1.2 Classification and origin of Coronaviruses

Coronaviruses belong to the subfamily Orthocoronavirinae (family Coronaviridae, order Nidovirales) and are a large group of enveloped, positive-sense RNA viruses with large genomes. Phylogenetic analyses group them into four genera, namely, Alphacoronavirus, Betacoronavirus, Gammacoronavirus, and Deltacoronavirus, based on their genetic composition and sequence homology, with each genus containing multiple subgenera (Fung and Liu, 2021) (Figure 1.1). To date, only seven species from the alpha and beta genera have been reported to infect humans. Among these, HCoV-229E, HCoV-NL63, HCoV-OC43 and HCoV-HKU1 are primarily called seasonals. To simplify terminology, these four species will be referred to collectively in this thesis as the HCoVs. HCoV-229E and HCoV-NL63 are alphacoronaviruses, while HCoV-OC43 and HCoV-HKU1 are betacoronaviruses; the other human-infecting betacoronaviruses (SARS-CoV, SARS-CoV-2 and MERS-CoV) cause more severe disease (Li *et al.*, 2020; Forni *et al.*, 2021a) (Figure 1.1). HCoV-NL63, HCoV-229E, HCoV-OC43 and HCoV-HKU1 are endemic strains that frequently infect humans, causing

mild symptoms such as the common cold and other minor upper respiratory infections. Still, they can lead to severe infections in infants, the elderly or immunocompromised individuals (Kim and Shin, 2021). Current sequence databases indicate that all HCoVs have zoonotic origins; HCoV-NL63 and HCoV-229E are believed to have originated in bats, while HCoV-OC43 and HCoV-HKU1 are assumed to have originated in rodents (Woo *et al.*, 2010).

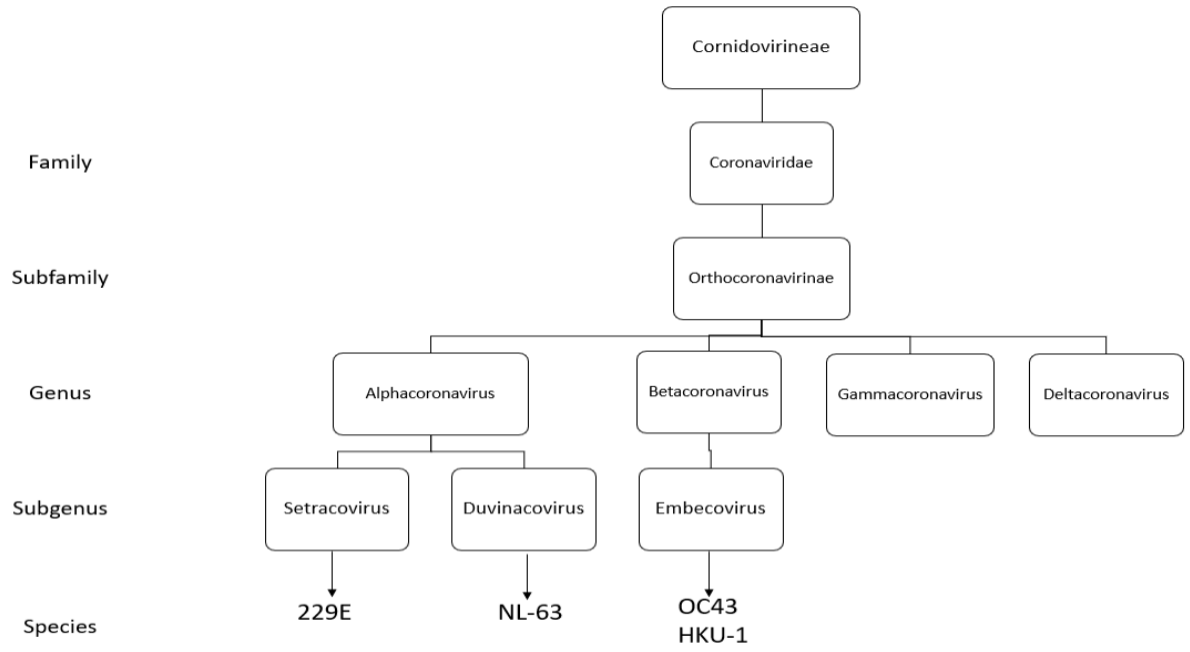

Figure 1.1: The International Committee on Virus Taxonomy has classified HCoVs.

Schematic summary of the four genera in Orthocoronavirinae (Alpha, Beta, Gamma and Delta), highlighting the four human coronaviruses and their assigned genera.

1.3 Genome and structure of Coronaviruses

When viewed under an electron microscope, coronaviruses have a characteristic crown-like (*corona* in Latin) appearance due to the spike glycoproteins on their surface, hence their name (Figure 1.2). They have the largest viral RNA genome of approximately 26–32 kilobases in length and 65–125 nm in diameter (Shereen *et al.*, 2020; Marra *et al.*, 2003), which is organised into a 5'-capped structure and 3'-polyadenylated tail that mimics host mRNA and is essential

for its stability and translation in the host cell (Harrison *et al.*, 2023). The 5'-cap, which makes up approximately two-thirds of the genome, typically encodes two large overlapping open reading frames (ORFs), ORF1a and ORF1b, which are translated into two polyproteins (Harrison *et al.*, 2023; Lu *et al.*, 1995). These polyproteins are subsequently cleaved by viral proteases into 16 non-structural proteins (NSPs) involved in the replication and transcription of the virus (Harrison *et al.*, 2023). The remaining one-third of the genome encodes the ORFs for structural proteins that include hemagglutinin-esterase (HE), which is encoded by HCoV-OC43 and -HKU1 only, spike (S), envelope (E), membrane (M), and nucleocapsid (N) (Figure 1.2) (Table 1.2) and several accessory proteins (Masters, 2006; Liu *et al.*, 2021a). The accessory proteins often play roles in modulating host responses and are not strictly necessary for replication but may enhance virus survival or virulence (Tan *et al.*, 2006).

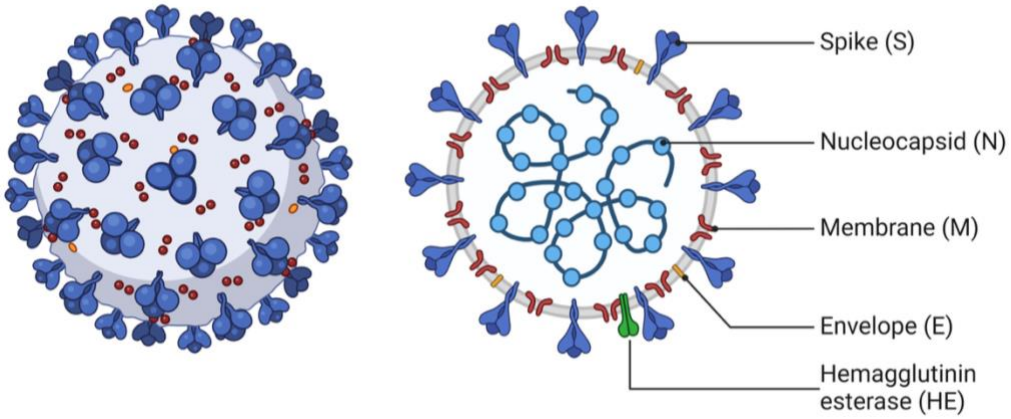

Figure 1.2: Structural organisation of a human coronavirus virion.

Schematic depiction of the enveloped, spherical coronavirus particle (left) and a longitudinal section through the virion (right). Key structural components are labelled: the spike glycoprotein (S), responsible for receptor binding and membrane fusion; the membrane protein (M), which shapes the viral envelope; the envelope protein (E), a small viroporin involved in assembly and release; the hemagglutinin-esterase (HE) lectin-esterase, present in HCoV-OC43 and related betacoronaviruses; and the nucleocapsid protein (N), which encapsulates the positive-sense RNA genome. The lumen of the virion contains the helical ribonucleoprotein complex formed by N and the viral RNA. (Created using Biorender, inspired by (Mingaleeva *et al.*, 2022)).

Table 1.2 Structural proteins of HCoVs and their functions

Protein	Functions	References
Spike protein (S)	Mediates attachment to host cells and induces the fusion of the virus envelope with the host cell membrane and determines species tropism. It can contribute to viral pathogenesis by activating the endoplasmic reticulum stress response.	(Hulswit *et al.*, 2019; Wang *et al.*, 2022)
Membrane protein (M)	Facilitates the assembly of the Coronavirus particle and gives the virion its shape. Essential for viral assembly and morphogenesis; interacts with other structural proteins to form the virion.	(Masters, 2006; Fung and Liu, 2019)
Envelope protein (E)	Modulates the assembly process and virion release contributing to viral pathogenesis.	(Stodola *et al.*, 2018; LIU and INGLIS, 1991)
Nucleocapsid protein (N)	Binds with viral genomic RNA to form a helical nucleocapsid in a 'bead-on-string-manner' and facilitates viral genome replication.	(Masters, 2006; Liu *et al.*, 2021a)
Hemagglutinin-esterase protein (HE)	Acts as a hemagglutinin and cofactor of the S protein to mediate cell entry.	(Hulswit *et al.*, 2019; Zeng *et al.*, 2008)

1.4 Coronavirus lifecycle and recombination

HCoVs undergo a multi-step replication cycle that influences their infectivity, tissue specificity and interaction with host defences (de Wilde *et al.*, 2018). The cycle starts when the viral S protein binds to specific host receptors. For example, HCoV-OC43 and -HKU1 recognise 9-O-acetylated sialic acid (Hulswit *et al.*, 2019), while HCoV-NL63 and SARS-CoV-2 engage ACE2 (Tang *et al.*, 2022; Bonavita *et al.*, 2024). Receptor binding activates the S2 subunit, allowing membrane fusion and viral entry. The virus enters either through direct fusion with the cell membrane or via receptor-mediated endocytosis, both of which require host protease activity and specific membrane lipids (de Klerk *et al.*, 2022).

Once inside, the viral RNA is released into the cytoplasm, where it acts as a template for protein synthesis, as coronaviruses have a positive-sense single-stranded RNA genome with a 5'-cap and poly-A tail, like host mRNA (Gildenhuys, 2020). The translation of ORF1a and ORF1b produces polyproteins pp1a and pp1ab, which are processed into NSPs. These NSPs assemble into the replication-transcription complex (RTC), located within virus-induced double-membrane vesicles (Gildenhuys, 2020).

The RTC oversees both the replication of full-length genomic RNA and production of a nested set of subgenomic RNAs (sgRNAs) through a distinctive process called discontinuous transcription (Morrison, 2020). This process is vital for creating structural proteins (S, M, E and N) and accessory proteins. These structural proteins are translated and transported into the endoplasmic reticulum-Golgi intermediate compartment (ERGIC), where they assemble with newly replicated genomic RNA to form mature virions (de Wilde *et al.*, 2018). The release of virions occurs through vesicular transport and exocytosis.

Temperature affects several stages of the coronavirus life cycle through effects on both viral processes and host cell biology. At the level of entry, membrane fluidity, lipid organisation, and

host protease activity are temperature sensitive, which may alter the efficiency of receptor engagement, endocytosis, and membrane fusion in the upper versus LRT (V'Kovski *et al.*, 2021; V'kovski *et al.*, 2021; Li *et al.*, 2022). Cooler temperatures in the URT may also affect the conformational dynamics of the spike protein and its interaction with host receptors, including sialylated glycans or ACE2, potentially favouring viral attachment or uptake in this environment (Hulswit et al., 2019; Tang et al., 2022). Following entry, temperature can influence the formation and stability of virus-induced replication organelles such as DMVs, which house the RTC. Host membrane remodelling, vesicle trafficking, and cellular metabolic activity are all temperature-dependent and may therefore impact the efficiency of viral RNA synthesis and transcription (Gildenhuys, 2020; V'Kovski et al., 2021). In parallel, temperature has a pronounced effect on host innate immune responses. These effects may differ between the URT at 33 °C and the lower respiratory tract (LRT) at 37 °C.

An essential feature of coronavirus biology is its propensity for high-frequency RNA recombination, which plays a key role in viral evolution and emergence. Unlike most RNA viruses, coronaviruses encode a proofreading exoribonuclease (nsp14-ExoN), which not only enhances replication fidelity but also facilitates template switching during RNA synthesis, thereby promoting recombination (Su *et al.*, 2020; Jimenez-Araya *et al.*, 2025). This process is mediated by transcription regulatory sequences and typically occurs during the synthesis of negative-strand RNA intermediates (Goldstein *et al.*, 2021). In seasonal HCoVs, recombination has contributed to the generation of genetically diverse lineages with varying receptor usage, antigenicity and host range (Lai *et al.*, 1985; Garcia *et al.*, 2024). For example, HCoV-OC43 is believed to have originated from a bovine-like coronavirus and has since undergone multiple recombination events that shaped its current genome architecture (Zhang *et al.*, 2004). Recombination hotspots often cluster around accessory genes and S gene regions, allowing for the selective alteration of immune evasion strategies and tissue tropism (Cui *et al.*, 2019).

Recent studies have suggested that RNA recombination in coronaviruses occurs preferentially at U-rich sequences and may be modulated by selective pressures such as host immune responses or species-specific bottlenecks (Gribble *et al.*, 2021; Jimenez-Araya *et al.*, 2025). While recombination has been extensively studied in zoonotic HCoVs (e.g., SARS-CoV and SARS-CoV-2), similar mechanisms are active in seasonal strains. Evidence from murine coronaviruses, which share evolutionary ancestry with HCoV-OC43, demonstrates recombination rates high enough to create functional chimeric viruses *in vivo* (Yang *et al.*, 2021; Masset *et al.*, 2020).

In the context of temperature-dependent replication, recombination may influence how HCoV-OC43 adapts to the URT environment, potentially selecting variants with an enhanced capacity to evade interferon (IFN) signalling at 33 °C. Although this remains speculative, it highlights the need for the continued surveillance of HCoV recombination patterns, especially regarding their immunomodulatory potential.

1.5 Host factors influencing coronavirus tropism and replication

Coronavirus tropism and replication efficiency are determined not only by viral factors but also by host cell determinants (Liu *et al.*, 2021a). The distribution of viral receptors across cell types dictates which tissues become infected. In primary human airway cultures, HCoV-OC43 and HCoV-HKU1 preferentially infect ciliated epithelial cells expressing O-acetylated sialic acids, whereas HCoV-229E targets non-ciliated cells expressing CD13 (Tang *et al.*, 2022). Host proteases also modulate entry: HCoV-229E can employ transmembrane serine protease 2 (TMPRSS2) at the cell surface or cathepsin L in endosomes to activate the S protein; HCoV-OC43 and HCoV-HKU1 typically utilise caveolin-1-dependent endocytosis; and the HCoV-NL63-mediated engagement of ACE2 recruits clathrin, with dynamin-mediated vesicle scission enabling internalisation (Liu *et al.*, 2021a). These entry routes influence exposure to endosomal

PRRs and impact the strength of the innate immune response. After entry, host factors, such as valosin-containing protein (VCP), and the early secretory pathway components, GBF1 and ARF1, are involved (Liu *et al.*, 2021a). Conversely, antiviral proteins like IFN-induced transmembrane proteins (IFITMs) can block viral fusion. However, differences in receptor usage, protease activation and antiviral effector expression contribute to the distinct tissue tropism and pathogenicity of the seasonal HCoVs (Zhao *et al.*, 2014; Liu *et al.*, 2021a).

1.6 Prevalence/epidemiology of HCoVs

HCoV-OC43, -229E, -NL63 and -HKU1 are widespread respiratory viruses that contribute to 10–30% of global URT infections (Wilson *et al.*, 2024; Kesheh *et al.*, 2022). Although these viruses generally cause mild and self-limiting illness, they remain clinically relevant, particularly in children and immunocompromised individuals. They are responsible for a considerable proportion of paediatric hospital admissions and can aggravate pre-existing respiratory or systemic conditions in high-risk populations (Kovacs *et al.*, 2024; Kume *et al.*, 2022).

1.6.1 Geographic patterns of circulation

HCoVs are globally distributed, but they show marked differences in regional dominance and climatic preferences. OC43 and HKU1, both β-coronaviruses, are more prevalent in temperate climates, particularly in North America, where they accounted for over 64% of HCoV detections between 2014 and 2021, with a clear winter peak (Shah *et al.*, 2022). In contrast, the α-coronaviruses HCoV-NL63 and HCoV-229E are more frequently detected in tropical and subtropical regions, such as sub-Saharan Africa and Southeast Asia, where transmission occurs year-round and intensifies during the rainy seasons (Kovacs *et al.*, 2024; Faye *et al.*, 2023).

A large-scale study from China (2016–2019) identified HCoV-OC43 as the most prevalent strain (36.3%), followed by HCoV-HKU1 (32.3%), NL63 (21.0%) and HCoV-229E (10.5%) (Ye *et al.*, 2023; Han *et al.*, 2023). Interestingly, HCoV-OC43 and HCoV-HKU1 exhibited semi-annual peaks in northern China but persistent year-round circulation in the southern regions, likely due to climatic variation (Shabani *et al.*, 2021).

1.6.2 Seasonal trends and climatic correlation

Seasonal variation in HCoV circulation aligns with both latitude and climate. In temperate zones, HCoV-OC43 and HCoV-HKU1 tend to peak in winter months (December to February), whereas NL63 and 229E are more prominent in the fall (September to November) (Shah *et al.*, 2022; Kakuya *et al.*, 2024). Tropical zones experience continuous transmission throughout the year, punctuated by peaks during the monsoon seasons, as observed in countries such as Malawi and Senegal (Faye *et al.*, 2023; Kovacs *et al.*, 2024).

The COVID-19 pandemic led to a temporary suppression of HCoV circulation in 2020 and 2021. However, subsequent data suggest a rebound in typical seasonal patterns, particularly for HCoV-OC43 in Japan during 2022. This underscores the resilience of endemic transmission cycles, emphasising the need for continuous vigilance (Kakuya *et al.*, 2024).

1.6.3 Age-related risk and disease burden

Children under five years of age represent the group most affected by seasonal HCoVs. These viruses are responsible for 5–15% of acute respiratory infections in this age group globally, with HCoV-OC43 and HCoV-HKU1 being more often implicated in severe cases that require hospitalisation (Kume *et al.*, 2022; Han *et al.*, 2023). Although neonates may initially have

maternal antibodies, seropositivity wanes by six months of age, leaving infants particularly susceptible (Luo *et al.*, 2023).

Infection rates peak between the first and second years of life, with positivity rates ranging from 25–30%. Rates progressively decline with age, dropping to under 5% in adults over 60 years old. Nevertheless, older adults remain at an increased risk of complications such as pneumonia, likely due to immunosenescence (Kakuya *et al.*, 2024; Lim *et al.*, 2016).

1.6.4 Vulnerability in immunocompromised individuals

Populations in high-exposure or immunosuppressed settings, including residents in homeless shelters and individuals living with HIV, demonstrate extended viral shedding and higher co-infection rates. In outbreak investigations within shelters, HCoVs have been found to exhibit rapid transmission, with secondary attack rates as high as 15%, facilitated by crowded living conditions and frequent contact (Chow *et al.*, 2022; Lim *et al.*, 2016).

1.6.5 Evolutionary dynamics and genomic epidemiology

Seasonal HCoVs continue to evolve through recombination and antigenic drift. HCoV-OC43 and HKU1 exhibit particularly high recombination rates, which could lead to the emergence of sublineages that may evade existing immunity or vaccine-induced protection, posing challenges to vaccine development and public health strategies (Ye *et al.*, 2023; Das and Roy, 2021). Similarly, NL63 exhibits a steady spike in protein evolution, averaging 1.5 amino acid substitutions per year, which could further complicate vaccine design and diminish the effectiveness of existing immunity (Wilson *et al.*, 2024).

Serological studies have suggested that immunity to seasonal HCoVs is short-lived. Antibody levels, particularly those against HCoV-NL63 and HCoV-229E, tend to decline within a year of infection, which explains the high rates of reinfection observed across the population, including in adults (De Thoisy *et al.*, 2023; Luo *et al.*, 2023).

1.6.6 Surveillance limitations

Despite their burden, seasonal HCoVs are rarely part of routine diagnostic testing due to their nonspecific clinical presentation. However, recent advances in multiplex PCR technologies, such as melting curve-based RT-PCR, have improved diagnostic throughput and detection accuracy (Wan *et al.*, 2016). The need for the broader implementation of these platforms is urgent to strengthen surveillance networks.

1.7 Innate immune response to coronaviruses

The first line of defence against a coronavirus infecting a host is the innate immune system. PAMPs are features of viruses recognised by innate immunity, which then quickly mount an antiviral response (Park and Iwasaki, 2020). Like other RNA viruses, coronaviruses activate natural sensors in immune cells and infected cells, leading to the production of IFNs and other cytokines, thereby establishing an antiviral state (Park and Iwasaki, 2020). Whether a coronavirus infection is cleared rapidly or progresses, this initial innate response significantly influences the outcome. However, the severity of illness can depend on the extent to which a coronavirus either activates or evades the host's innate immune defences. For example, while more pathogenic coronaviruses, such as MERS-CoV, are more effective at suppressing innate signals and result in uncontrolled viral replication, common cold coronaviruses usually trigger a noticeable IFN response. However, the virus will attempt to counteract it.

1.7.1 Pathogen Recognition Receptors

Pathogen recognition triggers the stimulation of PRRs, which are germline-encoded sensors primarily expressed by innate immune cells such as dendritic cells, macrophages, neutrophils and natural killer (NK) cells, as well as epithelial and other non-immune cells. These receptors are strategically positioned on the plasma membrane, within endosomal compartments or in the cytoplasm, where they detect conserved viral features known as PAMPs. In the case of viruses, PAMPs typically include ssRNA and dsRNA, and in the case of DNA viruses, unmethylated CpG DNA (Kawai and Akira, 2006).

Toll-like receptors (TLRs) on the cell surface identify extracellular pathogens, whereas endosomal TLRs identify pathogens after endocytosis. Intracellular pathogens are detected by intracellular PRRs, such as AIM2-like receptors (ALRs), retinoic acid-inducible gene (RIG)-1-like receptors (RLRs) and nucleotide oligomerisation domain-like receptors (NLRs) (Reikine *et al.*, 2014; Zhang *et al.*, 2021).

In RNA virus infections, such as those caused by the HCoVs, RIG-I and Melanoma Differentiation-Associated Protein 5 (MDA-5) play central roles in cytoplasmic viral sensing. RIG-I detects short dsRNA sequences, while MDA-5 recognises longer dsRNA sequences. The activation of these RLRs leads to the activation of TBK1 and IKKε, resulting in the phosphorylation of IRF3 and transcriptional induction of type I and type III IFNs (Kim and Shin, 2021; Odendall *et al.*, 2014). The expression of type III IFNs has, however, been shown to require the additional activation of IRF1 (Kim and Shin, 2021). MDA-5 and RIG-I can also trigger the formation of mitochondrial aggregate structures related to the mitochondrial antiviral-signalling sensors (MAVS), which also promote the phosphorylation of IRF3 and IRF7, leading to the production of IFN (Levy *et al.*, 2011).

TLRs sense viral nucleotides in endosomes using ligand-stimulated TLRs, such as TLR3, TLR7 and TLR8, with the help of the cytosolic adapter molecules, Myeloid Differentiation Primary Response 88 (MYD88) and TIR domain-containing adaptor inducing IFN-β (TRIF), to activate the IKKα/β/γ complex and TBK1/ IKKε kinases, leading to the induction of NF-kB-dependent proinflammatory cytokines and IRF3/IRF7-dependent type I and type III IFNs (Figure 3) (Odendall *et al.*, 2014; Kim and Shin, 2021).

1.7.2 IFNs and their signalling pathways leading to the production of ISGs

IFNs comprise a family of class II cytokines that were initially discovered more than 50 years ago for their ability to inhibit viral infection and confer viral resistance to host cells (Kim and Shin, 2021; Platanias, 2005b; Lazear *et al.*, 2019). Although IFNs are known for their ability to trigger an antiviral response, they also regulate a variety of immune processes, including inflammation, apoptosis and cellular differentiation (Kim and Shin, 2021; Alspach *et al.*, 2019). The ability of a cell to respond to IFNs depends on the presence of specific receptors that mediate signal transduction. They are divided into three types, namely, type I, type II and type III IFNs (Zhang *et al.*, 2021).

Type I IFNs are the most significant type of IFNs in humans, and they are mainly classified into IFN-α and IFN-β (Coccia *et al.*, 2004; Levy *et al.*, 2011). They are rapidly produced in response to viral infection and are crucial in establishing an antiviral state in cells. The heterodimeric receptor of type I IFN, consisting of the IFN-α receptor I (IFNAR1) and IFN-β receptor 2 (IFNAR2), is expressed on all cell types and is used in the recognition of type I IFNs (Coccia *et al.*, 2004; Levy *et al.*, 2011). IFNs activate the receptor-associated tyrosine kinases TYK2 and JAK1, responsible for the phosphorylation of STAT1 and STAT2, which form a trimeric complex known as IFN-stimulated gene factor 3 (ISGF3) with IRF9 (Zhang *et al.*, 2021; Ank *et al.*, 2006b). The ISGF3 complex further binds to IFN-stimulated response elements

(ISREs) in the nucleus to activate and promote the transcription of ISGs that inhibit viral RNA transcription and degradation (Kim and Shin, 2021). ISGs function to inhibit viral RNA transcription, degrade viral genomes and modulate host metabolism and immunity (Mahony *et al.*, 2017). Some ISGs, such as ISG15, act by covalently modifying host and viral proteins through a process analogous to ubiquitination, thereby restricting viral replication (Morales and Lenschow, 2013). However, not all ISGs are antiviral; some may exert pro-viral effects or remain poorly characterised (Darnell *et al.*, 1994) (Figure 1.3).

Type-II IFN is composed of IFN-γ only, which is secreted by NK, T helper 1 (Th1) and lymphoid cells during the later stages of infection (Alspach *et al.*, 2019). While they are not directly secreted by virus-infected cells, they play a crucial role in activating macrophages and mediating the inflammatory response (Alspach *et al.*, 2019). IFN-γ binds to the cell using the IFN-γ receptor (IFNGR1) and IFN-γ receptor 2 (IFNGR2) heterodimers, which also signal via the JAK/STAT pathway but via a distinct transcriptional route involving STAT1 homodimers that bind to gamma-activated sequences (GAS) elements rather than ISREs (Platanias, 2005a; Kim and Shin, 2021). IFN-γ is crucial in activating macrophages, enhancing antigen presentation and promoting Th1-driven inflammation, rather than directly limiting viral replication (Alspach *et al.*, 2019; Kim and Shin, 2021).

Type III IFNs have similar characteristics to type I IFNs but are structurally and receptor-wise different, hence their classification. They include IL29, IL28A and IL28B, also known as IFN-λ1, IFN-λ2 and IFN-λ3, respectively (Trinchieri, 2010; Kim and Shin, 2021; Ank *et al.*, 2006a). The type III IFN receptor comprises IFNLR1/interleukin (IL)-28Rα, which binds to IFN-λ only, and IL-10RB, which can bind to other IL-10 cytokines. Type III IFNs are mainly expressed on epithelial cells and signal via the JAK/STAT pathway, similar to type I IFNs, to induce the expression of ISGs using ISGF3, despite the receptor-wise differences (Figure 1.3) (Kim and

Shin, 2021; Lazear *et al.*, 2019). IFN-λ plays a particularly critical role at mucosal surfaces such as the respiratory and gastrointestinal epithelia, where it serves as a frontline defence against respiratory viruses, including human coronaviruses (Sommereyns *et al.*, 2008; Mordstein *et al.*, 2010; Wells and Coyne, 2018). Although both type I and III IFNs induce overlapping sets of ISGs, type I IFNs elicit a more rapid and robust ISG response compared to the slower, more sustained effects of type III IFNs (Lazear *et al.*, 2019; Kim and Lee, 2023).

The production of type I and III IFNs is initiated upon viral recognition by PRRs, including TLRs and RLRs (Takeuchi and Akira, 2009). These sensors detect viral PAMPs, such as dsRNA, 5'-triphosphate RNA or other non-self-nucleic acids, and initiate signalling cascades through adaptor proteins like MAVS and TRIF. This leads to the activation of transcription factors IRF3, IRF7, NF-κB and AP-1, which induce the expression of IFN-β and other pro-inflammatory cytokines (Wathelet *et al.*, 1998; Barber, 2001). A positive feedback loop is then established, where secreted IFN-β engages IFNARs on both the infected and neighbouring cells, further amplifying IFN-α production and antiviral gene expression.

Over 300 ISGs have been identified, with functions ranging from direct antiviral activity to the regulation of apoptosis and antigen presentation (Mahony *et al.*, 2017; Darnell *et al.*, 1994). While IFNs are essential for viral clearance, sustained or dysregulated IFN responses can contribute to immunopathology. In infections caused by HCoVs, excessive IFN-driven inflammation, coupled with chemokine induction, can lead to tissue damage, particularly in the lungs and central nervous system (Perlman and Netland, 2009).

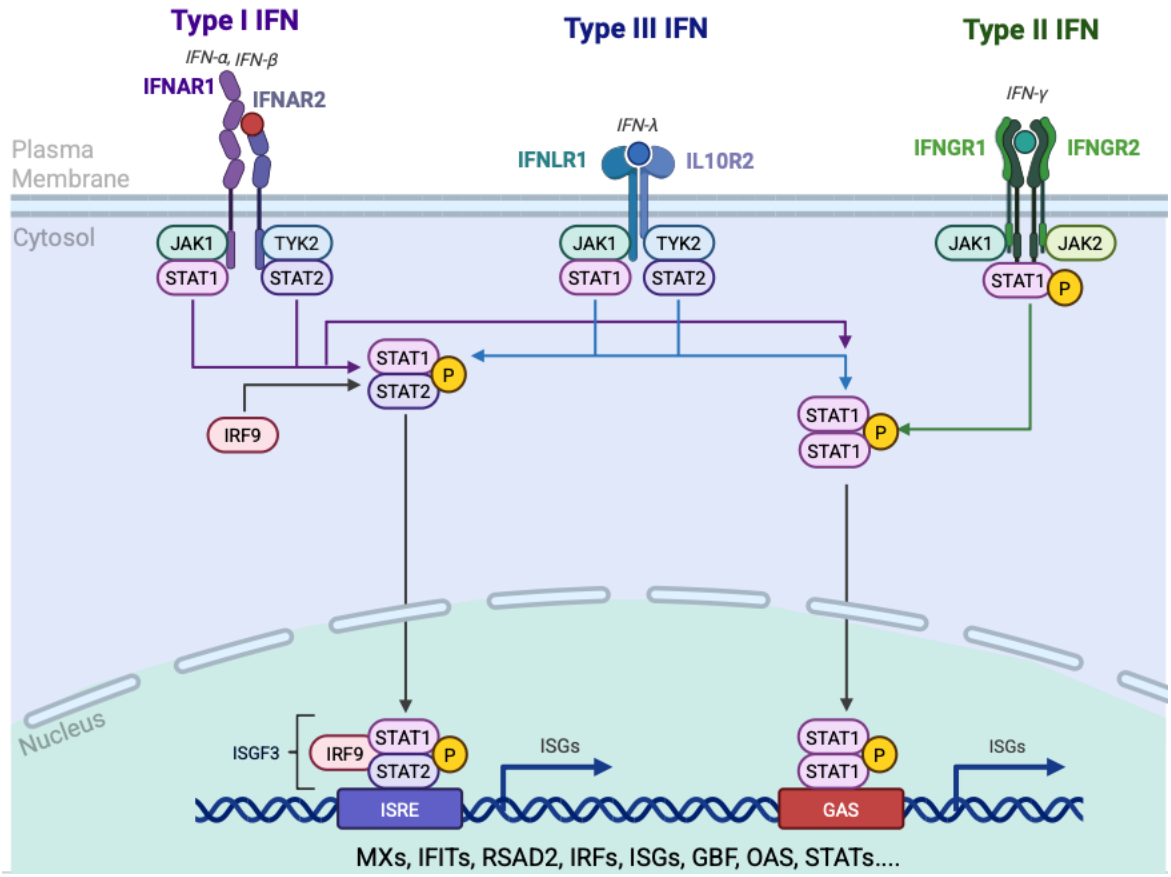

Figure 1.3: Schematic of type I, II and III interferon (IFN) signalling pathways.

This diagram illustrates the canonical JAK-STAT signalling cascades initiated by the three classes of IFNs. Type I IFNs (IFN-α and IFN-β) bind to the IFNAR1/IFNAR2 receptor complex, leading to the activation of JAK1 and TYK2 kinases and subsequent phosphorylation of STAT1 and STAT2. Phospho-STAT1/STAT2 heterodimers associate with IRF9 to form the ISGF3 complex, which translocates to the nucleus and binds the ISRE to drive the transcription of ISGs. Type III IFN (IFN-λ) engages the IFNLR1/IL10R2 complex, also activating JAK1/TYK2 and STAT1/STAT2 phosphorylation, and uses the same ISGF3–ISRE axis to induce a largely overlapping set of ISGs. Type II IFN (IFN-γ) signals through the IFNGR1/IFNGR2 receptor, activating the JAK1/JAK2 and STAT1 homodimer phosphorylation pathways; STAT1 homodimers then bind to the GAS element, upregulating a distinct but partially overlapping repertoire of immune genes. Downstream effectors include MX proteins, IFITs, OAS, RSAD2, IRFs, GBPs and other ISGs. (Created using Biorender).

1.7.3 IFN-inducible proteins

Antiviral responses are aided by proteins expressed by ISGs, which target multiple stages of the viral life cycle. IFITM proteins, for example, have been shown to prevent viral entry by

blocking viral envelope fusion with cellular membranes (Li *et al.*, 2013) or decreasing the intracellular trafficking of viral particles (Amini-Bavil-Olyaee *et al.*, 2013; Spence *et al.*, 2019). IFITM3 limits the replication of a wide range of enveloped viruses, including the influenza A virus, dengue virus, Zika virus and certain human coronaviruses. It does this by trapping incoming virions in endosomal compartments and stopping cytosolic release that depends on fusion (Li *et al.*, 2013; Amini-Bavil-Olyaee *et al.*, 2013; Spence *et al.*, 2019).

Proteins from the IFIT family have also been shown to suppress viral protein production by detecting RNAs lacking 2′-O methylation on their 5'-cap structures (Hui *et al.*, 2003). This is a frequent trait of non-self RNA, which enables them to distinguish viral RNAs from host mRNAs. For instance, IFIT1 hides these wrongly capped RNAs, such that they cannot be translated. Furthermore, IFIT proteins can stop the start of viral protein synthesis by interacting with the eukaryotic initiation factor 3 (eIF3) complex (Hui *et al.*, 2003; Daffis *et al.*, 2010; Diamond and Farzan, 2013).

Protein kinase R (PKR) is another important IFN-inducible antiviral effector. It is a cytoplasmic serine/threonine kinase that is activated when it binds to long dsRNA, which serves as a replication intermediate for many viruses (Pindel and Sadler, 2011). When activated, PKR adds a phosphate group to the alpha subunit of eukaryotic initiation factor 2 (eIF2α) (Pindel and Sadler, 2011). This stops protein translation throughout the body. This prevents the production of proteins by both the host and virus, and it can also induce apoptosis, thereby halting the spread and replication of the virus (García *et al.*, 2007).

Type I IFNs also induce the production of the IFI16 protein, a member of the PYHIN family of DNA sensors. It helps protect against viruses in both the cytoplasm and nucleus. It attaches to foreign dsDNA in the nucleus or cytoplasm and starts inflammatory reactions through the

STING pathway. IFI16 can also inhibit viral gene expression after transcription by blocking the translation of mRNA (Unterholzner *et al.*, 2010; Orzalli *et al.*, 2012).

The 2′-5′-oligoadenylate synthetase (OAS) family and its downstream effector RNase L make up another powerful antiviral axis (Kristiansen *et al.*, 2011). When OAS enzymes encounter viral dsRNA, they produce 2′-5′ linked oligoadenylates (2-5A), which subsequently activate RNase L (Kristiansen *et al.*, 2011). When RNase L is activated, it breaks down both viral and cellular RNAs, stopping the virus from replicating and sending out antiviral alarm signals (Li *et al.*, 2016).

Tetherin has been found to play a role in preventing viral release by hijacking budding virions on the cell surface late in the viral life cycle (Neil *et al.*, 2008). Although the roles of many other ISGs are unknown, IFN-induced proteins must be expressed and operate promptly to protect against viral invasion.

1.7.4 Accessory proteins and host interactions with HCoV-OC43

Coronaviruses, besides their essential structural and replicase genes, encode accessory proteins that affect interactions with host cells. These proteins frequently contribute to immune evasion and viral replication. HCoV-OC43 contains distinctive accessory genes that influence host-virus interactions. Numerous essential accessory proteins in HCoV-OC43 enhance these interactions.

1.7.4.1 Hemagglutinin-esterase

HCoV-OC43 is among the few human coronaviruses that encode the HE glycoprotein, situated on the viral envelope alongside the S, E, M and N proteins (Ujike and Taguchi, 2015). HE

attaches to O-acetylated sialic acids on the surfaces of host cells, which are similarly targeted by the spike protein (Zeng *et al.*, 2008). Nonetheless, HE possesses a secondary role: its acetyl-esterase activity facilitates the cleavage of sialic acid receptors, aiding in the viral detachment from host cells (Zeng *et al.*, 2008). This activity parallels the role of influenza neuraminidase, which promotes viral dissemination by inhibiting the virus from adhering to decoy receptors in mucus (Wallace *et al.*, 2023). In tissue culture and animal models, the presence of HE has been associated with alterations in cell tropism and pathogenesis, indicating its role in modifying infection efficacy and viral spread (Bakkers *et al.*, 2017).

1.7.4.2 NS12.9 (I Protein)

HCoV-OC43 encodes a small internal protein, NS12.9, with a molecular weight of approximately 12.9 kDa, produced via an alternative ORF overlapping the N gene. This protein is homologous to the "I" protein, also known as ORF9b in SARS-CoV or ORF8b in MERS-CoV (Hurtado-Tamayo *et al.*, 2023). The NS12.9 protein is characterised as a viroporin, forming ion channels through homo-oligomerization, which contributes to virion morphogenesis and pathogenesis in HCoV-OC43 (Zhang *et al.*, 2015). Although less studied in HCoV-OC43 compared to its betacoronavirus homologs, the NS12.9 protein is thought to localise to host cell membranes, potentially targeting mitochondria, as seen with the ORF9b of SARS-CoV, which interacts with mitochondrial antiviral signalling proteins to suppress IFN production (Hurtado-Tamayo *et al.*, 2023). By analogy, NS12.9 likely acts as an innate immune antagonist in HCoV-OC43, dampening the IFN response or other host defences (Beidas and Chehadeh, 2018; Hurtado-Tamayo *et al.*, 2023). Studies on related betacoronavirus accessory proteins, such as the NS4a and NS4b of MERS-CoV, further support the role of genus-specific accessory proteins in antagonising innate immunity (Comar *et al.*, 2019). Additionally, NS12.9 has undergone positive selection, underscoring its importance in viral adaptation and virulence

(Forni *et al.*, 2021b). Ongoing research continues to explore the precise mechanisms by which NS12.9 modulates host cell responses.

1.7.5 Additional host-interacting proteins

In addition to the critical roles of HCoV-OC43-specific accessory proteins in host interactions, structural proteins such as the N, M and E proteins also contribute to immune regulation. The N protein, known for its RNA-binding capacity, disrupts host protein synthesis and inhibits IFN production by sequestering viral RNA from immune sensors, as observed in other coronaviruses like SARS-CoV (Chang *et al.*, 2009; Mu *et al.*, 2020). Similarly, the M protein, which obstructs inflammasome activation in SARS-CoV, may have comparable but unconfirmed functions in HCoV-OC43 (Siu *et al.*, 2009). The E protein, despite its small size, exhibits ion channel activity as a viroporin, potentially disrupting host cell homeostasis and modulating inflammatory responses (Li *et al.*, 2014; Castaño-Rodriguez *et al.*, 2018). These multifaceted roles of HCoV-OC43 structural proteins highlight their significance in immune evasion, though further research is needed to confirm their specific activities in this virus.

1.8 Evasion of innate immunity by coronaviruses

Even though the innate immune system of the host possesses sophisticated antiviral defensive programmes via unique and overlapping viral sensing pathways, viruses continually find novel strategies to circumvent these programmes (Garcia-Sastre, 2017). Most viruses use their proteins to neutralise the innate immune system of their hosts by either targeting viral sensors or inhibiting antiviral signalling molecules (Garcia-Sastre, 2017; Kasuga *et al.*, 2021; Kindler *et al.*, 2016). Similarly, coronaviruses employ several viral proteins to impede the innate immune responses of their hosts. While coronaviruses that elicit moderate symptoms, such as HCoV-229E, stimulate strong type I IFN production (Mesel-Lemoine *et al.*, 2012), it has been

demonstrated that highly pathogenic coronaviruses that cause severe illness, such as SARS-CoV, MERS-CoV and SARS-CoV-2 (Hu *et al.*, 2022a), inhibit host antiviral programmes. Consequently, effective immune evasion is strongly linked to virulence and pathogenicity. To design and develop effective antiviral therapies, a detailed understanding of the immune-inhibiting mechanism employed by these viruses is necessary.

CoVs, like other positive-sense RNA viruses, organise their transcription/replication complexes within double-membrane vesicles, which are thought to aid in the concentration of viral and host factors required for efficient replication while shielding viral nucleic acids from detection by host antiviral sensors (Stertz *et al.*, 2007; Knoops *et al.*, 2008; Paul and Bartenschlager, 2013; Snijder *et al.*, 2020; Wolff *et al.*, 2020). Several other mechanisms also work to prevent viral RNA recognition. The CoV N protein has been shown to interfere with IFN induction at various levels. Through its RNA-binding ability, the N protein is thought to protect viral RNA from recognition by PRRs in the early stages of infection (Kopecky-Bromberg *et al.*, 2007; Lu *et al.*, 2011; Lei *et al.*, 2020). Furthermore, at later stages in the RIG-I activation pathway, both MERS-CoV and SARS-CoV-1 N proteins can interact with the E3 ubiquitin ligase TRIM25 to prevent RIG-I ubiquitination and downstream signalling activation (Hu *et al.*, 2017; Chang *et al.*, 2020).

The replicase complex of SARS-CoV-2, comprising NSP14 and NSP16, has also been implicated in IFN antagonism. NSP14 is a guanine-N7-methyltransferase that is involved in the formation of a viral RNA 5′-terminal cap structure that can mimic host mRNA (Chen *et al.*, 2009). Furthermore, NSP16 exhibits 2′-O-MTAse activity, which is necessary to prevent RNA recognition by MDA5 and IFIT proteins (Chen *et al.*, 2009). Similarly, the loss of NSP15 endoribonuclease activity has been reported to result in the robust activation of host dsRNA sensors and MHV attenuation due to an increase in the number of free dsRNA foci outside the

viral replication compartment (Deng *et al.*, 2017; Yuen *et al.*, 2020). Finally, it has been demonstrated that the MERS-CoV ORF4a protein binds to the RLR cofactor PACT in an RNA-dependent manner, suppressing antiviral signalling and promoting viral replication (Almazan *et al.*, 2013; Yang *et al.*, 2013; Siu *et al.*, 2014).

1.8.1 Inhibition of PRR and IFN signalling

The rapid and precise activation of RLR signalling is critical for initiating an effective antiviral response. As a result, the activities of RIG-I, MDA5 and LGP2 are regulated by a variety of posttranslational modifications, including ubiquitination, ubiquitin-like molecule conjugation and phosphorylation, among others (Cadena and Hur, 2019; Kato *et al.*, 2021). As a result, pathogenic CoVs have developed strategies to attack these critical regulatory mechanisms.

As previously stated, the N protein of SARS-CoV-1 can interact with TRIM25 and interfere with RIG-I ubiquitination (Hu *et al.*, 2017; Chang *et al.*, 2020). Similarly, SARS-CoV-2 NSP8 has been shown to bind to the CARD domains of MDA5, suppressing its K63-linked polyubiquitination and preventing the expression of type I IFNs and inflammatory cytokines (Yang et al., 2020b). Furthermore, CoVs express deubiquitinase proteins, which have been shown to target key components of the IFN induction pathway (Devaraj *et al.*, 2007; Frieman *et al.*, 2009; Bailey-Elkin *et al.*, 2014; Shin *et al.*, 2020; Liu *et al.*, 2021b). In this regard, many CoV papain-like proteases (PLPs) have been proposed to remove ubiquitin and the ubiquitin-like molecule ISG15 from cellular proteins (Clementz *et al.*, 2010; Klemm *et al.*, 2020).

Surprisingly, while SARS-CoV-1 preferentially cleaves ubiquitin from its substrates, SARS-CoV-2 PLP reduces the appearance of ISGylated protein substrates more efficiently (Shin *et al.*, 2020). SARS-CoV-2 PLP was found to bind specifically to MDA5, but not to RIG-I, and suppresses MDA5 CARD ISGylation, thereby preventing oligomerisation and downstream signalling events. Notably, this PLP-dependent mechanism of MDA5 antagonism appears to be

broadly conserved across different CoVs (SARS-CoV-1 and NL63), highlighting the critical role of MDA5 ISGylation in IFN induction during CoV infection (Liu *et al.*, 2021b).

1.8.2 Suppression and manipulation of proinflammatory responses

In addition to suppressing IFN, CoVs also target the inflammatory pathways, particularly those regulated by NF-κB, a vital transcription factor responsible for producing proinflammatory cytokines such as IL-6, TNF-α and IL-1β.

Several CoV proteins have been linked to changing or stopping the activation of NF-κB. The E protein, found in SARS-CoV, MERS-CoV and SARS-CoV-2, has been shown to activate the NLRP3 inflammasome and induce the release of IL-1β. This happens by changing the way ions move in and out of cells (Nieto-Torres *et al.*, 2015). On the other hand, some viral proteins, such as ORF6, ORF3b and NSP1, can inhibit NF-κB activation, depending on the type of cell and timing of the event (Frieman *et al.*, 2007; Miorin *et al.*, 2020; Zhang *et al.*, 2022).

ORF8 in SARS-CoV-2 reduces the expression of MHC-I, which may decrease immune-mediated cell death and indirectly lower cytokine feedback (Zhang *et al.*, 2021). Additionally, SARS-CoV-2 ORF3a has been shown to activate both the NF-κB and NLRP3 inflammasome pathways, which exacerbate inflammation and may contribute to the cytokine storm observed in patients with severe COVID-19 (Siu *et al.*, 2019; Ren *et al.*, 2021).

CoVs fine-tune the inflammatory milieu to avoid quick clearance by either suppressing early inflammatory signals or hyperactivating them later. They do this to take advantage of immune-mediated damage, which helps them spread or replicate.

1.9 Environmental influences on coronavirus infection dynamics

Environmental factors within the host, particularly temperature and humidity, significantly influence the replication efficiency, tissue tropism and transmission dynamics of respiratory viruses like seasonal coronaviruses (Eccles, 2021). The human respiratory tract displays a temperature gradient, with the upper airway (nasal passages and nasopharynx) maintained at approximately 32–34 °C. In contrast, the LRT, including the lungs, is maintained closer to the core body temperature (37 °C) (Foxman *et al.*, 2015; Iwasaki *et al.*, 2017; Eccles, 2021). Many respiratory viruses, such as rhinoviruses, influenza viruses and HCoVs, which mainly cause URT infections, replicate more efficiently at the cooler temperatures characteristic of their preferred infection sites. Temperature also affects the host immune response. The experimental infection of mouse airway epithelial cells with rhinovirus has demonstrated that the IFN response is stronger at 37 °C than at 33 °C. At cooler temperatures, this antiviral signalling is reduced, allowing increased viral replication. These findings suggest that temperature influences infection outcomes through a combination of viral replication kinetics and the host immune response (Foxman *et al.*, 2015).

1.9.1 Host defences and mucosal barriers

Cooler conditions in the nasal cavity appear to attenuate IFN-mediated antiviral signalling, whereas epithelial cells at the core body temperature induce stronger type I and type III IFN responses (Foxman *et al.*, 2015). Single-cell analyses of SARS-CoV-2 infection have revealed distinct IFN landscapes across the respiratory tract: the nasopharyngeal mucosa exhibit elevated type III IFN (IFN-λ), while in the lower airways of severely ill patients, both IFN-I and IFN-III are elevated, but ISG expression is reduced (Sposito *et al.*, 2021). These regional differences may reflect a lower abundance or altered composition of IFN signalling components in the upper airway, which could influence HCoV tissue tropism.

Physical barriers also play a role. The mucin-rich mucus layer and mucociliary clearance act as the first line of defence by trapping and removing inhaled pathogens. Low humidity and cold air can compromise these defences: the dehydration of the airway surface compresses the mucus hydrogel and thins the aqueous mucus layer (Edwards *et al.*, 2025). Studies have shown that airway surface liquid heights decrease as environmental dryness increases (Edwards *et al.*, 2025). A thinner mucus layer combined with reduced ciliary beating frequency in cold, dry conditions may facilitate viral access to epithelial cells, providing a possible explanation for the winter seasonality of HCoVs.

1.9.2 Viral and host factors influencing tropism

Some viral proteins are adapted to function optimally at specific temperatures. Pseudoviruses bearing HCoV-229E and SARS-CoV-2 spike proteins produced at 33 °C are more infectious than those produced at 37 °C, whereas spikes from SARS-CoV and MERS-CoV favour 37 °C (Laporte *et al.*, 2021). These observations indicate that the spike glycoprotein operates within a narrow biophysical window in which stability and reactivity must be carefully balanced. Spike must remain sufficiently stable to persist on the virion surface prior to receptor engagement, yet sufficiently to undergo rapid conformational arrangements once triggered (V'kovski *et al.,* 2021). Temperature can influence this balance by altering folding efficiency, glycan processing, trimer stability, and the exposure of proteolytic cleavage sites required for activation (Walls *et al.,* 2020; Tang *et al.,* 2022). Even modest thermal variation may therefore modify receptor binding affinity, susceptibility to host proteases, or kinetics of membrane fusion (Hoffmann *et al*., 2020). In viruses that predominantly replicate in the URT, cooler conditions may prolong the lifetime of entry-competent confirmations or favour structural states that enhance attachment of epithelial surfaces. In contrast, virus adapted to the LRT may require higher temperatures to achieve optimal fusion activity. Fine-tuning in this context thus reflects an

evolutionary alignment between spike protein behaviour and the thermal landscape of the host. The influence of temperature on the stability and activity of other viral enzymes remains underexplored for HCoV-OC43.

Host determinants also differ along the respiratory tract. The distribution of viral receptors, such as 9-O-acetylated sialic acids for HCoV-OC43, and activating proteases (e.g., TMPRSS2 and cathepsins) varies between nasal and bronchial epithelia, and their expression may shift with temperature. There is increasing interest in whether certain host factors vital for HCoV-OC43 replication are less abundant at 37 °C, potentially restricting viral spread to the lower lungs. Seasonal conditions that thin the mucin layer, impair mucociliary clearance and weaken IFN responses could further raise susceptibility to HCoV-OC43 infection in the upper airway (Foxman *et al.*, 2015; Edwards *et al.*, 2025).

The interplay between temperature-sensitive replication, mucosal barrier integrity, immune signalling differences and temperature-adapted viral proteins likely underlies the seasonal and tissue-specific patterns observed for HCoVs. However, the precise mechanisms remain an active area of research.

Temperature interacts with humidity and mucociliary clearance within the airways. Cold, arid air can compromise mucosal barriers and ciliary function, promoting viral entry and persistence (Iwasaki *et al.*, 2017). This elucidates the seasonality of respiratory viruses, particularly coronaviruses, which flourish during winter months due to the synergistic effects of reduced temperatures, arid air and compromised immune defences in the nasal passages. Temperature plays a crucial role in coronavirus-host interactions, influencing viral propagation, immunological evasion and disease progression.

1.10 Conclusion

Coronaviruses have garnered significant attention, particularly following the emergence of the COVID-19 pandemic, caused by SARS-CoV-2, which posed a major global pandemic. This intensified scientific interest in the study of coronaviruses. While extensive research has been conducted to understand the innate immune response to coronaviruses, many of these studies have focused on the more severe strains, such as SARS-CoV, SARS-CoV-2 and MERS-CoV, with relatively little research on endemic and less lethal coronaviruses, such as OC43. Some studies on coronaviruses have shown that SARS-CoV-2 suppresses IFN signalling compared to SARS-CoV-1, despite achieving significantly higher viral loads. Other research suggests that SARS-CoV-2 may not induce IFN expression at all but instead triggers a strong inflammatory response (Wölfel *et al.*, 2020; Loo *et al.*, 2020a). In the case of HCoV-OC43, recent studies have demonstrated that it is not sensitive to type I/II IFNs, while another showed that HCoV-OC43 infection leads to the minimal induction of an immune response in some cell lines. However, it remains unclear whether the innate immune response to HCoV-OC43 induces an effective immune response or allows the virus to evade detection. It is generally recognised that virus-host interactions can have a significant impact on the infection's progress and/or outcome. The molecular and cellular processes by which HCoVs interact with the host innate immune system, resulting in less severe effects, are yet unknown. Therefore, my hypothesis assumes that both erratic innate immune activation and immune evasion contribute to the mild respiratory disease caused by HCoVs.

1.11 Hypothesis

I hypothesise that the restriction of HCoV-OC43 to the URT is driven by the temperature-dependent regulation of the type I IFN response. At the cooler temperatures of the URT (33 °C), the initiation and amplification of IFN signalling are attenuated, allowing more efficient viral

replication. In contrast, at the core body temperature (37 °C), enhanced IFN activation and antiviral gene expression suppress HCoV-OC43 replication and limit its progression into the LRT.

1.12 Overall aim

To investigate how physiologically relevant respiratory tract temperatures shape the balance between HCoV-OC43 replication and type I IFN-mediated antiviral defence, thereby explaining the typical URT tropism of the virus and informing the development of optimised *in vitro* models of seasonal coronavirus innate immunity.

1.13 Research questions

1. Which continuous cell line supports the highest yield and most consistent replication of HCoV-OC43 and HCoV-229E?
2. How do the type I IFN signatures induced by HCoV-OC43 compare with those caused by HCoV-229E in primary nasal epithelial cultures and the selected continuous cell line?
3. To what extent do graded doses of exogenous IFN-α and IFN-λ modulate OC43 replication kinetics, ISG expression and N protein localisation?
4. How does incubation at 33 °C versus 37 °C alter OC43 growth curves, cytopathic effects and downstream ISG induction both with and without IFN pretreatment?
5. Does temperature alter upstream sensing (PRR activation) or downstream signalling (JAK/STAT-mediated ISG expression) within the IFN pathway?

1.14 Specific objectives

1. Compare viral replication and IFN induction kinetics at 33 °C and 37 °C in human primary airway epithelial cells and selected continuous lines to establish the temperature threshold for URT versus LRT infection.

2. Profile global ISG expression under HCoV-OC43 infection across both temperatures to identify candidates mediating cold-temperature susceptibility.
3. Assess the ability of exogenous IFN-α and IFN-λ to restore antiviral defence at 33 °C, identifying the most effective subtype and limiting step within the IFN network.
4. Combine cytokine secretion with phosphokinase analyses to map the temperature-dependent signalling nodes that control the early antiviral response and HCoV-OC43 replication dynamics.

Chapter 2

Methods

2.1 Cell culture and viral work

2.1.1 Cell lines

MRC-5 cells (human fetal lung fibroblasts, ATCC: CCL-171, UK) were cultured in Minimum Essential Media (MEM: Gibco, UK) supplemented with 10% heat-inactivated fetal bovine serum (HI-FBS: Sigma, UK) and 1% penicillin (Thermo Scientific, UK) streptomycin (Thermo Scientific, UK) (P/S). HRT-18G cells (human colorectal adenocarcinoma, ATCC: CRL-3609, UK), HEK293T (Human Embryonic Kidney cells, ATCC: CRL-3216, UK) and Mv1Lu cells (mink lung cells, ATCC: CCL-64, UK) were maintained in Dulbecco's Modified Eagle's Medium (DMEM: Gibco, UK) with 10% HI-FBS, 1% P/S and 2 mM glutamine. A549 cells (hypotriploid alveolar basal epithelial cells, ATCC: CCL-185, UK) were cultured in an F12K nutrient mixture containing 10% HI-FBS, 1% P/S and 2 mM glutamine. A549 RIG-I$^{-/-}$ Knockout (KO), A549 MAVS$^{-/-}$, A549 MDA5$^{-/-}$, A549 TBK1$^{-/-}$ and A549 IFNAR$^{-/-}$ cells were a kind gift obtained from Professor Brian Ferguson (University of Cambridge). The cells were cultured in DMEM supplemented with 10% HI-FBS, 1% P/S and 2 mM glutamine. All cell lines were grown at 37 °C in a humidified atmosphere with 5% CO_2.

2.1.2 Cell viability

Cells were harvested and centrifuged at 365 *g* for 5 min. Pellets were resuspended in 5 mL of culture media, after which 10 µL of the cell suspension was mixed at a 1:1 ratio with 0.4% trypan blue (Invitrogen, UK). The mixture was then incubated for 1–2 min. For automated counts (Thermo Fisher, UK), 10 µL of the mixture was loaded into the counting chamber according to the manufacturer's instructions. For manual counts, 10 µL was loaded into a haemocytometer under a coverslip and examined at 10× magnification. Viable (unstained) and

non-viable (blue-stained) cells were counted in ≥4 large squares, including cells touching the top/left borders and excluding those on the bottom/right (Butler and Spearman, 2007).

2.1.3 Cryopreservation and thawing of cells

The cell suspension was centrifuged at 365 *g* for 5 min at room temperature in a sterile centrifuge tube, after which the supernatant was discarded. The cells were then resuspended in a freezing mixture [10% dimethyl sulfoxide (DMSO) and 90% media] to an approximate concentration of 1.0×10^6 cells per mL. One-millilitre aliquots were transferred into sterile cryotubes and labelled with the cell types, passage numbers, dates and researcher's name. Vials were placed into Mr Frosty's freezing container with alcohol for 24 h at –80 °C, then transferred to liquid nitrogen (-196 °C) for long-term storage. Vials were taken from liquid nitrogen to thaw the cells and quickly defrosted in a 37 °C water bath. Pre-warmed at 37 °C, the culture medium was added dropwise into the cryotube and gently mixed. The cell suspension was transferred into a sterile tube containing 5 mL of culture media, mixed gently, and centrifuged at approximately 1000 *g* for 5 min at room temperature. The supernatant was discarded. Cell pellets were resuspended with 10 mL of fresh culture media, transferred to a flask, and incubated at 37 °C with 5% CO_2 in a humidified environment.

2.1.4 Air-liquid interface culture of hNECs

Air-liquid interface human nasal epithelial cells (hNECs) (Figure 1) were purchased from Epithelix (catalogue no. EP02MP) and derived from a pool of 14 donors (Appendix Table 1.1). The ages and genders of the donors are listed in Appendix section S1. The cells were maintained in Mucilair cell culture media (Epithelix, Germany) at 5% CO_2 and 37 °C before infection. Before infection, hNECs were washed with serum-free media to remove mucus and debris. The cells were infected with 200 µL of virus-containing serum-free DMEM on the apical surface

and incubated at 33 °C for 1 h to allow viral adsorption. After the incubation period, the inoculum was removed, and the cells were washed twice with sterile phosphate-buffered saline (PBS). Time points were taken at 24 and 72 h by adding 200 µL of serum-free DMEM and incubating for 10 min at 33 °C before removal and titration (Loo *et al.*, 2020c).

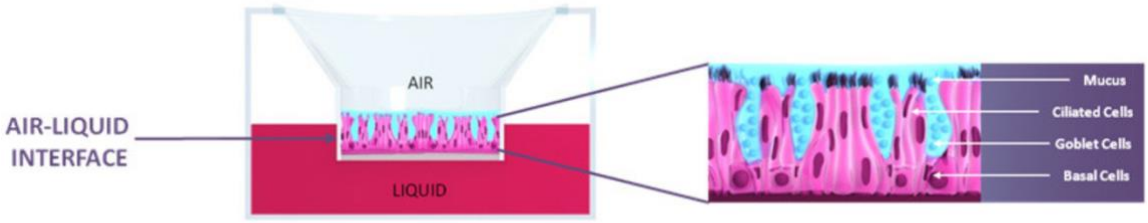

Figure 2.1: Air-liquid interface model representing the three cell types in MucilAir™.

Basal, ciliated and goblet cells (https://www.epithelix.com/products/mucilair). Accessed 12 September 2022.

2.1.5 Viral strains

All virus-related work was conducted in a Biosafety Level 2 (BSL-2) laboratory in compliance with the University of Essex Health and Safety guidelines. The viral strains HCoV-OC43 (VR-1558) and 229E (VR-740) were sourced from the ATCC, UK, and propagated in HRT-18G and MRC-5 cells, respectively. HRT-18G cells were infected with HCoV-OC43 when they reached 80–90% confluency, using DMEM supplemented with 2% heat-inactivated FBS (HI-FBS), 1% penicillin-streptomycin (P/S) and 1% L-glutamine. HCoV-229E was propagated in MRC-5 cells using MEM supplemented with 2% HI-FBS and 1% P/S. Both infected cultures were incubated at 33 °C with 5% CO_2 for 5 days, with daily monitoring of cytopathic effects (CPEs) using an EVOS M5000 microscope. After incubation, the supernatants from each culture were collected and centrifuged at 1000 rpm for 5 min to remove cell debris. The resulting supernatants were aliquoted and stored at −80 °C. A fraction of the virus stocks

(HCoV-OC43) was heat-inactivated by incubating at 56 °C for 30 min in a calibrated water bath prior to downstream assays.

2.1.6 Viral titration by plaque assay

One day before infection, 1×10^6 cells were seeded in each well of a 6-well plate to ensure cell adherence and confluency. On the day of the assay, the culture media were removed, and the cells were gently washed with warm PBS to remove any residual media. Viral samples were prepared in 10-fold serial dilutions using serum-free media, with 900 µL of the diluted virus added to each well. The plates were incubated for 2 h at 33 °C with 5% CO_2 to allow virus adsorption to the cells. After incubation, an overlay medium was applied to restrict the spread of the virus. Two different overlay media were tested during protocol optimisation: 0.5% (w/v) and 1% (w/v) agarose (Invitrogen) and 0.8% (w/v) and 1% (w/v) carboxymethylcellulose (CMC) (Sigma-Aldrich, UK). For each condition, 2 mL of the overlay medium was carefully added to each well without disturbing the monolayer, and the plates were returned to the incubator at 33 °C with 5% CO_2 for 5 days to allow plaques to form. Following incubation, the cells were fixed with 4% paraformaldehyde for at least 20 min to preserve the cell structure. The paraformaldehyde was then removed, and the cells were stained with 1% crystal violet for 1 h to visualise plaques. Excess crystal violet was washed away with tap water, enabling the precise observation and counting of viral plaques.

2.1.7 Virus titration by 50% tissue culture infectious dose ($TCID_{50}$)

Cells were seeded at a density of 0.01×10^6 cells per well in a 96-well plate and incubated overnight at 37 °C with 5% CO_2 to allow cell attachment. After 24 h, the media were carefully removed, and the cells were ready for infection with a series of viral dilutions. The serial dilutions were prepared, with 10 µL of viral stock added to wells A1–A4 containing 90 µL of

2% FBS media. This resulted in a 10^{-1} dilution in each well. Fresh tips were used at each step to prevent cross-contamination. Ten microlitres from well A1 were carefully transferred to well B1, containing 90 µL of 2% FBS media, achieving a 10^{-2} dilution. This process was repeated sequentially down the plate from wells A1–H1 to create a 10-fold serial dilution series, with each well decreasing by one order of magnitude in viral concentration. This meticulous dilution process was repeated similarly for wells A2–A4, creating four independent dilution series across columns 1–4.

Following the preparations, the plate was incubated at 33 °C with 5% CO_2 for 5 days to allow sufficient time for viral replication and the development of visible CPEs. At the end of the incubation period, each well was examined under a light microscope to record the presence or absence of CPEs. The scoring of infected versus uninfected wells was carefully carried out to ensure accuracy, as this data formed the basis of the $TCID_{50}$ calculation. To visualise the cell monolayers and confirm the CPE patterns, each well was fixed and stained with 1× crystal violet solution. The plates were incubated at room temperature for 1 h to allow adequate staining, after which the stain was carefully aspirated and plates were gently rinsed with tap water to remove excess dye, revealing distinct areas of cell loss or plaque-like formations indicative of viral infection.

The viral titres were calculated using the Reed-Muench formula to determine the 50% tissue culture infective dose ($TCID_{50}$/mL), which estimates the virus concentration required to infect 50% of the cell culture (Ramakrishnan, 2016).

2.1.8 Growth kinetics of viral growth in continuous cells

To determine the growth kinetics of HCoV-OC43, 12-well plates of MRC-5, HRT-18G, Mv1Lu, HEK293T and CHO cells (in triplicate) were infected with HCoV-OC43 at a multiplicity of infection (MOI) of 0.01 and incubated at 33 °C and 5% CO_2. Next, 150 µL of the supernatant

was collected at 0, 12, 24, 48, 72 and 96 h post-infection (hpi). The media were replaced with 150 µL of fresh 2% FBS media each time. The cells were monitored daily using the EVOS 5000 microscope (Invitrogen, UK) with a 10× objective. Growth kinetics were observed by the number of infectious particles in the supernatant using $TCID_{50}$ and viral copies in the supernatant by real-time quantitative polymerase chain reaction (qRT-PCR).

2.2 Cell stimulation

2.2.1 *In vitro* poly(I:C) transfection

Cells were seeded at a density of 1×10^6 cells per well in 6-well plates one day before the experiment and incubated at 33 °C and 37 °C with 5% CO_2. Stocks of the RNA synthetic analogue High-Molecular-Weight Polyinosinic:Polycytidylic acid (HMW poly I:C) (Invitrogen, UK) were prepared by dissolving 2 mg/mL in PBS and warming at 55 °C for 10 min. Poly I:C was then diluted to a concentration of 1 µg/mL in serum-free MEM by adding 1 µL to 0.99 mL of DMEM. A mixture of 125 µL of 8% lipofectamine (20 µL in 250 µL MEM) (Invitrogen, UK) in serum-free media was prepared for the induced cells. This mixture was combined with 125 µL of 1 µg/mL Poly I:C and left to stand for 15–30 min. Meanwhile, the cells were washed twice with serum-free MEM, with 1 mL of serum-free MEM added to each well. Next, 250 µL of the lipofectamine/Poly I:C mixture was added to the induced wells, while 250 µL of serum-free MEM was added to the uninduced cells. After 2 h, 1.25 mL of 1% MEM was added to the wells, and the plates were incubated overnight at 33 °C and 37 °C in the presence of 5% CO_2. The following day, the cells were harvested for RNA isolation.

2.2.2 Treatment with recombinant IFN-α and IFN-*λ*

One day prior to the experiment, cells were seeded at a density of 1×10^6 cells per well in 6-well plates and incubated at 37 °C with 5% CO_2. The cells were washed twice with PBS to remove residual serum, after which 1000 IU/mL of recombinant IFN-α (Invitrogen/PBL Assay

Science, UK) and IFN-λ (100 ng/mL: Bioscience, UK) were added to the growth medium. The plates were incubated for at least 6 h at 33 °C and 37 °C. The cells were subsequently harvested for RNA extraction to evaluate the induction of ISGs.

2.2.3 Cell stimulation and infection

Cells were grown to confluence in 12-well plates, incubated overnight at 33 °C or 37 °C, and counted before inoculation. The overnight incubation temperature did not affect the cell number (0.5×10^6 cells per well). Next, cells were inoculated with HCoV-OC43 at an MOI of 1 for 1 h at either 33 °C or 37 °C. Following the inoculation period, the inoculum was removed and medium was added; 1000 IU/mL of IFN (Invitrogen, UK) was added to the growth medium. Additionally, 1000 U/mL of IFN was added to other wells before inoculation with the virus. This was done to see the effect of treatment with IFNα before and after inoculation with the virus.

2.2.4 Cell stimulation with 5'pppdsRNA/LyoVec.

MRC-5 cells were seeded in 6-well plates at a density of 0.5×10^6 cells per well and cultured overnight in complete MEM supplemented with 10% FBS and P/S. Before stimulation, the cells were acclimatised to either 33 °C or 37 °C in a 5% CO_2 incubator for 48 h to ensure optimal adaptation to the experimental conditions. The 5′ppp-dsRNA/LyoVec complex is a synthetic ligand that mimics dsRNA, featuring a 5′-triphosphate group, a molecular pattern commonly associated with RNA viruses. This structure is recognised explicitly by the cytosolic PRR RIG-I, leading to the activation of downstream signalling pathways and induction of type I IFNs. Lyovec is a cationic lipid-based transfection reagent that facilitates the delivery of 5'ppp-dsRNA into the cytoplasm, ensuring the efficient stimulation of intracellular RNA sensors. The reagent was purchased pre-formed (25 µg; InvivoGen, cat. no. tllr-3prna/sec, UK) and resuspended in 500 µL of endotoxin-free water to prepare a stock solution of 50 µg/mL. For

stimulation, the complex was diluted in a serum-free medium, and 5 μg/mL of the diluted solution was added. Following stimulation, the cells were incubated at their respective temperatures (33 °C or 37 °C) with 5% CO_2 for 24 h. After incubation, the medium was replaced with a complete medium, and the cells were processed for downstream analyses. Control wells included cells treated with LyoVec alone to account for non-specific effects. All steps were performed under sterile conditions

2.3 RNA and gene expression analysis

2.3.1 RNA extraction from cells and supernatant using TRIzol

The supernatant (100 μL) was removed at different time points and transferred into a 1.5 mL Eppendorf tube. For the cells, 1.2×10^6 cells/mL were transferred to an Eppendorf tube. Next, 1 mL of TRIzol (Invitrogen, UK) was added to 100 μL of the supernatant or cell pellets, and the mixture was incubated at room temperature for 5 min. Chloroform (200 μL; Sigma-Aldrich, UK) was added per 1 mL of TRIzol, and the mixture was incubated for 15 min with occasional vortexing halfway through. Cells were centrifuged at 12,000 rpm for 15 min at 4 °C. The aqueous phase was carefully transferred to a new Eppendorf tube. To facilitate RNA precipitation, 500 μL of isopropyl alcohol was added, mixed gently, and incubated for 10 min. The cells were centrifuged at 12,000 *g* for 10 min at 4 °C. The supernatant was carefully discarded, and the pellets were washed with 75% ethanol (Sigma-Aldrich, UK). The sample was then centrifuged at 12,000 *g* for 15 min at 4 °C. The supernatant was removed and allowed to air dry. RNase-free water was then added to dissolve the pellet. The RNA concentration was determined using a Nanodrop (Thermo Scientific, UK) (Rio *et al.*, 2010).

2.3.2 Viral RNA isolation using the QIAamp viral RNA mini kit (centrifuge method)

The procedure for viral RNA isolation using the QIAamp Viral RNA Mini Kit (Qiagen, UK) (centrifuge method) was performed as follows. First, Buffer AW1 and Buffer AW2 were

prepared by adding the specified volume of ethanol (96–100%) to the concentrates, as indicated on the bottle labels. The buffers were mixed thoroughly and labelled accordingly. Next, 140 µL of the cell culture supernatant was transferred into a 1.5 mL microcentrifuge tube. To lyse the viral particles, 560 µL of Buffer AVL containing carrier RNA was added to the sample, and the mixture was vortexed for 15 s. The lysate was incubated at room temperature for 10 min to ensure complete lysis. After incubation, the tube was briefly centrifuged to remove droplets from the lid.

For RNA binding, 560 µL of ethanol (96–100%) was added to the lysed sample, and the mixture was vortexed for 15 s. The tube was centrifuged briefly to remove droplets, and 630 µL of the mixture was carefully transferred to a QIAamp spin column placed in a 2 mL collection tube, ensuring the rim of the spin column remained dry. The spin column was centrifuged at 8,000 rpm for 1 min, and the flow-through was discarded. The spin column was then returned to the same collection tube.

Washing was performed by adding 500 µL of Buffer AW1 to the spin column and centrifuging at 8,000 rpm for 1 min. The flow-through was discarded, and the spin column was returned to the collection tube. Next, 500 µL of Buffer AW2 was added to the spin column, and the column was centrifuged at maximum speed (14,000 rpm) for 3 min. The flow-through and collection tubes were discarded after this step. To dry the spin column membrane, the spin column was placed in a new 2 mL collection tube and centrifuged at maximum speed (14,000 rpm) for 1 min.

To elute the RNA, the spin column was transferred to a new 1.5 mL microcentrifuge tube, and 60 µL of Buffer AVE (elution buffer) was carefully added to the centre of the spin column membrane without touching the rim. The column was incubated at room temperature for 1 min and centrifuged at 8,000 rpm for 1 min to elute the RNA. The eluted RNA was stored at –20 °C

or –80 °C for long-term storage, with care taken to avoid repeated freeze-thaw cycles to maintain RNA integrity.

2.3.3 Reverse transcription

Total RNA samples were thawed on ice before reverse transcription. Complementary DNA (cDNA) synthesis was performed using the QuantiTect Reverse Transcription Kit (Qiagen, UK) according to the manufacturer's instructions, with special attention paid to ensure the complete removal of contaminating genomic DNA (gDNA). For gDNA elimination, 1 µg of total RNA was combined with 2 µL of gDNA Wipeout Buffer (provided in the kit) and RNase-free water to achieve a final volume of 14 µL. This mixture was incubated at 42 °C for 2 min to degrade contaminating DNA and immediately placed on ice to halt the reaction. A reverse transcription master mix was prepared on ice by combining 1 µL of Quantiscript Reverse Transcriptase, 1 µL of RT Primer Mix, and 4 µL of Quantiscript RT Buffer per reaction. Next, 6 µL of this master mix was added to each gDNA-treated RNA sample, resulting in a final reaction volume of 20 µL. Reverse transcription was carried out at 42 °C for 15 min to synthesise cDNA, followed by a heat inactivation step at 95 °C for 3 min. The resulting cDNA was either used immediately for a relative quantitative real-time PCR (qRT-PCR) analysis or stored at –20 °C for later use. All steps were performed under RNase-free conditions to maintain RNA integrity and ensure reproducibility of downstream analyses.

2.3.4 Quantitative real-time PCR

Relative qRT-PCR was performed to measure target gene expression levels relative to those of internal reference genes. All reactions were set up in duplicate on a 96-well plate, with cDNA aliquots and primers (Appendix table 1.2) thawed on ice immediately before use to preserve integrity. Each 10-µL reaction contained 2 µL of cDNA template, 5 µL of 2x qPCRBIO

SyGreen Blue Mix (PCRBiosystems, UK), 0.4 µL of the forward primer (10 µM), 0.4 µL of the reverse primer (10 µM), and 2.2 µL of nuclease-free distilled water (ddH_2O). After the addition of the primer, the plate was sealed with optically clear PCR film and briefly centrifuged to collect the reaction mixture at the bottom of each well. A second brief centrifugation was performed following the addition of cDNA to ensure homogeneity and prevent air bubbles. Amplification and detection were performed on a real-time PCR instrument using the cycling conditions outlined in Table 2.1. The programme included polymerase activation at 95 °C for 2 min. This was followed by 40 amplification cycles, each consisting of denaturation at 95 °C for 5 s and annealing/extension at 60 °C for 30 s. The cycle threshold (Ct) values obtained were normalised to the geometric mean of the housekeeping genes GAPDH and/or RPS11 for each sample. Relative expression levels were calculated using the $2^{(-\Delta\Delta C)}$ method (Pfaffl, 2001), relative to the mean of the mock cells. All data are presented as the mean and standard error of the mean (SEM).

Table 2.1 Reaction conditions for PCR

Stage Number	Description of Stage	Temperature	Length of Time	Number of cycles
1	Polymerase activation	95 °C	2 min	1
2	Denaturation	95 °C	5 s	40 cycles
3	Annealing/extension	60 °C	30 s	

2.3.5 Detection and monitoring of viral infection using real-time quantitative PCR

The absolute quantification of HCoV-OC43 and HCoV-229E RNA was conducted using the Superscript™ III Platinum® One-Step qRT-PCR Kit (Thermo Scientific, UK) following the manufacturer's instructions. Ten-fold serial dilutions of synthetic RNA standards corresponding to the nucleocapsid (N) gene sequences of HCoV-OC43 (VR-1558DQ) and HCoV-229E (BR740DQ) were prepared, ranging from 10^5 to 10^0 copies for HCoV-OC43 and 10^4 to 10^0 copies for HCoV-229E, and run in duplicate to create standard curves for quantification. Forward and reverse primers, along with TaqMan hydrolysis probes targeting conserved regions of the viral N gene, were obtained and synthesised by Sigma (UK). For HCoV-OC43, the primer sequences used were as follows: forward primer 5′-CGATGAGGCTATTCCGACTAGGT, reverse primer 5′-CCTTCCTGAGCCTTCAATATAGTAACC, and probe 5′-FAM-TCCGCCTGGCAGGTACTCCCT-TAMRA. For HCoV-229E, the primer sequences were as follows: forward primer 5′-CAGTCAAATGGGCTGATGCA, reverse primer 5′-AAAGGGCTATAAAGAGAATAAGGTATTCT, and probe 5′-FAM-CCCTGACGACCACGTTGTGGTTCA-TAMRA. All the primers used were reported in a study published by (Loo *et al.*, 2020b). Reactions were prepared by mixing the Platinum Taq mix with primers, probes and the RNA template in nuclease-free water. All the reactions were run in duplicate for both the standards and experimental samples. The qRT-PCR cycling conditions are shown in Table 2.3.

Table 2.2 Cycling conditions for the absolute quantification of HCoV-OC43 and HCoV-229E RNA

Stage Number	Step Description	Temperature	Time	Number of Cycles
1	Reverse transcription	55 °C	20 min	1
2	Polymerase activation	94 °C	2 min	1
3	Denaturation	94 °C	15 sec	40 cycles
4	Annealing	65 °C	30 sec	
5	Extension	68 °C	1 min	
6	Final denaturation	95 °C	15 sec	1
7	Final extension	68 °C	5 min	1

2.3.6 RNA sequencing (RNA-seq) and downstream analysis

Approximately 1 µg of high-quality total RNA from each sample was used for constructing the sequencing library. mRNA enrichment was performed using poly(A) selection to isolate coding transcripts, and sequencing libraries were prepared by Novogene (Cambridge, UK) according to standard Illumina protocols. Libraries were sequenced on an Illumina platform to generate paired-end reads, with output provided in FASTQ format for downstream analysis.

2.3.6.1 Data import and pre-processing

Raw sequencing reads were imported into Partek Flow (version 10.0, build 10.0.23.0531; Partek Inc., St. Louis, MO, USA) for quality assessment and processing. Initial quality control

(QC) utilised the pre-alignment QA/QC module, which produced summaries of base quality scores, GC content distribution, read length distribution and per-base sequence composition. Quality metrics were inspected to identify potential anomalies such as low Phred scores, abnormal GC content or overrepresented sequences. The reads were then processed using the Trim Bases function to remove low-quality bases with a Phred score < 20 from both the 5′ and 3′ ends, as well as adapter sequences identified from Illumina's adapter library. Reads shorter than 30 nucleotides after trimming were discarded to ensure the retention of informative sequences.

2.3.6.2 Read alignment

High-quality trimmed reads were aligned to the *Homo sapiens* reference genome (GRCh38/hg38) using the Spliced Transcripts Alignment to a Reference (STAR) aligner (version 2.7.8a) within Partek Flow. Default settings were applied, enabling spliced alignments to capture exon–intron junctions characteristic of eukaryotic transcripts. Multimapping was restricted to a maximum of 10 genomic loci, and a mismatch tolerance of two bases per read was applied. Alignment statistics, including the total mapping rate, percentage of uniquely mapped reads and distribution across genomic features, were reviewed to verify mapping quality.

2.3.6.3 Gene quantification and normalisation

Gene-level quantification was performed using Partek Flow's Quantify to Annotation Model function with the Ensembl Transcripts annotation model (release 104 v2) as the reference transcriptome. The expectation–maximisation (E/M) algorithm was used to assign reads to genes, accounting for multi-mapping events and overlapping exons to ensure accurate count estimation. To correct for sequencing depth differences and RNA composition bias, raw read

counts were normalised using the counts per million method. Normalised data distributions were visualised to confirm consistency across biological replicates.

2.3.6.4 Principal component analysis

To explore global transcriptional variation and detect potential outliers, a principal component analysis (PCA) was performed in Partek Flow using the normalised expression matrix. The first two or three principal components were plotted in two- and three-dimensional scatterplots, with samples coloured by experimental group to evaluate clustering patterns. The PCA was used to assess the influence of experimental conditions, identify batch effects and confirm sample quality before proceeding to the differential expression analysis.

2.3.6.5 Differential gene expression analysis

A differential expression analysis was carried out using the Gene Specific Analysis module in Partek Flow. Experimental groups were defined based on treatment conditions and/or time points. For each gene, a negative binomial generalised linear model was fitted, and statistical significance was determined using Wald tests. P-values were adjusted for multiple hypothesis testing using the Benjamini–Hochberg method to control the false discovery rate (FDR). Genes were considered differentially expressed if they met the thresholds of FDR < 0.05 and an absolute fold change ≥ 2.

2.3.6.6 Gene set enrichment and pathway analysis

The biological significance of the differentially expressed genes (DEGs) was explored through a Gene Set Enrichment Analysis (GSEA) using Partek Flow's Enrichment Analysis tool. Analyses were performed against curated gene sets from the Molecular Signatures Database (MSigDB), including Hallmark, KEGG and Reactome collections. Enrichment scores were

calculated from ranked gene lists, and pathway significance was assessed using permutation testing, with pathways having an FDR < 0.05 reported as significantly enriched. A functional pathway analysis was conducted using the Gene Ontology (GO) database (http://geneontology.org/) and ShinyGO (http://bioinformatics.sdstate.edu/go/) to identify enriched Biological Processes (BPs), Molecular Functions (MFs), Cellular Components (CCs), as well as Kyoto Encyclopedia of Genes and Genomes (KEGG) pathways. The KEGG database is a comprehensive resource for understanding high-level biological functions and interactions, providing curated pathway maps that integrate molecular-level information from genomic, chemical and systemic functional datasets. Special focus was placed on pathways related to ISGs, type I IFN signalling and proinflammatory cytokines. Input gene identifiers (Ensembl IDs or Gene Symbols) were standardised to ensure compatibility with annotation databases, and enrichment results were retrieved for biological interpretation. Significant terms and pathways were visualised using enrichment plots, bar charts and pathway diagrams to support integration into the Results and Discussion sections.

2.3.7 R-based analysis

The data analysis was conducted using R (version 4.4.0) within the RStudio integrated development environment. The workflow encompassed data preprocessing, visualisation and a functional enrichment analysis, employing a suite of R packages tailored to each analytical step. Data were imported into R from comma-separated value (CSV) files using the *read.csv ()* function, followed by preprocessing to handle missing values and normalise the dataset as required. Missing values were addressed using the *na.omit()* function, ensuring a complete case analysis for downstream applications.

UpSet plots were generated using the UpSetR package to visualise set intersections. This approach was chosen to efficiently represent complex set relationships, particularly for overlapping gene sets or experimental conditions. The *upset ()* function was utilised, adjusting parameters to display the desired number of sets and intersections. Heatmaps were constructed to visualise patterns in the data, such as gene expression profiles or correlation matrices, using the pheatmap package. Rows scaled the data to emphasise relative differences and applied hierarchical clustering using Euclidean distance as the metric.

A functional pathway analysis was performed to identify biologically relevant pathways enriched within the dataset. The clusterProfiler package was employed for the GO enrichment analysis, with the *enrichGO()* function used to map genes to BPs, MFs, and CCs. The analysis was adjusted for multiple tests using the Benjamini–Hochberg method to control the FDR. The results were summarised and visualised using dot plots and bar plots generated by clusterProfiler and ggplot2.

Data visualisation was a critical analysis component facilitated by the ggplot2 package. Custom visualisations, including scatter plots, bar plots and line graphs, were created to explore trends and relationships within the data. The theme_minimal() function was applied to ensure clean and interpretable visual outputs. To enhance reproducibility, the R session information, including package versions, was recorded using the sessionInfo() function.

2.4 Protein and cytokine analysis

2.4.1 Protein isolation

Cells were lysed directly in RIPA buffer (Sigma-Aldrich, UK) to extract total protein from the cell culture samples. The culture medium was aspirated, and the monolayers were washed twice with cold PBS. Cold RIPA buffer supplemented with protease and phosphatase inhibitors (Thermo Scientific, UK) was added directly to each well, using approximately three to five

times the estimated pellet volume. The cells were then scraped to release their cellular contents. The lysate was collected into pre-chilled microcentrifuge tubes and incubated on ice for 30 min, with occasional gentle mixing to promote complete lysis. Following incubation, the samples were centrifuged at 12,000 *g* for 15 min at 4 °C to pellet insoluble debris and gDNA. The clear supernatant containing solubilised proteins was transferred to fresh tubes, and protein concentration was determined using a Bradford assay.

2.4.2 Determination of protein concentrations using the Bradford assay method

A 2 mg/mL (2000 µg/mL) stock solution of bovine serum albumin (BSA) (Sigma-Aldrich, UK) was used to construct the standard curve to measure the unknown samples. Eight standard solutions with different concentrations (2000, 1500, 1000, 750, 500, 250, 125 and 0 µg/mL) were prepared. Standards and samples were added in triplicate to a 96-well plate, with 5.0 µL of each standard or sample allocated per well. The Bradford reagent dye (1X) (Thermo Scientific, UK) was mixed by inverting the bottle, which assisted in dissolving the dye while avoiding the formation of dye-dye aggregates. Next, 250 µL of the mixture was dispensed into each well. The plate was incubated at room temperature for 5 min. The CLARIOstar microplate reader (BMG Labtech, Germany) was used to measure the protein concentration. Absorbance was measured at 595 nm using a single-wavelength mode rather than a dual-mode instrument. A standard curve was established using the $y = mx + c$ equation, with y denoting absorbance.

2.4.3 Preparation of 12% SDS–PAGE

The resolving and stacking gels were prepared sequentially to prepare a 12% SDS–PAGE gel for protein separation. First, the glass plates, spacers and casting stand were assembled, and a water test was conducted to ensure there were no leaks. For the 12% resolving gel, a mixture was prepared by combining 8 mL of 30% acrylamide/bis-acrylamide solution, 5 mL of 1.5 M Tris-HCl (pH 8.6), 6.6 mL of deionised water, 200 µL of 10% SDS, 200 µL of 10% ammonium

persulfate (APS) (Sigma-Aldrich, UK) and 5 µL of TEMED (Sigma-Aldrich, UK). The solution was mixed gently but thoroughly to avoid air bubbles and poured into the space between the glass plates, leaving approximately 1–2 cm from the top of the shorter glass plate for the stacking gel. The resolving gel was carefully overlaid with water to ensure a flat surface and allowed to polymerise for 20–30 min at room temperature.

Once the resolving gel had polymerised, a Whatman filter paper was used to suck up all the water at the top of the gel. For the 4% stacking gel, a mixture was prepared by combining 0.85 mL of 30% acrylamide/bis-acrylamide solution, 0.63 mL of 0.5 M Tris-HCl (pH 6.8), 3.5 mL of deionised water, 50 µL of 10% SDS, 100 µL of 10% APS and 5 µL of TEMED. The solution was mixed gently and poured onto the resolving gel. A clean comb was immediately inserted to form the wells, ensuring no air bubbles were trapped. The stacking gel was allowed to polymerise for 20–30 min at room temperature. After polymerisation, the comb was carefully removed, and the wells were rinsed with deionised water to remove any unpolymerised acrylamide. The gel was assembled in the electrophoresis apparatus, and the inner and outer chambers were filled with running buffer (1× Tris-Glycine-SDS).

2.4.4 SDS–PAGE

Once all the sample volumes had been determined to obtain a final concentration, the samples were prepared accordingly. The sample buffer (4X) (Invitrogen, UK) was added at a 1:4 ratio of the total volume, while the loading buffer (10X) (Invitrogen, UK) was added at a 1:10 ratio. The remaining volume was adjusted with water to reach a total volume of 16 µL per sample. The prepared samples, sample buffer, loading buffer and water were transferred to 1.5 mL Eppendorf tubes and briefly spun down (10–15 s) to eliminate air bubbles. The samples were then heated at 70 °C for 10 min. While the samples were heating, running buffer (1X) was prepared by diluting 100 mL of running buffer (10X) with 900 mL of Milli-Q water. The inner

chamber of the electrophoresis apparatus was filled with running buffer (1X) until the wells were completely covered. A 6 µL protein ladder (250 kDa) (Thermo Scientific, UK) was loaded into the first well, followed by 16 µL of each sample, ensuring the pipette tip was placed at the edge of the well to prevent overflow. An additional ladder was optionally added beside the last sample. The outer chamber was then filled with a running buffer (1X). Electrophoresis was initiated at 100 V for a few minutes, followed by an increase to 200 V for 1 h. While the transfer was running, PBST was prepared by dissolving two PBS tablets in 1 L of Milli-Q water and adding 1 mL Tween-20 (Sigma-Aldrich, UK).

2.4.5 Western blotting

A Bio-Rad transfer system was used for western blotting. While waiting for the SDS–PAGE run to complete, two pieces of Whatman filter paper were prepared for each gel and one nitrocellulose membrane. Once electrophoresis was complete, the gel was carefully removed using a gel knife and trimmed, taking care not to overtrim. The membrane, Whatman filter paper, gel and filter pads were soaked in transfer buffer comprising 2.4 g of Tris base, 14.2 g of glycine, 200 mL of methanol and 1 mL of 10% (w/v) SDS in distilled water, up to 1 L, and pre-cooled to 4 °C. A shallow tray filled with transfer buffer held the cassette. A pre-wetted filter pad was then added to the black side of the cassette, followed by a sheet of Whatman filter paper. The gel was carefully peeled off the electrophoresis chamber after marking the left corner with a blade and inverted onto the Whatman filter paper. Next, the gel had a membrane on top, with one of the corners cut out to confirm proper orientation. The transfer sandwich was completed with another Whatman filter paper and a filter pad on top of the membrane. The cassette was closed and inserted into the electrophoresis module, which was immersed in a tank (previously chilled to 4 °C with an ice block) filled with transfer buffer.

Protein was transferred at 100 V for 1 h for blotting onto the membrane. After transfer, the membrane was carefully removed with the protein side up. Blocking was performed using 5% non-fat milk in PBST (blocking buffer) for 1 h at room temperature with constant rocking. During this blocking step, a 5% BSA solution was prepared. The dilution factor and host species of the primary antibody were verified to ensure compatibility with the appropriate secondary antibody. For each membrane, 5 mL of 5% BSA was mixed with the designated volume of primary antibody, depending on its dilution factor. After blocking, the membrane was transferred to a 50 mL tube, ensuring it faced upward. The primary antibody solution was then added to the tube and incubated overnight at 4 °C on a rotator. All dilutions and antibodies used are provided in Appendix Table 1.3.

The following day, the primary antibody solution was transferred into a 15 mL tube for reuse, allowing up to three reuses with 20% fresh primary antibody. The membrane was washed in PBST five times for 5 min each or three times for 20 min each. A fresh 5% non-fat milk solution was prepared for the secondary antibody incubation. A 1:10,000 dilution of the appropriate secondary antibody (e.g., anti-rabbit) was prepared by adding 5 µL antibody per 50 mL of 5% non-fat milk. The membrane was incubated in the secondary antibody solution for 1 h at room temperature (maximum of 3 h) on a rotator. The secondary antibody was then removed and stored in a 50 mL tube, allowing up to two reuses at –20 °C. The membrane was washed five times for 5 min each in PBST. Following the final wash, the Enhanced Chemiluminescence (ECL) detection (Thermo Fisher, UK) reagent was prepared by mixing equal volumes of Solution A and Solution B (e.g., 500 µL each) and pipetting up and down to mix. The mixture was evenly spread over the membrane. The membrane was transferred into the image LI-COR Odyssey XF, where chemiluminescence detection was selected. A preview was performed to ensure the membrane was aligned correctly before acquiring an exposure image (set between 30-120 seconds). If no signal was detected, the exposure time was increased accordingly. Once

imaging was complete, the membrane was washed thrice for 5 min each to remove residual ECL reagents (Thermo Scientific, UK).

For housekeeping protein detection, a 5% BSA solution was freshly prepared. Housekeeping antibodies were selected based on molecular weight differences to ensure they did not overlap with the target protein. The membrane was placed in a 50 mL tube, ensuring it faced upward, and the primary antibody solution was added. The tube was then incubated overnight at 4 °C on a rotator. The western blotting protocol for Day 2 was repeated to detect housekeeping proteins. The molecular weight of the protein was estimated using the PageRuler™ Plus Prestained Protein Ladder (Thermo Fisher, UK).

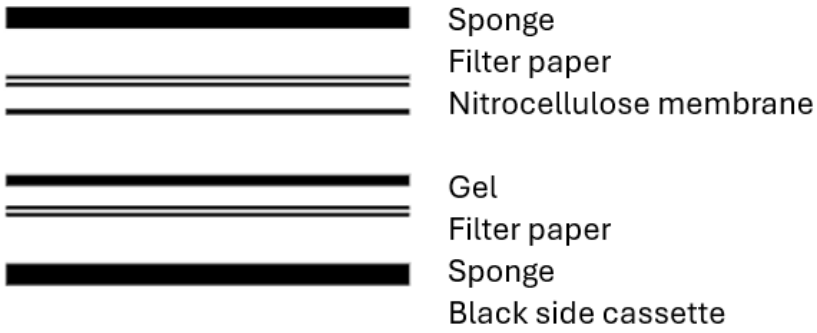

Figure 2.2: Schematic of western blot transfer "sandwich"

The gel membrane assembly is arranged as follows (from the cathode side toward the anode side): a sponge pad, two layers of filter paper, the nitrocellulose membrane, the polyacrylamide gel, two more layers of filter paper, a second sponge pad, all enclosed within the black-side cassette. This configuration ensures uniform contact and efficient electrotransfer of proteins from the gel onto the membrane.

2.4.6 Human XL cytokine antibody array assay.

A human cytokine antibody array (covering 105 cytokines) (Table 2.3) was performed using a kit from R&D Systems (Biotechne) to detect multiple cytokines in the cell culture supernatant, following the manufacturer's instructions. In brief, the array membranes were first incubated at room temperature for 1 h in a blocking buffer. Meanwhile, the cell culture supernatant was collected, centrifuged, and prepared according to the kit guidelines. The prepared samples were diluted in array buffer 6 and then applied to the membranes for overnight incubation at 4 °C on a rocking platform shaker. After incubation, the membranes were washed three times for 10 min each in 1x wash buffer. They were then treated with a detection antibody and incubated with streptavidin-HRP and a chemi reagent mix. Excess reagents were removed by washing, and the membranes were exposed to chemiluminescent detection reagents for 1 minute. Images of the membranes were captured for analysis, and the intensity of each spot was measured using ImageJ software (National Institutes of Health, Bethesda, MD, USA), with adjustments for background and normalisation to the positive control spots.

Table 2.3 – The alignment of 105 cytokines on the human XL cytokine array

	1 2	3 4	5 6	7 8	9 10	11 12	13 14	15 16	17 18	19 20	21 22	23 24
A	Positive Control	Acrp30	ApoA1	Angiogenin	Ang-1	Ang-2	Blys	BDNF	C5	CD14	CD30	Reference Spots
B		CD40L	CHI3L1	Adipsin	CRP	Cripto-1	CST3	Dkk-1	CD26	EGF	CD147	
C		CXCL5	CD105	CD178	FGF-2	KGF	FGF-19	FLT3LG	CSF3	MIC-1	CSF2	
D	CXCL1	GH	SF	CD54	IFNG	IGFBP-2	IGFBP-3	IL-1F1	IL-1F2	IL-1F3	IL-2	IL-3
E	IL-4	IL-5	IL-6	CXCL8	IL-10	IL-11	IL-12	IL-13	IL-15	IL-16	IL-17A	IL-18 Bpa
F	IL-19	IL-22	IL-23	IL-24	IL-27	IL-31	IL-32	IL-33	IL-34	IP-10	CXCL11	PSA
G	Leptin	LIF	NGAL	CCL2	CCL7	CSF1	MIF	CXCL9	CCL3	CCL20	CCL19	CLG4B
H	MPO	OPN	PDGF-AA	PDGF-AB	PTX3	CXCL4	RAGE	CCL5	RBP-4	RLN2	ADSF	CXCL12
I	Serpin E1	ABP	ST2	CCL17	TFF3	CD71	TGFA	TSP-1	TNFSF1A	PLAUR	VEGF	
J	Reference Spots		VDB	CD31	TIM-3	CD106						Control (-)

2.4.7 Human phosphokinase array assay

The phosphokinase array utilised the Proteome Profiler Human Phospho-Kinase Array Kit (Biotechne, UK) to assess the relative phosphorylation levels of various kinases and their substrates (Table 2.4). MRC-5 cells were plated in 6-well plates at a density of 2×10^5 cells per

well and incubated overnight in complete DMEM containing 10% FBS and penicillin-streptomycin at 37 °C with 5% CO_2. Cells underwent treatment under specified experimental conditions for designated time points. After treatment, the cells underwent two washes with ice-cold PBS to eliminate residual media and were subsequently incubated on ice. The lysis buffer was prepared by combining the supplied lysis buffer with protease and phosphatase inhibitors according to the manufacturer's instructions. Cells were lysed by adding 300 µL of supplemented lysis buffer to each well, followed by gentle rocking on ice for 30 min to ensure complete lysis. Lysates were obtained through scraping and subsequently transferred to pre-chilled microcentrifuge tubes. The samples underwent centrifugation at 14,000 × g for 10 min at 4 °C to eliminate debris, and the resulting clarified supernatant was collected for subsequent analysis. Protein concentrations were quantified using the BCA protein assay (Thermo Scientific, Cat. No. 23227) to ensure uniform sample loading. Each sample was diluted with 1.5 mL of Array Buffer 1 provided in the kit, containing 200-300 µg of protein. The phosphokinase array membranes underwent pre-blocking by incubation in 2 mL of Array Buffer 1 at room temperature for 1 h on a rocking platform. After blocking, the membranes were incubated overnight at 4 °C on a rocking platform with the prepared lysate samples to facilitate the binding of phosphorylated proteins to their corresponding capture antibodies immobilised on the membrane. Following overnight incubation, the membranes underwent three washes with 20 mL of the provided Wash Buffer, each lasting 10 min, to eliminate unbound proteins. The detection antibody cocktail was prepared following the manufacturer's instructions, with 2 mL added to each membrane. The membranes were incubated with detection antibodies for 2 h at room temperature on a rocking platform. After antibody binding, the membranes underwent three additional washes with Wash Buffer to eliminate excess detection antibodies. A Streptavidin-HRP solution was prepared, and 2 mL was added to each membrane. The membranes were then incubated for 30 min at room temperature with gentle

rocking. The membranes underwent thorough washing to eliminate unbound HRP-conjugates and mixing and applying chemiluminescent detection reagents. The membranes were then exposed to a chemiluminescent substrate for one minute and then visualised with a LI-COR (Biosciences). Signal intensity for each spot was quantified utilising ImageJ software. Spot intensities were normalised to the reference spots on the array and analysed following the manufacturer's guidelines to ascertain relative levels of kinase phosphorylation (R&D Systems, 2023).

Table 2.4 The alignment of the 46 human phosphokinase array

Membrane A	1 2	3 4	5 6	7 8	9 10	Membrane B	11 12	13 14	15 16	17 18
A	RS						Akt1/2/3(T308)	Akt 1/2/3 (S473)		RS
B		CREB (S133)	EGF R (Y1086)	eNOS (S1177)	ERK1/2 (T202/Y204, T185/Y187)		Chk-2 (T68)	c-Jun (S63)		
C		Fgr (Y412)	GSK-3α/β (S21/S9)	GSK-3β (S9)	HSP27 (S78/S82)		p53 (S15)	p53 (S46)	p53 (S392)	
D		JNK1/2/3 (183/Y185, T221/Y223)	Lck (Y364)	Lyn (Y397)	MSK1/2 (S376/S360)		p70 S6 Kinase (T389)	p70 S6 Kinase (T421/S424)	PRAS40 (T246)	
E		p38α (T180/Y182)	PDGF Rβ (Y751)	PLCγ1 (Y783)	Src (Y419)		PYK2 (Y402)	RSK1/2 (S221/S227)	RSK1/2/3 (S380/S386/S377)	
F		STAT2 (pY690)	STAT5a/b (Y694/Y699)	WNK1 (T60)	Yes (Y426)		STAT1 (Y701)	STAT3 (Y705)	STAT3 (S727)	
G	RS	β-Catenin			PBS (NC)		STAT6 (Y641	HSP60		PBS (NC)

Key: RS (Reference Spot); NC (Negative control)

2.4.8 Immunofluorescence assay targeting OC43 N antibody

MRC-5 cells, seeded in a 12-well plate, underwent pretreatment with 1000IU/mL of rIFN-α for 24 h before infection with HCoV-OC43 (MOI: 0.1). Additionally, a parallel set of cells was solely infected with HCoV-OC43 (MOI: 0.1) overnight. The following day, the supernatant was carefully removed, and the cells were washed once with PBS. Subsequently, cells were fixed in 4% paraformaldehyde at 4 °C for 30 min, followed by three washes with PBS. To enable intracellular staining, cells were permeabilised with 0.5% Triton X in PBS for 10 min and washed three times with PBS. Blocking was then performed using a blocking buffer (0.1%

Tween, 2% BSA) for 30 min. Immunostaining begins with the addition of HCoV-OC43 N antibody (MAB9013) diluted 1:1000 in PBS-T, and the cells are incubated overnight at 4 °C. After three PBS washes, a secondary antibody (AlexaFluor), diluted 1:750 in PBS with 2% BSA, was added, and cells were incubated for 1 h at room temperature in the dark. Following another three washes with PBS, a drop of Prolong Diamond Antifade Mountant with DAPI (fluorescent stain) (Invitrogen, UK) was applied for nuclear staining. The imaging process was carried out using EVOS 5000 microscopy (Invitrogen, UK) to analyse the immunofluorescent signals comprehensively.

2.4.9 Dual Glo luciferase assay.

HEK293T cells were seeded into 96-well plates at a density of 1×10^4 cells/well and incubated for 24 h before transfection. Each well was transfected with 200 ng/well of pISRE-Luc, pNF-κB-Luc, or pIFNβ-Luc plasmid, co-transfected with 20 ng/well of Renilla luciferase plasmid as an internal control, using FuGENE HD transfection reagent (Promega, UK) according to the manufacturer's protocol. After 24 h post-transfection, the cells were infected with live HCoV-OC43 or heat-inactivated OC43 at an MOI of 1 and incubated for 48 h. Following the infection period, cells were treated with 1000 IU/mL of IFN-α for pISRE-Luc for 24 h, poly I: C for pIFNβ-Luc for 24 h, and PMA for pNF-κB-Luc for 30 min to stimulate specific signalling pathways. At the end of the 98 h experimental period, cells were lysed with 25 µL of Dual-Glo® Luciferase Assay System (Promega, UK) and incubated with gentle shaking for 15 min. The lysate was transferred to 96-well microplates, and luminescence was measured to assess Firefly luciferase activity. Subsequently, 20 µL of Dual-Glo Stop and Glo reagent (Promega, UK) was added to each well and incubated under the same conditions to measure Renilla luminescence for normalisation. Luminescence readings were obtained using the FLUOstar® Omega plate reader (BMG Labtech, Germany). For data processing, Firefly luciferase readings were first normalised to the corresponding Renilla luciferase readings for each well to control

for transfection efficiency and cell number variation. Background luminescence from untransfected wells was subtracted from all values. Relative luciferase activity was then calculated as fold induction compared to untreated control wells for each plasmid type. Data are presented as mean ± SEM from biological replicates.

2.5 Clustered Regularly Interspaced Short Palindromic Repeats/CRISPR-associated-9 (CRISPR/Cas9) construction

The gRNA sequences targeting IFNAR, IRF3, MAVS, TBK1, and DDX58 were designed using the online CRISPR tool in Cas-designer (http://www.rgenome.net/cas-designer). Sequence details are provided in Table 2.5. The oligos were ordered from Eurofins Scientific.

Table 2.5 List of oligonucleotides used for CRISPR

Gene names	Forward oligos	Reverse Oligos
IFNAR 1	CACCGTGCGCGAACATGTAACTGG	AAACCCAGTTACATGTTCGCGCAC
IFNAR 2	CACCGTAACTGGTGGGATCTGCGG	AAACCCGCAGATCCCACCAGTTAC
IFNAR 3	CACCTGCGCGAACATGTAACTGGT	AAACACCAGTTACATGTTCGCGCA
IFNAR 4	CACCACGGGGCGATGGCGGCTGAG	AAACCTCAGCCGCCATCGCCCCGT
IRF3 1	CACCTAGGGGCGGGAACAGCCCAG	AAACCTGGGCTGTTCCCGCCCCTA
IRF3 2	CACCTAACAGACCCAAAAGCCGAT	AAACATCGGCTTTTGGGTCTGTTA
IRF3 3	CACCGTAACAGACCCAAAAGCCGA	AAACTCGGCTTTTGGGTCTGTTAC
IRF3 4	CACCAGACCCAAAAGCCGATGGGA	AAACTCCCATCGGCTTTTGGGTCT
MAVS 1	CACCGATCTTACCTCGGGTACCCC	AAACGGGGTACCCGAGGTAAGATC

MAVS 2	CACCCCGGGAAGCGATCTTACCTC	AAACGAGGTAAGATCGCTTCCCGG
MAVS 3	CACCGTACCCCCGGCCCTGAGACC	AAACGGTCTCAGGGCCGGGGGTAC
MAVS 4	CACCTCGCCAGGTCTCAGGGCCGG	AAACCCGGCCCTGAGACCTGGCGA
TBK1 1	CACCCTGAGTCTCGAGGAGGCCGC	AAACGCGGCCTCCTCGAGACTCAG
TBK1 2	CACCGGTCTCCGCCGCGCCACCGC	AAACGCGGTGGCGCGGCGGAGACC
TBK1 3	CACCGCGGTGGCGCGGCGGAGACC	AAACGGTCTCCGCCGCGCCACCGC
TBK1 4	CACCAGGCCGCGGGAGCCCGCCGG	AAACCCGGCGGGCTCCCGCGGCCT
DDX58 1	CACCGGATTATATCCGGAAGACCC	AAACGGGTCTTCCGGATATAATCC
DDX58 2	CACCCTTCCGGATATAATCCTGGA	AAACTCCAGGATTATATCCGGAAG
DDX58 3	CACCCAGGCTGCGTCGCTGCTCGG	AAACCCGAGCAGCGACGCAGCCTG
DDX58 4	CACCGGGTCTTCCGGATATAATCC	AAACGGATTATATCCGGAAGACCC

2.5.1 Annealing of oligonucleotide pairs

The annealing of oligonucleotide pairs involved combining 1 µL of forward oligonucleotide (100 µM), 1 µL of reverse oligonucleotide (100 µM), and 8 µL of sterile water to create a 10 µL mixture. These mixtures underwent thermal annealing at 95 °C for 5 min and were left at room temperature for 1 h to cool.

2.5.2 Plasmid digestion using BbsI

For plasmid digestion using BbsI, 2 µL of 10X buffer provided with the restriction enzyme BbsI, which cleaves after recognising the palindromic DNA sequence ‘GAAGAC,’ was added

to 1 µg of the pAC152 plasmid (Figure 2.3) (Cheng *et al.*, 2013). Sterile water was added to reach a final volume of 20 µL, and the reaction was incubated at 37 °C for 1 hour.

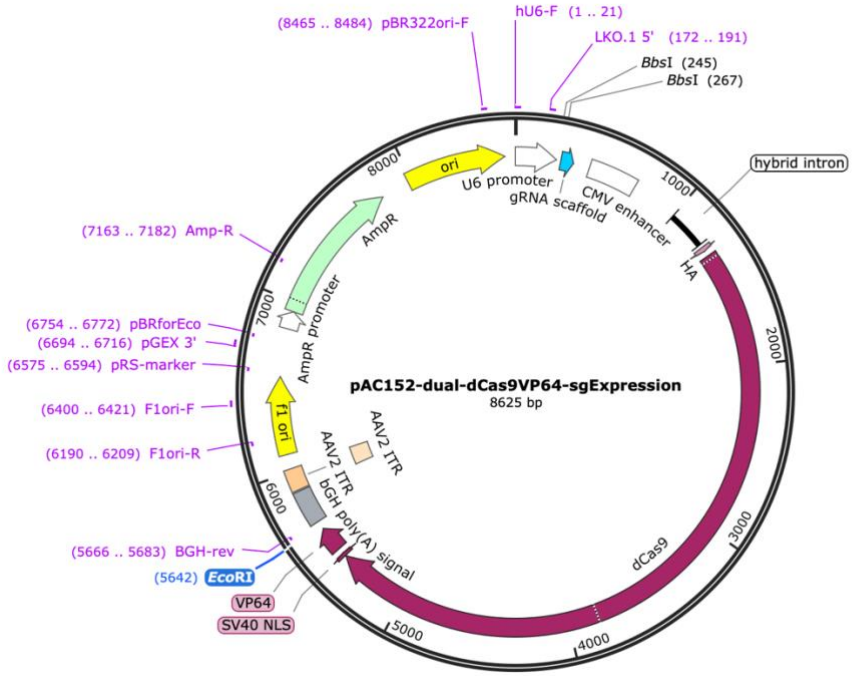

Figure 2.3: Dual expression construct expressing dCas9VP64 and sgRNA from separate promoters. The plasmid shows a restriction site for the oligonucleotides.

2.5.3 Ligation of annealed oligos

Following plasmid digestion, the annealed oligos were ligated into the digested plasmid. This involved adding 2.5 µL of the 10X T4 ligase buffer to 1 µL of each annealed oligo (final concentration of 0.4 µM), and 1.5 µL of T4 DNA ligase was added to the mixture. The reaction was incubated at 37 °C for 1 h.

2.5.4 Transformation in *E. coli cultures*

For transformation in *E. coli,* 2 µL of the ligation reaction was transformed into 25 µL of TOP10 One Shot chemically competent *E. coli* (Invitrogen) cells and mixed. Transformation reactions were incubated on ice for 15 min, heat-shocked for 30 seconds at 45 °C and immediately transferred to ice. Then, 250 µL of SOC medium (Invitrogen, UK) was added, and the tubes were placed on a platform shaker at 37 °C for 30 min. 50 µL from the transformation mixture was spread onto selective media plates (Luria Agar (Sigma-Aldrich, UK) containing 100 µg/ml ampicillin), followed by overnight incubation at 37 °C. The next day, plates were stored in cold storage, colonies were picked, and cultures were initiated in universal bottles. The same steps were repeated for controls containing empty plasmids.

2.5.5 Generation of competent cells

Competent cells were generated utilising the calcium chloride method. A 10 mL culture of LB medium was inoculated with either a glycerol stock or a single colony from an agar plate and incubated overnight at 37 °C in a shaking incubator set to 180 rpm. The following day, 1 mL of the overnight culture was used to inoculate 100 mL of fresh LB medium. This mixture was incubated at 37 °C in a shaking incubator at 180 rpm until the culture achieved an OD600 of 0.4-0.6, indicative of the mid-log phase, which took approximately 2.5-3 h. Cells were collected via centrifugation at 4000 rpm for 20 min at 4 °C. The pellet was resuspended in 20 mL of ice-cold 100 mM calcium chloride ($CaCl_2$) and incubated on ice for 20 min. Cells were centrifuged at 4000 rpm for 20 min at 4 °C and resuspended in 2.4 mL of ice-cold 100 mM $CaCl_2$ containing 20% glycerol. Aliquots of 50 µL were prepared in sterile, pre-chilled microcentrifuge tubes, flash-frozen in dry ice, and subsequently stored at –80 °C until required. All procedures involving $CaCl_2$ were conducted on dry ice to preserve cell viability and competency.

2.5.6 Plasmid DNA isolation

Plasmid DNA extraction from *E. coli* cells was performed using the GeneJET Miniprep kit (Thermo Fisher, UK) following the manufacturer's instructions. Overnight cultures (5 mL) with plasmid and control cultures without inserts were utilised. In 2 x 2 ml microcentrifuge tubes, 2 mL of culture was transferred, and after centrifugation at 13,400 rpm for 1 minute, the supernatant was discarded. The cell pellet was resuspended by vortexing the bacterial cells in 250 µL of resuspension buffer (with RNAse A). Subsequently, 250 µL of lysis solution and 350 µL of neutralisation solution were added and mixed. After centrifugation at 13,400 rpm for 10 min, the supernatant was collected in GeneJET columns. It was centrifuged for 1 minute, and the flow-through was discarded. The column was washed thrice by adding 0.5 mL of wash buffer. DNA was eluted by adding 30 µL of water to each column, and after centrifugation for 2 min, the concentration of plasmid DNA was measured using a Nanodrop and stored at –20 °C.

2.5.7 Restriction enzyme digestion and gel electrophoresis

2.5.7.1 Agarose gel preparation

A 0.8% agarose gel was prepared using 1X TAE buffer, with the volume of agarose and buffer adjusted based on the requirement for a mini gel (8 wells) or a midi gel (20 wells). The mixture was heated until boiling in a microwave, allowed to cool for 5-10 min, poured into the gel case and combs, ensuring the absence of air bubbles, and allowed to solidify for 20-30 min.

2.5.7.2 Gel electrophoresis setup

The electrophoresis tank was filled with 1X TAE buffer to cover the gel fully. GeneRuler 1Kb DNA ladder (Thermo Fisher, UK) mixed with GelRed dye (Biotium cat: 4200) was loaded into lane 1. GelRed dye could also be added to restriction digest samples before incubation at 37 °C.

2.5.7.3 Restriction digest and sample loading

A Master Mix for 30 reactions consisted of 10X Reaction Buffer (New England Biolabs cat: B72025), GelRed DNA dye (Biotium), MilliQ Water, BbsI, and EcoRI enzymes. Each reaction involved adding 200-500 ng of DNA to a clean tube, followed by adding the Master Mix. After incubation at 37 °C for 1 h, 6X DNA Loading Buffer (Thermo Fisher, UK) was added to the samples as shown in Table 2.6

Table 2.6 Required volumes for each component in preparing the master mix for restriction digestion

	Undigested Control	Double digest	Master mix (30 reactions)
Bbsl	---	0.5	15
EcoR1	---	0.5	15
Plasmid DNA	2(200-500ng)	2(200-500ng)	---
10X Reaction buffer	1	1	30
Gel Red (1:10,000 dilution)	5	5	150
Sterile water	2	1	30
Total Volume	10	10	240

2.5.7.4 Running of gel electrophoresis

The samples, including the DNA ladder 1 KB (Thermo Fisher, UK), were loaded onto the gel, and electrophoresis was carried out at specified voltage settings. The gel was run until the dye line had migrated approximately 75-80% down the gel. The power was turned off, the electrodes disconnected, and the gel carefully removed from the tank.

2.5.7.5 Visualisation and Analysis

The gel was visualised using a UV transilluminator at 302 or 312 nm. Successful cloning was confirmed by a single band near the top of the gel exceeding 10 kb. The negative control, empty plasmid pAC152, typically showed two bands at approximately 6-7 and 4-5 kb.

2.5.8 Transfection of plasmids into mammalian cells

One day before transfection, 0.5×10^6 cells were seeded in 12-well plates and incubated overnight to reach 50-70% confluency. The cells were transfected with 0.5 µg, 1 µg, and 1.5 µg of plasmid DNA using 2.5 µL of Lipofectamine 3000 according to the manufacturer's instructions (Thermo Fisher, UK). After 48 h, the cells were stimulated with 1,000 U/mL of IFNα overnight. At 72 h, the cells were visualised with EVOS 5000 microscopy, and RNA was subsequently isolated using Trizol.

2.5.9 Scratch assay

The Incucyte® 96-Well Scratch Wound Migration Assay (Sartorius, UK) was performed to assess the effects of gene knockouts on cell migration. Cells with specific gene knockouts targeting key genes of interest were used to evaluate the migratory capabilities compared to control wells. Cells were seeded at a density of 20,000 cells per well into a 96-well Plate and incubated in a standard cell culture incubator at 37 °C with 5% CO_2 for 6-18 h to allow cell

attachment and the formation of a confluent monolayer. After incubation, the plate was removed, and uniform wounds were created in each well using the Incucyte® 96-Well Woundmaker Tool, following the manufacturer's wounding procedure to ensure precise and reproducible wound formation.

Following wounding, the media was carefully aspirated from each well, and the wells were gently washed twice with fresh culture media to remove dislodged cells and prevent their reattachment. After washing, 100 µL of fresh culture media was added to each well. Any bubbles in the assay plate were carefully removed to ensure optimal imaging conditions. The plate was then placed into the Incucyte® Live-Cell Analysis System, and cell migration was monitored and quantified at regular intervals over the desired time course. Data were analysed using Incucyte® software to determine the rate and extent of wound closure.

2.6 Statistical analyses

All statistical analyses and data visualisations were performed using GraphPad Prism software (version 10.1; GraphPad Software, San Diego, CA, USA). Before applying statistical tests, all datasets were assessed for normality using the Shapiro-Wilk test to determine whether the data met the assumptions of a parametric distribution. Where the assumption of normality was met, parametric statistical tests were applied; otherwise, non-parametric tests were used. For comparisons involving more than two groups, either one-way or two-way analysis of variance (ANOVA) was performed, depending on the number of independent variables. One-way ANOVA was used for single-factor experiments, whereas two-way ANOVA was used for multifactorial designs (e.g., comparing multiple treatments across different time points or temperatures). Where ANOVA indicated a statistically significant overall effect, appropriate post hoc tests were performed, Tukey's multiple comparisons test for pairwise group comparisons in balanced designs, or Sidak's multiple comparisons test where fewer

comparisons were required. For data that did not pass the normality test, non-parametric equivalents were applied. The Kruska-Wallis test was used as the non-parametric alternative to one-way ANOVA, followed by Dunn's post hoc test for multiple comparisons. For two-group comparisons, an unpaired Student's t-test was used for normally distributed data. At the same time, the Mann-Whitney U test (Wilcoxon rank-sum test) was applied for non-parametric data. In cases involving paired measurements, the paired t-test (parametric) or Wilcoxon signed-rank test (non-parametric) was used, depending on normality.

For all statistical tests, a P-value of ≤ 0.05 was considered statistically significant and is denoted in figures as follows: $p \leq 0.05$ (*), $p \leq 0.01$ (**), $p \leq 0.001$ (***), and $p \leq 0.0001$ (****). All experiments were conducted with at least two replicate samples per group and repeated independently at least twice to ensure reproducibility. The statistical test applied to each dataset, along with the number of replicates and the specific post hoc test (if applicable), is stated in the corresponding figure legend in the results section.

Chapter 3

Optimising viral culture techniques for HCoV-OC43 and HCoV-229E: insights into propagation and quantification

3.1 Introduction

Human coronaviruses (HCoVs) have been recognised as respiratory pathogens since the 1960s, when HCoV-229E and HCoV-OC43 were first identified (Weiss and Leibowitz, 2011; Buckall *et al.*, 1972). Among the seven known human coronaviruses, HCoV-OC43, -HKU1, -229E, and -NL63 are classified as seasonal coronaviruses (HCoVs) and generally cause mild to moderate respiratory infections, particularly in vulnerable individuals. In contrast, strains like SARS-CoV, MERS-CoV, and SARS-CoV-2 can cause severe disease (Bhardwaj, 2020). Historically, HCoVs attracted limited research attention due to their mild disease presentation and the difficulty of sustaining robust replication *in vitro* (Fung and Liu, 2019). However, the emergence of SARS-CoV-2 has renewed interest in HCoVs, both as surrogate models and as valuable comparators for studying host-virus interactions (Bracci *et al.*, 2020; Fausto *et al.*, 2023). Their classification as Biosafety Level 2 (BSL-2) pathogens further makes them accessible for detailed laboratory investigation (Greenberg, 2016).

SARS-CoV-2 and HCoV-OC43 share similarities as members of the Betacoronavirus genus (Lu *et al.*, 2020). Both viruses can be transmitted through respiratory droplets, and they can replicate in the cells lining the respiratory tract of humans (Kutter *et al.*, 2018). While HCoV-OC43 generally causes mild upper respiratory infections, it can occasionally lead to severe conditions such as necrotising encephalitis, particularly in immunocompromised individuals (Bracci *et al.*, 2020). Studies on the neurotropic and neuroinvasive properties of HCoV-OC43 have highlighted its ability to cause cytopathic effects in human neural cells, especially in animal models (Jacomy and Talbot, 2003). Due to its structural and replication similarities with SARS-CoV-2, the American Society for Testing and Materials (ASTM) has concluded that

human coronavirus HCoV-OC43 is an appropriate surrogate for SARS-CoV-2 research (Schirtzinger *et al.*, 2022).

For this study, HCoV-OC43 was chosen both as a model of general coronavirus biology and as a practical surrogate for SARS-CoV-2. Like other HCoVs, HCoV-OC43 shares important structural and functional features with SARS-CoV-2, including comparable cellular tropism and infection mechanisms (Forni *et al.*, 2021b). At the same time, its reduced pathogenicity and lower biosafety requirements allow systematic exploration of viral replication dynamics, host responses, and experimental optimisation in standard laboratory conditions (Greenberg, 2016).

A common challenge in HCoV research is the production of sufficiently high-titre viral stocks for *in vitro* experiments. While methods for propagating HCoV-OC43, -229E, and -NL63 have been reported, they are often associated with low yields, inconsistent replication, and significant variability in outcomes between laboratories (Bracci *et al.*, 2020; Woo *et al.*, 2005). Studies have shown that cell line choice is a critical determinant of replication efficiency. HCoV-OC43 has been propagated in a variety of systems, including Mv1Lu (mink lung) (Bracci *et al.*, 2020), CHO (Chinese hamster ovary) (Butler *et al.*, 2006), HRT-18G (human colorectal adenocarcinoma) (Schirtzinger *et al.*, 2022), Vero (African green monkey kidney) (Hirose *et al.*, 2021), Huh7 (human hepatocellular carcinoma) (Savoie and Lippe, 2022), and MRC-5 (human lung fibroblasts) (Hu *et al.*, 2022b). Other lines, such as HEK293T and A549, have not been consistently reported to support HCoV-OC43 replication.

In addition to cell line differences, multiple titration approaches are used across laboratories, further contributing to variability. These include tissue culture infectious dose 50% ($TCID_{50}$) assays and plaque assays, with overlays such as agarose, methylcellulose, or Avicel applied at varying concentrations to promote plaque formation (*et al.*, 1979; Lambert, 2012; Fausto *et al.*, 2023). Detection methods range from immunoperoxidase staining to crystal violet, neutral red,

and immunofluorescence. Furthermore, incubation temperatures vary between 33 °C (to approximate the upper airway) and 37 °C (to model core body conditions), and infection durations span from 2 to 7 days, depending on cell line permissiveness and experimental goals. This lack of standardisation poses a significant barrier to HCoV research. Cell lines such as HRT-18G and Vero are highly permissive but lack immunocompetence, while human-derived MRC-5 cells provide a more physiologically relevant system for studying both replication and host immune responses (Collins, 1993; Kim *et al.*, 2019). Without a consensus approach, comparing results across studies remains difficult, and experimental reproducibility is limited.

In this chapter, I aimed to establish a reproducible and efficient system for HCoV-OC43 propagation and titration. Specifically, I compared replication efficiency across multiple cell lines, assessed cytopathic effect and viral yields, and optimised titration assays, including both $TCID_{50}$ and plaque assays with different overlays. The outcome of this optimisation provides the foundation for subsequent mechanistic studies on innate immune responses (Chapters 4-6).

3.2 Results

3.2.1 Propagation of HCoV-OC43 in different cell lines.

The first objective of my work was to compare the replication of HCoV-OC43 in different cell lines to identify a suitable *in vitro* model for subsequent experiments. Cells were initially incubated at 37 °C, and following HCoV-OC43 infection, the cultures were maintained at 33 °C to mimic the conditions of the upper respiratory tract (URT) and provide an optimal environment for viral replication. I observed variations in apparent cytopathic effects (CPE) among the different cell lines. In HRT-18G cells, less CPE, such as cell rounding or lysis, was observed (Figure 3.1). This suggests that HRT-18 cells may be less susceptible or more resistant to the infection compared to the other examined cell lines.

However, some cell lines displayed evident CPE following HCoV-OC43 infection. In MRC-5 cells, this included cell rounding, detachment, and progressive cell loss starting from day 2 and continuing through day 5 post-infection (Figure 3.1). Similarly, MV1Lu and HEK293T cells exhibited evident CPE, characterised by cell rounding and lysis, which commenced on day 2 and persisted until day 5. The cytopathic reactions observed in these cell lines indicate their increased vulnerability to HCoV-OC43, making them ideal for further studies on viral pathogenesis and host interactions.

However, no detectable CPE was observed in A549 and HRT-18G cells for the entire observation period. The lack of cytopathic effects in these cell lines may be attributed to their intrinsic resistance or reduced susceptibility to HCoV-OC43.

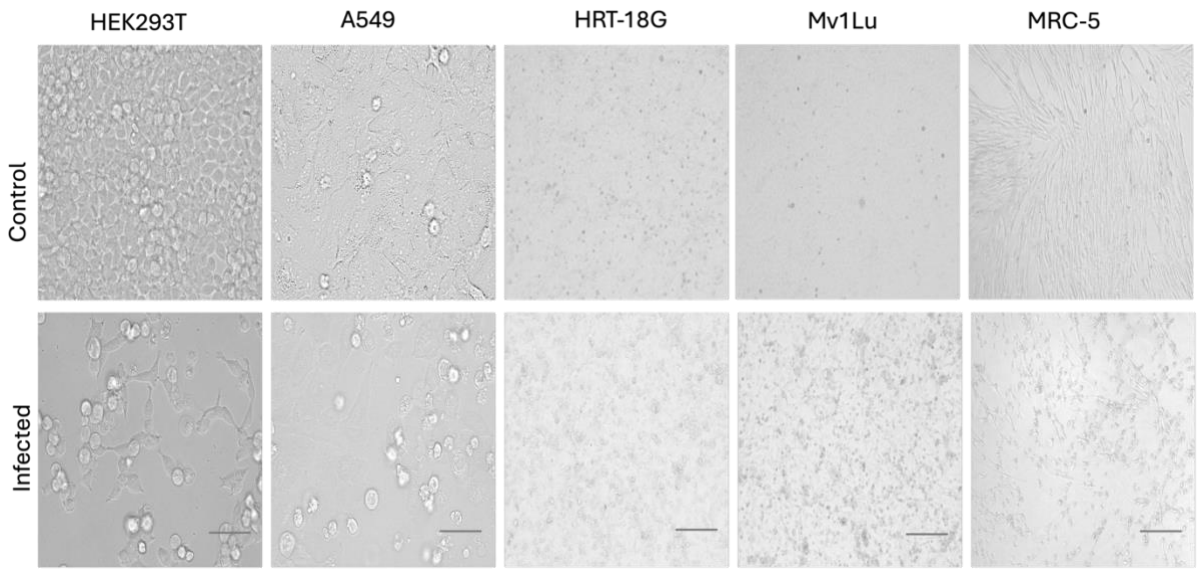

Figure 3.1: Comparison of HCoV-OC43 infection in various cell lines.

The figure displays images of different cell lines (HEK293T, A549, HRT-18G, Mv1Lu, and MRC-5). The control images show the morphology of uninfected cells, while the infected images demonstrate the cytopathic effects induced by HCoV-OC43 infection. Changes in cell morphology and cell death are evident in infected cells compared to those in the control group. Scale bars represent 75 µm.

3.2.2 Susceptibility and cytopathic effects of HCoV-229E infection in Mv1Lu and MRC-5 cell lines

To optimise growth conditions for HCoV-229E before infecting primary airway epithelial cells, I propagated HCoV-229E in two commonly used cell lines: Mv1Lu and MRC-5 (Figure 3.2). The images in the left column show control (uninfected) cells, while those on the right display cells infected with HCoV-229E. In Mv1Lu, uninfected cells form a robust monolayer with an elongated, fibroblast-like morphology. In contrast, infected cells show clear cytopathic effects, such as rounding and detachment, indicative of viral replication and cell death. Similarly, uninfected MRC-5 cells maintain a healthy, spindle-shaped morphology. Upon infection, MRC-5 cells exhibit pronounced cytopathic effects, including shrinkage and detachment, consistent with effective HCoV-229E replication and associated cytopathology. Figure 3.2 illustrates the susceptibility of these cell lines to HCoV-229E infection and the resulting cytopathic effects.

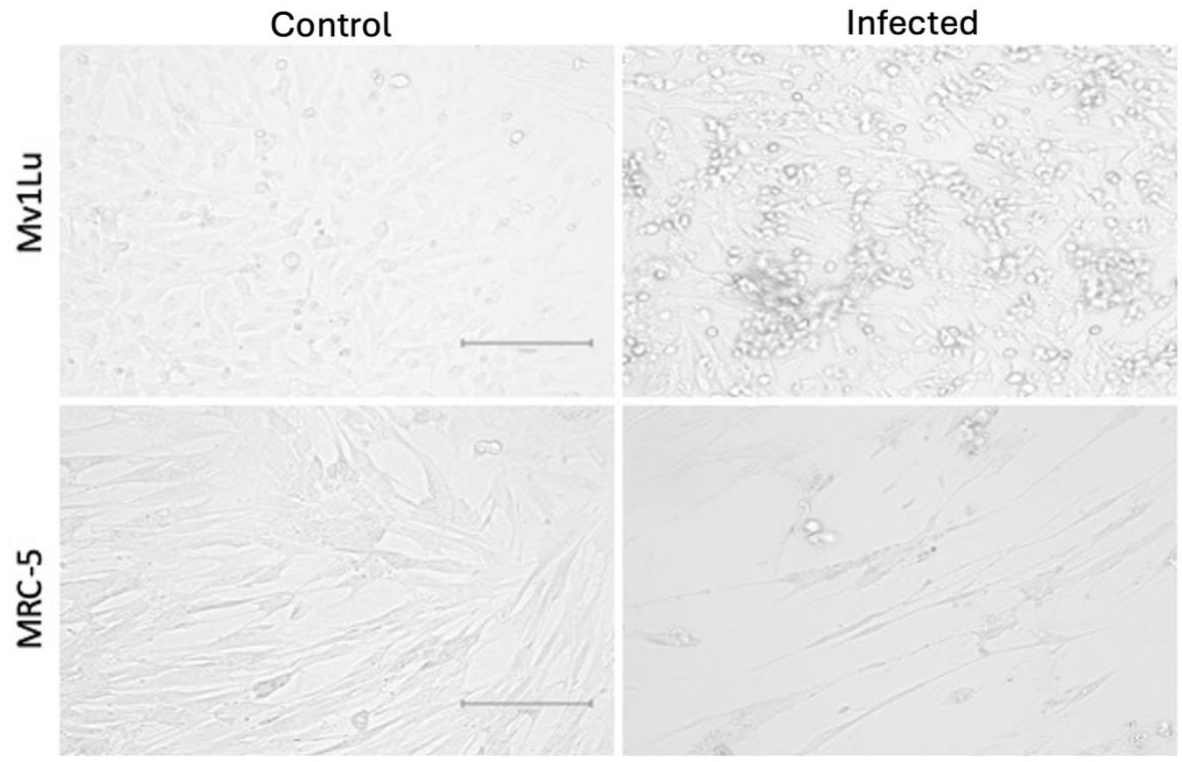

Figure 3.2 HCoV-229E growth in Mv1Lu and MRC-5 cells.

Phase-contrast micrographs of mock-infected controls (left column) and HCoV-229E-infected cultures (right column) for Mv1Lu (top) and MRC-5 (bottom). Infected monolayers show characteristic rounding and detachment compared with the confluent, spindle-shaped appearance of controls. Scale bars: 75 µm.

3.2.3 Measuring 229E and OC43 concentration in continuous cell lines using plaque assays

Different ways to quantify coronaviruses are used routinely and include plaque assays using different semisolid overlay media (*e.g.*, low-melting agarose, methylcellulose), $TCID_{50}$ assays based on CPE and real-time quantitative PCR assays for viral genes (Bracci *et al.*, 2020). Previously, researchers have utilised MRC-5 cells to quantify titres (titration) of HCoV-229E and HCoV-OC43 (Kim *et al.*, 2019; Warnes *et al.*, 2015; Funk *et al.*, 2012). To establish an infection model for my subsequent studies, I evaluated the efficiency of alternative traditional virus quantification techniques, including the plaque assay.

My initial studies aimed to determine if MRC-5 and Mv1Lu cells can be used to titrate HCoV 229E and OC43 by the methylcellulose plaque assay method in a reproducible manner. Each strain's ability to generate plaques in a carboxymethylcellulose (0.8% methylcellulose overlay medium in 2% FBS) was evaluated. Additionally, the influence of the presence or absence of the inoculum in the wells for 2 h or throughout the duration of infection (continuous infection) on plaque formation was assessed.

Overall, plaque assays for HCoV-229E and HCoV-OC43 using different concentrations of overlay media (methylcellulose) and dye (i.e. crystal violet) did not provide reproducible results because of the small size or poor definition of the plaques (Savoie and Lippe, 2022). The latter is consistent with my observations. Neither 2 h nor continuous infection of MRC-5 and HRT-18G cells resulted in visible viral plaque formation. There was CPE when viewed under the microscope, but plaques were not visible or countable after staining with crystal violet (Supplementary Figure 4). Furthermore, Mv1Lu, a mink lung cell line, which was used for the propagation of various respiratory viruses (Bracci *et al.*, 2020), was assessed as a plaque-forming cell substrate for HCoV-229E and HCoV-OC43. After a 5-day incubation period, HCoV-229E and HCoV-OC43 induced apparent CPE, but no plaques were visible. Different overlay media concentrations ranged from 0.5% to 0.8% and 1%. No plaques were visible in all combinations/concentrations, but CPE was consistently visible, suggesting that an assay measuring CPE would be more appropriate for titrating the two HCoVs.

Next, I sought to determine whether MRC-5 and Mv1Lu cells are suitable for quantifying HCoV-229E and HCoV-OC43 using the agarose plaque assay method. The capacity of each strain to generate plaques was assessed. Furthermore, the impact of the presence or absence of the inoculum in the wells on plaque formation was investigated. It was observed that when the inoculum was present in the wells for the entire 5-day incubation period, the monolayer of

MRC-5 cells remained undamaged and was suitable for producing plaques. Nevertheless, MRC-5 cells did not exhibit plaque formation in the conditions tested. However, under the same conditions, Mv1Lu cells did produce visible plaques, indicating their suitability for plaque assays (Figure 3.3).

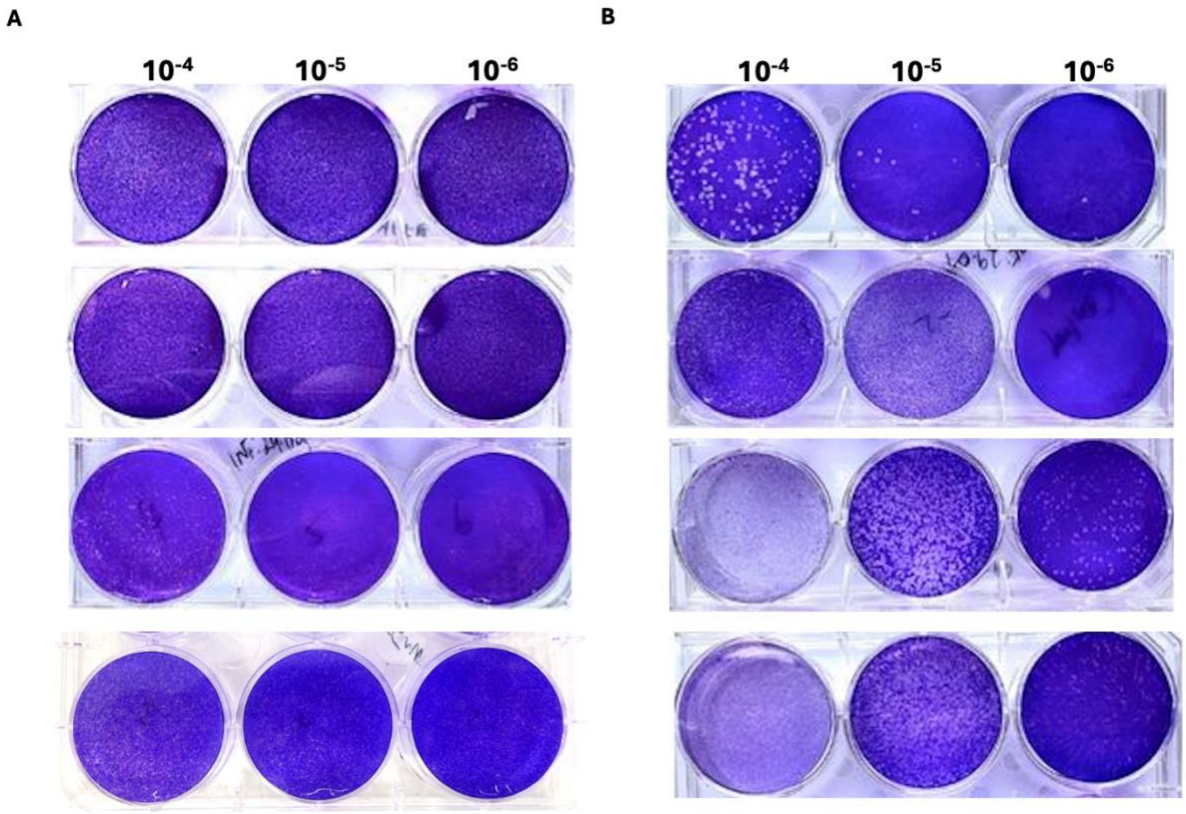

Figure 3.3 Plaque assay of HCoV-229E and HCoV-OC43 viruses in Mv1Lu cells with agarose (1%) and carboxymethylcellulose (CMC, 0.8%) overlays.

(A) 229E virus plaques at dilutions 10^4 and 10^5, showing minimal plaque formation in agarose and not CMC. (**B**) OC43 virus plaques at dilutions 10^4 and 10^5, showing clear, distinct plaques in agarose and less defined viral spread in CMC. Control wells with no virus were included for comparison.

3.2.4 $TCID_{50}$ method as an alternative to titrate HCoV-229E and -OC43.

The 50% Tissue Culture Infectious Dose ($TCID_{50}$) assay was next evaluated as an alternative titration method, given the inconsistent plaque formation observed in previous experiments. This assay quantifies infectious viral particles based on the proportion of wells showing CPE

after inoculation with serial dilutions of virus. The $TCID_{50}$ is a virus titration experiment that can quantify virus titres by investigating the cytopathic effects of a virus on an inoculated host cell culture.

For these experiments, cells were seeded into 96-well plates and incubated overnight to achieve approximately 90% confluency. Ten-fold serial dilutions of virus stock were prepared, and four replicate wells were inoculated at each dilution (Figure 3.4). Plates were examined daily for the presence or absence of CPE by both the naked eye and light microscopy, and final titres were calculated using the Reed-Muench method (Ramakrishnan, 2016).

Pilot experiments demonstrated that MRC-5 and Mv1Lu cells consistently developed visible CPE across multiple dilutions for both OC43 and 229E, whereas HRT-18G cells showed only subtle microscopic changes that did not translate into visible differences after crystal violet staining. Importantly, titres obtained in MRC-5 and Mv1Lu cells were reproducible across biological replicates, with mean values for OC43 (3.5×10^6 $TCID_{50}$/mL) and for 229E (4.6×10^5 $TCID_{50}$/mL) (Figure 3.4). No statistically significant differences were observed between titres measured in MRC-5 and Mv1Lu cells. Taken together, $TCID_{50}$ in Mv1Lu and MRC-5 represent the best method of titrating the virus. Given the consistency of this method across replicates, $TCID_{50}$ was adopted as the standard titration approach for all subsequent experiments in the study.

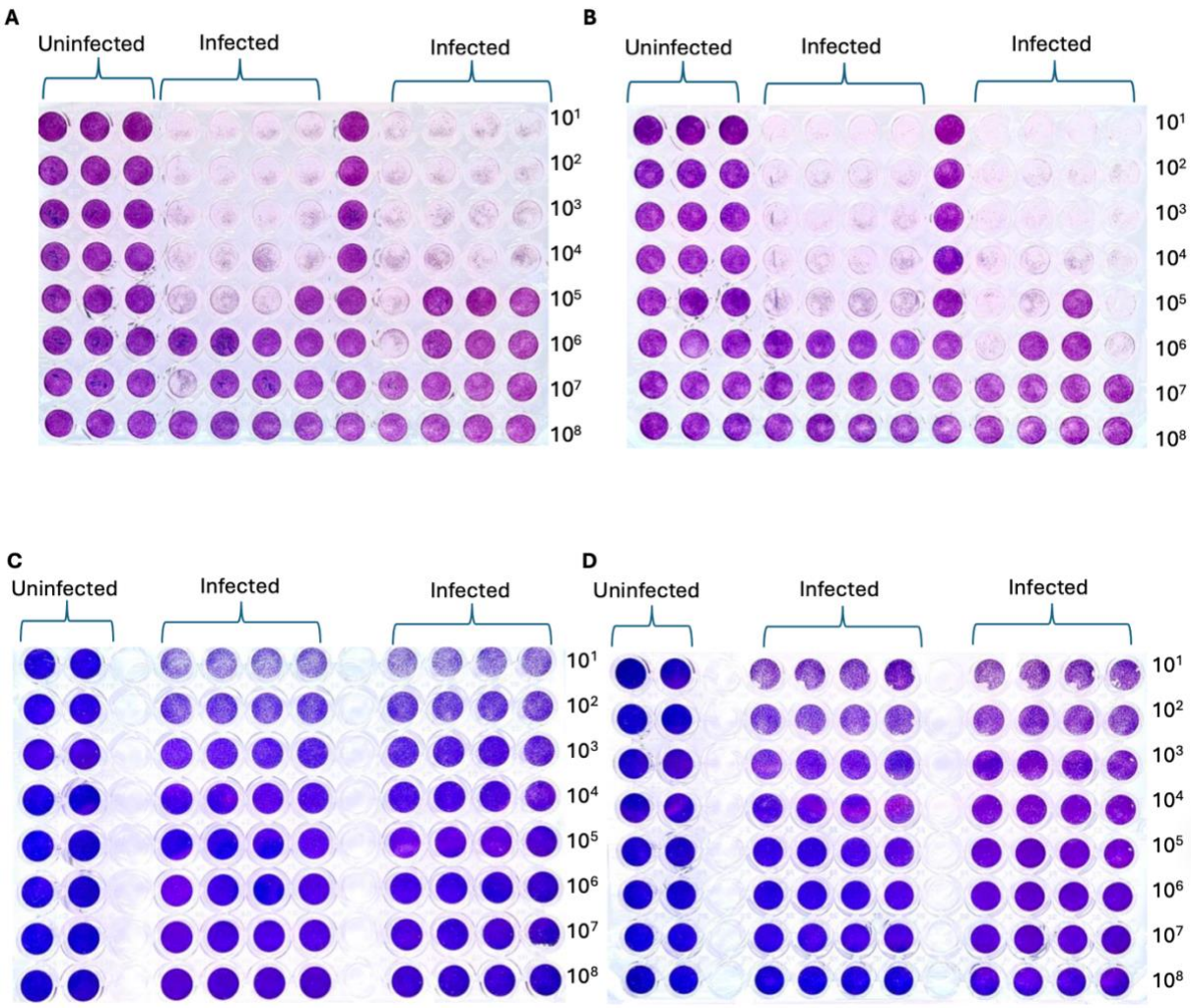
A
Uninfected
Infected
Infected
10^1
10^2
10^3
10^4
10^5
10^6
10^7
10^8
B
Uninfected
Infected
Infected
10^1
10^2
10^3
10^4
10^5
10^6
10^7
10^8
C
Uninfected
Infected
Infected
10^1
10^2
10^3
10^4
10^5
10^6
10^7
10^8
D
Uninfected
Infected
Infected
10^1
10^2
10^3
10^4
10^5
10^6
10^7
10^8

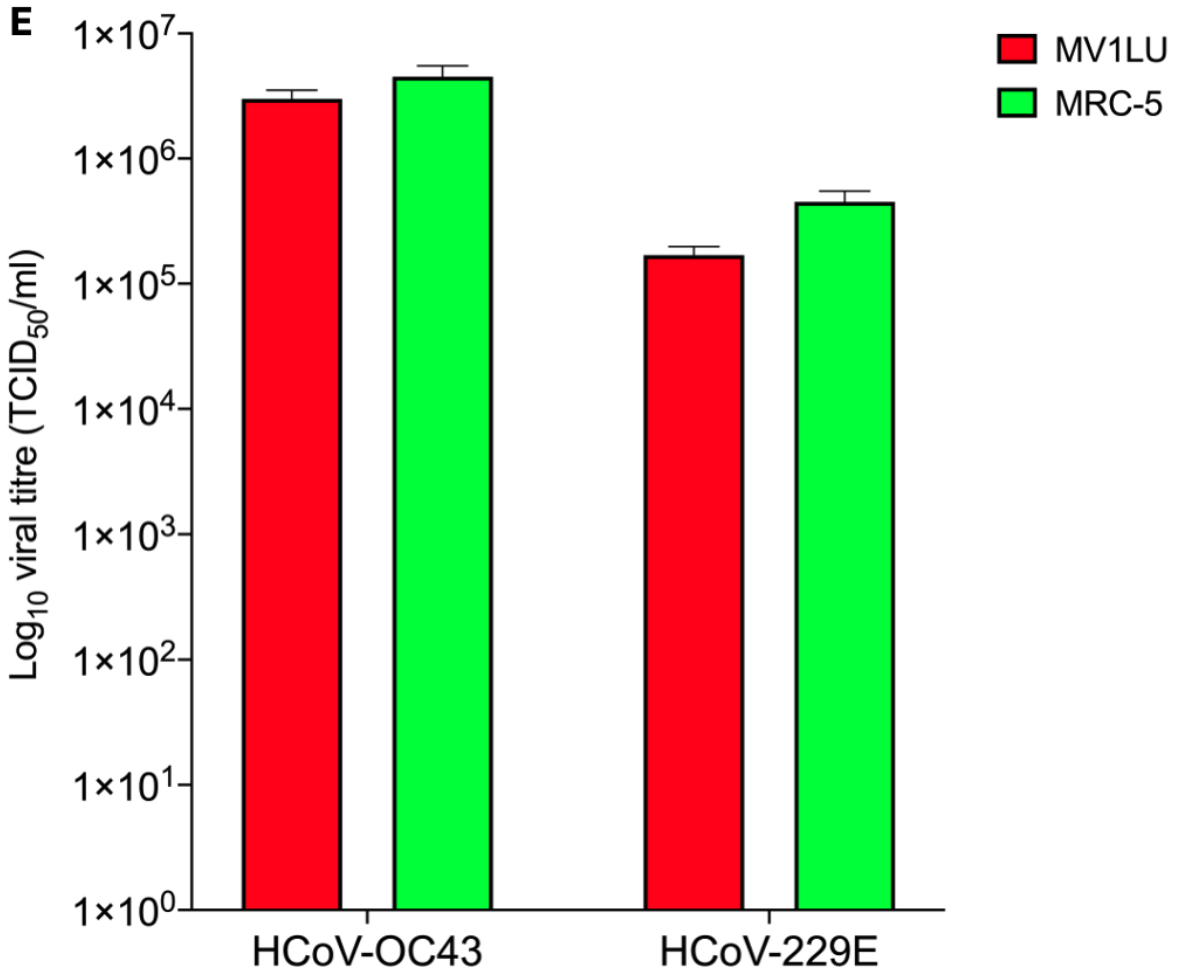

Figure 3.4: Titration of HCoV-OC43 and HCoV-229E in Mv1Lu and MRC-5 cells and resulting infectious titres.

(A) $TCID_{50}$ plate for HCoV-OC43 on Mv1Lu cells. **(B)** $TCID_{50}$ plate for HCoV-OC43 on MRC-5 cells. (C) $TCID_{50}$ plate for HCoV-229E on MRC-5 cells. **(D)** $TCID_{50}$ plate for HCoV-229E on Mv1Lu cells. For each panel, clarified supernatants were serially diluted tenfold (indicated at left) and inoculated in replicate wells; the uninfected columns serve as mock controls. After incubation to endpoint, monolayers were fixed and stained with crystal violet; wells with cytopathic effect appeared decolourised relative to intact, uniformly stained controls. **(E)** Quantification of infectious titres expressed as log10 $TCID_{50}$/mL. Bars show mean with individual replicate points; error bars indicate SEM. Red bars, Mv1Lu; green bars, MRC-5. Titres were calculated by Reed-Muench from the dilution series shown in panels A-D.

To summarise the outcomes of the optimisation experiments, I compiled the results of plaque assays and $TCID_{50}$ assays across all tested cell lines (Table 3.1). The table highlights the

presence or absence of CPE, plaque formation, and reproducibility in each cell substrate, as well as their suitability for $TCID_{50}$. This comparison shows that while Mv1Lu and CHO supported plaque formation, the reproducibility was poor. Although MRC-5 cells consistently yielded reliable titres, their slow growth rate and longer time to reach confluence made them less practical for routine titration. Therefore, Mv1Lu cells were selected as the standard substrate for all subsequent titration experiments, as they combined reproducibility with faster growth and ease of handling.

Table 3.1 Comparison of plaque assay and $TCID_{50}$ outcomes for HCoV-229E and HCoV-OC43 across different continuous cell lines

Cell line	Overlay type tested	CPE observed	Plaque formation	Reproducibility of plaques	TCID50 suitability	Remarks
MRC-5	Methylcellulose, agarose	Yes	No	N/A	Yes	Consistent CPE; robust and reproducible TCID50 titres (OC43: 3.5 × 10^6; 229E: 4.6 × 10^5).
HRT-18G	Methylcellulose, agarose	Subtle (microscopic only)	No	N/A	Limited	CPE not evident after staining; unsuitable for plaque assay or TCID50.
Mv1Lu	Methylcellulose, agarose	Yes	Small plaques	Poor	Yes	Plaques difficult to count reliably; TCID50 titres reproducible and comparable to MRC-5.
CHO	Agarose	Yes	Large, distinct plaques	Poor (10-40 plaques across repeats)	Not tested	Plaque clarity better than Mv1Lu, but highly variable counts across replicates.
A549	Not tested	N/A	N/A	N/A	No	

3.2.5 Comparative analysis of HCoV-OC43 viral growth rates in HRT-18G, Mv1Lu, and MRC-5 cells

To characterise the replication dynamics of HCoV-OC43, multi-step growth curves were performed at a multiplicity of infection (MOI) of 0.01 in MRC-5, Mv1Lu, HRT-18G, A549 and HEK293T cells. Supernatants were harvested at 0, 24, 48, 72, 96 and 120 hpi and quantified for both infectious particles by $TCID_{50}$ and viral RNA copy numbers by qRT-PCR. All assays were performed in triplicate, and values are reported as the mean ± SEM.

Infectious virus production, as measured by $TCID_{50}$ on Mv1Lu cells, rose rapidly in all three lines but with distinct kinetics (Figure 3.5A). At 12 hr post-infection, low-level infectivity was already measurable (HRT-18G: 3.5×10^5 $TCID_{50}$/mL; Mv1Lu: 2.0×10^5; MRC-5: 1.6×10^6). Between 12 and 48 hpi, each cell line entered a log-linear growth phase: MRC-5 climbed to 1.1×10^7 by 24 h and then to 1.98×10^7 by 48 hpi, whereas Mv1Lu increased from 6.25×10^5 at 12 hr to 6.25×10^6 at 24 hpi and 6.25×10^7 at 48 hpi. HRT-18G followed a similar pattern, rising from 3.51×10^5 to 6.25×10^6 and then to 1.98×10^7 over the same interval. After 48 hpi, MRC-5 plateaued near its 48 hpi maximum (8.25×10^7 by 96 hpi), Mv1Lu peaked at ~9×10^7 by 72 hpi before a slight decline at 96 hpi, and HRT-18G continued a modest upward trajectory to 6.20×10^7 $TCID_{50}$/mL by 96 hpi. These data identify Mv1Lu as the fastest early producer of infectious virus, MRC-5 as the highest early yielder, and HRT-18G as the only line sustaining titre increases through 96 hpi.

Parallel measurements of viral genome copies per mL revealed an even broader dynamic range (Figure 3.5B). At 12 h, MRC-5 already harboured ~2×10^7 copies/mL, compared to ~8×10^6 in Mv1Lu and ~6×10^6 in HRT-18G. Between 12 and 48 hpi, RNA levels surged by more than two orders of magnitude in all three lines, reaching ~1×10^{10} copies/mL in MRC-5, ~9×10^9 in Mv1Lu,

and ~8×10⁸ in HRT-18G. By 72 hpi, MRC-5 and Mv1Lu held at ~1×10¹⁰ and ~8×10⁹, respectively, while HRT-18G continued climbing to ~5×10⁹ copies/mL. At 96 hpi, genome levels in HRT-18G caught up to ~9 × 10⁹, whereas MRC-5 and Mv1Lu showed slight plateauing or decline. Statistical tests confirm that MRC-5 produces significantly more RNA early on, but HRT-18G overtakes Mv1Lu at later time points.

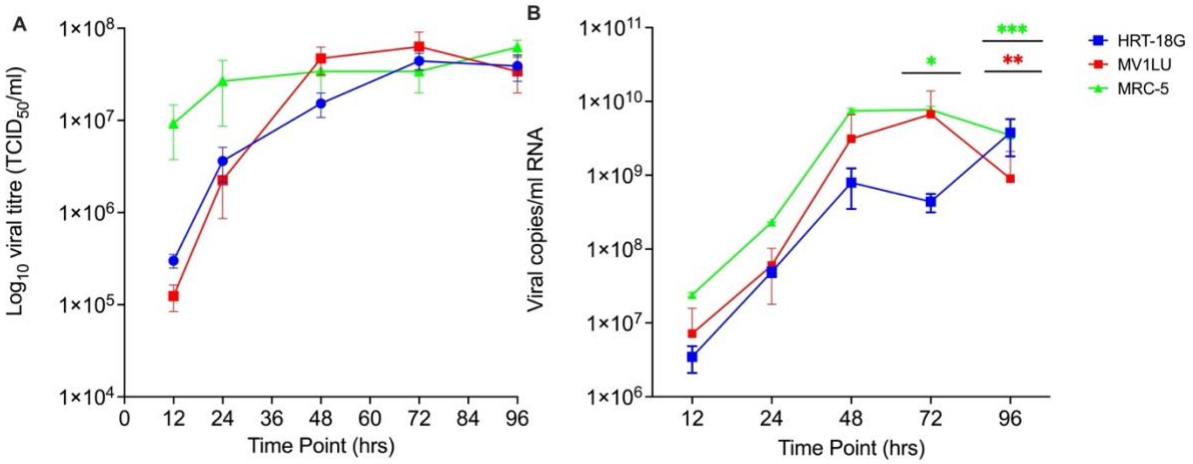

Figure 3.5: Replication kinetics of HCoV-OC43 in HRT-18G, Mv1Lu, and MRC-5 cells over 96 h.

(A) $TCID_{50}$ determined infectious titres in culture supernatants on Mv1Lu indicator cells at 12, 24, 48, 72 and 96 hpi. Data are plotted as $\log_{10}(TCID_{50}/mL)$ for HRT-18G (blue circles), Mv1Lu (red squares) and MRC-5 (green triangles), and represent the mean ± SEM of three independent biological replicates. Two-way repeated-measures ANOVA with Tukey's post-hoc test revealed no statistically significant differences between cell lines at any time point. **(B)** QRT-PCR quantified viral genome copies per mL on the same supernatants and time points. Data are shown on a $\log_{10}$ scale for HRT-18G, Mv1Lu and MRC-5; mean ± SEM, n = 3. Statistical comparisons were performed by two-way repeated-measures ANOVA with Tukey's post-hoc test (*$p < 0.05$; ** $p < 0.01$; *** $p < 0.001$).

To extend these observations to additional human-derived cell substrates, I performed growth curve analyses in A549 and HEK293T cells. Both lines were permissive to HCoV-OC43,

although titres were lower compared to MRC-5 and Mv1Lu. In A549, titres rose slowly from $3.5 \times 10^3 \pm 0.0$ at 24 hpi to $2.6 \times 10^6 \pm 8.4 \times 10^5$ at 120 hpi. By contrast, HEK293T cells reached their peak earlier, with titres of $2.4 \times 10^6 \pm 9.4 \times 10^5$ at 72 hpi, before declining slightly to $1.7 \times 10^6 \pm 4.0 \times 10^5$ at 120 hpi.

Together, these data demonstrate a marked discrepancy between viral RNA synthesis and the production of infectious particles in A549 and HEK293T cells, in contrast to the closer correspondence observed in MRC-5 and Mv1Lu cells. This suggests that while A549 and HEK293T cells support robust viral genome replication, they are comparatively less efficient at virion assembly and release than MRC-5 cells.

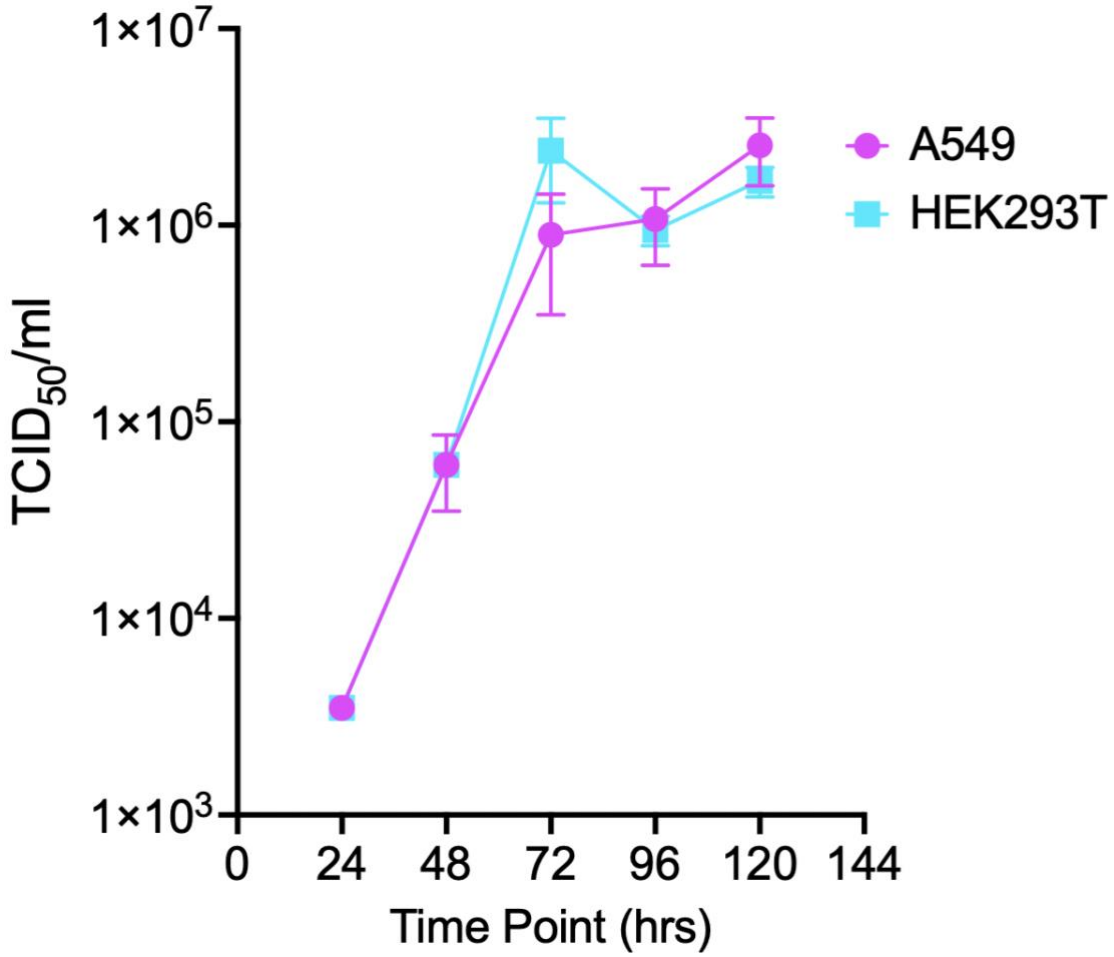

Figure 3.6: Replication kinetics of HCoV-OC43 in A549 and HEK293T cells at 33 °C.

A549 and HEK293T monolayers were infected with HCoV-OC43 (MOI 0.01) and supernatants harvested at 24, 48, 72, 96 and 120 hpi. Infectious titres were determined by $TCID_{50}$ assay on Mv1Lu indicator cells and are plotted on a log_{10} scale; data represent mean ± SEM of three independent biological replicates. Two-way ANOVA with Šídák's multiple comparisons test was used to compare cell lines at each time point. No significant differences were observed between A549 and HEK293T at any time point.

In summary, HCoV-OC43 replicated most rapidly and reproducibly in MRC-5 and Mv1Lu, achieving titres of 10^7–10^8 TCID/mL within 48-96 hpi, with corresponding RNA loads of 10^9-10^{10} copies/mL. HRT-18G supported slower replication but reached the highest titres by 120 hpi. A549 and HEK293T were permissive, but virus production was limited to ~10^6 TCID/mL despite abundant RNA synthesis, highlighting cell-line-dependent differences between viral replication and infectious output. Based on these findings, Mv1Lu cells were selected as the standard cell substrate for routine titrations due to their reproducibility and rapid growth. At the same time, MRC-5 was prioritised for studies of host immune responses owing to its human lung origin.

3.2.6 Comparative analysis of HCoV-OC43 viral growth rates in continuous cell lines

To further characterise replication kinetics, I calculated the viral growth rate (μ) and doubling time (t_d) of HCoV-OC43 in each cell line during the exponential phase of infection (Wang and Bushman, 2006). Growth rates were derived by linear regression of log_{10}-transformed infectious titres ($TCID_{50}$/mL) against time, focusing on the interval corresponding to the steepest rise in viral titres. The slope of this regression (b, log_{10}/h) was converted to μ (per hour) using the relation $\mu = b \times \ln(10)$, and doubling times were calculated as $t_d = \ln(2)/\mu$.

In HEK293T cells, HCoV-OC43 replicated with the fastest kinetics. Titres increased from 3.5 × 10^3 at 24 hpi to 2.4 × 10^6 at 72 hpi, corresponding to a calculated μ of 0.153 h^{-1} and a doubling time of 4.5 h. This rapid rise was followed by a plateau and slight decline after 72 hpi, suggesting that viral replication in HEK293T is highly efficient during the early phase but not sustained at later time points. Similarly, A549 cells showed rapid early amplification, with titres rising from 6.0 × 10^4 at 48 hpi to 2.0 × 10^6 at 72 hpi, yielding a growth rate of 0.146 h^{-1} and a doubling time of 4.8 h. However, the subsequent increase between 96 and 120 hpi was modest ($\mu = 0.0105\ h^{-1}$, $t_d \sim 66$ h), indicating that replication in A549 slows considerably after the initial expansion.

Mv1Lu cells exhibited robust replication but with slightly slower kinetics compared to HEK293T and A549. Titres increased from 3.9 × 10^6 at 24 hpi to 4.7 × 10^7 at 48 hpi, corresponding to a growth rate of 0.104 h-1 and a doubling time of 6.7 h. Interestingly, a secondary amplification phase was observed between 96 and 120 hpi, during which titres rose again to reach 1.1 × 10^8, suggesting that Mv1Lu cells support both rapid early replication and prolonged infectious virus production at later stages.

In HRT-18G cells, viral growth was slower, with titres rising from 3.6 × 10^6 at 24 hpi to 1.5 × 10^7 at 48 hpi, giving a growth rate of 0.060 h-1 and a doubling time of 11.5 h. Although initial replication was modest, titres continued to increase throughout the course of infection, reaching 1.7 × 10^8 at 120 hpi. This pattern suggests that HRT-18G cells are less efficient for early viral amplification but are capable of sustaining replication over prolonged periods, ultimately achieving the highest terminal titres.

By contrast, MRC-5 cells displayed relatively slow growth during the exponential phase. The steepest rise occurred between 72 and 96 hpi, where titres increased from 3.4 × 10^7 to 6.2 × 10^7. This translated to a growth rate of 0.025 h^{-1} and a doubling time of 27.6 h. Despite supporting

robust overall replication, the rate of increase was markedly slower than in the other cell lines. This indicates that although MRC-5 cells are suitable for high-titre stock production and mechanistic studies, they are not optimal for rapid virus amplification.

These analyses reveal striking cell-line-dependent differences in the growth rates of HCoV-OC43. HEK293T and A549 cells supported the fastest replication, with doubling times of approximately 4.5-5 h, though infectious titres plateaued at relatively modest levels. Mv1Lu cells replicated more slowly (doubling ~6.7 h) but sustained higher titres for more extended periods, reaching $>10^8$ $TCID_{50}$/mL. HRT-18G cells grew slowly (t_d ~11.5 h) yet ultimately supported the highest terminal titres. In comparison, MRC-5 cells displayed the slowest replication (t_d ~27.6 h) but remained valuable due to their human origin and consistency in immune-relevant assays. These data underscore the importance of cell line selection in HCoV-OC43 research, as replication kinetics, yield, and host relevance vary considerably between substrates.

3.3 Discussion

In this chapter, I optimised methods for propagating, titrating, and characterising the replication kinetics of HCoV-OC43 in continuous cell lines. My findings emphasise significant differences in susceptibility and replication dynamics across substrates, alongside the strengths and limitations of commonly used titration techniques. Together, these results establish a methodological foundation for the subsequent chapters of this thesis.

Cytopathic effects (CPE) were clearly observed in MRC-5, Mv1Lu, and HEK293T cells, but absent in A549 and HRT-18G, consistent with published reports demonstrating cell-type-dependent variation in coronavirus cytopathology (Kim *et al.*, 2019; Lambert, 2012; Funk *et al.*, 2012). The absence of evident CPE in some cell lines, despite measurable replication, highlights the challenge of relying solely on morphological endpoints and emphasises the importance of quantitative assays.

My comparison of titration methods underscored these difficulties. Plaque assays, though considered a "gold standard" for many viruses, proved inconsistent for HCoV-OC43 and HCoV-229E in most human-derived lines. Attempts using carboxymethylcellulose (CMC) overlays failed to yield reproducible plaques, consistent with previous reports that seasonal coronaviruses form small, diffuse plaques that are difficult to visualise (Savoie and Lippe, 2022). Switching to agarose improved plaque clarity, and Mv1Lu and CHO cells supported plaque formation; however, reproducibility was poor, and counts varied significantly between experiments. Importantly, plaques were not visible in human-derived lines (MRC-5, HRT-18G), highlighting a key limitation for their use in studies aiming to model human host-virus interactions.

In contrast, $TCID_{50}$ assays yielded reliable and reproducible results in both MRC-5 and Mv1Lu, mainly when based on consistent CPE scoring. $TCID_{50}$ has the benefit of being less dependent

on overlay conditions or plaque morphology, which can vary with seasonal coronaviruses, but it also has limitations. Scoring CPE is inherently subjective and may vary between observers; the method does not differentiate subtle variations in plaque size or morphology that can sometimes provide insights into viral fitness. Nevertheless, $TCID_{50}$ proved to be the most consistent method and was adopted as the standard titration technique for the remainder of this thesis.

These findings underline a broader issue in the field: the lack of standardisation in seasonal coronavirus titration protocols. The literature shows considerable variability in cell substrates, overlays, incubation periods, and detection methods (Woo *et al.*, 2005; Butler *et al.*, 2006; Warnes *et al.*, 2015), which complicates comparisons between studies. My data contribute to improving this methodological area by illustrating that although plaque assays may be helpful in specific non-human substrates such as Mv1Lu, $TCID_{50}$ in permissive lines like MRC-5 and Mv1Lu offers greater reproducibility and practicality.

Growth curve analyses reinforced the cell-line dependence of HCoV-OC43 replication. MRC-5 and Mv1Lu supported rapid amplification with titres of 10^7 - 10^8 $TCID_{50}$/mL, while HRT-18G cells displayed slower but ultimately higher yields by 120 hpi. A549 and HEK293T cells were permissive but generated disproportionately high RNA copy numbers relative to infectious titres, suggesting inefficient assembly or release. Growth rate calculations confirmed these differences, with the fastest replication in HEK293T and A549 (doubling times 4.5-5 h), intermediate kinetics in Mv1Lu (6.7 h), slower growth in HRT-18G (11.5 h), and the slowest replication in MRC-5 (27.6 h). These results are consistent with published reports, which show that HCoV-OC43 growth kinetics vary substantially depending on the cell type and conditions (Vabret *et al.*, 2003; Bracci *et al.*, 2020).

From a methodological standpoint, each approach had clear trade-offs. Plaque assays provide spatial information on viral spread but were not reproducible in human-derived cell lines, thereby limiting their relevance to immune studies. $TCID_{50}$ provided consistency and reproducibility but required subjective CPE scoring. Mv1Lu cells support robust titres and reproducible titrations, but are non-human, which restricts their relevance for host-immune response studies. In contrast, MRC-5 cells are human-derived and immune-competent, making them more biologically relevant, though they grow more slowly and are less practical for high-throughput titrations.

Implications for the remainder of this thesis are clear. The difficulty in visualising plaques in human-derived cell lines, the variability of plaque formation depending on overlays and incubation conditions, and the limitations of non-human substrates all highlight the challenges of working with seasonal coronaviruses. By adopting $TCID_{50}$, Mv1Lu, and MRC-5 as the standard methods, this chapter provides a reproducible basis for subsequent experiments on innate immune responses (Chapters 4-6). Simultaneously, the cell-line comparisons presented here offer new insights into how host background affects replication efficiency, infectious yield, and viral growth rates, which will aid in interpreting the immunological data presented later.

Together, these findings establish a strong experimental platform for investigating HCoV-OC43-host interactions under physiologically relevant conditions and serve as the basis for the mechanistic studies detailed in the following chapters.

Chapter 4

Comparative transcriptomic analysis of type I IFN responses to HCoV-OC43 and HCoV-229E in primary nasal epithelium and MRC-5.

4.1 Introduction

The human respiratory tract represents the primary portal of entry for a multitude of viral pathogens, yet its complex epithelial architecture and innate immune defences typically constrain infections to the upper airway, preventing widespread lower-respiratory involvement (Hiemstra *et al.*, 2015; Hewitt and Lloyd, 2021). The pseudostratified, ciliated epithelium of the nasal cavity and conducting airways, comprising ciliated cells, mucus-secreting goblet cells and basal progenitors, forms a dynamic barrier that not only traps inhaled particles but also mounts immediate antiviral responses (Hiemstra *et al.*, 2015; Parker and Prince, 2011). PRRs expressed on and within airway epithelial cells detect viral components, triggering the production of type I and III IFNs alongside pro-inflammatory cytokines and chemokines. This concerted response curtails initial viral replication, recruits professional immune cells, and preserves tissue integrity (Rehwinkel and Gack, 2020; Johnston *et al.*, 2021).

Despite the potency of this frontline defence, many respiratory viruses, including HCoVs, influenza A virus (IAV), respiratory syncytial virus (RSV) and SARS-CoV-2, have evolved mechanisms to subvert or modulate epithelial innate immunity (V'Kovski *et al.*, 2021; Beyer and Forero, 2022). Primary airway models and single-cell profiling show virus-specific transcriptional programs, with influenza typically inducing strong early IFN-stimulated genes such as *MX1* and *IFITM* family members, while other viruses bias toward prolonged NF-κB-linked chemokines (Chan *et al.*, 2010; Pizzorno *et al.*, 2020; Ravindra *et al.*, 2021). For SARS-CoV-2, multiple studies report a muted or delayed type I IFN response relative to inflammatory cytokines in airway epithelium and patient samples, a pattern associated with enhanced viral

replication and tissue damage (Blanco-Melo *et al.*, 2020; Ziegler *et al.*, 2021; Hatton *et al.*, 2021).

Continuous human cell lines, including MRC-5 and A549 cells, remain useful for analysing antiviral pathways and for scalable screening, even though they lack the full cellular diversity and mucociliary function of primary cultures (Lim *et al.*, 2016; Wyler *et al.*, 2021). These models retain essential RIG-I-JAK-STAT circuitry and facilitate kinetic studies and perturbations that complement primary epithelium findings (Rehwinkel and Gack, 2020; Ezeonwumelu *et al.*, 2021).

Seasonal human coronaviruses generally cause mild upper respiratory illness but can contribute to exacerbations in susceptible hosts (Lim *et al.*, 2016; Park *et al.*, 2020). In well-differentiated primary bronchial epithelial cells, HCoV-229E and HCoV-OC43 display distinct kinetics and IFN profiles: HCoV-229E reaches peak viral load early with robust type I/III IFN and ISG induction, whereas HCoV-OC43 shows slower kinetics with blunted IFN responses (Loo *et al.*, 2020). Comparative work across matched primary and continuous systems remains limited yet is essential for distinguishing virus-intrinsic strategies from universal epithelial defence programs (Jonsdottir and Dijkman, 2016).

Accordingly, this chapter conducts a comparative transcriptomic study to clarify host immune responses to HCoV-229E and HCoV-OC43. I used well-differentiated primary human nasal epithelial cells (hNECs) cultured at the air-liquid interface to capture physiologically relevant reactions in the upper airway. In parallel, I re-analysed publicly available RNA-seq datasets from MRC-5 cells infected with 229E or HCoV-OC43, using identical bioinformatic pipelines to ensure comparability. My main aim is to delineate common and divergent patterns of PRR activation, IFN/ISG kinetics, and inflammatory signalling across both models.

4.2 Results

4.2.1 Infection of primary human nasal epithelial cells (hNECs)

To gain a comprehensive insight into how HCoV-229E and HCoV-OC43 interact with the host innate immunity at the cellular level, I infected primary human nasal epithelial cells (hNECs) cultured at their air-liquid interface. Cells were inoculated with each virus at an MOI of 0.1. RNA was collected at two representative time points, 24 and 72 hpi, representing the early and late stages of infection. The RNA-sequencing libraries and subsequent sequencing were outsourced to Novogene (Cambridge, UK), and downstream analysis was conducted using Partek Flow (v12.7.0) (Figure 4.1). All raw sequencing data have been deposited in GEO under accession GSE238079 and were first reported in our recent publication in the Journal of Medical Virology (Ogunjinmi *et al.*, 2024).

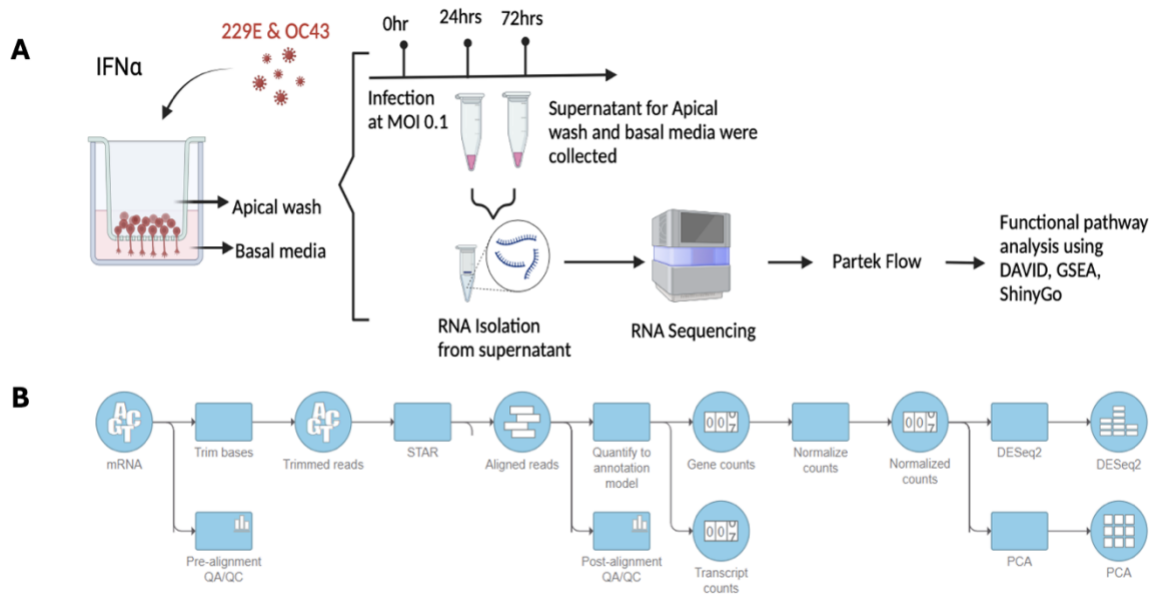

Figure 4.1: Schematic representation of infection in hNECs and workflow analysis.

(A) HCoV-229E and HCoV-OC43 were infected with an MOI of 0.1 and incubated for 1 hr. Cells and apical/basal supernatants were collected at 24 and 72 hpi. Cellular RNA was isolated, and RNA sequencing was outsourced to Novogene Cambridge. **(B)** RNA-seq processing and statistics: raw reads QC, trimming, alignment to GRCh38 with STAR in Partek Flow, post-alignment QC, gene-level counting, normalisation, differential expression with DESeq2, and downstream exploratory analyses including PCA and pathway enrichment DAVID, GSEA, ShinyGO. Experiments used n = 2 biological replicates per condition. The figure is created with Biorender.

Following the workflow in Figure 4.1, all raw FASTQ files underwent pre-alignment QA/QC in Partek Flow: per-base Phred scores stayed above 35 across the full 150 bp read length, and over 95% of reads per library exceeded a Phred score of 30. Mean GC content was distributed from 50% to 53%, and ambiguous (N) calls were below 0.01% in every sample (Table 4.1), confirming high-quality libraries. After adapter and low-quality base trimming, reads were aligned to the human reference genome (GRCh38) using STAR, achieving greater than 96% alignment in all samples. Unique paired alignment rates exceeded 88%, and mean genome-wide

coverage depths ranged from 50× to 75× (Appendix Table 1.4). These metrics validate the integrity and consistency of my sequencing data, providing a solid foundation for accurate quantification of transcript abundance.

Table 4.1 Summary of experimental design and key sequencing-quality metrics (n = 10 libraries).

Sample ID	Virus	Time (hpi)	MOI	Replicate	Total Reads (millions)	Mean Phred Score	Aligned Reads (%)
Mock_A	None	0	—	A	41.6	35.03	97.25 %
Mock_B	None	0	—	B	35.5	35.05	97.08 %
E229_24A	229E	24	0.1	A	31.7	35.83	97.80 %
E229_24B	229E	24	0.1	B	23.8	35.89	97.90 %
E229_72A	229E	72	0.1	A	24.4	35.84	97.25 %
E229_72B	229E	72	0.1	B	27.5	35.76	96.93 %
OC43_24A	OC43	24	0.1	A	25.0	35.88	97.91 %
OC43_24B	OC43	24	0.1	B	25.3	35.78	97.94 %
OC43_72A	OC43	72	0.1	A	24.5	35.81	97.21 %
OC43_72B	OC43	72	0.1	B	30.6	35.91	97.93 %

4.2.2 qPCR confirms robust HCoV-OC43 replication in hNECs.

To validate the successful infection of hNECs with HCoV-229E and HCoV-OC43, I measured intracellular viral RNA using the qPCR *N* gene to determine the kinetics of viral replication over 72 h. Viral RNA was quantified in cell lysates and reported as viral copies/mL of total

RNA (Figure 4.2). At the time of adsorption (0 h), baseline RNA levels were low for both viruses (HCoV-229E: 5.8×10^5 copies/mL; HCoV-OC43: 1.06×10^7 copies/mL), reflecting residual inoculum. By 24 h, HCoV-229E underwent a sharp burst of replication, reaching a mean of 4.6×10^7 copies/mL, a roughly 80-fold increase over baseline, before declining to 3.9×10^6 copies/mL by 72 h. In contrast, HCoV-OC43 increased more modestly to 1.9×10^7 copies/mL at 24 h (~1.8-fold rise) but continued to accumulate through 72 h, reaching 2.4×10^7 copies/mL.

These profiles highlight fundamentally different kinetics in the same primary cell model: HCoV-229E replicates rapidly and peaks early, then is largely cleared or suppressed by 72 h, whereas HCoV-OC43 displays slower early growth but sustained accumulation over three days. This temporal distinction will inform subsequent analyses of host responses, indicating that sampling for transcriptomic or proteomic changes should be timed to capture the distinct peak of HCoV-229E at 24 h versus the later plateau of HCoV-OC43 at 72 h.

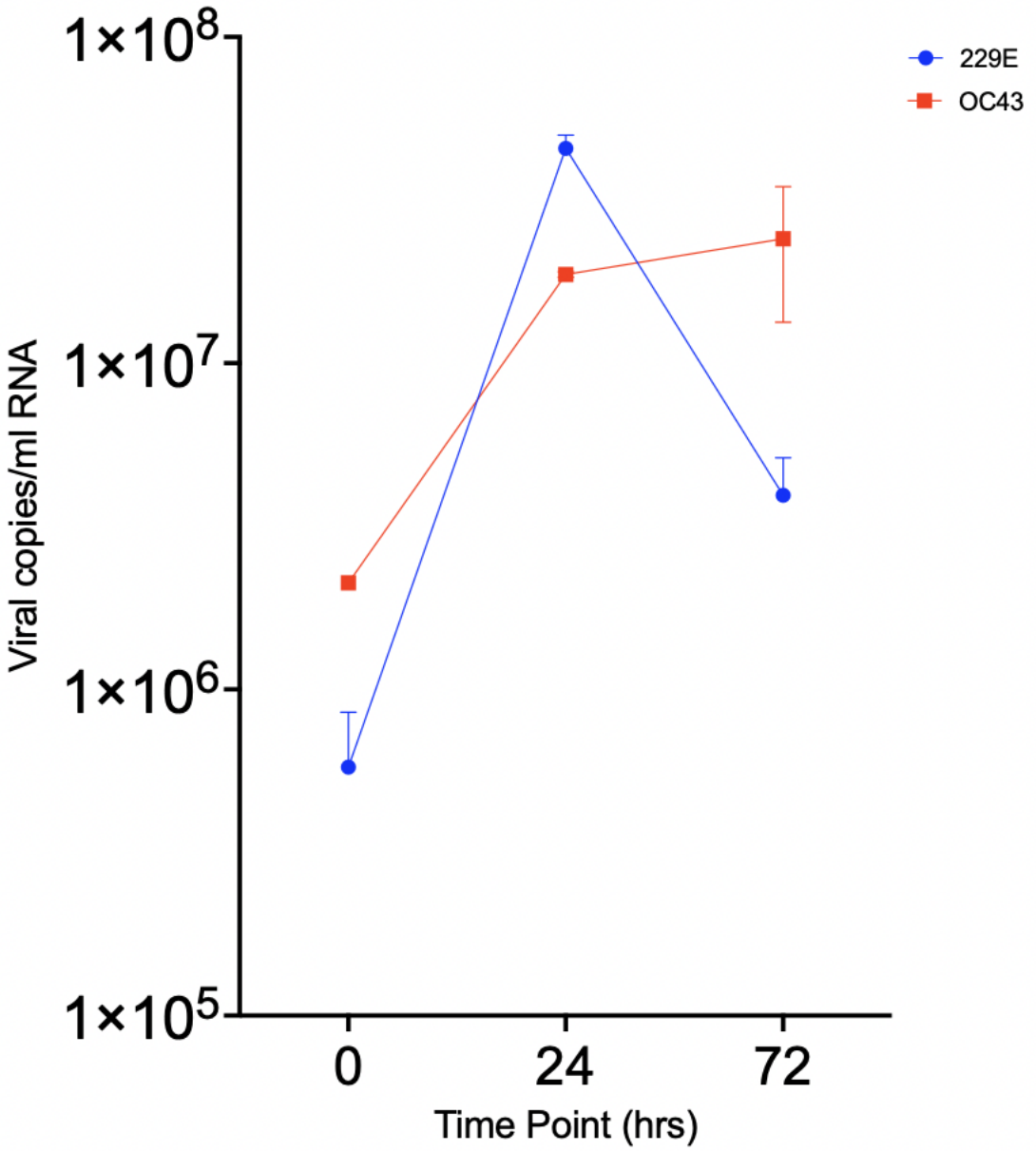

Figure 4.2: Intracellular replication kinetics of HCoV-229E and HCoV-OC43 in primary human nasal epithelial cells.

hNECs were infected at an MOI of 0.1 with HCoV-229E (blue circles) or HCoV-OC43 (red squares). Intracellular viral RNA was quantified by qRT-PCR targeting the N gene at 0, 24 and 72 hpi and expressed as copies per mL of total RNA. Data represent mean ± SEM of three biological replicates. Statistical significance between viruses at each time point was assessed by two-way ANOVA with Šídák's multiple comparisons test (* $p < 0.05$, ** $p < 0.01$).

4.2.3 Principal Component Analysis (PCA) reveals virus and time-specific transcriptional signatures.

To assess global variation, verify sample structure, and screen for outliers before differential analyses, I first applied principal component analysis (PCA). This approach allows for an unbiased, dimension-reduced view of the host response. PCA was performed using log-transformed, normalised gene expression data from all infected and mock samples. The first two principal components (PC1 and PC2) accounted for 33.7% and 17.5% of the total variance, respectively.

The PCA showed clear grouping of samples based on infection status and time point (Figure 4.3). Mock-infected samples formed a close cluster in the upper right area, indicating little transcriptional change in uninfected conditions. Conversely, HCoV-229E and HCoV-OC43 samples were separated from controls and each other, demonstrating virus-specific transcriptional responses. In cells infected with 229E, samples at 24 and 72 hpi gradually diverged along principal component 1 (PC1), reflecting time-dependent changes in host gene expression. OC43-infected samples exhibited a similar trend, remaining closely clustered at 24 hpi and becoming more dispersed at 72 hpi.

The OC43_72A sample noticeably differed from its biological replicate, OC43_72B, along PC2. This suggests biological variability in the strength or timing of the host response at 72 hpi. It's possible that OC43_72A showed a more vigorous activation of inflammatory or IFN-stimulated genes, which could affect its placement in PCA, as the technique is more sensitive to features with high variability. Alternatively, minor technical differences in RNA quality or sequencing depth might have contributed to the observed variation. Nonetheless, since other replicate pairs are consistent, biological variation is likely the main cause.

These data show that both HCoV-229E and HCoV-OC43 induce different and time-dependent transcriptional responses in hNECs, with HCoV-OC43 exhibiting variation within the group during later stages of infection.

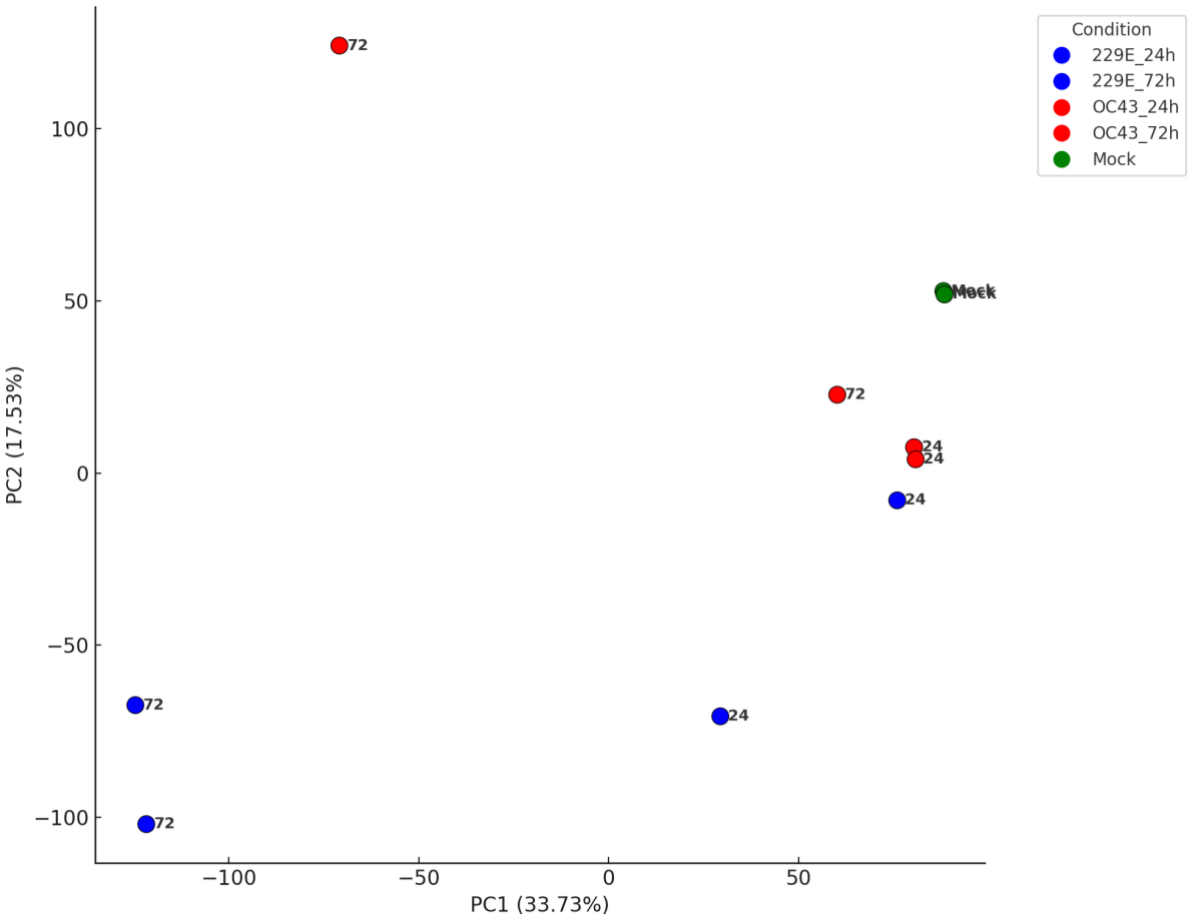

Figure 4.3: PCA plot of hNEC RNA-seq profiles.

PCA of global gene-expression profiles for mock-treated samples (green) and cells infected with HCoV-229E (blue: 24 h, 72 h) or HCoV-OC43 (red: 24 h, 72 h). Each point is one biological replicate, labelled by hpi. The x-axis (PC1, 33.73%) and y-axis (PC2, 17.35%) indicate the percentage of total variance in the dataset captured by the first and second principal components, respectively. Counts were normalised and log-transformed before PCA. The analysis was performed in R using the "prcomp" function and plotted with ggplot2.

4.2.4 Differential gene expression reveals distinct transcriptional responses to HCoV-229E and HCoV-OC43.

Guided by the PCA structure, I set to define how HCoV-229E and HCoV-OC43 reshape the nasal epithelial transcriptome, I aligned reads to GRCh38 in Partek Flow (v12.7.0) using STAR and identified differentially expressed genes (DEGs) with DESeq2, applying a uniform threshold of False Discovery Rate (FDR) ≤ 0.05; absolute $\log_2$ fold change ($\log_2$FC) ≥ 1. All comparisons were made relative to mock controls ($n = 2$ biological replicates per condition).

Out of a total of 15,123 quantified transcripts, HCoV-229E-infected cells relative to mock upregulated or downregulated substantially more genes than HCoV-OC43-infected cells relative to mock, with 2,646 meeting these cutoffs at 24 hpi, of which 1,440 were upregulated and 1,206 were downregulated. In contrast, 1,298 DEGs were yielded in HCoV-OC43-infected cells relative to mock (758 up; 540 down) at the same time point (Figure 4.4A, C and E, F). By 72 hpi, the number of DEGs in HCoV-229E-infected versus mock response rose to 6,613 DEGs (3,385 up; 3,228 down), reflecting a widespread host-shutoff signature. HCoV-OC43-infected cells versus mock, however, displayed a more modest shift, with 3,317 DEGs in total (2,034 up; 1,283 down), indicating that HCoV-OC43 maintains a balance of gene regulation (Figure 4.4B, D).

A direct side-by-side comparison of the two viruses with the mocks reveals their distinct strategies. By 24 hpi, HCoV-229E upregulated nearly double the number of transcripts compared to HCoV-OC43. By 72 hpi, 229E continued to downregulate thousands of host genes, whereas HCoV-OC43 sustained both up- and down-regulation, with robust upregulation of key ISGs (e.g MX1, IFIT3) but limited overall transcript shutdown. Having established robust sets of upregulated and downregulated genes at each time point, I next map these lists to curated pathways and IFN signatures to evaluate biological coherence.

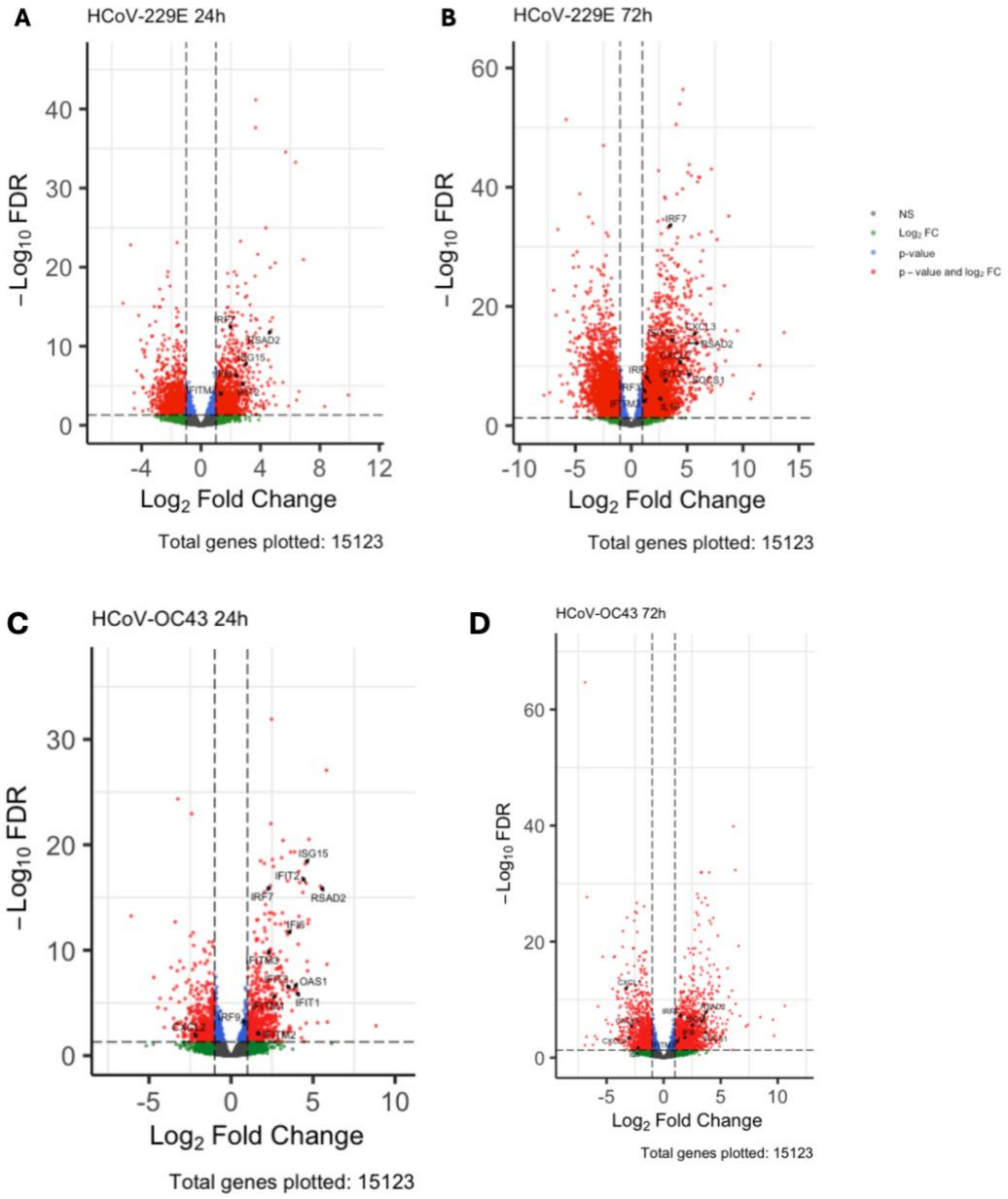
A
HCoV-229E 24h
B
HCoV-229E 72h
C
HCoV-OC43 24h
D
HCoV-OC43 72h
−Log10 FDR
Log2 Fold Change
Total genes plotted: 15123
NS
Log2 FC
p-value
p – value and log2 FC
IRF7
RSAD2
ISG15
IFIT2
IFI6
IFITM3
OAS1
IFIT1
IFITM2
IRF9
CXCL13
SOCS1
IL18

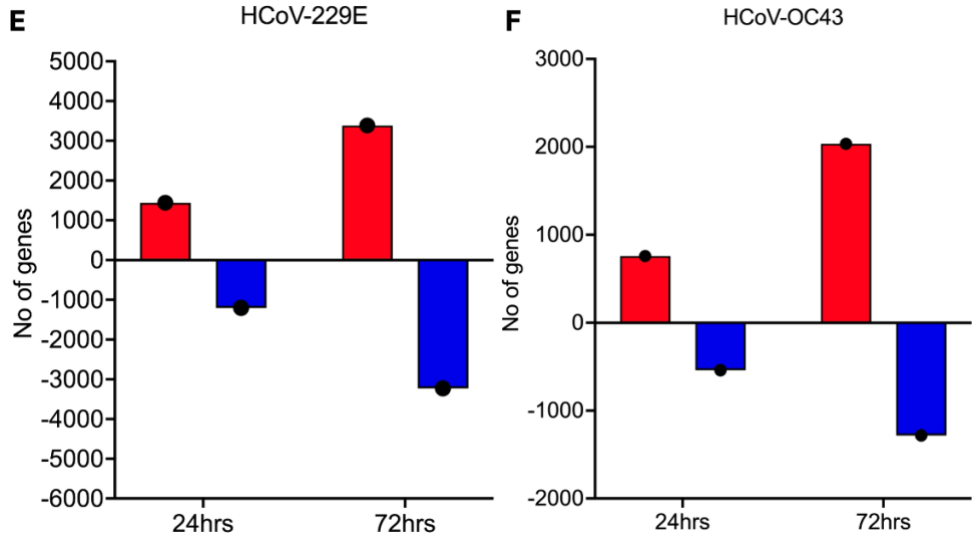
E
HCoV-229E
F
HCoV-OC43
No of genes
24hrs
72hrs

Figure 4.4: Differential transcriptional response of hNECs to HCoV-229E and HCoV-OC43 infection.

Transcriptome-wide changes in primary human nasal epithelial cells (hNECs) were assessed by RNA-seq at 24 and 72 hpi with HCoV-229E or HCoV-OC43 (MOI 0.1). Reads were aligned to GRCh38 using STAR and DEGs called with DESeq2 (FDR ≤ 0.05; $\log_2$ fold-change ≥ 1). Each point represents one of 15,123 quantified transcripts; red points indicate genes that are significantly expressed. Vertical dashed lines mark $\log_2$ FC = ±1; horizontal dashed line marks $-\log_{10}$ P = $-\log_{10}(0.05)$. **(A)** HCoV-229E at 24 hpi. **(B)** HCoV-229E at 72 hpi. **(C)** HCoV-OC43 at 24 hpi. **(D)** HCoV-OC43 at 72 hpi. Selected ISGs and key regulators are labelled for emphasis. Bar charts show the number of upregulated (red) and downregulated (blue) transcripts per condition. Black dots denote the absolute count value. **(E)** Comparison for HCoV-229E at 24 h and 72 h. **(F)** Comparison for HCoV-OC43 at 24 h and 72 h

4.2.5 Comparison of ISGs between viral infection and IFNα stimulation

Building on the observed global transcriptional separation in the PCA and the DE contrasts, I next aimed to determine whether HCoV-229E and HCoV-OC43 infection in hNECs elicits a canonical type I IFN response. To achieve this, I compared their transcriptomic signatures to those observed following exogenous rIFNα stimulation. DEGs upregulated at 24 and 72 hpi (FDR ≤ 0.05, $\log_2$ fold change ≥ 1) were compared with those induced by IFNα. UpSet plots were generated using RStudio to visualise the number of shared and unique upregulated transcripts among these datasets. An upset plot gives a graphical visualisation of the intersection of multiple sets.

At 24 hpi (Figure 4.5A), HCoV-229E upregulated 1440 transcripts compared to the mock, of which 877 were unique to HCoV-229E. IFNα treatment alone upregulated 77 unique transcripts that were not observed in either coronavirus infection. The pairwise overlaps were significant: 468 genes were shared between HCoV-229E and HCoV-OC43, HCoV-OC43 and IFNα shared 74, and 40 were shared between HCoV-229E and IFNα alone. Only 6 transcripts were commonly upregulated across all three conditions. These findings indicate that although each stimulus drives a distinct upregulated transcriptome, there is a core overlap, likely bona fide

ISGs, most prominent between the two coronaviruses, reflecting virus-virus and virus-IFN interactions.

By 72 hpi (Figure 4.5B), the overall response expanded. There were 2,029 unique transcripts for HCoV-229E, with IFNα now independently up-regulating 119 genes. The shared 229E+OC43 signature increased to 1,254 genes, while overlaps with IFNα were modest, with 33 genes associated with HCoV-OC43 and 32 with HCoV-229E. A set of 13 transcripts remained common across all three conditions. Although the total overlaps with IFNα slightly increased, they account for a smaller proportion of the expanded IFNα-induced gene set compared to 24 h, indicating that virus-specific programmes increasingly dominate over the canonical IFN response as infection progresses.

At both time points, HCoV-229E causes the most extensive transcriptomic changes, while HCoV-OC43 and IFNα maintain a core set of ISGS that remains stable but decreases in proportion by 72 h. The significant overlap between HCoV-229E and HCoV-OC43 suggests common host pathways targeted by both viruses and identifies potential genes for broad-spectrum antiviral strategies investigation.

To better visualise the fold change in expression of canonical ISGs, I plotted a curated set of IFN-regulated genes (Figures 4.5C and 4.5D). At 24 hpi, cells infected with HCoV-OC43 showed strong upregulation ($log_2FC > 4$) of genes like *CXCL11, IFIT3, OASL*, and *IFIT2*, which are also highly increased by IFNα with similar fold changes. Conversely, 229E upregulated a more moderate response, with *IFIT3* and *OASL* upregulated to a lesser degree (log_2FC ~2-3). Remarkably, *CXCL11* was specifically upregulated by HCoV-OC43 but was not detected in the 229E dataset at 24 hpi. By 72 hpi, both viruses induced notable levels of *CXCL10* ($log_2FC > 5$ in HCoV-OC43; approximately 4 in HCoV-229E), a chemokine commonly associated with IFN responses. Several other ISGs, including *RSAD2, MX2*, and *IFIT1*, were

also increased, although their levels remained higher in HCoV-OC43-infected cells compared to those infected with HCoV-229E.

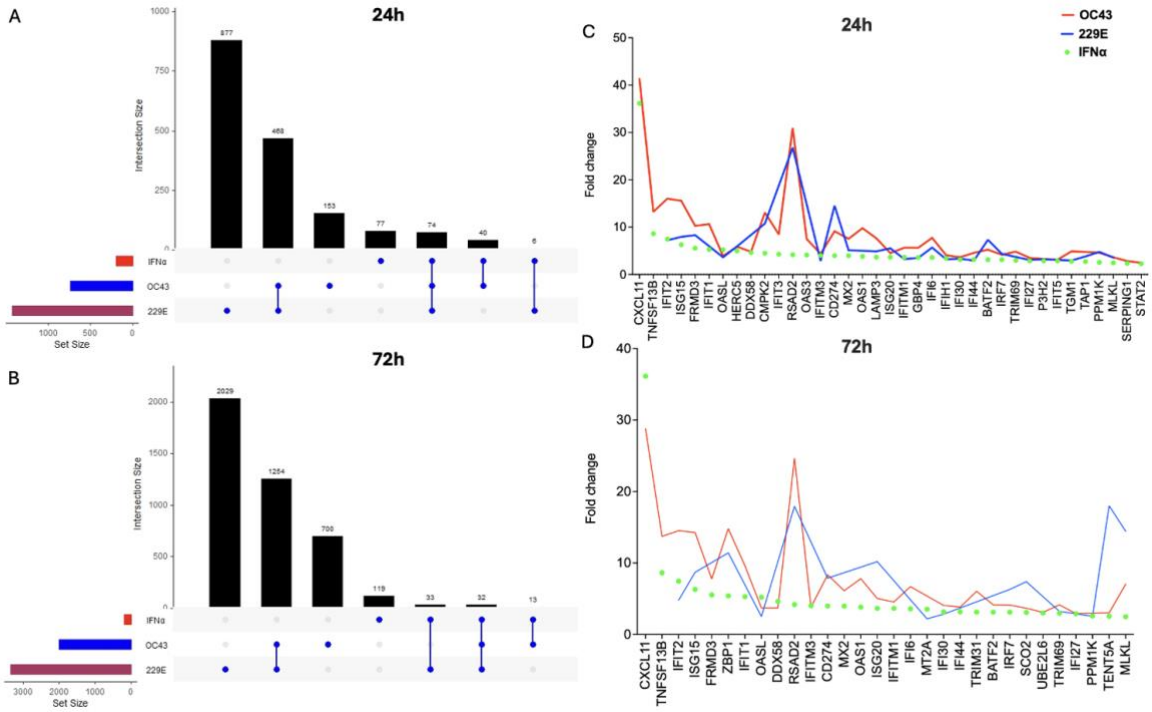

Figure 4.5: Comparative analysis of ISG induction by HCoV-229E, HCoV-OC43, and IFNα stimulation in hNECs.

(A-B) UpSet plots depict the number of significantly upregulated genes (FDR ≤ 0.05, $\log_2$FC ≥ 1) in hNECs infected with HCoV-229E, HCoV-OC43, or stimulated with IFNα, along with the intersections between these groups at 24 hpi/stimulation **(A)** and 72 h **(B).** Dots below each bar indicate the group(s) contributing to each intersection. The size of each set and the number of shared genes are shown on the y-axis. (C-D) Line plots of selected IFN-stimulated genes showing fold change in expression (relative to mock) in hNECs infected with HCoV-OC43 (red), HCoV-229E (blue), or stimulated with IFNα (green dots). **(C)** displays ISG expression at 24 hpi; **(D)** shows the same genes at 72 hpi. The gene set includes canonical ISGs such as *CXCL10, IFIT3, OASL, RSAD2*, and IFITM family members. HCoV-OC43 consistently induced stronger ISG responses than HCoV-229E across both time points, with broader overlap with the IFNα-induced transcriptional profile.

4.2.6 Functional pathway enrichment confirms activation of immune signalling pathways.

The observed overlap between virus-upregulated ISGs and canonical IFN-responsive genes prompted a broader functional assessment of the host response. To characterise the transcriptomic changes beyond individual genes, Kyoto Encyclopedia of Genes and Genomes (KEGG) pathway enrichment analysis was conducted on differentially expressed genes in HCoV-229E and -OC43-infected primary hNECs, using RStudio with an FDR threshold of ≤0.05. The analysis focused on both upregulated and downregulated genes at 24 and 72 hpi, relative to mock-infected controls. Only pathways relevant to immune signalling are shown (Figure 4.6A-B).

At 24 hpi, both viruses strongly enriched core pattern-recognition and cytokine-signalling pathways. In HCoV-229E-infected hNECs, the "regulation of innate immune response" BP contained 55 upregulated transcripts ($-\log_{10}$FDR = 9.2), while HCoV-OC43 infection upregulated 58 transcripts in the same BP ($-\log_{10}$FDR = 12.5). "Positive regulation of innate immune response" was enriched with 44 upregulated transcripts for both HCoV-229E ($-\log_{10}$FDR = 8.7) and HCoV-OC43 ($-\log_{10}$FDR = 11.3), respectively. The canonical "response to type I IFN" BP showed 17 upregulated transcripts following HCoV-229E infection ($-\log_{10}$FDR = 6.4) and 22 for HCoV-OC43 ($-\log_{10}$FDR = 7.1). Toll-like receptor signalling, including both MyD88-dependent and TRIF-dependent branches, was also enriched: HCoV-229E upregulated 7 TLR-pathway genes ($-\log_{10}$FDR = 5.2), whereas HCoV-OC43 upregulated 9 such genes ($-\log_{10}$FDR = 6.8).

At the pathway level, KEGG analysis mirrored these findings (Figure 4.6A). "Cytokine–cytokine receptor interaction" was enriched with 22 upregulated genes for 229E ($-\log_{10}$FDR = 7.4) and 18 for HCoV-OC43 ($-\log_{10}$FDR = 9.0). The "JAK–STAT signalling pathway"

contained 19 and 11 upregulated transcripts for HCoV-229E ($-\log_{10}$FDR = 6.1) and HCoV-OC43 ($-\log_{10}$FDR = 7.3), respectively. "RIG-I-like receptor signalling" was also prominent, with 13 upregulated genes in HCoV-229E ($-\log_{10}$FDR = 5.8) and 13 in HCoV-OC43 ($-\log_{10}$FDR = 8.2).

Several of the same BP and KEGG pathways exhibited downregulated components, suggesting internal feedback or pathway-specific repression. For example, in the "regulation of innate immune response" BP, HCoV-229E downregulated 8 transcripts ($-\log_{10}$FDR = 4.3) and HCoV-OC43 downregulated 11 transcripts ($-\log_{10}$FDR = 5.6). Similarly, within the "Toll-like receptor signalling pathway", HCoV-229E downregulated 5 genes ($-\log_{10}$FDR = 3.9), whereas HCoV-OC43 downregulated 7 genes ($-\log_{10}$FDR = 4.8).

These enrichment results demonstrate that by 24 hpi, both HCoVs chiefly activate classic innate-immune and IFN pathways in hNECs, with HCoV-OC43 generally driving stronger enrichment (higher gene counts and lower FDRs) than HCoV-229E at this early time point.

At 72 hpi, KEGG and BP enrichment continued to highlight innate-immune signalling in both HCoV-229E- and HCoV-OC43-infected hNECs, albeit with altered gene counts and statistical significance (Figure 4.6B). In the BP category (Figure 4.6B), HCoV-229E infection upregulated 48 transcripts associated with "regulation of innate immune response" ($-\log_{10}$FDR = 5.5), compared with 38 transcripts for HCoV-OC43 ($-\log_{10}$FDR = 4.2). "Positive regulation of innate immune response" included 43 upregulated transcripts in 229E ($-\log_{10}$FDR = 5.1) and 36 in HCoV-OC43 ($-\log_{10}$FDR = 3.8). The "response to type I IFN" biological process was enriched, compared to mock, with 29 upregulated transcripts in HCoV-229E ($-\log_{10}$FDR = 4.6) and 24 for HCoV-OC43 ($-\log_{10}$FDR = 4.0). Toll-like receptor signalling pathways were likewise upregulated compared to mock, with HCoV-229E upregulating 20 transcripts ($-\log_{10}$FDR = 3.9) compared to 17 upregulated by HCoV-OC43 ($-\log_{10}$FDR = 3.5).

In KEGG (Figure 4.6B), “cytokine-cytokine receptor interaction” showed 37 upregulated transcripts in HCoV-229E ($-\log_{10}$FDR = 6.2) and 32 in HCoV-OC43 ($-\log_{10}$FDR = 5.4). “JAK-STAT signalling pathway” was enriched with 28 upregulated transcripts for HCoV-229E ($-\log_{10}$FDR = 5.8) and 25 for HCoV-OC43 ($-\log_{10}$FDR = 5.0). “RIG-I-like receptor signalling” contained 22 upregulated transcripts in HCoV-229E ($-\log_{10}$FDR = 5.0) and 19 in HCoV-OC43 ($-\log_{10}$FDR = 4.3).

In the BP set, HCoV-229E downregulated 14 transcripts in “regulation of innate immune response” ($-\log_{10}$FDR = 3.1) and HCoV-OC43 downregulated 12 ($-\log_{10}$FDR = 2.8). “Negative regulation of innate immune response” included 11 downregulated transcripts for HCoV-229E ($-\log_{10}$FDR = 2.9) and 9 for HCoV-OC43 ($-\log_{10}$FDR = 2.6). In KEGG, HCoV-229E downregulated 9 transcripts in the “Toll-like receptor signalling pathway” ($-\log_{10}$FDR = 2.7) and HCoV-OC43 downregulated 8 ($-\log_{10}$FDR = 2.4); “cytokine–cytokine receptor interaction” saw 7 downregulated transcripts in HCoV-229E ($-\log_{10}$FDR = 2.5) and 6 in HCoV-OC43 ($-\log_{10}$FDR = 2.2).

Overall, by 72 hpi, both viruses continued to show strong enrichment of key innate-immune and IFN pathways, with HCoV-229E generally up-regulating a greater number of transcripts per pathway than HCoV-OC43. The downregulated component within the same pathways suggests dynamic feedback regulation or selective repression alongside ongoing immune activation.

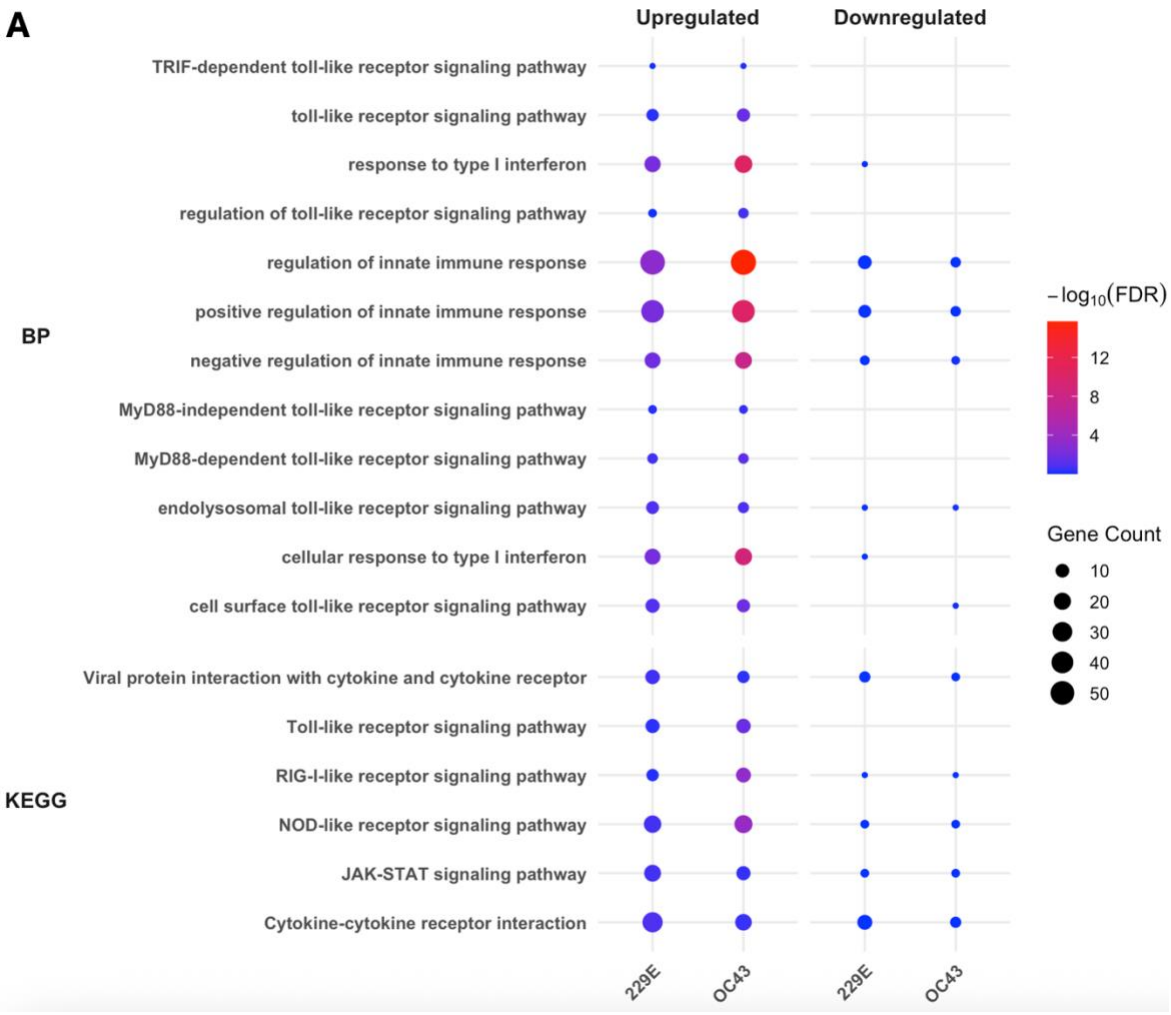
A
Upregulated
Downregulated
TRIF-dependent toll-like receptor signaling pathway
toll-like receptor signaling pathway
response to type I interferon
regulation of toll-like receptor signaling pathway
regulation of innate immune response
positive regulation of innate immune response
negative regulation of innate immune response
MyD88-independent toll-like receptor signaling pathway
MyD88-dependent toll-like receptor signaling pathway
endolysosomal toll-like receptor signaling pathway
cellular response to type I interferon
cell surface toll-like receptor signaling pathway
BP
Viral protein interaction with cytokine and cytokine receptor
Toll-like receptor signaling pathway
RIG-I-like receptor signaling pathway
NOD-like receptor signaling pathway
JAK-STAT signaling pathway
Cytokine-cytokine receptor interaction
KEGG
229E
OC43
229E
OC43
−log10(FDR)
12
8
4
Gene Count
10
20
30
40
50

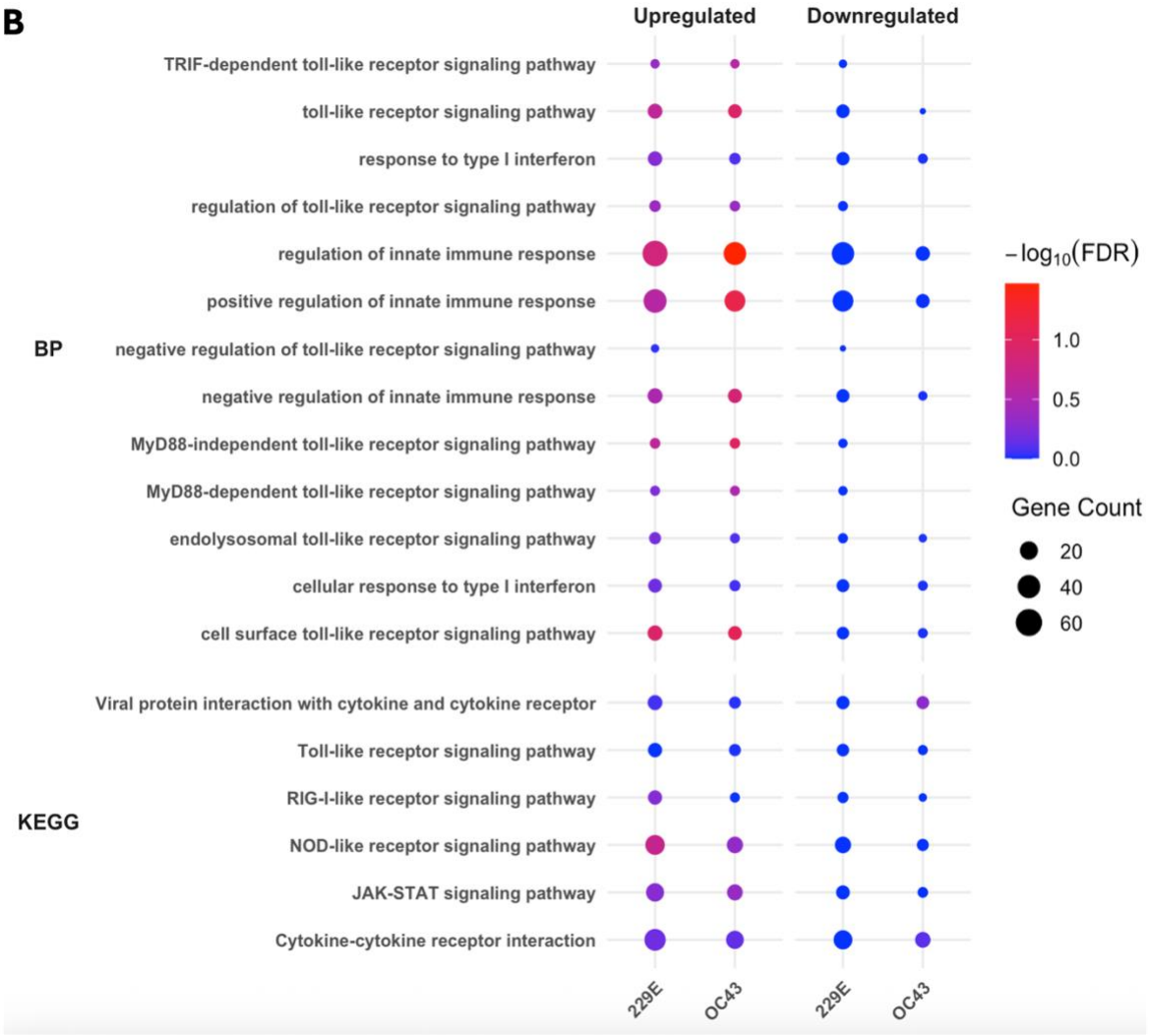

Figure 4.6: KEGG and GO Biological Process pathway enrichment in hNECs at 24 and 72 h post-infection (hpi).

(A) Enrichment of upregulated (left two columns) and downregulated (right two columns) genes in key GO Biological Process (BP, upper panel) and KEGG (lower panel) pathways at 24 hpi with HCoV-229E (first and third columns) or HCoV-OC43 (second and fourth columns), relative to mock-infected controls. Circle size reflects the number of DEGs mapping to each pathway; circle colour indicates statistical significance ($-\log_{10}$FDR), with redder hues denoting lower FDR values. HCoV-OC43 uniquely enriches the endolysosomal Toll-like receptor signalling pathway at 24 hpi. **(B)** As in (A), but for DEGs at 72 hpi. Both viruses continue to enrich core innate-immune pathways, such as regulation of innate immune response, response to type I IFN, cytokine-cytokine receptor interaction, and JAK-STAT signalling, with 229E showing higher gene counts in several pathways at this later time point.

4.2.7 Transcriptional profiling of MRC-5 cells infected with HCoV-229E or HCoV-OC43

To extend my observations beyond primary nasal epithelial cells, I re-analysed publicly available MRC-5 RNA-seq datasets (GSE155986 for HCoV-229E; GSE252692 for HCoV-OC43) in Partek Flow (v12.7.0). The same pipeline was applied for methodological consistency: adapter and quality trimming, STAR alignment to GRCh38, transcript quantification, and differential expression analysis with DESeq2 (FDR ≤ 0.05; $|\log_2 FC| \geq 1$), with biological replicates ($n = 3$ per condition) at each time point and mock controls included. By comparing responses in primary airway epithelial cells and immortalised fibroblasts, I aimed to separate cell-type–specific effects from virus-driven programmes, providing a broader view of how HCoVs modulate innate immunity in different human systems.

4.2.8 Sequencing quality and alignment metrics

Table 4.2 summarises sequencing-quality metrics for fifteen libraries: triplicate replicates of mock (0 hpi) and 229E-infected MRC-5 cells at 6, 24, 48, and 72 hpi (MOI: 0.01). Total read counts ranged from 23.25 million to 27.74 million per library. Mean Phred scores were consistently high (35.62–35.74), and alignment rates to GRCh38 exceeded 99% in all mock samples. Among infected libraries, alignment rates varied from 62.9% (6 hpi) to 99.1% (mock), with the lowest mapping efficiency at 6 hpi. Additional QC metrics include % ambiguous bases, GC content, unique versus non-unique paired alignments, and mean coverage depth, which are provided in Appendix Table 1.5.

Table 4.2 Key QC metrics for MRC-5 cells infected with HCoV-229E (MOI: 0.01)

Sample ID	Time (hpi)	Replicate	Total Reads (millons)	Mean Phred Score	Aligned Reads (%)

GSM4718629	0 (Mock)	A	24.37	35.62	99.01
GSM4718630	0 (Mock)	B	23.68	35.63	99.10
GSM4718631	0 (Mock)	C	24.11	35.65	99.12
GSM4718632	6	A	27.35	35.66	99.11
GSM4718633	6	B	23.35	35.70	98.08
GSM4718634	6	C	26.52	35.74	62.89
GSM4718635	24	A	24.90	35.73	64.89
GSM4718636	24	B	25.22	35.74	64.01
GSM4718637	24	C	27.74	35.74	77.59
GSM4718638	48	A	23.25	35.73	78.02
GSM4718639	48	B	24.47	35.71	78.92
GSM4718640	48	C	23.48	35.73	75.16
GSM4718641	72	A	25.17	35.73	74.85
GSM4718642	72	B	25.17	35.73	74.85
GSM4718643	72	C	25.17	35.73	74.85

Table 4.3 presents metrics for twenty-seven libraries: triplicate mock samples (–1 hpi) and triplicate HCoV-OC43-infected samples at 1.5, 3, 6, 9, 12, 18, 24, and 30 hpi (MOI 0.01). Total

read counts ranged from 41.43 M to 83.71 M. The mean Phred score was consistently 30.00 across all libraries. Alignment rates varied by more than 32.97% at 24 hpi versus up to 98.12% at 3 hpi, while mock controls aligned at 96.96-98.05%. Complete alignment and coverage statistics are available in Appendix Table 1.6.

Table 4.3 Key QC metrics for MRC-5 cells infected with HCoV-OC43 (MOI 0.01)

Sample ID	Virus	Time (hpi)	Replicate	Total Reads (M)	Mean Phred Score	Aligned Reads (%)
GSM8005236	Mock	–1	A	73.21	30.00	96.96
GSM8005244	Mock	–1	B	63.05	30.00	98.05
GSM8005252	Mock	–1	C	47.28	30.00	97.12
GSM8005245	OC43	1.5	A	69.69	30.00	97.69
GSM8005265	OC43	1.5	B	51.11	30.00	96.68
GSM8005253	OC43	1.5	C	49.21	30.00	97.50
GSM8005237	OC43	3	A	78.70	30.00	98.05
GSM8005246	OC43	3	B	73.58	30.00	98.12
GSM8005266	OC43	3	C	41.43	30.00	97.21
GSM8005238	OC43	6	A	65.53	30.00	97.30
GSM8005255	OC43	6	B	51.50	30.00	92.19
GSM8005267	OC43	6	C	55.38	30.00	96.35

GSM8005239	OC43	9	A	61.43	30.00	79.54
GSM8005247	OC43	9	B	70.80	30.00	82.91
GSM8005256	OC43	9	C	53.51	30.00	70.55
GSM8005240	OC43	12	A	71.35	30.00	51.96
GSM8005248	OC43	12	B	67.66	30.00	53.83
GSM8005257	OC43	12	C	45.38	30.00	45.55
GSM8005241	OC43	18	A	71.94	30.00	35.30
GSM8005249	OC43	18	B	74.09	30.00	35.38
GSM8005258	OC43	18	C	47.24	30.00	35.86
GSM8005242	OC43	24	A	69.26	30.00	34.27
GSM8005250	OC43	24	B	65.77	30.00	32.97
GSM8005269	OC43	24	C	59.46	30.00	46.39
GSM8005243	OC43	30	A	81.19	30.00	35.24
GSM8005251	OC43	30	B	71.14	30.00	36.45
GSM8005272	OC43	30	C	83.71	30.00	37.79

4.2.9 PCA separates mock and infected MRC-5 cells along virus- and time-dependent axes

To assess global variation and verify sample structure before differential, I next applied PCA to the MRC-5 datasets to capture global transcriptomic variation across all infected and mock conditions. PCA reduces high-dimensional gene-expression data into orthogonal components, allowing us to visualise whether samples segregate by virus, time point, or infection status. By mapping each sample's position in principal component space, one can assess the relative magnitude and kinetics of the host response and identify any outlier replicates.

PCA was performed on log_2-transformed, normalised counts for mock (-1 hpi) and HCoV-OC43-infected MRC-5 cells at 1.5, 3, 6, 9, 12, 18, 24 and 30 hpi (n = 3 each). The first two principal components, PC1 and PC2, accounted for 29.47 % and 7.39 % of the total variance, respectively. In PC1-PC2 space (Figure 4.7), mock samples form a tight cluster with PC1 values around +60 and PC2 around +40, reflecting minimal transcriptional change in uninfected cells. Early HCoV-OC43 time points (1.5-6 hpi) overlay closely with mock along PC1, indicating a muted early response. From 9 hpi onward, samples shift progressively left along PC1 and downward along PC2, with each subsequent time point occupying a more extreme position. By 30 hpi, all three biological replicates cluster at PC1 ~ -180 and PC2 ~ +60 (Figure 4.7A; Table 4.3). This trajectory illustrates a steady, time-dependent remodelling of host transcriptomes, with late HCoV-OC43 infection driving the most significant transcriptional divergence from mock.

I applied the same PCA approach to HCoV-229E-infected samples at 0 (mock), 6, 24, 48, and 72 hpi (n = 3 each). Here, PC1 accounted for 38.97% and PC2 for 19.11% of the variance. In Figure 4.7B, the mock replicates cluster near PC1 at ~10 and PC2 at ~40. The earliest time point (6 hpi) remains close to mock along PC1 but shifts downward on PC2 (~10). At 24 hpi,

all three replicates move sharply downward (PC2 ~125) and slightly to the right (PC1 ~10. By 48 hpi, the samples diverge notably, with PC1 ~-90 and PC2 ~-65, indicating the onset of the late, robust response. The 72 hpi cluster sits at PC1 ~ –110 and PC2 ~ -20. The nonlinear trajectory, with initial proximity to the mock, a mid-phase plateau, and then late-phase separation, mirrors the biphasic dynamics of DEG in HCoV-229E infection.

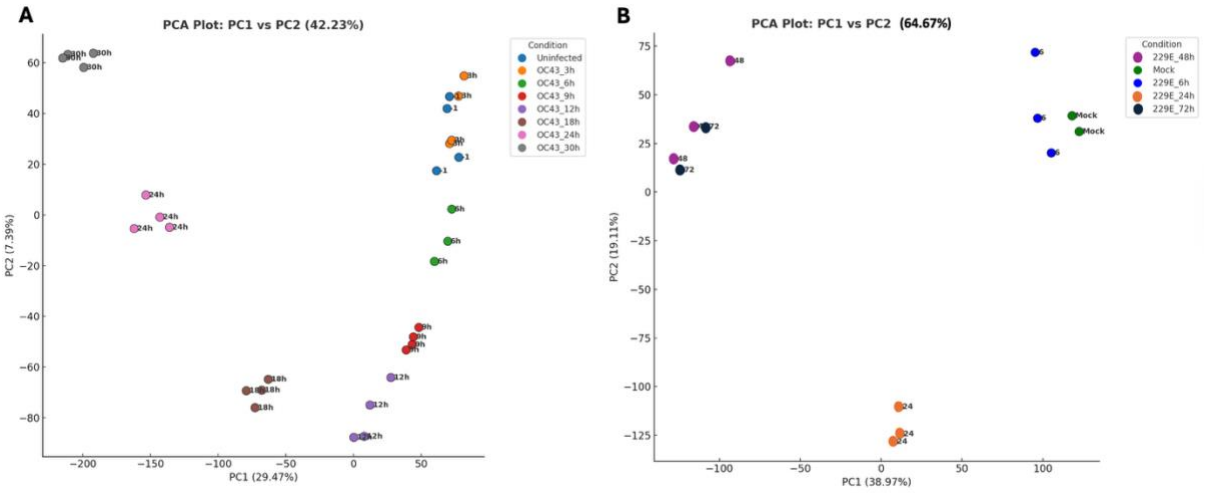

Figure 4.7: PCA of global transcriptomic HCoV-infected in MRC-5 cells

(A) HCoV-OC43 time course (MOI 0.01): mock (-1 hpi) and infected cells at 1.5, 3, 6, 9, 12, 18, 24 and 30 hpi (n = 3 per time point). **(B)** HCoV-229E time course (MOI 0.01): mock (0 hpi) and infected cells at 6, 24, 48 and 72 hpi (n = 3 per time point). PCA was performed in Partek Flow on log_2-transformed, library-size, normalised counts derived from STAR-aligned reads to GRCh38, using the same pipeline as for hNECs. Each point represents one biological replicate; colours denote condition, and the numeric labels indicate the sampling time (hpi). Axis labels show the percentage of total variance explained by PC1 and PC2.

4.2.10 Differential expression dynamics in MRC-5

Throughout the course of HCoV-OC43 infection in MRC-5 cells, a gradual and sustained transcriptional response was observed. Using a uniform threshold of FDR ≤ 0.05 and $|log_2FC| \geq 1$, a total of 14,379 unique transcripts met these criteria at one or more time points. At 1.5 hpi,

129 genes were upregulated and 34 were downregulated compared to mock controls. This response was intensified by 3 hpi (326 up; 136 down) and 6 hpi (294 up; 124 down), indicating early activation of host defences. By 9 hpi, upregulated transcripts increased to 413 and downregulated to 226, and this trend continued through 12 hpi (844 up; 561 down) and 18 hpi (2,312 up; 1,623 down). The number of regulated genes peaked at 30 hpi, when 5,036 transcripts were upregulated and 5,451 were downregulated (Figure 4.8A). These data demonstrate that HCoV-OC43 infection triggers a progressively stronger host response, with both induction and suppression programmes expanding steadily over 30 h.

In contrast, HCoV-229E, compared to the mock, triggered a biphasic transcriptional programme involving a total of 15,413 DEGs over the 6-72 hpi. At 6 hpi, 773 genes were upregulated and 943 were downregulated, indicating an early wave of host modulation. This response plateaued by 24 hpi (951 up; 904 down) before surging again at 48 hpi, with 1,486 transcripts upregulated and 1,594 downregulated. The most significant shift occurred at 72 hpi, when 3,670 genes were upregulated and 3,440 were downregulated compared to mock-infected controls (Figure 4.8B). Therefore, HCoV-229E infection is characterised by an initial moderate response, a transient stabilisation, and a second robust phase of host-transcript remodelling.

Together, these patterns indicate that HCoV-OC43 induces a consistent build-up of regulated genes, peaking at later stages, whereas HCoV-229E triggers an early response, followed by a plateau, and a transcriptional shift at later stages. Both viruses activate broad host programmes, up-regulating antiviral and inflammatory genes and down-regulating metabolic and structural transcripts. However, the distinct timing of these responses likely reflects differences in viral replication dynamics and immune evasion strategies between the two viruses.

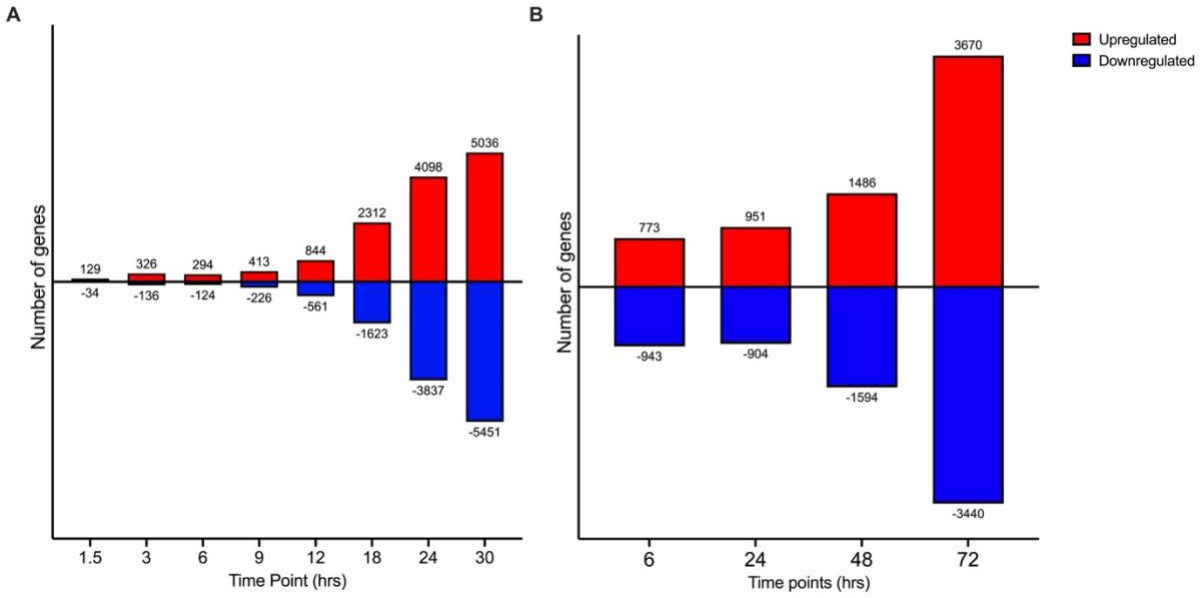

Figure 4.8: Time-resolved differential gene expression in MRC-5 cells infected with seasonal coronaviruses.

(A) HCoV-OC43 (MOI 0.01): numbers of upregulated (red, above zero) and downregulated (blue, below zero) transcripts at 1.5, 3, 6, 9, 12, 18, 24 and 30 hpi, each comparison made against time-matched uninfected controls from the same study. **(B)** HCoV-229E (MOI 0.01): corresponding counts at 6, 24, 48 and 72 hpi. Bars show genes meeting the differential-expression threshold FDR ≤ 0.05 and $|\log_2 FC| \geq 1$. Numeric labels indicate the exact gene counts for each direction at each time point. RNA-seq datasets were re-analysed in Partek Flow using a standard pipeline (STAR alignment; DE testing as per original study design) for GSE252692 (HCoV-OC43) and GSE155986 (HCoV-229E). Each time point is evaluated independently; a gene may be counted at multiple time points if it meets criteria in more than one comparison.

4.2.11 ISG kinetics split by virus: contrasting IFN programmes under HCoV-OC43 and HCoV-229E

Following the global sample relationships revealed by PCA (Figure 4.7) and the differential gene analysis (Figure 4.8), I next asked whether these global patterns were driven by differences in the magnitude and kinetics of antiviral programmes. I examined the temporal regulation of canonical ISGs and inflammatory mediators in MRC-5 cells infected with HCoV-229E or HCoV-OC43. Two curated gene panels were visualised as heatmaps: (i) classical ISGs/antiviral

effectors, and (ii) inflammatory and cytokine-related genes. Log_2 fold-change values shown in the heatmaps are relative to mock controls. These gene sets were derived from the Hallmark IFNα response and inflammation collections and are presented as log_2 fold-change values relative to mock controls.

To explore the behaviour of key ISGs, I examined representative antiviral effectors and signalling molecules in HCoV-229E-infected MRC-5 cells compared with mock controls (Figure 4.9A). All values reported below are log2 fold change relative to time-matched mock controls (positive values suggest higher expression; negative values suggest lower expression). *IFITM2* shifted from -0.6 at 6 hpi to -1.1 at 24 hpi, then to -3.8 at 48 hpi and -3.6 at 72 hpi; *IFITM1* from -1.0 to -1.3, then to -3.4 and -3.0; and *IFITM3* from -0.7 to -1.0, then to -3.1 and -3.0. *IFIT1* remained negative throughout the series (-1.3 at 6 hpi; -0.4 at 24 hpi; -1.4 at 48 hpi; -1.8 at 72 hpi). By contrast, several signalling and sensor transcripts increased at later time points: *IRF1* rose from -1.4 (6 hpi) to 0.8 (24 hpi) and then to 2.2 (48 hpi) and 2.4 (72 hpi); *MX1* shifted from -0.3 (6 hpi) to 0.4 (24 hpi), then to 1.2 (48 hpi) and 2.1 (72 hpi); STAT2 increased from -0.8 (6 hpi) to 0.6 (24 hpi), then to 1.0 (48 hpi) and 0.7 (72 hpi). *IFIH1* changed from -0.6 (6 hpi) to 0.4 (24 hpi) and reached 1.1-1.2 at 48-72 hpi; *ISG20* reached 2.2 at both 48 hpi and 72 hpi. Several other ISGs remained near baseline at one or more early time points.

In the HCoV-OC43-infected MRC-5 cells compared to the mock (Figure 4.9B), IFIT and IFITM family members also showed a downward trend, with *IFITM1* decreasing from -0.3 at 6 hpi) to -1.8 at 18 hpi), -2.7 at 24 hpi) and -2.5 (30 hpi), and *IFITM2* declined from -0.2 at 6 hpi) to -1.5 at 18 hpi), -2.4 at 24 hpi) and -3.3 at 30 hpi). *IFIT3* values remained negative throughout but were less extreme by 30 hpi (-0.8, -1.2, -1.4, -0.9, -0.5, -0.3 across 6-30 hpi). Against this background, several mediators exhibited earlier positive shifts than in the HCoV-229E-infected cells. *MX1* reached 1.2 at 24 hpi and 2.7 at 30 hpi (compared to 1.2 at 48 hpi and

2.1 at 72 hpi in HCoV-229E). *IRF2* was 1.0 at 18 hpi, 1.2 at 24 hpi and 1.3 at 30 hpi; STAT2 increased to 0.7-1.1 between 24 and 30 hpi. *IFIH1* was negative at 6-12 h (as low as -1.6 at 12 hpi) and approached small positive values by 24-30 hpi (0.1-0.9).

The result highlights both shared patterns and timing differences in canonical ISG regulation. IFIT/IFITM family members are predominantly downregulated in both infections, with more pronounced negative values at later measurements. In contrast, a group of transcriptional and antiviral mediators shows increasing positive values over time in each dataset, but with different kinetics: *MX1, IRF2*, and *STAT2* become positive earlier in HCoV-OC43 (18-30 hpi) than in HCoV-229E (48-72 hpi), while *IRF1* exhibits a marked late rise in expression in HCoV-229E (2.2-2.4 at 48-72 hpi) compared to mock samples and remains closer to baseline across the HCoV-OC43 series. *IFIT1* stays negative in 229E through 72 hpi, whereas in HCoV-OC43 it approaches baseline by 30 hpi (0.0).

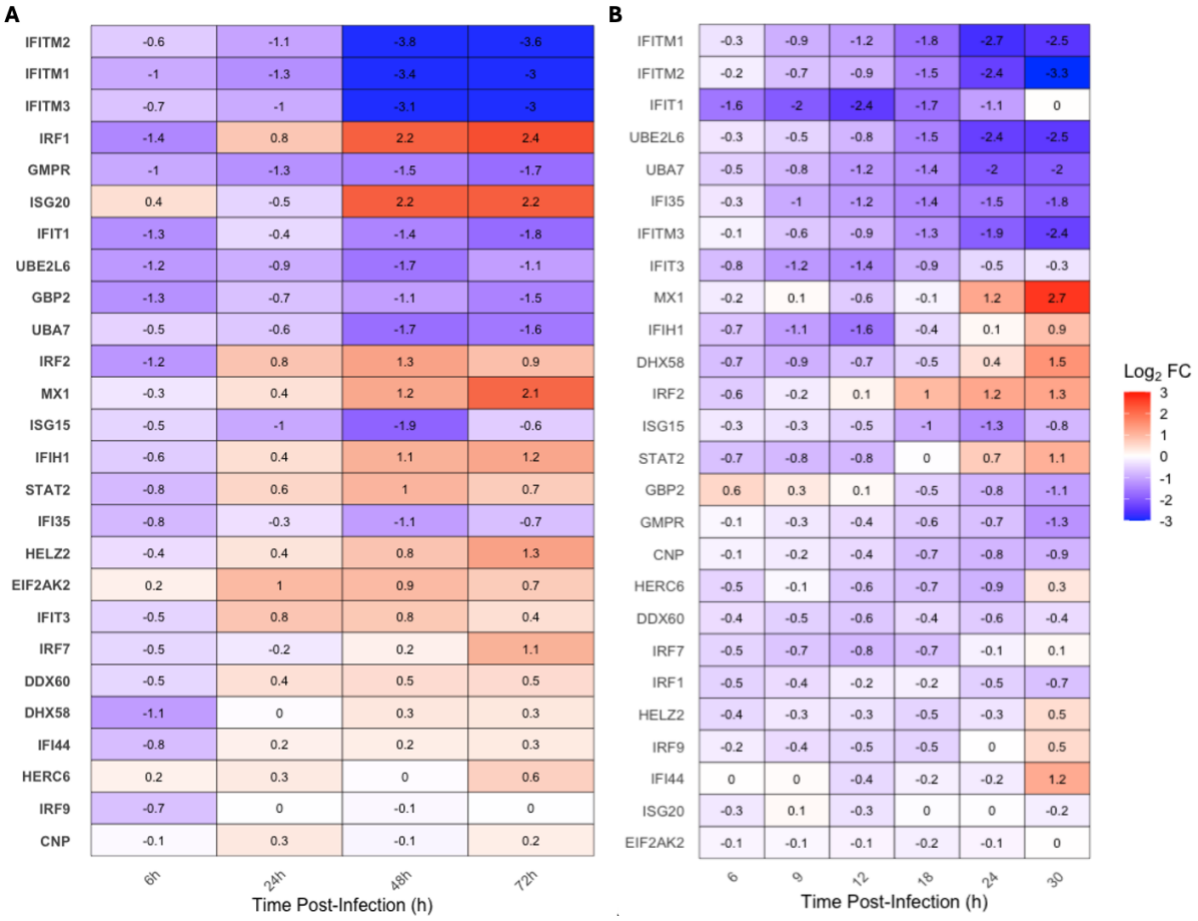

Figure 4.9: Canonical ISG expression in MRC-5 cells infected with seasonal coronaviruses.

(A) HCoV-229E ISG heatmap (6, 24, 48, 72 hpi). **(B)** HCoV-OC43 ISG heatmap (6, 9, 12, 18, 24, 30 hpi). Values are $\log_2$ fold-change relative to mock (DESeq2). Circle markers indicate cells where the gene meets FDR ≤ 0.05 and $|\log_2 FC| \geq 1$. Rows use an identical ISG list and order across panels; columns are ordered by time. Colour scale is shared across panels (-3 to +3)

4.2.12 Inflammatory signalling profiles reveal divergent kinetics of HCoV-OC43 and HCoV-229E.

The HCoV-229E, compared to the mock inflammatory panel (Figure 4.10A), shows marked late increases across multiple chemokines and cytokines. *CXCL2* rose from 0.5 at 6 hpi to 6.0 at 24 hpi and reached 11.5 at 48 hpi and 11.8 at 72 hpi. *CXCL3* increased from 1.1 at 6 hpi to 4.7 at 24 hpi and 10.0-10.4 at 48-72 hpi. *CXCL8* moved from 1.7 (6 hpi) to 2.6 (24 hpi) and then 10.2-10.5 (48-72 hpi). *CXCL1* changed from -0.6 (6 hpi) to 1.3 (24 hpi) and 6.7-6.8 at 48-72 hpi. Cytokine transcripts followed similar trajectories: *IL6* progressed from -0.3 (6 hpi) to 1.1 (24 hpi) and 6.1-6.0 (48-72 hpi); *IL1A* increased from -1.9 (6 hpi) to 3.0 (24 hpi) and 7.1-7.2 (48-72 hpi). NF-κB pathway components were also elevated at later time points: NFKBIA moved from -0.9(6 hpi) to 0.8 (24 hpi) and 4.4-5.1 (48-72 hpi); *NFKB1* rose from 0.2 (6 hpi) to 1.5 (24 hpi) and ~4.0 at 48-72 hpi. A minority of genes showed negative values at one or more time points, for example, *CCL2* was -1.3 at 6-24 hpi and -1.1 at 72 hpi, and *TNFSF15* changed from -1.6 (6 hpi) to -3.0 (24 hpi) before increasing to 1.6 (48 hpi) and 1.9 (72 hpi).

The HCoV-OC43 inflammatory heatmap (Figure 4.10B) indicates earlier onset and sustained elevation of chemokines across the 6-30 h series. *CXCL8* was already high at 5.8 (6 hpi) and 5.2 (9 hpi), remained 4.9-3.8 at 12-18 hpi, and stayed positive through 3.1-2.6 at 24-30 hpi. *CXCL2* rose progressively from 1.9 (6 hpi) to 2.3 (9 hpi), 3.2 (12 hpi), 3.8 (18 hpi), 4.7 (24 hpi)

and 5.3 (30 hpi); *CXCL3* increased from 2.7 (6 hpi) to 1.9 (9 hpi), 2.7 (12 hpi), 3.0 (18 hpi), 3.5 (24 hpi) and 4.1 (30 hpi). *CXCL1* was 2.9 at 6 hpi, peaked around 4.2 at 12 hpi, and remained 3.5-2.7 through 30 hpi. *IL6* showed sustained positive values from 1.7 (6 hpi) to 3.4 (30 hpi). *NF-κB* pathway markers were consistently elevated: *NFKBIA* ranged 1.2-2.4 between 6-18 hpi and remained 1.6 at 30 hpi; *NFKB1* lay between 1.1-1.9 over 6-30 hpi. Some transcripts showed small late decreases, for example, *CCL2* moved from 1.9 (6 hpi) to -0.3 (30 hpi) and *CNTF* from 0.0 (6 hpi) to -0.7 (30 hpi).

Placing the heatmaps side by side highlights the shared distinct features of the inflammatory response in MRC-5 cells. Both HCoV-229E and HCoV-OC43 upregulate chemokines (*CXCL8, CXCL2, CXCL3, CXCL1*) and elevate NF-κB-related transcripts (*NFKBIA, NFKB1*). The timing and magnitude differ: HCoV-OC43shows earlier and sustained chemokine induction (for example, *CXCL8* 5.8 at 6 hpi), whereas HCoV-229E exhibits larger late increases at 48–72 hpi (for example, *CXCL2* 11.5-11.8, *CXCL3* 10.0-10.4, *CXCL8* 10.2-10.5). *IL6* is positive throughout both series, rising earlier in HCoV-OC43 and attaining higher values later in HCoV-229E. These patterns are visualised in Figure 4.10A-B

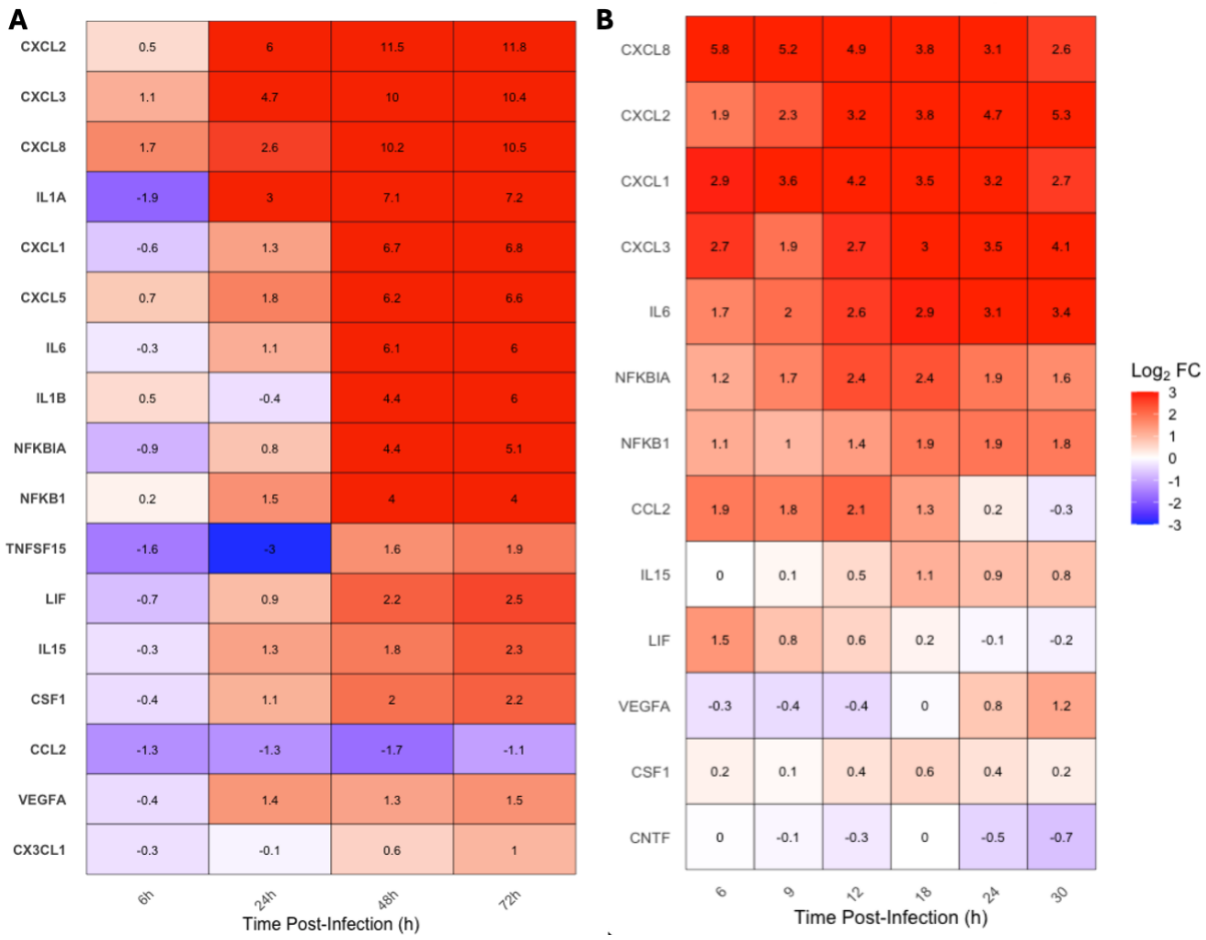

Figure 4.10: Inflammatory and cytokine gene expression in MRC-5 cells infected with seasonal coronaviruses.

(A) HCoV-229E inflammatory/cytokine heatmap (6, 24, 48, 72 hpi). (B) HCoV-OC43 inflammatory/cytokine heatmap (6, 9, 12, 18, 24, 30 hpi). Display and thresholds as in Figure 4.8. Gene rows and colour scale are identical across panels to support direct visual comparison.

4.2.13 Functional pathway analysis of HCoV-OC43 infection in MRC-5 cells

The PCA and heatmaps established that HCoV-229E and HCoV-OC43 trigger distinct kinetics of ISG and inflammatory gene modulation in MRC-5 cells (Figures 4.9-4.10). To determine whether these gene-level patterns aggregate into coordinated innate-immune programmes, I performed pathway enrichment on the differentially expressed transcripts from each time point.

This step provides a systems view of the host response and reduces redundancy across individual genes by summarising them into biological processes and signalling cascades.

For each virus and time point, upregulated and downregulated transcript sets (DESeq2; FDR ≤ 0.05, $|\log_2 FC| \geq 1$) were analysed in ShinyGO against the expressed-gene background for the corresponding dataset (HCoV-229E: 15,413 genes; HCoV-OC43: 14,379 genes). I focused on GO Biological Process terms relevant to innate immunity and KEGG pathways covering viral sensing and cytokine/JAK-STAT signalling. ShinyGO outputs (gene counts and FDR values) were exported and visualised in R as dot plots in which point size represents the number of input genes annotated to a term and colour encodes enrichment strength as $\log_{10}$(FDR). Because the MRC-5 datasets originate from independent studies with different sampling grids, all enrichment tests were performed within each dataset relative to its matched mock; cross-panel comparisons are qualitative, with direct alignment only at 24 hpi.

At 1.5 hpi, upregulated transcripts were enriched for NOD-like receptor signalling (8 genes; -LogFDR = 3.58), including *CXCL1*, *CXCL2* and *CXCL8*. Toll-like receptor signalling (4 genes; -LogFDR = 1.68) and RIG-I-like receptor signalling (2 genes (*CXCL8*, *NFKBIA)*; -LogFDR = 0.72) were also enriched, consistent with early detection of viral patterns. JAK–STAT signalling was detected at lower strength (1 gene (*LIF)*; -LogFDR = 0.18).

Early immune activation persisted through 3 and 6 hpi. At 3 hpi, cell surface Toll-like receptor signalling (2 genes (*NFKBIA*, *TLR5)*; -LogFDR = 0.88) and RIG-I-like receptor signalling (2 genes (*GBP1*, *USP25)*; -LogFDR = 0.14) remained enriched. By 6 hpi, viral protein interaction with cytokine and cytokine receptor (1 gene (*SOCS3)*; -LogFDR = 0.012) and JAK-STAT signalling (1 gene (*SOCS3)*; -LogFDR = 0.012) were returned among upregulated pathways.

A transition emerged around 9-12 hpi. At 9 hpi, RIG-I-like receptor signalling (3 genes (*IFNB1*, *IKBKG*, *IRF3)*; -LogFDR = 0.009) was enriched among upregulated transcripts. By 12

hpi, antiviral terms started to decline: response to type I IFN (1 gene-*IRF3*; -LogFDR = 0.012) appeared in the downregulated set.

Suppression became clearer at 18 hpi, with RIG-I-like receptor signalling (1 gene (*STING1)*; -LogFDR = 0.005) and JAK-STAT signalling (1 gene (*IFI35)*; -LogFDR = 0.005) returned among downregulated pathways. By 24-30 hpi, the profile had shifted decisively towards reduced IFN-linked activity. At 24 hpi, cellular response to type I IFN (4 genes; -LogFDR = 0.017) was downregulated, including *IFITM1*, *IFITM2* and *IFITM3*. At 30 hpi, both response to type I IFN (6 genes; -LogFDR = 0.024) and cellular response to type I IFN (6 genes; -LogFDR = 0.031) were downregulated. In parallel, positive regulation of innate immune response was also reduced (26 genes; -LogFDR = 0.011). These pathways calls align with the decreases observed for *IFITM1*, *IFITM2* and *IFITM3* in the late HCoV-OC43 ISG heatmap.

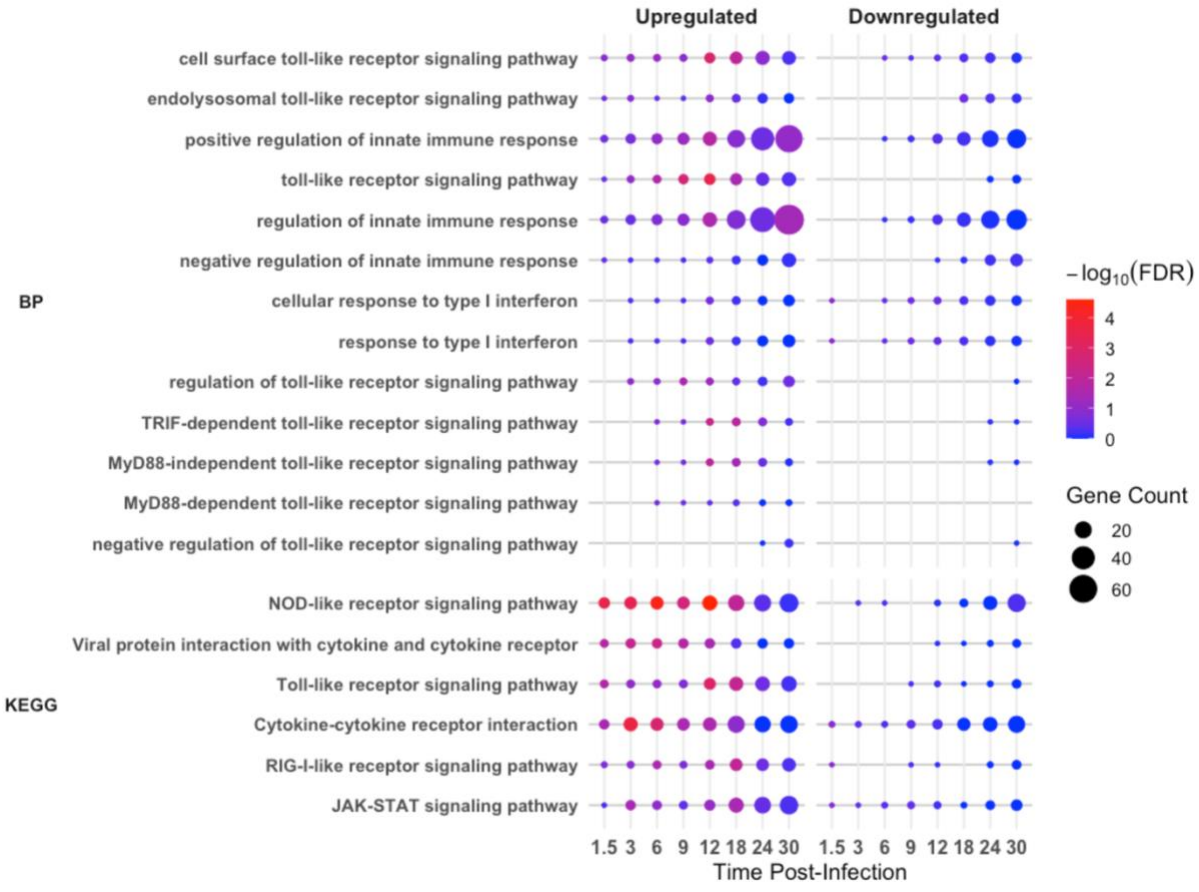

Figure 4.11: Functional pathway enrichment for HCoV-OC43 innate-immune and cytokine signalling in MRC-5 cells.

HCoV-OC43 (1.5, 3, 6, 9, 12, 18, 24, 30 hpi). Upregulated and downregulated transcript sets (DESeq2; FDR ≤ 0.05; $|\log_2 FC| \geq 1$) were analysed separately in ShinyGO. Dot size indicates the number of input genes contributing to each term; colour shows $-\log_{10}$(FDR). Only innate-immune GO Biological Process and KEGG pathways are displayed.

Pathway enrichment across the HCoV-229E time course indicated sustained activation of innate-immune and antiviral signalling families, with IFN-linked terms detectable at late time points.

At 6 hpi, upregulated transcripts already returned enrichment for RIG-I-like receptor signalling (1 gene (*CXCL8)*; -LogFDR = 0.00015), Toll-like receptor signalling (1 gene (*CXCL8)*; -LogFDR = 0.00015), JAK-STAT signalling (2 genes (*IL11*, *EGF)*; -LogFDR = 0.00015) and cytokine-cytokine receptor interaction (4 genes; -LogFDR = 0.00015), consistent with rapid initiation of host defences.

The robust antiviral state was maintained and even strengthened as the infection progressed. At 24 hpi, the JAK-STAT signalling pathway remained significantly upregulated (2 genes, (*IRF9* and *SOCS3*), -LogFDR=1.63), a key finding that shows a continued active ISG response.

By 48 hpi, enrichment remained broad: RIG-I-like receptor signalling (1 gene (*CXCL8)*; -LogFDR = 0.00012) and Toll-like receptor signalling (1 gene (*CXCL8)*; -LogFDR = 0.00012) persisted, and the BP term response to type I IFN showed strong upregulation (1 gene (*SETD2)*; -LogFDR = 0.000004), in keeping with a pronounced ISG signature.

At 72 hpi, the antiviral programme was still evident, though some pathways showed signs of reduction. Response to type I IFN remained upregulated (1 gene, *SETD2*; -LogFDR = 0.0049).

In the downregulated sets, NOD-like receptor signalling (3genes (*CCL2*, *GBP2*, *GABARAP)*; -LogFDR = 3.58×10^{-6}) and JAK–STAT signalling (1 gene (*IRF9)*; -LogFDR = 3.58×10^{-6}) were returned, suggesting selective dampening of specific arms of innate signalling at the late time point.

In summary, HCoV-229E triggered rapid and sustained enrichment of antiviral and inflammatory pathways throughout the time course, whereas HCoV-OC43 showed an early chemokine-dominant profile in MRC-5 from 6-30 hpi with strong increases in *CXCL8* and *CXCL2* but limited ISG induction, followed by attenuation or absence of enrichment for type I IFN gene sets later in the course.

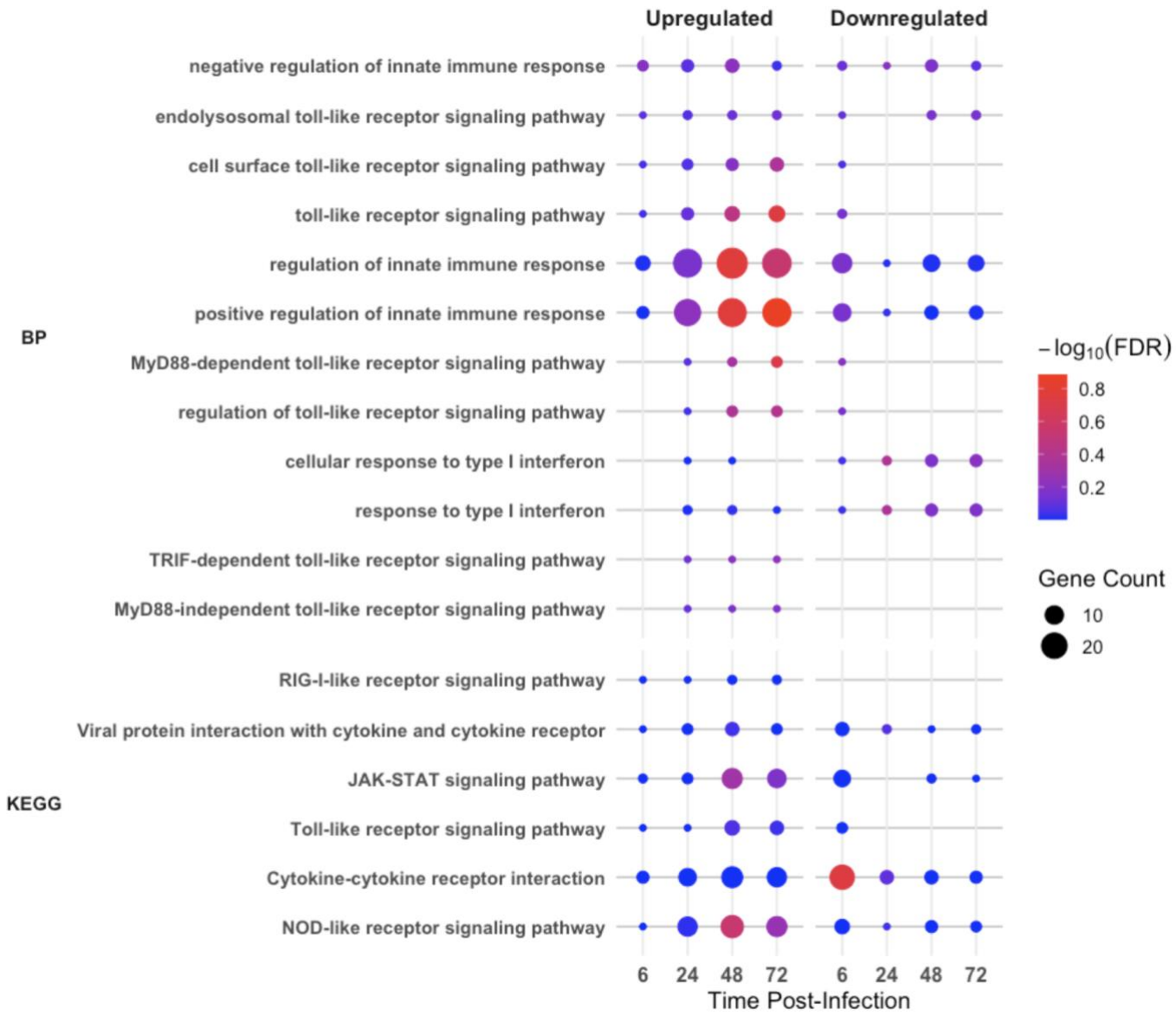

Figure 4.12: Functional pathway enrichment for HCoV-229E innate-immune and cytokine signalling in MRC-5 cells.

HCoV-229E (6, 24, 48, 72 hpi), upregulated and downregulated transcript sets (DESeq2; FDR ≤ 0.05; $|\log_2 FC| \geq 1$) were analysed separately in ShinyGO. Dot size indicates the number of input genes contributing to each term; colour shows $-\log_{10}(FDR)$. Only innate-immune GO Biological Process and KEGG pathways are displayed.

4.3 Discussion

Overview of principal findings

This chapter explored how seasonal coronaviruses HCoV-229E and HCoV-OC43 influence type I IFN and inflammatory pathways in two cellular models: primary human nasal epithelial cells (hNECs, air-liquid interface) and the continuous lung cell line MRC-5. In both systems, infections showed enrichment of gene sets annotated to canonical innate modules, including PRR (Toll-like receptor, RIG-I-like receptor, and NOD-like receptor signalling), cytokine-cytokine receptor interactions, and JAK-STAT signalling. The timing and strength of responses varied by virus and model. In hNECs, differential expression analysis (DESeq2, FDR ≤ 0.05; $|\log_2 FC| \geq 1$) compared to mock controls revealed that HCoV-229E induced more upregulated and downregulated transcripts than HCoV-OC43 at both 24 and 72 hpi (Figure 4.4). PCA distinguished samples based on infection and time (Figure 4.4) and overlaps between virus-induced upregulated transcripts and IFNα-stimulated controls confirmed a core set of ISGs shared across conditions (Figure 4.5). While direct IFN transcripts were not strongly detected, the earlier induction of selected ISGs and the stronger 24 h overlap with IFNα signatures suggest that HCoV-OC43 elicits an earlier IFN-like transcriptional response in hNECs than HCoV-229E. However, whether this reflects bona fide IFN production or IFN-independent ISG activation cannot be resolved from these datasets alone (Figure 4.5C-D).

In MRC-5 cells, side-by-side heatmaps revealed an early and sustained chemokine response in HCoV-OC43 (for example, *CXCL8*, *CXCL2*, *CXCL3* from 6-30 hpi), contrasted with significantly larger, later increases in chemokines during HCoV-229E at 48-72 hpi (Figure 4.9A-B). Canonical ISG profiles showed earlier positive responses for *MX1*, *STAT2*, and *IRF2* with HCoV-OC43 (18-30 hpi), and later increases for *IRF1*, *MX1*, and *STAT2* with

HCoV-229E (48-72 hpi), while transcripts from the IFIT/IFITM family were reduced across both infections (Figure 4.8A-B). ShinyGO analysis, visualised in R, condensed these gene-level changes into enriched pathways with consistent kinetics: HCoV-OC43 exhibited early enrichment of pattern-recognition and cytokine pathways from the initial sampling window, whereas HCoV-229E showed broad, sustained enrichment that was strongest at 48-72 hpi (Figure 4.10A–B). Overall, these findings suggest that both viruses activate the same innate pathways, but HCoV-OC43 tends to respond earlier in fibroblasts, while HCoV-229E induces a broader response at later stages, especially in hNECs.

A consistent feature of respiratory viruses is early detection by endosomal Toll-like receptors (such as TLR3, TLR7/8) and cytosolic RIG-I-like receptors (*RIG-I, MDA5*), which activate IRF3/7 and *NF-κB* pathways to induce IFNs and chemokines (Iwasaki, 2012; Killip *et al.*, 2015). Influenza A virus, rhinoviruses, and respiratory syncytial virus typically trigger rapid chemokine responses in airway epithelium, with *CXCL8, CXCL10*, and *CCL5* among the most consistently upregulated transcripts (Killip *et al.*, 2015; Jacobs *et al.*, 2013). In my MRC-5 dataset, HCoV-OC43 mirrors only part of this pattern: from 6 to 30 hpi I observe marked transcript increases in chemokines, particularly *CXCL8* and *CXCL2*, while most canonical ISGs remain near baseline. By contrast, HCoV-229E shows stronger pathway enrichment across IFN-related gene sets between 24 and 72 hpi, with broader ISG involvement than HCoV-OC43 in the same cell type. Where pathway analysis is applied, I refer to enrichment of gene sets rather than functional activation, and I interpret these profiles as evidence of an early chemokine-dominant response to HCoV-OC43 in fibroblasts, versus a broader IFN-linked program with HCoV-229E over time. Differences between viruses and cell types likely contribute, as both viruses show IFN-related pathway enrichment in primary nasal epithelial cells at 24 hpi, with 229E remaining broader at 72 hpi, consistent with previous epithelial

transcriptome studies of seasonal coronaviruses and influenza (Menachery *et al.*, 2014; Loske *et al.*, 2022).

Coronaviruses are characterised by strong antagonism of type I IFN signalling through multiple accessory proteins and proteases that target *MAVS-TBK1-IRF3, STAT1/2*, or ISG effectors (Kindler *et al.*, 2016; Park and Iwasaki, 2020). Research on SARS-CoV, MERS-CoV, and SARS-CoV-2 has highlighted delayed or diminished early IFN responses followed by inflammatory surges (Blanco-Melo *et al.*, 2020; Hadjadj *et al.*, 2020; Kindler *et al.*, 2016). In this context, my observation suggests that the early HCoV-OC43 phenotype in MRC-5 is chemokine-led with limited ISG induction, consistent with sensing at the transcript level but not direct evidence of signalling activity. In contrast, the stronger late breadth with HCoV-229E suggests a more expansive IFN-like program despite ongoing viral antagonism (Figures 4.9-4.10). Downregulation of IFITM family transcripts in MRC-5 cells during both infections also supports reports that coronaviruses modulate IFITM expression or function to facilitate entry or spread (Zhao *et al.*, 2014; Shi *et al.*, 2017). Finally, the greater overlap between virus-induced genes and IFNα-responsive transcripts for HCoV-OC43 at 24 hpi in hNECs matches studies showing robust nasal epithelial priming and early ISG readiness in the upper airway (Ziegler *et al.*, 2021; Loske *et al.*, 2022).

Three mechanistic themes emerge. First, sensor engagement and timing. The early HCoV-OC43 signature in MRC-5 features enrichment of RIG-I-like, NOD-like and Toll-like receptor signalling at 1.5-12 hpi, with *NFKBIA*, *IRF3*, *IFNB1* and adaptor-linked terms identified in the pathway lists (Figure 4.10B). This pattern indicates an intact upstream detection axis and early transcriptional output. In contrast, the strongest 229E enrichment occurs at 48-72 hpi (Figure 4.10A), coincident with the largest chemokine values in Figure 4.9A. The delayed rise

of *IRF1*, *MX1* and *STAT2* in HCoV-229E (Figure 4.8A) suggests that either upstream sensing is slower or that antagonism is overcome later in infection.

Second, effector composition. *IFIT* and *IFITM* family transcripts are reduced in MRC-5 during both infections (Figure 4.8), while *MX1*, *STAT2* and *IRF2* return later positive values. This mixture is captured at the pathway level by the presence of upregulated JAK-STAT and RIG-I-like signatures alongside downregulated innate-immune terms at late time points (for example downregulated JAK-STAT or NOD-like receptor entries at 72 hpi for HCoV-229E; Figure 4.10A). One interpretation is that coronaviruses selectively repress ISG subsets that restrict entry or membrane fusion (*IFITM1-3*), while leaving other antiviral modules partially active or restored later (Schoggins, 2019; Park and Iwasaki, 2020). A related mechanism is transcriptional feedback secondary to high chemokine output, where negative regulators such as *SOCS3* or *USP25* shape pathway tone; both appear in HCoV-OC43 pathway lists at early times.

Third, cell-type context. hNECs are polarised, mucociliary epithelia with high basal ISG tone and abundant pattern-recognition receptors (Comer *et al.*, 2012; Loske *et al.*, 2022). MRC-5 cells lack ciliation and mucus secretion, differ in the abundance and localisation of TLRs and RLRs, and have distinct basal cytokine profiles. These differences are evident in the datasets. In hNECs, HCoV-229E produces markedly more upregulated and downregulated transcripts than HCoV-OC43 at both 24 and 72 hpi (Figure 4.4) and overlaps with IFNα capture a canonical ISG core (Figure 4.5). In MRC-5, the kinetics are more pronounced: HCoV-OC43 acts early; HCoV-229E acts late; both display negative values for IFITM genes (Figures 4.8-4.9). These patterns are consistent with the idea that epithelial cells, particularly in the nose, are primed to sense and contain infection rapidly (Ziegler *et al.*, 2021; Loske *et al.*, 2022), whereas cells reveal how coronaviruses reshape innate tone over an extended time course.

Using a single analysis pipeline mitigated technical confounders and allowed systematic contrasts. At 24 hpi, a shared time point, hNECs showed a greater number of differentially expressed transcripts for HCoV-229E versus mock than for HCoV-OC43 versus mock (Figure 4.4), while MRC-5 highlighted broader early innate-sensing enrichment for HCoV-OC43 (Figure 4.10B) and moderate but expanding programmes for HCoV-229E (Figure 4.10A). By 72 hpi in hNECs, HCoV-229E produced extensive transcriptional changes, including thousands of downregulated transcripts, whereas HCoV-OC43 maintained a more balanced profile with persistent ISG induction (Figure 4.4). In MRC-5, HCoV-229E reached its peak transcriptomic breadth at 48-72 hpi meaning the highest number of counts of DE genes together with the most pathways enriched, and HCoV-OC43 displayed early peaks with a later tendency to reduce ISG-enriched pathways (Figures 4.9-4.10). The IFNα benchmark in hNECs confirmed that both viruses engage bona fide ISGs; the more substantial 24 h overlap with IFNα for HCoV-OC43 provides an internal reference absent from the MRC-5 datasets (Figure 4.5). Functionally, both models converge on the same pathway families, including pattern recognition, cytokine interactions, and the JAK-STAT pathway, and differ in timing and relative amplitude. These features probably reflect the basal state and architecture. The nasal epithelium provides physical and immunological barriers, characterised by high PRR expression and tonic ISG levels, which favour rapid containment (Comer *et al.*, 2012; Loske *et al.*, 2022). Fibroblasts lack mucociliary features and may exhibit a distinct balance between NF-κB-driven chemokines and type I IFN modules, highlighting how coronaviruses regulate innate tone throughout the infection cycle.

The data support three main implications for the seasonal biology of coronavirus. First, early intervention is crucial. HCoV-OC43's pathway analysis in hNECs shows enrichment of gene sets annotated to PRR signalling rather than direct evidence of pathway activation, along with the immediate increase in chemokines in MRC-5 cells, indicating a narrow window to influence

the disease course through pre- or post-exposure treatments that modulate PRR engagement or amplify early JAK-STAT dependent ISG induction (Totura and Baric, 2012; Park and Iwasaki, 2020). Second, effector selectivity. The consistent decrease in *IFITM* transcripts in MRC-5 cells across both infections, combined with the later restoration or increase of *MX1* and *STAT2*, suggests selective antagonism of entry-restricting ISGs, whereas JAK-STAT-responsive effectors are inducible at later time points (Schoggins, 2019; Zhao *et al.*, 2014). Third, tissue context. The hNEC data, with clear IFNα benchmarks and strong late-stage breadth for HCoV-229E, suggest that nasal epithelial cells can initiate broad antiviral programmes that differ from MRC-5 cell responses, supporting the use of airway models for assessing prophylactic IFN or PRR agonists (Vanderheiden *et al.*, 2020; Loske *et al.*, 2022). Comparing these findings with other respiratory viruses provides further context. Influenza A typically triggers a vigorous early type I IFN response and chemokine surge in airway cells (Killip *et al.*, 2015), while RSV can induce strong chemokine responses with variable IFN levels depending on strain and cell type (Van Royen *et al.*, 2022). SARS-CoV-2 often exhibits delayed type I IFN responses, accompanied by a surge of inflammatory mediators later in the disease (Blanco-Melo *et al.*, 2020; Hadjadj *et al.*, 2020). The HCoV-OC43-early/HCoV-229E-late pattern observed in MRC-5 cells, along with the broader late response for HCoV-229E in hNECs, aligns within this spectrum, highlighting how sampling timing and cell type influence observed IFN/ISG dynamics.

Chapter 5

Assessing the role of type I IFN-α and type III IFN-λ in shaping HCoV-OC43 replication and host responses.

5.1 Introduction

HCoV-OC43 is a seasonal respiratory pathogen responsible for a significant proportion of common cold cases worldwide (Gaunt *et al.*, 2010; Bhardwaj, 2020). In most individuals, HCoV-OC43 infections remain mild and are primarily confined to the upper respiratory tract. Severe lower respiratory tract involvement is rare, typically occurring only in immunocompromised patients or those with underlying comorbidities (Nickbakhsh *et al.*, 2020). This raises important questions about how HCoV-OC43 interacts with host innate immune defences, especially the IFN system, which forms the first line of antiviral protection.

IFNs are key mediators of antiviral defence and are classified into type I (e.g. IFN-α/β), type II IFN-γ, and type III IFN-λ families. Both type I and type III IFNs signal through the JAK/STAT pathway to induce ISGs, which inhibit viral replication via various mechanisms (Schindler *et al.*, 2007; de Weerd and Thao, 2012). Respiratory viruses show considerable variation in their sensitivity to IFNs. Influenza A virus and respiratory syncytial virus (RSV) are generally restricted by IFN-α, although both have evolved proteins that counteract IFN signalling (Spann *et al.*, 2004; Killip *et al.*, 2015). Similarly, SARS-CoV-2 is strongly inhibited by type I IFNs *in vitro* (Wickenhagen *et al.*, 2021), whereas other coronaviruses like HCoV-229E display only partial sensitivity (Loo *et al.*, 2020c). Reports on HCoV-OC43 suggest it is relatively resistant to IFN treatment, though the strength and context-dependence of this resistance remain unclear (Zhao *et al.*, 2014).

My transcriptomic profiling (Chapter 4) demonstrated that HCoV-OC43 induces IFN-related transcripts in primary nasal epithelial cells, with strong upregulation of ISGs such as *RSAD2* (at 72 hpi) alongside chemokines, for example, *CXCL11* (at 24 hpi). In MRC-5 cells, however, the picture was less clear: I observed an early chemokine-dominant pattern, such as *CXCL8*, with limited breadth of ISG induction and increased expression of regulators like *SOCS1* and components of inflammatory pathways such as *NFKB1*. These findings indicate transcript-level engagement of IFN-linked gene sets in hNECs but leave open whether MRC-5 mounts a robust IFN response or whether HCoV-OC43 diverts the host program toward inflammatory cascades while constraining a broader ISG output.

This uncertainty motivated a functional test. If HCoV-OC43 truly suppress IFN responses in fibroblasts, exogenous IFN might have little effect on replication; if the pathways remain inducible, priming with IFN should restrict the virus. I therefore evaluated the impact of type I IFN IFN-α and type III IFN IFN-λ on HCoVOC43 replication in MRC-5 cells using live-virus assays, quantifying viral RNA and infectious titre alongside a focused RT-qPCR panel of IFN-responsive transcripts. The goal was to determine whether HCoV-OC43 is sensitive to IFN in this cell type and to reconcile the RNA-seq observations by distinguishing suppression of IFN responses from a shift toward inflammatory gene expression.

In summary, this chapter asks a simple, testable question arising from the complexity of the transcriptomic data: Does exogenous IFN curtail HCoV-OC43 replication in MRC-5 despite the muted ISG signature observed during unprimed infection, and can targeted transcriptional readouts under priming clarify whether HCoV-OC43 suppresses IFN responses or primarily drives inflammatory programs in fibroblasts?

5.2 Results

5.2.1 Differential ISG induction by IFN-α and IFN-λ in MRC-5 and A549 cells

Given that ISGs are critical effectors of the innate immune response, I next sought to investigate whether IFN stimulation led to the activation of type I IFN signalling pathways in MRC-5 cells. To assess whether MRC-5 cells are immunocompetent and capable of responding to exogenous IFNs, cells were treated with recombinant IFN-α (1000 IU/mL) or IFN-λ (100 ng/mL), followed by measurement of ISG induction. I focused on *RSAD2* and *CXCL11*, two ISGs that were strongly upregulated in my transcriptomic analyses of HCoV-OC43 infection in nasal epithelial cells.

To assess IFN responsiveness in different cellular contexts, I compared the effects of type I and type III IFN stimulation in fibroblast (MRC-5) and epithelial (A549) cell models. Stimulation with recombinant IFN-α induced strong expression of both *RSAD2* and *CXCL11* in MRC-5 cells, with fold increases of approximately 150- to 200-fold compared to mock-treated controls (Figure 5.1A). In contrast, IFN-λ treatment did not elicit detectable expression of either ISG in MRC-5 cells (Figure 5.1B), consistent with the absence of IFN-λ receptor signalling in fibroblasts. To confirm that the lack of response was not due to an experimental artefact, IFN-λ stimulation was also tested in A549 epithelial cells, which express the IFN-λ receptor. In this context, IFN-λ treatment strongly induced both *RSAD2* and *CXCL11*, with fold changes of around 120-fold and 350-fold, respectively (Figure 5.1C).

These findings demonstrate that MRC-5 cells are immunocompetent regarding type I IFN signalling but lack responsiveness to type III IFNs. In contrast, epithelial-derived A549 cells mount a strong ISG response to IFN-λ.

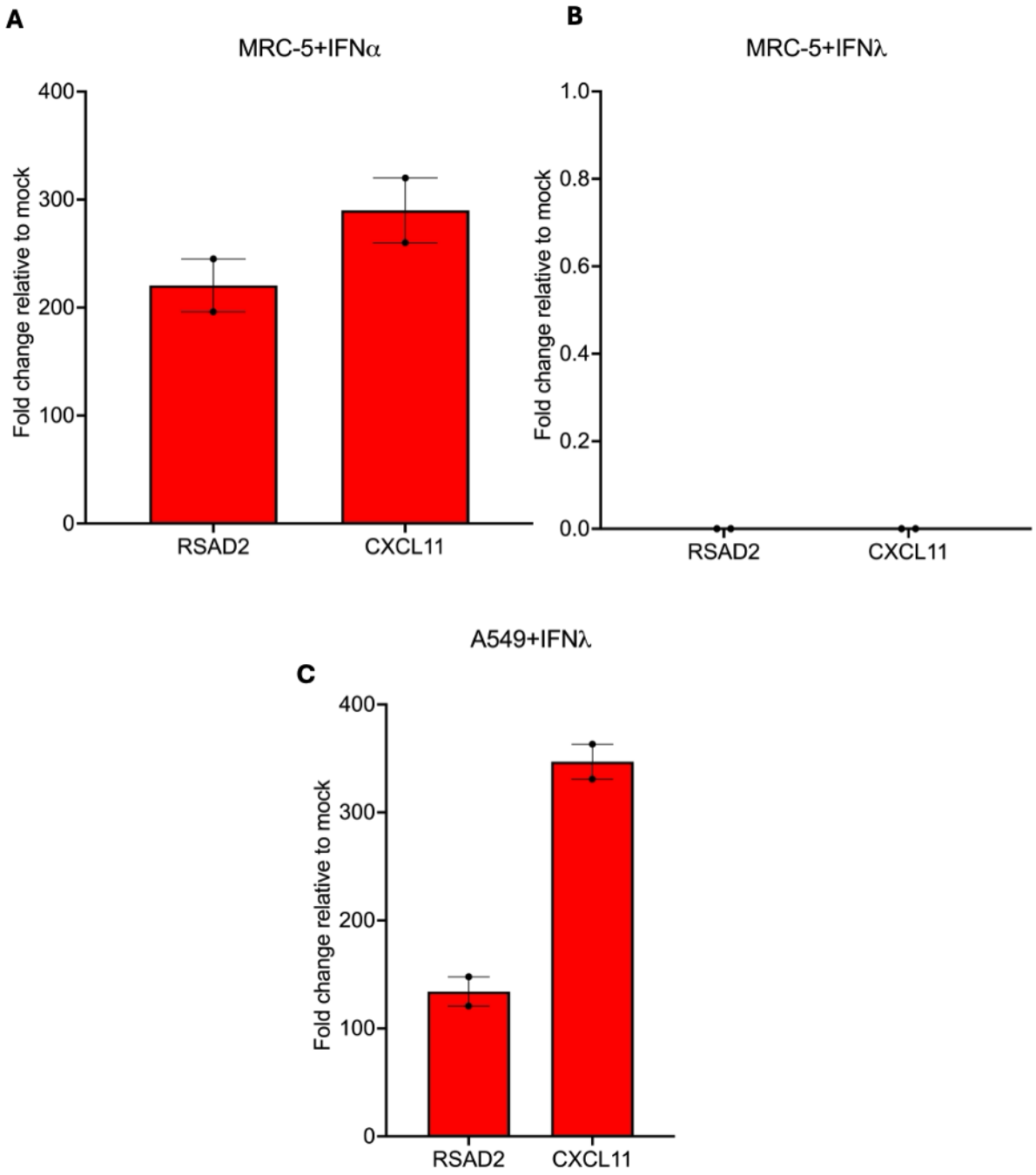

Figure 5.1: Expression of ISGs in MRC-5 and A549 cells treated with recombinant IFN-α and IFN-λ respectively.

RT-qPCR quantification showing the expression levels of **(A)** *RSAD2* and *CXCL11* in MRC-5 cells treated with 1000 IU/mL of IFN-α, **(B)** *RSAD2* and *CXCL11* in MRC-5 cells treated with 100 ng/mL of IFN-λ and **(C)** *RSAD2* and *CXCL11* in A549 cells treated with 100ng/mL of IFN-λ. The fold change values are presented as relative to the mock-treated cells as calculated using the $2^{-\Delta\Delta Ct}$ (Pfaffl) method. Error bars represent the standard error of the mean ± SEM from 2 technical duplicates.

5.2.2 Validation of IFN responsiveness by protein-level assays

To confirm that ISG induction in MRC-5 cells was not limited to transcriptional activity, I examined *RSAD2* and *CXCL11* protein expression after stimulation with IFN-α, IFN-γ, or the synthetic dsRNA analogue Poly I:C. Western blotting showed that both *RSAD2* and *CXCL11* were strongly induced in response to IFN-α, with levels considerably higher than in mock-treated controls (Figure 5.2, left panel). IFN-γ also triggered detectable expression of both proteins, albeit at lower levels, while Poly I:C induced RSAD2 strongly but had a weaker effect on CXCL11.

Densitometric analysis confirmed these observations, showing over 8000-fold induction of CXCL11 and approximately 3000-fold induction of RSAD2 in IFN-α–treated cells compared to untreated controls (Figure 5.2, right panel). Induction by Poly I:C reached about 2500-fold for RSAD2 and around 2000-fold for CXCL11, while IFN-γ stimulation led to approximately 5000-fold induction of CXCL11 and roughly 1800-fold induction of RSAD2.

Taken together, these results confirm that MRC-5 cells are functionally capable of mounting an IFN response at the protein level. The strong induction of RSAD2 and CXCL11 following IFN-α treatment validates the findings from qRT-PCR, supporting the use of this system for subsequent HCoV-OC43 replication assays. Furthermore, these results align with previous reports describing MRC-5 cells as an immunocompetent cell model where both ISG induction and canonical IFN signalling pathways are intact, making them suitable for studying host–virus interactions.

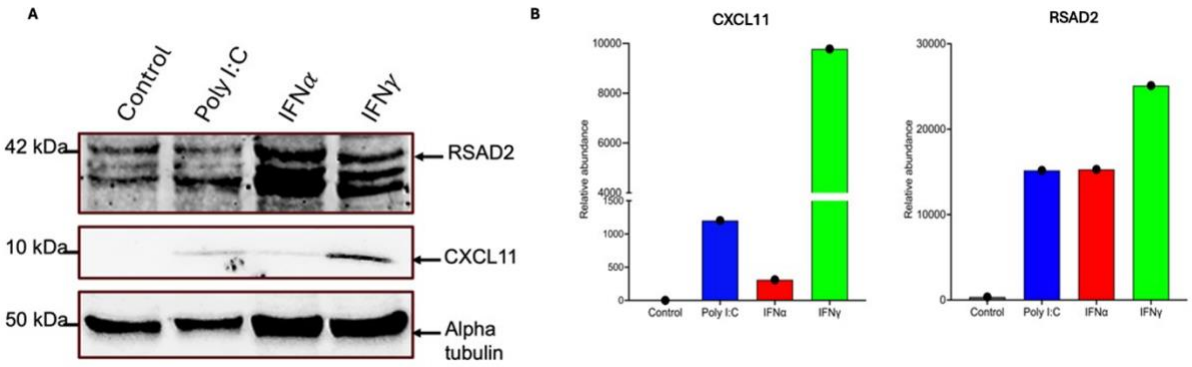

Figure 5.2: Induction of IFN-stimulated proteins in MRC-5 cells following innate immune stimulation.

MRC-5 cells were treated for 24 hr with polyinosinic: polycytidylic acid (poly I:C; 1 µg/mL), recombinant IFN-α (1,000 U/mL) or recombinant IFN-γ (1,000 U/mL). Whole-cell lysates were probed by a western blot for *RSAD2* and C*XCL11*, with α-tubulin as a loading control. Blots represent two independent experiments. Band intensities were quantified by densitometry in ImageJ: regions of interest were drawn around each band, background values were subtracted, and each ISG signal was normalised to its corresponding α-tubulin signal. Bar graphs show mean ± SEM of normalised intensities from both experiments, illustrating robust Type I IFN pathway activation upon poly I:C and IFN-α stimulation.

5.2.3 HCoV-OC43 replication is restricted by exogenous IFN treatment, indicating sensitivity to IFN-α and IFN-λ.

To assess whether exogenous type I IFN limits HCoV-OC43 replication in MRC-5 cells, the cells were pre-treated with increasing doses of recombinant IFN-α (100-1000 IU/mL) prior to infection. Viral replication was measured by RT-qPCR targeting the N-gene and validated by $TCID_{50}$ titration of infectious supernatants.

In untreated MRC-5 cells, HCoV-OC43 replicated efficiently, reaching viral loads of approximately 4×10^5 $TCID_{50}$/mL and $>4 \times 10^9$ RNA copies/mL at 48 hpi (Figure 5.3A-B). IFN-α pre-treatment significantly reduced viral replication in a dose-dependent manner. At 100

IU/mL, viral RNA levels decreased by nearly one order of magnitude compared to untreated controls, and replication was further suppressed at 500 and 1000 IU/mL, where titres approached background levels. Consistent with the RNA data, infectious virus titres were reduced by more than 90% at the highest IFN-α concentration tested.

These results show that HCoV-OC43 replication is very sensitive to exogenous IFN-α in MRC-5 cells, contradicting earlier reports of strong IFN resistance. Instead of being naturally insensitive, HCoV-OC43 might avoid or delay triggering type I IFN signalling during infection, enabling replication to continue without prior IFN exposure.

5.2.4 Effect of type III IFN-λ on HCoV-OC43 replication in epithelial cells

Since MRC-5 cells lack functional IFN-λ receptor signalling, the effect of type III IFN was assessed using A549 epithelial cells, in which HCoV-OC43 replication is less efficient but receptor expression remains intact. Cells were pre-treated with increasing concentrations of IFN-λ (1-100 ng/mL) before infection, and viral replication was quantified by RT-qPCR targeting the *N* gene. In untreated A549 cells, HCoV-OC43 reached titres of approximately 9×10^6 RNA copies/mL (Figure 5.3C). Pre-treatment with IFN-λ reduced viral replication at all tested doses, with over 70% reduction at 10 ng/mL and almost complete suppression at 100 ng/mL. These findings confirm that type III IFN exerts antiviral activity against HCoV-OC43 in epithelial cells.

Given that IFN-α demonstrated a stronger antiviral effect in MRC-5 cells, I next aimed to visualise its impact at the cellular level by assessing the extent of viral infection in the presence or absence of treatment.

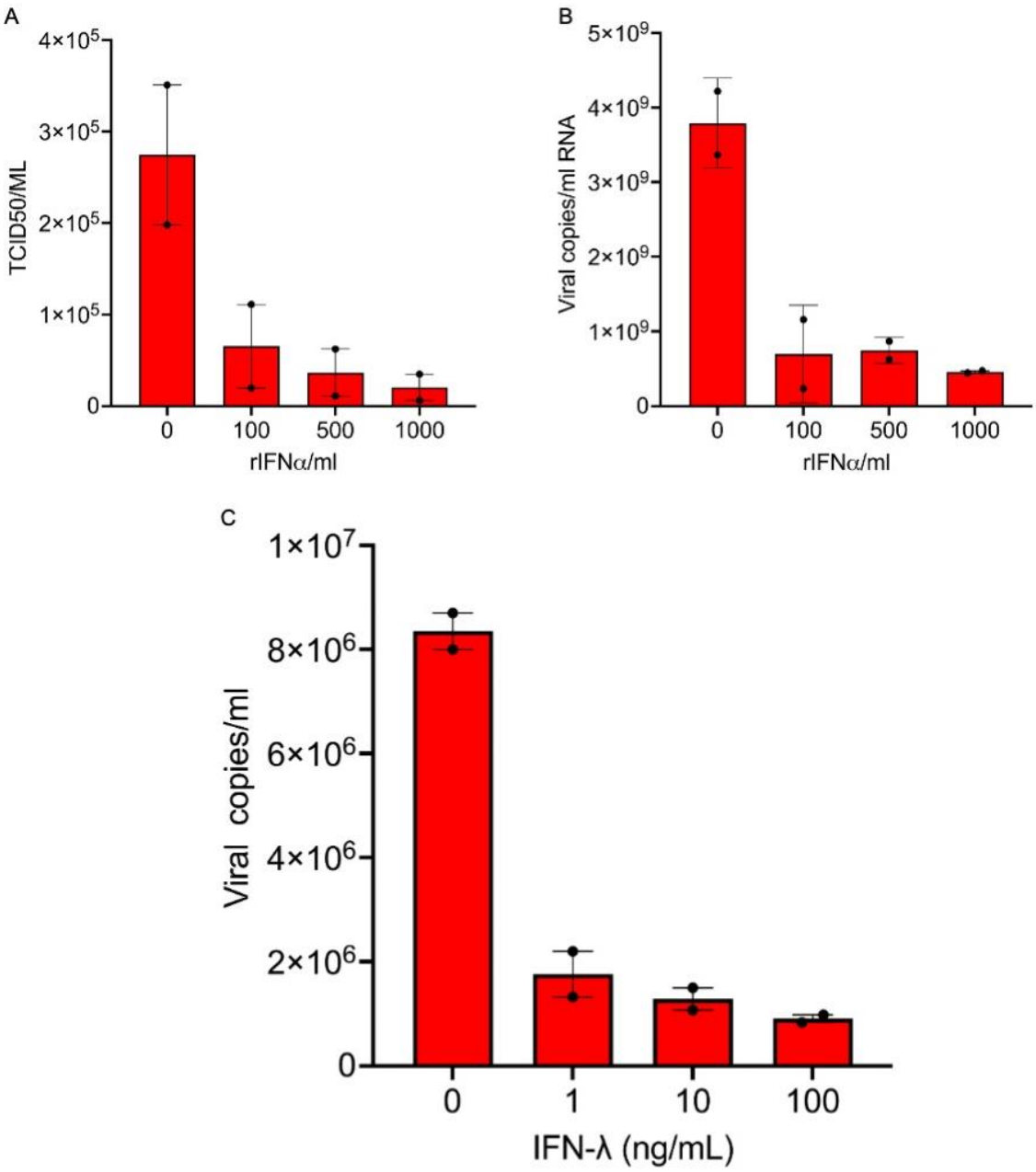

Figure 5.3: Effect of IFNs α and λ treatment on HCoV-OC43 replication in MRC-5 and A549 cells.

(A) RT-qPCR quantification of viral copies in untreated MRC-5 cells and those treated with 100, 500 and 1000 IU/mL of IFN-α before infection. **(B)** $TCID_{50}$ assay on supernatants from infected cells treated with IFN-α showing infectious titre. **(C)** RT-qPCR quantification of viral copies in untreated A549 cells and those treated with 1, 10 and 100 ng/mL of IFN-λ before infection. Error bars represent ± SEM of technical duplicate. Statistical

significance was determined using Kruskal-Wallis with Dunn's multiple comparisons test and was not statistically significant (ns).

5.2.5 Immunofluorescence confirms that IFN-α strongly reduces HCoV-OC43 infection in MRC-5 cells

To complement the RNA and infectious titre assays and to directly visualise the impact of IFN-α on viral spread, I performed immunofluorescence (IF) staining of MRC-5 cells for the viral nucleocapsid protein after HCoV-OC43 infection, with or without IFN-α pre-treatment. In untreated cells, extensive nucleocapsid staining was observed throughout the cytoplasm at 37 °C, confirming strong HCoV-OC43 infection (Figure 5.4A). Conversely, cells pre-treated with IFN-α before infection showed significantly reduced nucleocapsid signal, with only sparse clusters of positive cells. Quantification revealed that approximately 50% of untreated MRC-5 cells were positive for nucleocapsid, whereas only about 8% of cells remained positive following IFN-α treatment (Figure 5.4B). This indicates roughly a sixfold decrease in the proportion of infected cells. Together with the qPCR and $TCID_{50}$ assays, these findings confirm that exogenous IFN-α markedly inhibits HCoV-OC43 replication in MRC-5 cells, both at the population and single-cell levels.

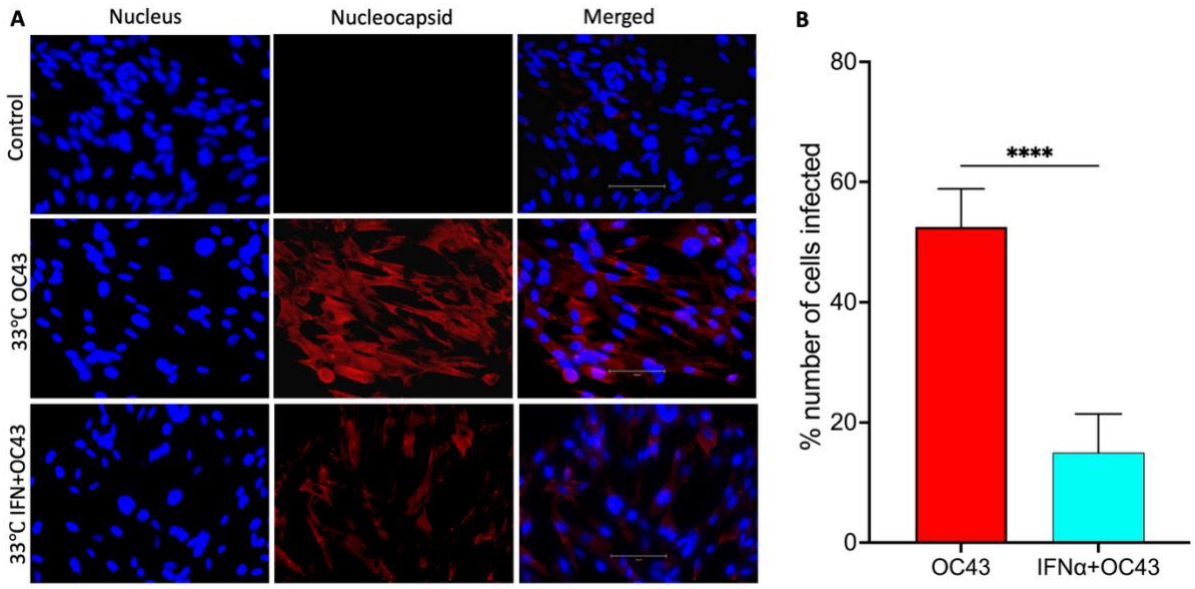

Figure 5.4: IFN-α pre-treatment inhibits HCoV-OC43 infection in MRC-5 cells.

(A) MRC-5 cells were either mock-treated (Control), infected with HCoV-OC43 at 33 °C (HCoV-OC43), or pre-treated with IFN-α (1,000 U/mL) for 6 hr then infected with HCoV-OC43 at 33 °C (IFNα + HCoV-OC43). After 48 hr, cells were fixed and stained with DAPI (blue) to visualise nuclei and with an antibody against HCoV-OC43 nucleocapsid protein (red). Representative fields are shown for each condition: nucleus (left), nucleocapsid (middle), and merged channels (right). Images were captured at 40× magnification (Scale bar 75 m). **(B)** The percentage of infected cells was quantified by counting nucleocapsid-positive cytoplasmic signals across three independent experiments (≥500 cells per condition). Bars represent mean ± SEM. IFN-α pre-treatment reduced HCoV-OC43 infection from ~50 % to ~5 % of cells ($p < 0.0001$, Student's t-test).

5.2.6 HCoV-OC43 infection activates ISRE and NF-κB signalling but fails to induce IFN-β promoter activity strongly

My earlier results demonstrated that MRC-5 cells mount a vigorous ISG response to IFN-α, and that exogenous IFN restricts HCoV-OC43 replication. Those assays quantify downstream outputs. To ask whether HCoV-OC43 modulates upstream promoter activity in antiviral pathways, I used luciferase reporter assays by the human IFN-β promoter, an IFN-stimulated

response element (ISRE), and an NF-κB-responsive element. Based on the optimisation chapter, HEK293T cells support HCoV-OC43 replication and provide high transfection efficiency, yielding robust reporter signals. I initially attempted the assay in MRC-5 and A549, but reporter activity was at baseline, likely due to low transfection efficiency and poor signal-to-noise in these cells. I therefore ran the luciferase experiments in HEK293T to obtain interpretable promoter-level readouts.

HEK293T cells were co-transfected with pIFNβ-luc, ISRE-luc, or NF-κB-luc reporter constructs along with a Renilla luciferase plasmid for signal normalisation. After 24 h, cells were infected with live HCoV-OC43 or heat-inactivated HCoV-OC43 at an MOI of 1. At 24 hpi, cells were stimulated with poly I:C for the IFN-β reporter, IFN-α for the ISRE reporter, or PMA for the NF-κB reporter, and luciferase was measured. ISRE activity was significantly enhanced by HCoV-OC43 infection, increasing from approximately 40 relative luciferase units (RLU) in the mock to about 90 RLU in infected cells ($p < 0.01$). Heat-inactivated virus had no effect. The addition of IFN-α further elevated ISRE activity across all groups, with infected cells reaching around 120 RLU, indicating that HCoV-OC43 infection stimulates ISRE signalling but does not impair responsiveness to exogenous IFN. Although IFN-β promoter activity remained generally low, with baseline levels of approximately 0.15 RLU in mock cells, HCoV-OC43 infection alone caused only a slight increase to around 0.20 RLU. However, stimulation with poly I:C raised reporter activity to roughly 0.28 RLU in infected cells compared with about 0.18 RLU in controls ($p < 0.05$). This indicates that viral replication primes cells for a stronger response to polyI:C but does not independently induce robust IFN-β activation. NF-κB activity was also increased by infection, rising from roughly 2.0 RLU in mock to approximately 3.5 RLU in HCoV-OC43-infected cells ($p < 0.05$). Conversely, heat-inactivated virus failed to induce NF-κB activity, confirming that active replication is necessary. PMA stimulation further amplified NF-κB activity, with both infected and mock cells reaching

around 4-5 RLU, demonstrating that HCoV-OC43 does not hinder responsiveness to external activation. Overall, these findings show that HCoV-OC43 activates ISRE- and NF-κB-driven transcriptional programmes but only weakly stimulates the IFN-β promoter. This pattern aligns with the RNA-seq data, which revealed strong induction of ISGs (*CXCL11, RSAD2*) and NF-κB-related genes (*NFKB1, SOCS1*), but relatively modest upregulation of IFN-β itself. These results support a model in which HCoV-OC43 delays or evades type I IFN induction, while still triggering downstream antiviral and inflammatory pathways.

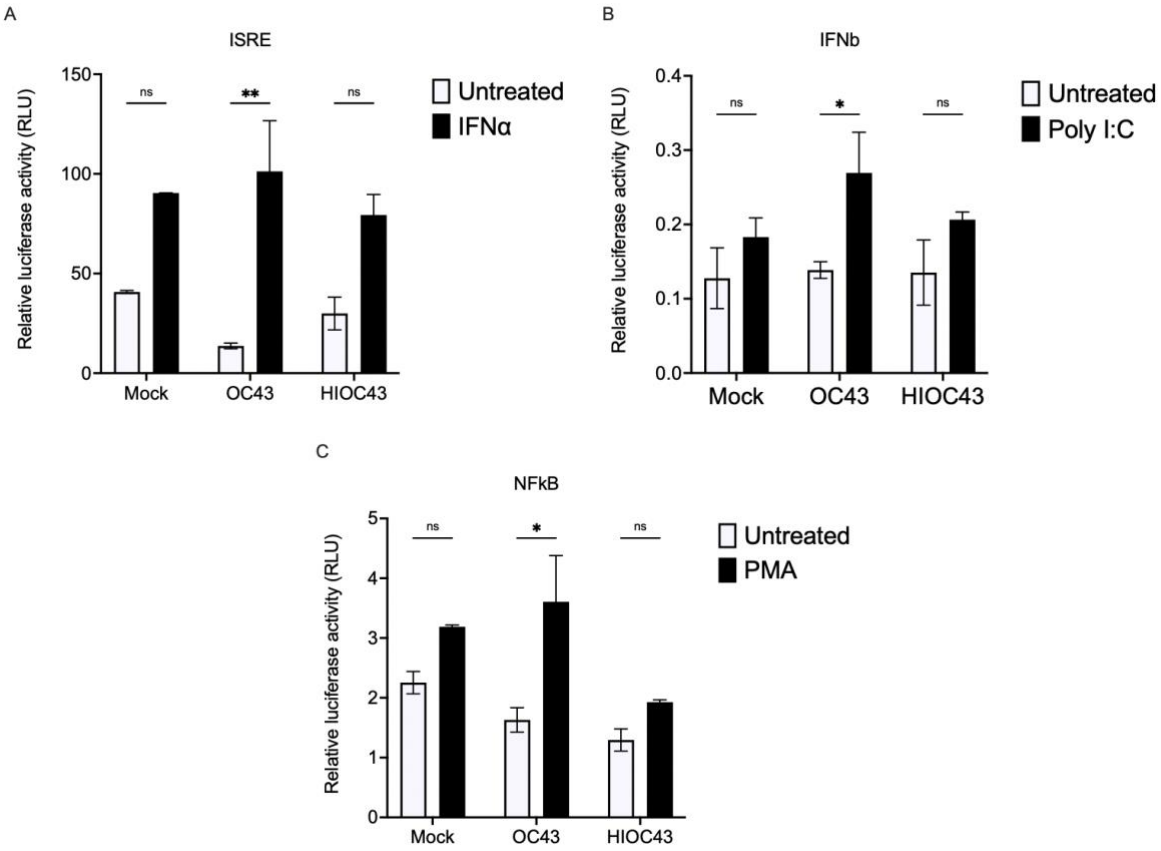

Figure 5.5: Dual-luciferase reporter assay of IFN-β, ISRE, and NF-κB promoter activity during HCoV-OC43 infection.

HEK293T cells were transfected with firefly luciferase reporter plasmids under the control of the IFN-β promoter, ISRE, or NF-κB response elements, together with a Renilla luciferase plasmid for normalisation. After 24 h, cells were infected with live HCoV-OC43 or heat-inactivated (HI) HCoV-OC43 at an MOI of 1 or left uninfected (Mock). At 24 hpi, cells were stimulated with Poly I:C (for IFN-β), recombinant IFN-α (for ISRE), or PMA (for NF-κB), and luciferase activity was measured using the Dual-Glo system. Data are normalised to Renilla and expressed as fold change relative to mock controls. Results show that live HCoV-OC43 infection significantly enhanced ISRE and NF-κB activity but only weakly induced the IFN-β promoter, whereas HI-HCoV-OC43 did not elicit reporter activation. Stimulation with Poly I:C, IFN-α, or PMA further enhanced reporter activity, confirming pathway responsiveness. Bars represent mean ± SEM from three independent experiments performed in technical duplicates. Statistical significance was determined by two-way ANOVA with Tukey's post-hoc test (*$p < 0.05$, **$p < 0.01$, ***$p < 0.001$).

5.2.7 HCoV-OC43 infection downregulates antiviral ISGs but selectively induces CXCL8

Given that exogenous IFN-α treatment strongly induced ISGs in MRC-5 cells (Figures 5.1-5.2) and that luciferase assays suggested HCoV-OC43 activates ISRE-dependent transcription while weakly engaging the IFN-β promoter (Figure 5.6), I next examined how infection itself influences ISG expression over time. MRC-5 cells were infected with HCoV-OC43 at an MOI of 0.1, and RNA was collected at 8, 24, 48, and 72 hpi for RT-qPCR analysis of *OASL, RSAD2, IFIT1, IFIT2*, and *CXCL8* (Figure 5.6A-E). In all cases, rIFN-α used as a positive control induced robust ISG expression, reaching approximately 20-30-fold over mock in *OASL, IFIT1, and IFIT2*, around 15-fold in *RSAD2*, and about 20-fold in *CXCL8*. In contrast, HCoV-OC43 infection triggered only a modest and transient increase in ISG expression, mainly detectable at 8 hpi, when *OASL, RSAD2, IFIT1*, and *IFIT2* rose to about 2-4 times above mock levels, and *CXCL8* exhibited a similar early elevation. By 24 hpi, however, the expression of all genes had returned to baseline or fallen below mock levels, and this suppression persisted through 48 and

72 hpi. This pattern suggests that although HCoV-OC43 infection can trigger an initial wave of ISG transcription, it does not sustain this response, with expression declining to levels lower than those in uninfected controls at later time points. These findings are consistent with the earlier results, which showed that HCoV-OC43 replication is highly sensitive to exogenous IFN-α treatment (Figures 5.3-5.4). This implies that the virus does not replicate because it is resistant to ISGs, but rather because it can interfere with or suppress the endogenous IFN response once infection is established (Figure 5.6).

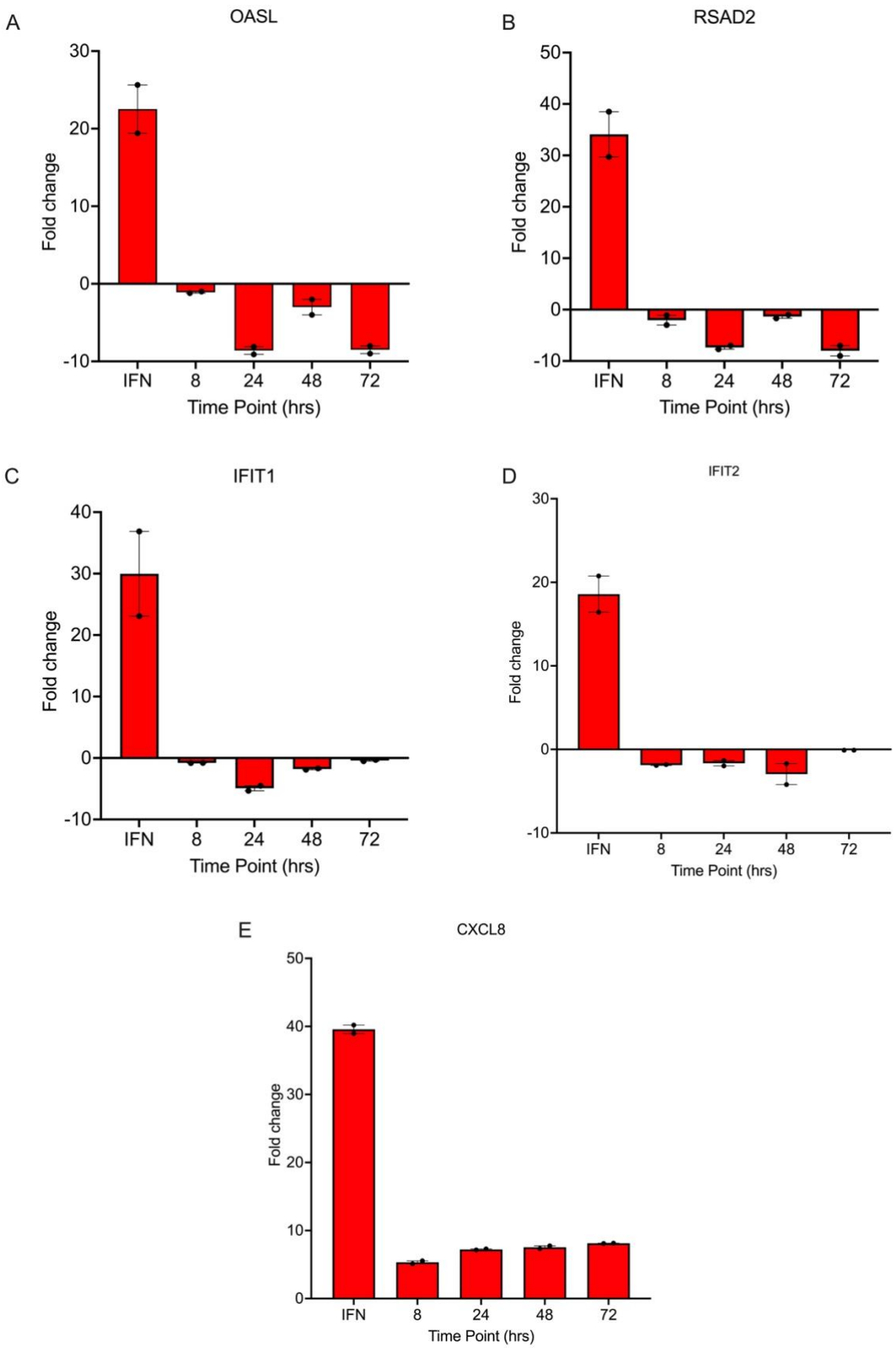
A
OASL
Fold change
30
20
10
0
-10
IFN
8
24
48
72
Time Point (hrs)
B
RSAD2
Fold change
50
40
30
20
10
0
-10
IFN
8
24
48
72
Time Point (hrs)
C
IFIT1
Fold change
40
30
20
10
0
-10
IFN
8
24
48
72
Time Point (hrs)
D
IFIT2
Fold change
30
20
10
0
-10
IFN
8
24
48
72
Time Point (hrs)
E
CXCL8
Fold change
50
40
30
20
10
0
IFN
8
24
48
72
Time Point (hrs)

Figure 5.6: Time-course analysis of ISG expression in MRC-5 fibroblasts following HCoV-OC43 infection.

MRC-5 cells were infected with HCoV-OC43 at an MOI of 0.1 and harvested at 8, 24, 48, and 72 hpi. RNA was extracted, reverse transcribed, and analysed by RT-qPCR for expression of selected ISGs**: (A)** *OASL***, (B)** *RSAD2*, **(C)** *IFIT1*, **(D)** *IFIT2*, and **(E)** *CXCL8*. For comparison, cells treated with recombinant IFN-α (1000 IU/mL, 6 h) were included as a positive control. Expression levels are presented as fold change relative to mock-treated controls, calculated using the $2^{-\Delta\Delta Ct}$ method and normalised to housekeeping genes. Data show robust induction of all ISGs following IFN-α treatment, whereas HCoV-OC43 infection led to transient or suppressed expression of *OASL, RSAD2, IFIT1*, and *IFIT2*, with *CXCL8* showing modest sustained induction. Bars represent mean ± SEM from from two independent experiments.

5.2.8 IFN priming differentially enhances antiviral gene expression in MRC-5 and A549 cells during HCoV-OC43 infection.

Since the replication assays showed that exogenous IFN-α inhibits HCoV-OC43 in MRC-5 cells and IFN-λ inhibits replication in A549 epithelial cells, I asked whether pre-exposure to the relevant IFN increases the transcript abundance of predefined IFN-responsive genes during infection. To address this, MRC-5 cells were pre-treated with IFN-α (1000 IU/mL) and A549 cells with IFN-λ (100 ng/mL), followed by infection with HCoV-OC43 at an MOI of 0.1. The expression levels of *STAT1*, *NF-κB, SOCS1*, and *IFIT1* were measured using RT-qPCR and compared to those of mock-treated controls.

In MRC-5 cells, HCoV-OC43 infection alone modestly increased the expression of *STAT1* (~3-fold), *NF-κB* (~6-fold), *SOCS1* (~4-fold), and *IFIT1* (~5-fold). Pre-treatment with IFN-α prior to infection significantly boosted the expression of *STAT1* (~12-fold) and *IFIT1* (~15-fold), while *NF-κB* and *SOCS1* levels remained similar to infection alone (Figure 5.8A). This

indicates that type I IFN priming enhances canonical antiviral transcriptional responses but has limited additional impact on *NF-κB* and *SOCS1* expression after infection.

In A549 cells, HCoV-OC43 infection caused only modest changes in the same set of genes. However, pre-treatment with IFN-λ notably increased the expression of *STAT1* (~8-fold), *SOCS1* (~6-fold), and *IFIT1* (~10-fold), compared to infection alone, while *NF-κB* activation remained moderate (Figure 5.8B). These findings confirm that epithelial cells respond robustly to IFN-λ priming, in contrast to MRC-5 cells, which lack IFN-λ receptor expression.

Overall, these results demonstrate that IFN priming enhances antiviral gene expression in both fibroblasts and epithelial cells, with distinct patterns depending on the IFN type. Type I IFN promotes *STAT1*- and ISG-driven responses in fibroblasts, whereas type III IFN induces a broader activation of *STAT1, SOCS1*, and *IFIT1* in epithelial cells. This supports earlier replication assays showing that IFN-α inhibits HCoV-OC43 in MRC-5 cells, whereas IFN-λ limits replication in A549, highlighting distinct cell type- and IFN type-specific host responses to infection. Statistical significance was assessed using two-way ANOVA and Tukey's multiple comparisons, with notable differences indicated by $*p < 0.05$. All together, these findings provide mechanistic insights into how IFNs modulate host antiviral defences and suggest that their efficacy may be contingent upon both cell type and viral countermeasures.

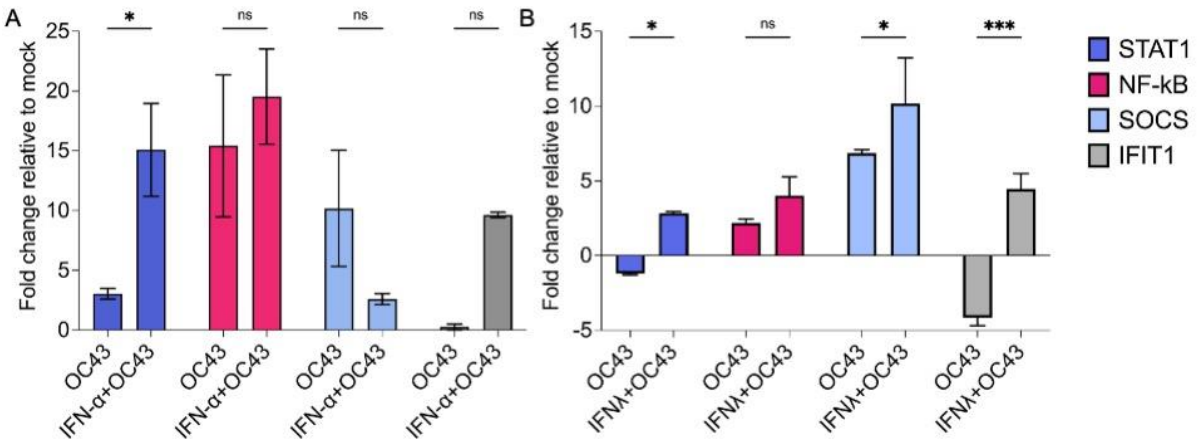

Figure 5.7: Expression of ISGs and IFN signalling pathway genes in MRC-5 and A549 cells.

(A) expression levels of *STAT1, NF-kB, SOCS* and *IFIT1* in MRC-5 cells treated with 1000 IU/mL of IFN-α, and then infected with HCoV-OC43. **(B)** *STAT1, NF-kB, SOCS* and *IFIT1* were expressed in A549 cells treated with 100 ng/mL of IFN-λ before HCoV-OC43 infection. The graph represents the fold change in the expression levels of the genes relative to the mock. Error bars represent the mean ± SEM of technical duplicates. Statistical significances were determined by two-way ANOVA and Tukey's multiple comparisons and are indicated by * (p<0.05) and non-significant (ns).

5.3 Discussion

The experiments in this chapter demonstrate that HCoV-OC43 is not intrinsically refractory to IFN but instead relies on timing and cellular context to evade their effects. In MRC-5, exogenous IFN-α established a strong antiviral state, characterised by the robust induction of STAT1- and ISG-driven programs, accompanied by a corresponding decrease in viral RNA and infectious titre; in epithelial cells, IFN-λ achieved a similar outcome. These findings align HCoV-OC43 with other respiratory viruses that antagonise IFN pathways during infection, yet remain suppressible when IFN is present ahead of replication. Influenza A encodes NS1, which limits RIG-I signalling and IFN production while still leaving the virus vulnerable to exogenous IFN *in vitro* and *in vivo*; RSV uses NS1/NS2 to block STAT signalling but is likewise restricted when cells are primed; parainfluenza viruses suppress STAT phosphorylation via C proteins yet remain sensitive to IFN pretreatment (García-Sastre *et al.*, 1998; Lo *et al.*, 2005; Palosaari *et al.*, 2003). Among coronaviruses, SARS-CoV-2 is potently inhibited by type I IFN in cell culture despite multiple antagonists, and 229E shows moderate sensitivity, whereas MERS-CoV and SARS-CoV tend to be less responsive because of stronger accessory protein inhibitors (Mantlo *et al.*, 2020; Wickenhagen *et al.*, 2021; Kindler *et al.*, 2016; Menachery *et al.*, 2014). HCoV-OC43 fits the pattern of being suppressible by IFN provided the host response is in place before the virus gains momentum. Cell type explains much of the apparent inconsistency in the literature. MRC-5 cells lacked functional IFN-λ responsiveness, consistent with low IFNLR1 expression in stromal cells, so only type I IFN priming curbed replication in this system; epithelial A549 cells, by contrast, responded strongly to IFN-λ with clear reductions in viral burden. This division of labour mirrors physiology in the airway, where type III IFN dominates at mucosal barriers and type I IFN provides broader tissue protection (Galani *et al.*, 2017; Klinkhammer *et al.*, 2018). It also helps rationalise HCoV-OC43 tropism: in the upper airway,

epithelial IFN-λ can restrain spread, whereas deeper stromal compartments depend on type I IFN delivered locally or systemically. The data therefore reconcile reports of "resistance" by showing that the outcome is contingent on which IFN system is engaged, when it is involved, and in which cell type. The transcriptional readouts reinforce this view. When I supplied IFN-α, classical antiviral ISGs were strongly induced in MRC-5 cells; during infection without prior IFN, HCoV-OC43 drove the opposite pattern, suppressing *OASL, RSAD2, IFIT1*, and *IFIT2*, while leaving *CXCL8* selectively upregulated. This skew toward inflammation with blunted antiviral tone is familiar from other respiratory pathogens: SARS-CoV-2 samples and models repeatedly show low IFN signatures with high chemokine expression; RSV and influenza exploit NF-κB to promote cytokines while dampening IFN programs through NS proteins and NS1, respectively (Blanco-Melo *et al.*, 2020; Shingai *et al.*, 2008; Killip *et al.*, 2015; Palosaari *et al.*, 2003). In my reporter assays, live HCoV-OC43 activated NF-κB and ISRE elements but induced only weak IFN-β promoter activity, echoing prior work implicating the HCoV-OC43 nucleocapsid and nonstructural proteins in tilting signalling away from IFN induction and toward NF-κB-dependent genes (Lai *et al.*, 2014; Dolliver *et al.*, 2022). Heat-inactivated virus lost these effects, indicating that active replication is required. Together, the datasets converge on a simple explanation: HCoV-OC43 can trigger inflammatory transcription while simultaneously avoiding or delaying robust type I IFN induction; if the IFN system is already active, replication is curtailed. These results also clarify why the timing of pretreatment matters. Across influenza, RSV and coronaviruses, early IFN exposure reduces replication, while late administration often has limited benefit and can exacerbate inflammation (García-Sastre *et al.*, 1998; Lo *et al.*, 2005; Felgenhauer *et al.*, 2020). The priming experiments fit that rule. They do not imply that HCoV-OC43 is unusually sensitive compared with all coronaviruses; instead, they show that in both fibroblasts and epithelial cells, the antiviral program is fully competent when appropriately engaged. The fact that MRC-5 cells do not respond to IFN-λ is a crucial

negative control for interpreting type III IFN biology in stromal systems, which explains why I switched to A549 for those assays. Finally, the pattern of ISG suppression with selective *CXCL8* induction provides a mechanistic bridge to pathogenesis. Neutrophil-recruiting chemokines without a matching antiviral ISG program are consistent with mild, symptomatic upper-airway disease that supports transmission. That phenotype contrasts with the severe lower-respiratory pathology of highly pathogenic coronaviruses, in which antagonism is stronger and tissue damage is driven by dysregulated inflammation; however, it shares the same broad strategy of uncoupling IFN induction from inflammatory outputs (Blanco-Melo *et al.*, 2020; Kindler *et al.*, 2016). The take-home is that HCoV-OC43 does not replicate because IFNs "do not work"; it replicates because it reaches target cells before the IFN system is fully engaged. When I provide IFN exogenously or when epithelial IFN-λ is robustly induced, replication is inhibited. In summary, this chapter establishes three points that underpin the next set of experiments. First, HCoV-OC43 remains susceptible to type I and type III IFNs, provided the host response is present early. Second, the outcome is cell type-specific: fibroblasts depend on type I IFN because they lack the IFN-λ receptor. Both systems protect epithelia, but especially IFN-λ at the airway surface. Third, during unprimed infection, HCoV-OC43 suppresses canonical antiviral ISGs while favouring NF-κB-driven chemokines. These conclusions raise a clear question for the next chapter: how does airway temperature, which differs between the upper and lower tracts, modulate both viral replication dynamics and the kinetics of type I IFN induction, which I have shown to be decisive?

Chapter 6

Temperature-dependence of HCoV-OC43 and the induction of type I IFN-α response.

6.1 Introduction

HCoVs comprise a group of respiratory pathogens that differ in tissue tropism, host immune modulation, and clinical outcomes. While zoonotic coronaviruses such as SARS-CoV, MERS-CoV, and SARS-CoV-2 are associated with severe respiratory disease, the endemic seasonal coronaviruses, including HCoV-OC43 and HCoV-229E, are primarily linked to mild upper respiratory tract infections (Greenberg, 2016). Nevertheless, these endemic viruses remain clinically relevant, particularly in infants, older adults, and immunocompromised patients, where occasional spread into the lower respiratory tract can result in significant morbidity (Nickbakhsh *et al.*, 2020). A key question is why seasonal coronaviruses such as HCoV-OC43, despite their ability to antagonise host IFN signalling, rarely progress to cause severe lower respiratory tract pathology. One possibility is that their replication and associated host responses are constrained by temperature-dependent innate immune programs that differ between the upper and lower airways.

The human respiratory tract offers a complex cellular and physiological environment for viral infection. It is made up of multi-ciliated cells, mucus-producing secretory cells, columnar epithelial cells, and basal cells that together create a physical and immunological barrier against inhaled pathogens (Hewitt and Lloyd, 2021). Importantly, the respiratory tract is not a uniform environment; instead, it is characterised by a temperature gradient, with the upper airways maintained at approximately 33 °C, while the lower respiratory tract is closer to core body temperature at 37 °C (Li *et al.*, 2022). This temperature difference influences both viral replication dynamics and host immune responses. Rhinoviruses replicate more efficiently at cooler temperatures, where innate antiviral responses are weaker, compared to warmer

conditions in the lungs (Foxman *et al.*, 2015). Similarly, influenza B viruses are more temperature-sensitive than influenza A viruses, showing reduced infectivity and HA receptor-binding activity at fever-range temperatures compared with 33 °C (Takada *et al.*, 2024)

For HCoV-OC43, early research demonstrated that replication is enhanced at 33 °C compared to 37 °C (Savoie and Lippe, 2022). This finding aligns with its tropism for the upper respiratory tract, where mild symptomatic infections are usually established. However, the mechanistic basis for this temperature preference remains unclear. An important unresolved question is whether the preferential replication of HCoV-OC43 at cooler temperatures arises from intrinsic effects on viral polymerase activity and replication kinetics, or from temperature-dependent modulation of host innate immunity, particularly the induction of type I IFNs.

The transcriptomic analysis of HCoV-OC43 infection in primary nasal epithelial and MRC-5 cells revealed a strong induction of specific ISGs (such as *IFIT1, IFIT2, IFI44L, RSAD2*) in hNEC and the upregulation of negative regulators of IFN signalling like *SOCS1*, along with inflammatory transcription factors such as *NF-κB* in MRC-5 cells. These findings suggest that HCoV-OC43 does not entirely suppress host responses but instead redirects them towards a more inflammatory phenotype. What remains unknown is how airway temperature might influence these interactions. Studies on other respiratory viruses suggest that temperature can modulate both replication and innate immune control. In airway mouse models, rhinoviruses replicate better at cooler temperatures, in part because RIG-I-like receptor signalling and type I IFN production are attenuated at 33 °C compared with 37 °C (Foxman *et al.*, 2015). In differentiated human airway epithelium, influenza A infection elicits stronger and earlier ISG responses at 37 °C than at 33 °C, coinciding with greater restriction of viral growth at the warmer temperature (Laloli *et al.*, 2022). Evidence for RSV is mixed; while replication differences with temperature have been reported, direct demonstrations that cooler temperature

broadly suppresses type I IFN in human airway cells remain limited. Against this background, I asked whether analogous mechanisms underlie the temperature sensitivity of HCoV-OC43.

In this chapter, I examine how temperature influences the replication of HCoV-OC43 and the induction of type I IFN responses in human MRC-5 cells. By comparing infection at 33 °C and 37 °C, I seek to determine whether the observed temperature dependence of HCoV-OC43 growth results from intrinsic viral replication efficiency or differential activation of the host's innate immune system. This will provide new insights into how seasonal coronaviruses adapt to the unique physiological environment of the respiratory tract and may help explain why they are mostly confined to the upper airways and cause mild disease.

6.2 Results

6.2.1 Initial assessment of HCoV-OC43 replication and CPE effects at different temperatures

Before conducting detailed replication kinetics, I first compared CPE and viral yields in MRC-5 cells infected with HCoV-OC43 at 33 °C or 37 °C. At 1-day post-infection (dpi), bright-field microscopy showed minimal morphological changes at either temperature. By 4 dpi, however, cells at 33 °C exhibited pronounced CPE, including cell rounding, detachment, and syncytia formation, whereas cells at 37 °C displayed milder alterations (Figure 6.1A).

To quantify the effect of temperature on viral yield, supernatants collected at 1 dpi and 4 dpi were titrated using the $TCID_{50}$ assay. Titres on day 1 were statistically higher at 33 °C (~2×10^6 $TCID_{50}$/mL) than at 37 °C (~1×10^6 $TCID_{50}$/mL). By day 4, titres at 33 °C (~1×10^8 $TCID_{50}$/mL) were significantly higher than at 37 °C (~5×10^7 $TCID_{50}$/mL; $p<0.01$) (Figure 6.1B). These initial findings indicated that cooler incubation enhances HCoV-OC43 replication and cytopathic effects in MRC-5 cells.

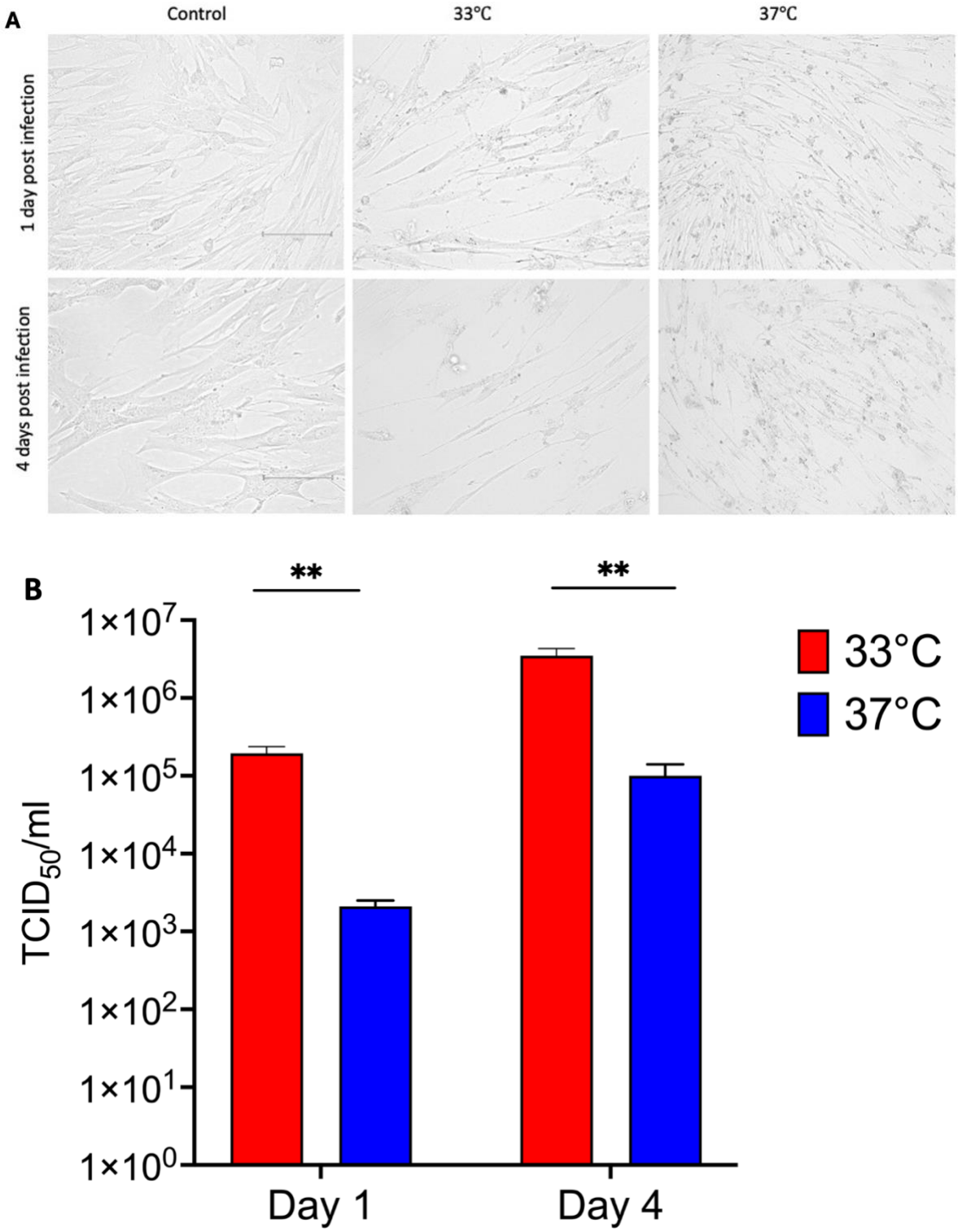

Figure 6.1: HCoV-OC43 replicates more efficiently at 33℃.

MRC-5 cells were seeded, incubated overnight, and acclimated for 2 days at either 33℃ or 37℃. Cells were infected with an MOI of 0.1 and incubated at either 33℃ or 37℃ for 4 days. **(A)** Bright-field images at 1 and 4 days dpi show CPE in both conditions, with more extensive cell rounding and detachment at 33 ℃ by 4 dpi: scale

bars, 75 µm. **(B)** Supernatants collected at 1 and 4 dpi were titrated by $TCID_{50}$. Bars show mean ± SEM from **n = 2** biologically independent experiments performed in parallel at each temperature. Statistics: two-way ANOVA (factors: temperature, time) with Tukey's post-hoc test. Day 1, ($P < 0.01$ **); Day 4, ($P < 0.01$ **).

6.2.2 Multi-cycle growth curves reveal significantly higher HCoV-OC43 replication at 33 °C compared to 37 °C in MRC-5 cells

To examine how temperature impacts the replication cycle, I performed multi-step growth curves in MRC-5 cells at a low multiplicity of infection (MOI 0.01). Supernatants were sampled from 2 hpi to 96 hpi, and viral output was measured using both $TCID_{50}$ and RT-qPCR.

At 33 °C, infectious titres steadily increased from approximately 2×10^3 $TCID_{50}$/mL at 2 hpi to around 5×10^7 $TCID_{50}$/mL by 96 hpi, with the most rapid growth occurring between 24 and 72 hpi. Titres at 37 °C displayed a similar pattern but were consistently lower, stabilising at about 2×10^7 $TCID_{50}$/mL by 96 hpi (Figure 6.2A). Viral RNA levels reflected this trend: genome copy numbers increased from roughly 1×10^5 copies/mL at 2 hpi to approximately 8×10^9 copies/mL at 96 hpi at 33 °C, compared to about 3×10^9 copies/mL at 37 °C (Figure 6.2B). The alignment between infectious titres and RNA levels confirms strong replication at both temperatures, with significantly higher yields from 72 hpi onwards at 33 °C.

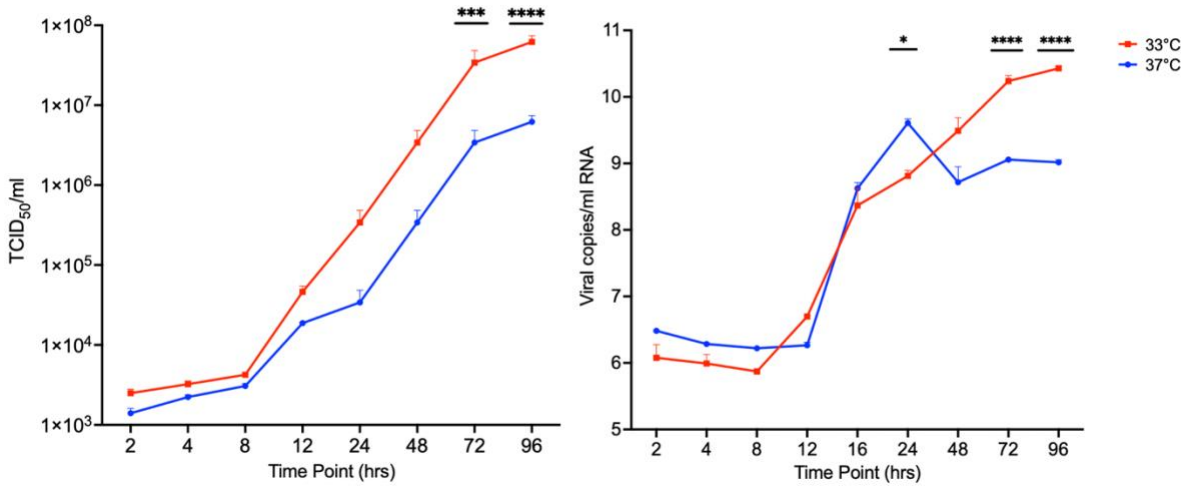

Figure 6.2: Temperature-dependent replication kinetics of HCoV-OC43

MRC-5 cells were infected with HCoV-OC43 at an MOI of 0.01 and incubated at 33 °C or 37 °C. After a 1 h adsorption period, the cells were washed, and fresh medium was added. Incubation continued at the respective temperatures. Supernatants were harvested at various times post-infection to quantify virus output. **(A)** Growth curve based on infectious titre ($TCID_{50}$/ml) in the supernatant over time. **(B)** Parallel measurement of viral genome copies in the supernatant by quantitative RT-PCR. Replication at 33 °C (blue curve) proceeded more rapidly and achieved higher titres and viral RNA copy numbers compared to 37 °C (red curve). Data points represent the mean ± SEM of three independent experiments (with two technical replicates each). Statistically significant differences between 33 °C and 37 °C, at given time points are indicated (*$p < 0.05$, **$p < 0.01$, ***$p < 0.001$, ****$p < 0.0001$; (two-way ANOVA with Tukey's multiple comparison test).

6.2.3 Early replication kinetics at high MOI exhibit no significant temperature effect during entry; however, a modest advantage emerges at 33 °C by 4 h.

To determine whether the observed temperature advantage in multi-cycle growth originates during the initial entry and uncoating stages, I repeated the assay using a high inoculum (MOI 1; 1 infectious unit per cell from a stock of 1.98×10^6 PFU/mL) to synchronise infection. MRC-5 cells were incubated at either 33 °C or 37 °C, and viral RNA in the supernatant was quantified over the first 4 hpi.

At 0 hpi (immediately after inoculum addition, before adsorption), viral RNA was slightly higher at 37 °C (~5×10^8 copies/mL) than at 33 °C (~3×10^8 copies/mL). This difference likely reflects residual inoculum variability rather than a biological effect, since adsorption had not yet occurred. Both conditions showed a marked decrease by 1 hpi, consistent with virus adsorption and internalisation (~7×10^7 at 37 °C; ~1×10^8 at 33 °C). By 2 hpi, RNA levels converged (~1.5×10^8 copies/mL), after which a modest divergence emerged. At 33 °C, viral RNA increased steadily to approximately 5×10^8 copies/mL by 4 hpi, whereas at 37 °C, it remained near the post-adsorption level (~1×10^8 copies/mL) (Figure 6.3).

These findings indicate that temperature-dependent differences in multi-cycle replication are not due to defects in early entry or uncoating at 37 °C. Rather, the modest divergence emerging at 3–4 hpi suggests that cooler temperatures confer an advantage during the first round of genome replication or other early post-entry processes. While differences became more pronounced at later stages, these kinetics point to replication dynamics, rather than inoculum carryover or entry efficiency, as the main driver of the temperature effect. I next examined whether temperature influences replication more prominently in subsequent stages of the viral life cycle and across multiple cell types.

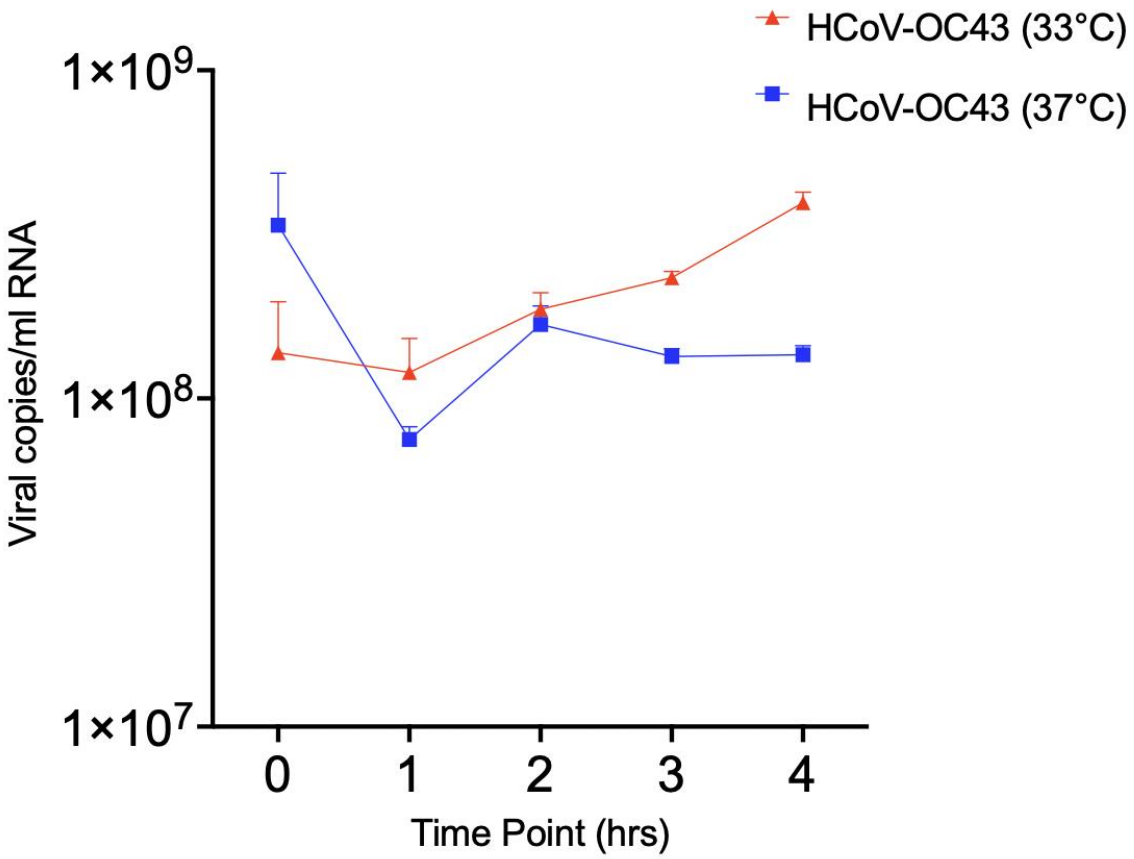

Figure 6.3: Early replication kinetics of HCoV-OC43 at 33 °C and 37 °C.

MRC-5 cells were infected with HCoV-OC43 at an MOI = 1 and incubated at either 33 °C (red triangles) or 37 °C (blue squares). Supernatants were collected at the indicated time points (0-4 hpi), and viral RNA was quantified

by qPCR targeting the N gene. Data are presented as viral copies per mL of RNA (mean ± SEM, n = 3). Although no statistically significant differences were detected, viral RNA levels tended to remain higher at 33 °C than at 37 °C during the early stages of infection.

6.2.4 The 33 °C replication of HCoV-OC43 advantage is conserved across diverse cell lines

To establish a foundational understanding of how physiologically relevant temperatures influence HCoV-OC43 replication, I performed multi-step growth kinetics in three human cell substrates: A549, HEK293T and MV1Lu cells. Parallel cultures were infected at a low multiplicity (MOI 0.01) and maintained at either 33 °C, to mimic the cooler environment of the upper airway or at 37 °C, representing core body temperature. Supernatants were sampled at multiple time points up to 6 days post-infection, and viral titres were determined by $TCID_{50}$. Across all three lines, HCoV-OC43 propagated more rapidly and reached higher peak titres at 33 than at 37 °C. In A549 cells, titres at 33 °C rose from ~2×10^3 $TCID_{50}$/ml at 24 h to ~1×10^6 $TCID_{50}$/ml by 72 h, plateauing around 1–2×10^6 through 120 h. By contrast, at 37 °C, A549 cultures lagged, starting at ~5×10^2 $TCID_{50}$/ml and peaking only at ~5×10^5 $TCID_{50}$/ml by 120 h before a decline. HEK293T cells displayed a similar pattern: 33 °C titres climbed from ~5×10^3 to ~6×10^6 $TCID_{50}$/ml by 72 h, versus a 37 °C peak of ~5×10^5 $TCID_{50}$/ml. MV1Lu cells showed the most pronounced temperature sensitivity, with 33 °C cultures reaching ~8×10^7 $TCID_{50}$/ml at 72 h compared to ~6×10^5 $TCID_{50}$/ml at 37 °C, and sustained higher titres through 120 h (Figure 6.4).

These data demonstrate that a modest 4 °C decrease in incubation temperature consistently accelerates HCoV-OC43 replication and sustains higher viral yields across disparate substrates. Establishing this “lower temperature advantage” provides a robust foundation for dissecting the

underlying molecular mechanisms ranging from viral polymerase function to host innate sensing and IFN signalling in subsequent experiments.

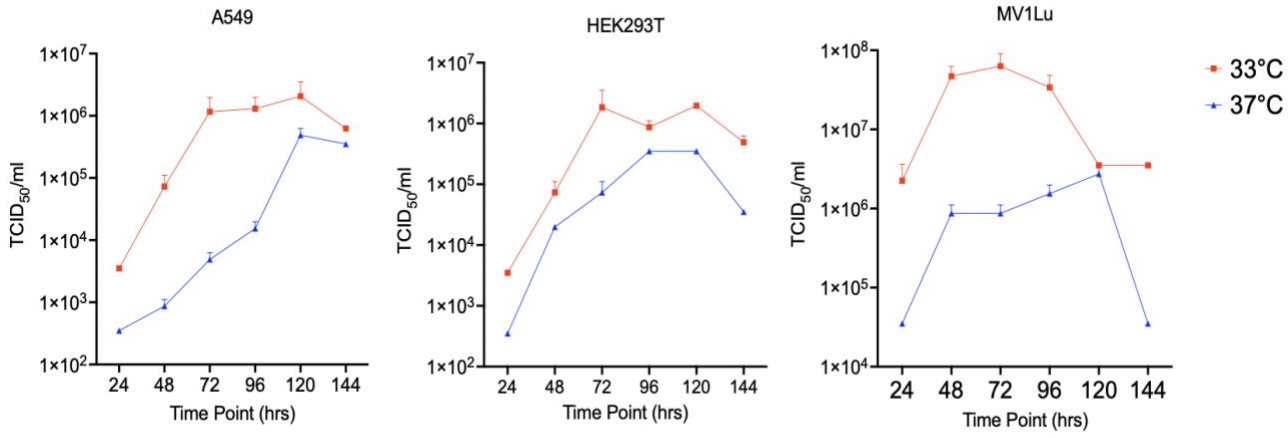

Figure 6.4: Temperature-dependent replication kinetics of HCoV-OC43 in three cell lines

A549, HEK293T, and Mv1Lu cells were maintained at 33 °C or 37 °C and infected with HCoV-OC43 at an MOI of 0.01. Supernatants were harvested at 24, 48, 72, 96, 120, and 144 hpi, and viral titres were determined by $TCID_{50}$. In all three cell lines, HCoV-OC43 replicates more rapidly and reaches higher peak titres at the lower temperatures than at the higher temperatures. Asterisks indicate significant temperature-related differences (Two-way ANOVA with Šídák's multiple comparisons test)

6.2.5 Sensitivity of HCoV-OC43 to IFN-α

The number of virus offspring released from infected cells reflects the complex interaction between viral replication and its regulation by cellular defence mechanisms, including various ISGs. To evaluate how IFN stimulation at different temperatures affects the replication dynamics of HCoV-OC43, MRC-5 cells were pretreated with varying doses (100, 500, and 1000 IU/ml) of rIFNα for 24 h prior to infection. After pretreatment, the cell medium was

replaced with IFN-free medium, and cells were then exposed to HCoV-OC43 virus at an MOI of 0.1 at either 33 °C or 37 °C for a total of 24 h. qPCR analysis of the virus in the supernatant showed a significant reduction in Hcov-OC43 replication when treated with 1000 IU/ml of type I IFN, regardless of the incubation temperature (33 °C or 37 °C), as shown in Figure 6.5. Additionally, rIFNα treatment for 24 h before HCoV-OC43 infection led to a notable decrease in viral presence, emphasising the antiviral role of IFN.

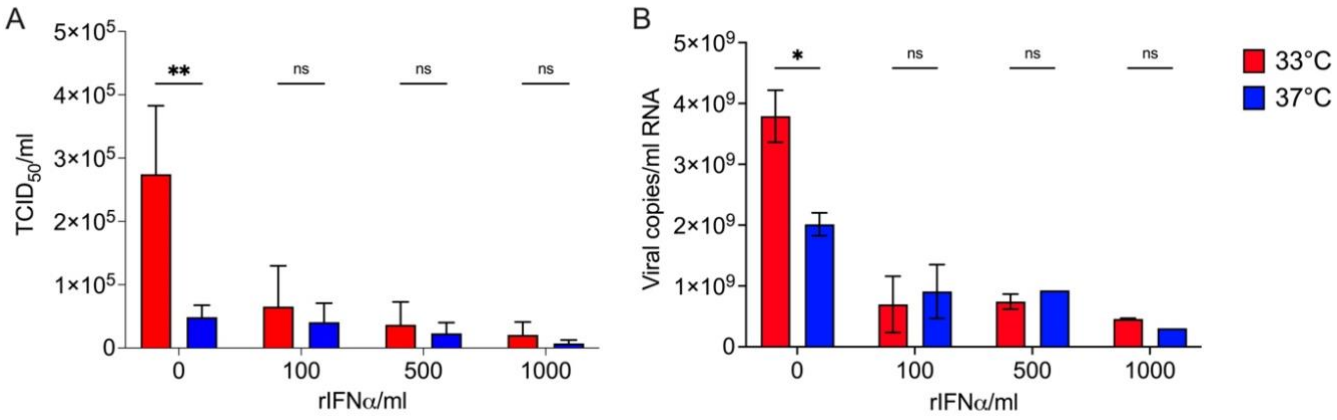

Figure 6.5: Sensitivity of HCoV-OC43 to rIFN-α pretreatment

MRC-5 cells were pretreated with rIFN-α for 24 h prior to infection with HCoV-OC43 at MOI 0.1. rIFN-α was applied at 0 (no IFN control), 100, 500, or 1000 IU/ml, and infections were performed at both 33 °C and 37 °C. Virus yield was assessed 24 hpi by two methods. **(A)** Infectious titre determined by $TCID_{50}$/ml on cell supernatants. **(B)** Viral RNA levels in the supernatant were measured by qPCR. In both results, increasing doses of IFN-α caused a progressive reduction in HCoV-OC43 replication. At 1000 IU/ml, viral titres and RNA copies were substantially lower than in untreated controls, although not completely inhibited. The inhibitory effect of IFN was observed at both temperatures, demonstrating that HCoV-OC43 is sensitive to IFN. Error bars show the standard deviation of three independent experiments. Statistical analysis by two-way ANOVA (Sidak's multiple comparisons) indicates significant differences in viral yield between IFN-treated and untreated conditions (*$p <$ 0.05).

Immunofluorescence staining using an anti-OC43 N antibody revealed an intriguing pattern of viral replication. Untreated cells infected with HCoV-OC43 exhibited increased (N) staining, indicating active viral replication. Interestingly, the virus was detected not only in the nucleus but also in the cytoplasm, consistent with the known life cycle of coronaviruses (Park and Iwasaki, 2020). One notable observation was the temperature-dependent regulation of HCoV-OC43 replication. Cells maintained at 33 °C exhibited a higher abundance of the virus compared to those at 37 °C. This finding highlights the significance of environmental factors, such as temperature, in determining the efficiency of HCoV-OC43 replication within host cells (Figure 6.6). These results suggest that temperature-dependent differences in viral replication may be linked to differences in ISG induction.

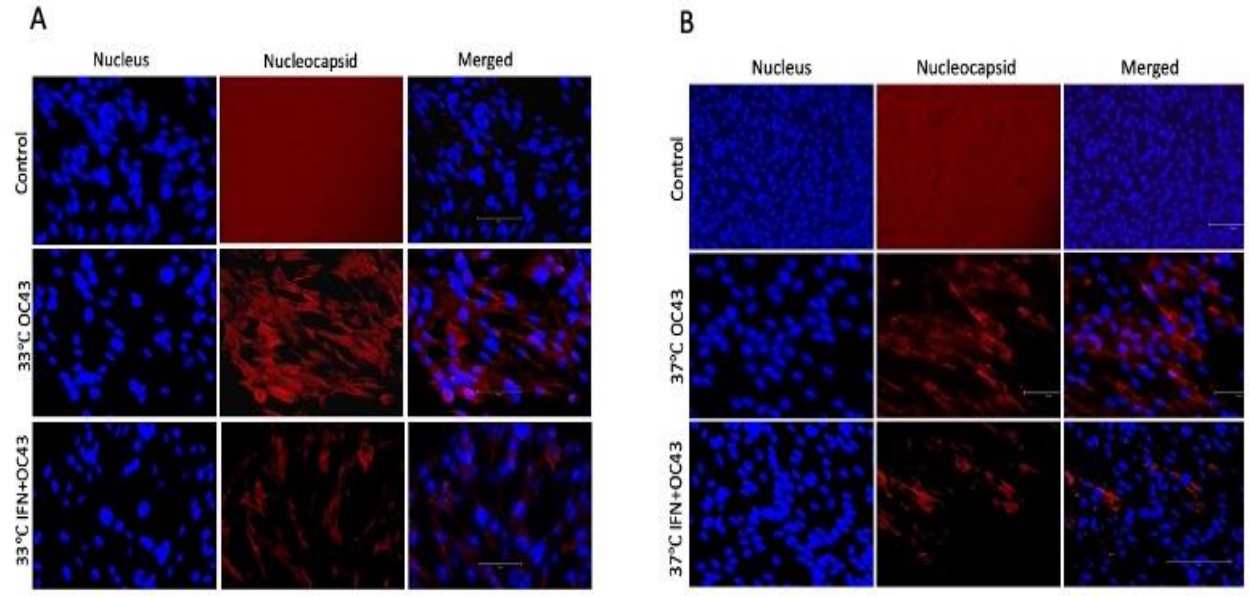
A
Nucleus
Nucleocapsid
Merged
Control
33°C OC43
33°C IFN+OC43
B
Nucleus
Nucleocapsid
Merged
Control
37°C OC43
37°C IFN+OC43

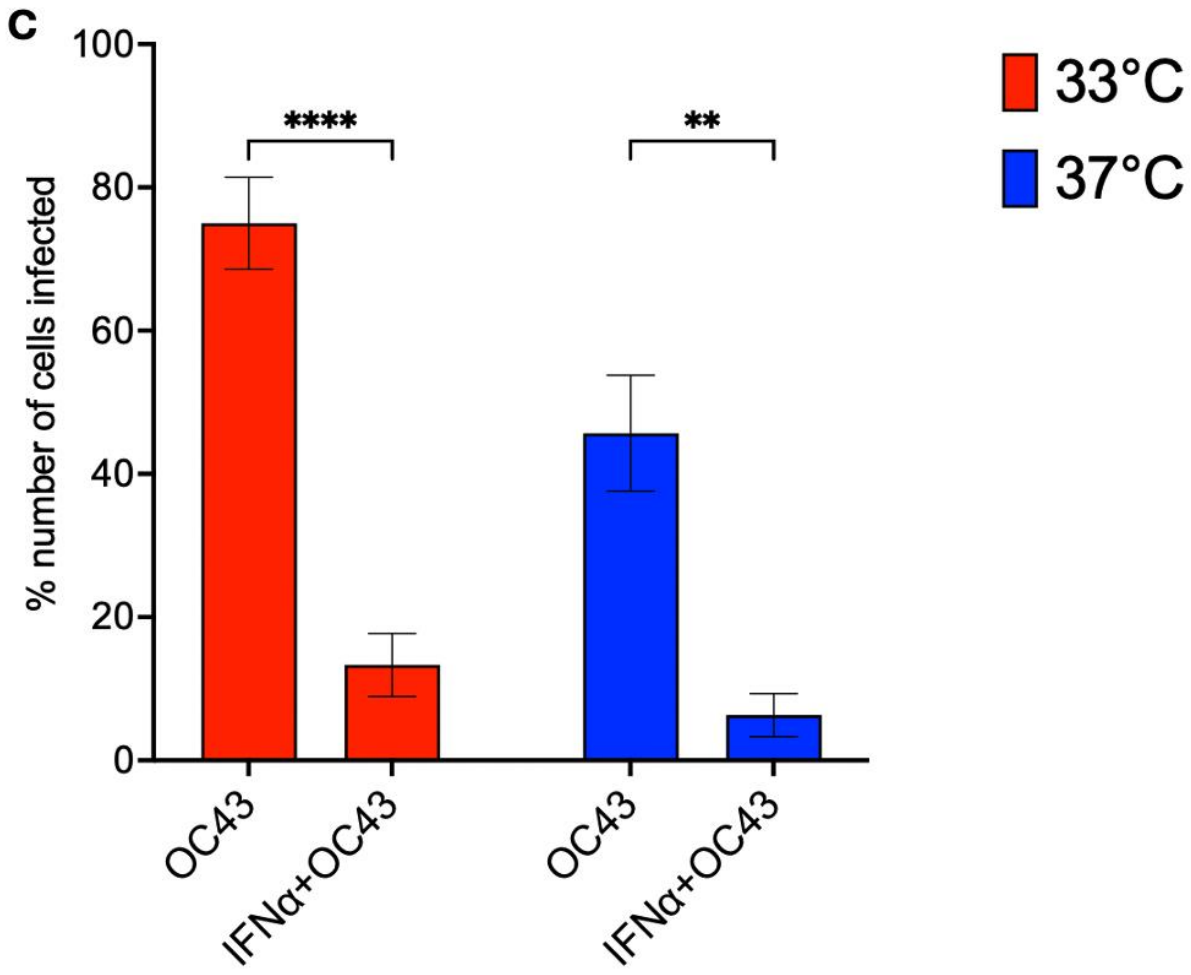
C
100
80
60
40
20
0
% number of cells infected
****
**
33°C
37°C
OC43
IFNα+OC43
OC43
IFNα+OC43

Figure 6.6: Immunofluorescence analysis using an anti-HCoV-OC43 N antibody reveals distinctive patterns of HCoV-OC43 coronavirus replication in MRC-5 cells.

MRC-5 cells were infected with HCoV-OC43 (MOI 0.1) at either 33 °C or 37 °C and fixed at 24 hpi for immunofluorescent staining of the viral N protein. Prior to infection, one set of cultures was pretreated with IFN-α (1000 IU/ml for 24 h), while another set received no pretreatment. Cells were stained with an anti-HCoV-OC43 N protein antibody (red fluorescence) to detect viral antigen, and nuclei were counterstained with DAPI (blue). **(A)** Representative fields of infected cells at 33 °C. In the absence of IFN, numerous cells exhibit bright N protein staining in the cytoplasm, indicating robust viral replication and N protein accumulation. With IFN-α pretreatment, N protein staining is nearly absent, reflecting a drastic reduction in the number of infected cells and viral protein levels. **(B)** Representative fields at 37 °C. Untreated infected cells at 37 °C show fewer N-positive cells and generally weaker fluorescence than the 33 °C condition, consistent with lower viral replication at the higher temperature. IFN-α pretreatment at 37 °C further diminishes N protein signals to no detectable levels. These images illustrate that IFN pretreatment significantly suppresses HCoV-OC43 infection, and they underscore the higher viral load present at 33 °C compared to 37 °C in untreated infections. **(C)** Quantification of infection rates from the images in (A-B). For each condition, nuclei were segmented, and HCoV-OC43 N-positive cells were identified using intensity thresholding; the percentage of infected cells was calculated as the number of N-positive cells divided by the total number of nuclei × 100. Quantification was done using ImageJ. Bars show mean ± SEM from 3 replicate fields across 2 independent experiments. Statistics: two-way ANOVA with Tukey's post-hoc test. IFN-α pretreatment significantly reduced the fraction of infected cells at 33 °C (**** $P < 0.0001$) and at 37 °C (** $P < 0.01$).

6.2.6 RPS11 is the most stable reference gene for temperature-comparative qPCR analysis

Before assessing ISG induction, I evaluated candidate housekeeping genes for their stability at 33 and 37 °C. Reliable normalisation is essential for every qPCR assay, so I first measured the transcript abundance of seven candidate HKGs in uninfected MRC-5 cells maintained at 33 and 37 °C. Cycle-threshold (Ct) values for GAPDH, ACTB, RPS11, B2M, TBP, HPRT1 and RPLP0 were obtained from three biological replicates, each amplified in technical

triplicate. Figure 6.6 summarises the distribution of Ct values for each gene under the two temperature conditions.

Across the panel, Ct values ranged from ~16-30, indicating several orders of magnitude difference in transcript abundance. GAPDH displayed the lowest Ct values at 33 °C but shifted upward at 37 °C; the two box-plot distributions did not overlap, and the temperature effect was highly significant ($p < 0.0001$). ACTB was slightly less abundant at 33 °C and likewise showed a small but significant increase at 37 °C. RPS11 produced tightly clustered Ct values around 17.5-18 at both temperatures, with nearly identical inter-quartile ranges and no detectable temperature effect. B2M fell into the mid-abundance range and exhibited overlapping red and blue boxes, indicating minimal variation between 33 °C and 37 °C.

In contrast, low-abundance transcripts TBP and HPRT1 yielded high Ct values. TBP showed a modest but statistically significant shift, whereas HPRT1 remained broadly unchanged, albeit with wider whiskers that suggest greater biological variability. Finally, RPLP0 exhibited the broadest distribution: Ct values centred near 24 at 33 °C but decreased and narrowed markedly at 37 °C, a highly significant difference (Figure 6.7).

These measurements indicate that some commonly used HKGs vary with temperature, while others remain stable in this cell system. Establishing such baseline behaviour is critical, because every downstream qRT-PCR experiment in this thesis will compare samples grown at 33 °C and 37 °C. Without a temperature-insensitive reference gene, apparent changes in viral or host transcripts could simply reflect differential normalisation rather than true biological effects. I selected RPS11 as the sole reference gene for all qRT-PCR normalisations because its expression remained highly stable across both temperatures, showing minimal variance (<2%) in Ct values.

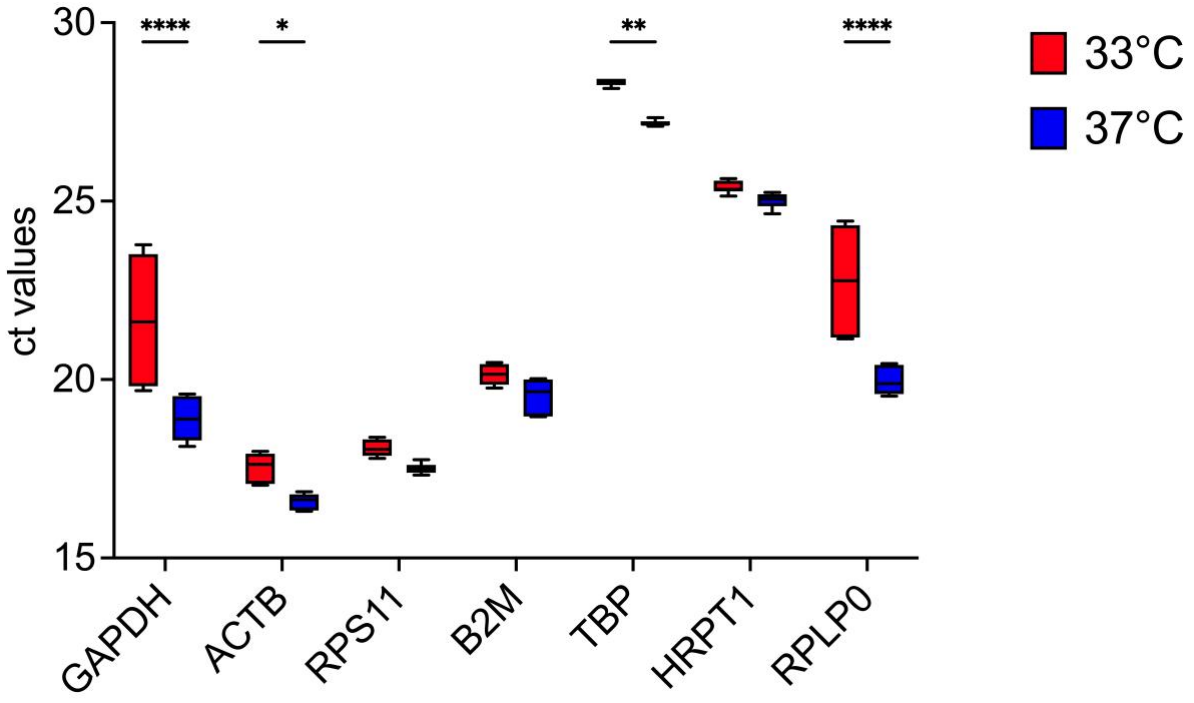

Figure 6.7: Ct distributions of seven candidate housekeeping genes at 33 °C and 37 °C

MRC-5 cells were cultured for 24 h at 33 or 37 °C. Total RNA was reverse-transcribed, and each target was amplified in triplicate qPCR reactions (n = 3 biological replicates). Boxes show the inter-quartile range; horizontal lines denote medians; whiskers represent the full range. Asterisks indicate significant temperature-related differences (two-way ANOVA with Tukey's correction): * $p < 0.05$; ** $p < 0.01$; **** $p < 0.0001$.

6.2.7 Analysis of the kinetics of ISGs following infection at different temperatures

Given the substantial impact of temperature on replication and the observed decline in viral load post-IFN pretreatment, I shifted my focus towards understanding how temperature variations could influence the induction of ISGs in response to HCoV-OC43. To evaluate the effect of temperature on ISG responses during HCoV-OC43 infection, qPCR analysis was performed on selected ISGs under three experimental conditions: infection with HCoV-OC43 (MOI 0.1) alone, stimulation with IFNα (1000IU/ml) alone, and combined IFNα pre-treatment

followed by HCoV-OC43 infection. Each condition was assessed at both 33 and 37 °C to simulate the differential environments of the upper and lower respiratory tract, respectively.

Across all genes, a consistent trend was observed whereby stimulation with IFNα alone led to the most potent induction of ISG expression compared to HCoV-OC43 infection alone or the combined treatment. This was particularly evident for ISGs such as *CXCL11, IFIT1, ISG20*, and *OASL*, where fold changes were markedly higher under IFNα treatment relative to HCoV-OC43 infection, which produced relatively modest upregulation. The results suggest that exogenous type I IFN is a more potent inducer of antiviral genes than HCoV-OC43, consistent with the virus's known ability to evade or suppress host innate responses (Figure 6.5).

Another interesting observation was that gene expression was generally higher at 37 °C than at 33 °C under IFNα stimulation alone, although the differences were not statistically significant. This trend was especially pronounced in genes such as *CXCL11, IFIT2, IRF7*, and *OASL*. This temperature effect was attenuated in the HCoV-OC43-only condition, where ISG expression remained low and largely comparable between 33 and 37 °C. These findings support the notion that HCoV-OC43 may suppress the IFN response regardless of temperature, although its suppression appears more effective at the lower temperature.

Interestingly, in the combined IFNα and HCoV-OC43 condition, ISG expression was reduced compared to IFNα alone in most cases, indicating that HCoV-OC43 actively antagonises IFN-induced transcription even in the presence of exogenous IFN signalling. The extent of this suppression varied between genes, but the pattern was broadly consistent across the dataset. At 37 °C, the magnitude of suppression by HCoV-OC43 following IFN pre-treatment remained substantial for many ISGs, but expression remained higher than levels observed in the virus-only condition. At 33 °C, the virus’s suppressive effect was more pronounced, in some cases

reducing expression levels close to or below baseline, highlighting a potential temperature-dependent advantage for viral immune evasion in cooler airway environments (Figure 6.5).

Overall, these results show that IFNα induces robust ISG expression at both temperatures, but more effectively at 37 °C. HCoV-OC43 alone exhibited a limited ability to induce ISGs and appeared to suppress IFN-mediated responses, with the inhibitory effect being more pronounced at 33 °C. These trends support the notion that HCoV-OC43's immune evasion strategies are more effective under cooler conditions, potentially facilitating its preferential replication in the upper respiratory tract.

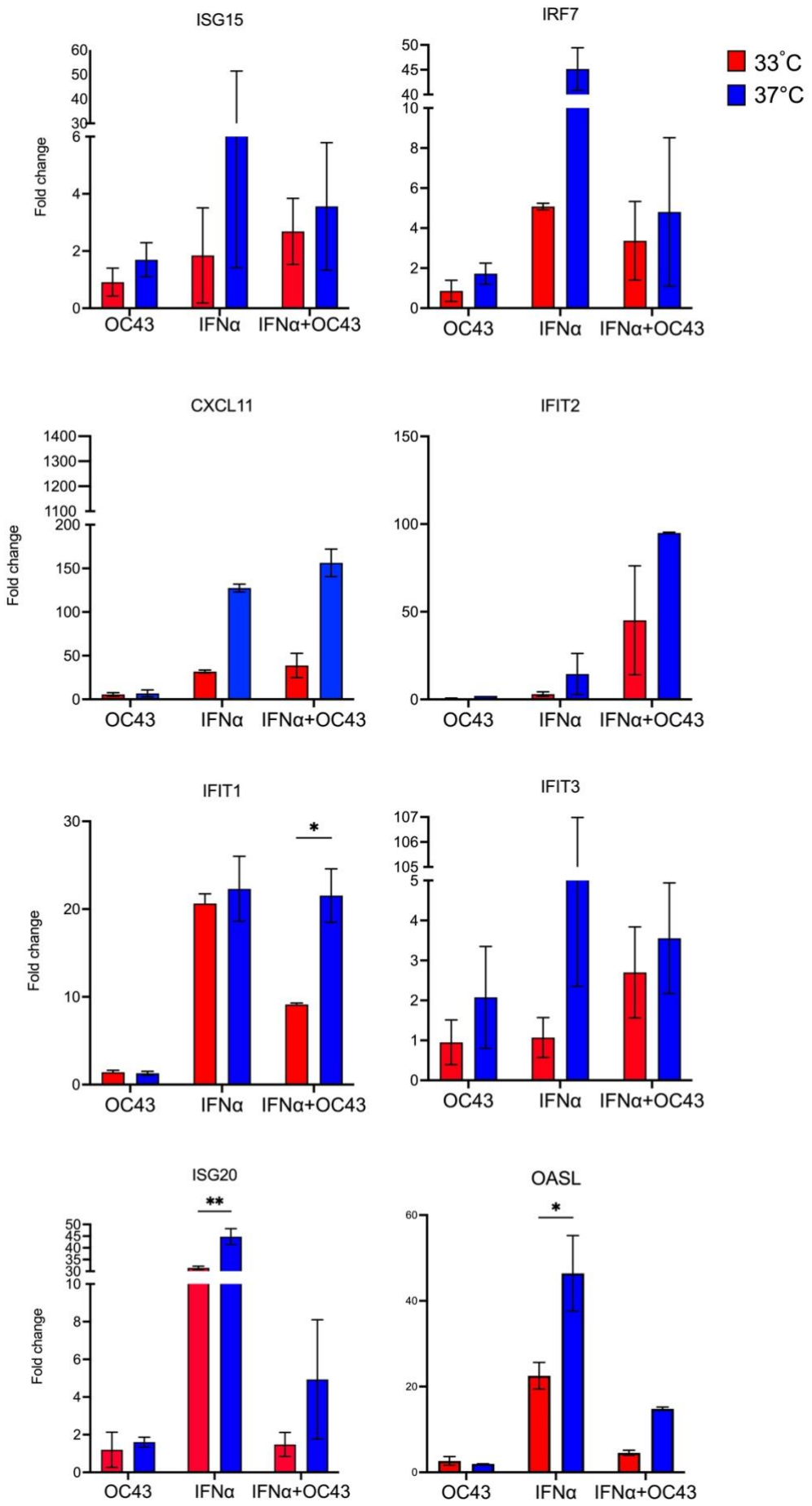
ISG15
IRF7
33˚C
37°C
Fold change
OC43
IFNα
IFNα+OC43
CXCL11
IFIT2
IFIT1
IFIT3
ISG20
OASL
*
**

Figure 6.8: Temperature-dependent expression of ISGs in MRC-5 cells following rIFNα treatment and HCoV-OC43 infection.

qPCR analysis of selected ISGs was performed to assess gene expression under three conditions: HCoV-OC43 infection, IFN-α treatment alone, and IFN-α pre-treatment followed by HCoV-OC43 infection. Cells were treated with 1000 IU/ml of rIFNα for 16 h, followed by infection with HCoV-OC43 for 24 h. Experiments were conducted at 33 °C and 37 °C to reflect upper and lower airway temperatures, respectively. Data are presented as fold change relative to unstimulated, uninfected controls. Bars represent mean ± SEM. Asterisks indicate statistically significant differences between temperatures for the indicated condition (*$p < 0.05$, **$p < 0.01$). Results demonstrate that IFNα induces robust ISG expression in a temperature-dependent manner, while HCoV-OC43 alone induces minimal ISG activation and dampens IFN-mediated responses, particularly at 33 °C.

6.2.8 IFNα treatment suppresses HCoV-OC43 replication at both 33 °C and 37 °C over multiple cycles

To test whether exogenous IFN signalling can override the temperature advantage of HCoV-OC43 replication, MRC-5 cells were pretreated with recombinant IFNα (1000 IU/mL) and subsequently infected with HCoV-OC43 (MOI 0.1). Cultures were maintained at 33 or 37 °C, and viral replication was tracked by $TCID_{50}$ and viral RNA quantification in the supernatant over 96 h.

In untreated infections, replication was consistently higher at 33 °C than at 37 °C, with titres diverging significantly from 72 hpi onwards ($p < 0.001$) (Figure 6.9A). By 96 hpi, titres at 33 °C exceeded 10^7 $TCID_{50}$/mL, nearly an order of magnitude above those at 37 °C. Viral RNA levels mirrored this pattern, reaching ~1×10^{11} copies/mL at 33 °C compared to ~1×10^{10} copies/mL at 37 °C ($p < 0.01$) (Figure 6.9B).

IFN-α treatment markedly suppressed viral replication at both temperatures. At 33 °C, titres fell by nearly 2 logs, from ~10^7 to ~10^5 $TCID_{50}$/mL by 96 hpi ($p < 0.0001$). Viral RNA levels similarly dropped from ~1×10^{11} to ~3×10^{10} copies/mL ($p < 0.001$). At 37 °C, IFN-α reduced

titres from ~10^6 to ~10^4 $TCID_{50}$/mL and viral RNA from ~1×10^{10} to ~1×10^9 copies/mL by 96 hpi. These reductions were significant at 48-96 hpi ($p < 0.0001$).

Importantly, IFN-α treatment largely abolished the replication advantage normally observed at 33 °C. By 96 hpi, titres and viral RNA levels in IFN-treated cultures were similar between 33 °C and 37 °C, with no significant difference.

Together, these results confirm that exogenous IFN-α imposes a potent antiviral block on HCoV-OC43 replication, substantially attenuating the cooler-temperature advantage. This suggests that the temperature sensitivity of HCoV-OC43 replication in untreated cells is tightly linked to the relative strength of IFN responses.

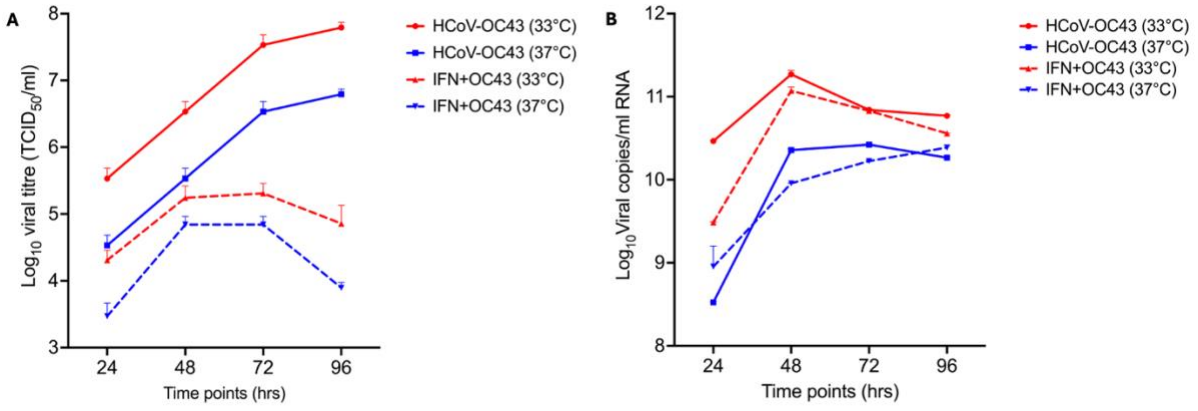

Comparison	24	48	72	96
HCoV-OC43 (33°C) vs. HCoV-OC43 (37°C)	ns	ns	***	****
HCoV-OC43 (33°C) vs. IFN+OC43 (33°C)	ns	ns	****	****
HCoV-OC43 (33°C) vs. IFN+OC43 (37°C)	ns	ns	****	****
HCoV-OC43 (37°C) vs. IFN+OC43 (33°C)	ns	ns	ns	ns
HCoV-OC43 (37°C) vs. IFN+OC43 (37°C)	ns	ns	ns	ns
IFN+OC43 (33°C) vs. IFN+OC43 (37°C)	ns	ns	ns	ns

Comparison	24	48	72	96
HCoV-OC43 (33°C) vs. HCoV-OC43 (37°C)	*	****	***	**
HCoV-OC43 (33°C) vs. IFN+OC43 (33°C)	*	****	ns	ns
HCoV-OC43 (33°C) vs. IFN+OC43 (37°C)	*	****	****	**
HCoV-OC43 (37°C) vs. IFN+OC43 (33°C)	ns	****	**	ns
HCoV-OC43 (37°C) vs. IFN+OC43 (37°C)	ns	ns	ns	ns
IFN+OC43 (33°C) vs. IFN+OC43 (37°C)	ns	****	***	ns

Figure 6.9: Growth kinetics of HCoV-OC43 in the presence of IFN-α at 33 °C and 37 °C.

MRC-5 cells were pretreated with recombinant human IFN-α (1000 IU/mL) for 24 h prior to infection with HCoV-OC43 (MOI 0.1) and maintained at either 33 °C or 37 °C. Viral replication was quantified over 96 h by **(A)** infectious virus titres in supernatants (log_{10} $TCID_{50}$/mL) and **(B)** viral RNA copies (log_{10} copies/mL) determined

by qRT-PCR. Data represent mean ± SEM of three independent experiments. Statistical analysis was performed using two-way ANOVA with Tukey's post hoc test. Significant differences are indicated: *$p < 0.05$, **$p < 0.01$, ***$p < 0.001$, ****$p < 0.0001$; ns, not significant. IFN-α markedly reduced replication at both temperatures, abolishing the replication advantage normally observed at 33 °C.

6.2.9 JAK/STAT inhibition restores HCoV-OC43 replication, confirming IFN signalling as the key temperature-dependent barrier

To assess whether the temperature-associated restriction of HCoV-OC43 replication was mediated by IFN signalling via the JAK/STAT pathway, MRC-5 cells were infected with HCoV-OC43 (MOI 0.1) and treated with Ruxolitinib (Rux; 2 μM), a selective JAK1/2 inhibitor that blocks STAT activation and downstream IFN responses. Infected cultures were maintained at 33 °C or 37 °C, and replication was monitored by $TCID_{50}$ and viral RNA quantification over 96 h.

In untreated infections, viral replication again showed a clear temperature effect, with titres at 33 °C significantly higher than those at 37 °C from 72 hpi onwards ($p < 0.001$) (Figure 6.10A). Viral RNA levels followed the same pattern, reaching ~1×10^{11} copies/mL at 33 °C compared to ~1×10^{10} copies/mL at 37 °C (Figure 6.10B).

The addition of Ruxolitinib restored replication at 37 °C to levels comparable to those at 33 °C. By 72–96 hpi, titres in Rux-treated 37 °C cultures reached ~10^7 $TCID_{50}$/mL, eliminating the ~1-log deficit observed in untreated conditions. Viral RNA levels were similarly elevated, approaching those of 33 °C cultures and showing no significant temperature difference. At 33 °C, Rux treatment did not markedly alter replication, consistent with the weaker IFN-mediated restriction observed at this cooler temperature.

Statistical analysis confirmed that Rux abolished the significant divergence between 33 °C and 37 °C observed in untreated cultures ($p < 0.0001$ at 48 hpi; $p < 0.001$ at 72 hpi). This effect was most apparent at later time points, when innate antiviral responses are typically strongest.

Together, these findings demonstrate that the reduced replication of HCoV-OC43 at 37 °C is attributable mainly to IFN-dependent JAK/STAT signalling. By blocking this pathway, Ruxolitinib removes the temperature-associated restriction, allowing replication at 37 °C to match the levels observed at 33 °C. This provides direct functional evidence that the differential antiviral state established by IFN signalling is the primary driver of HCoV-OC43's temperature sensitivity in MRC-5 cells.

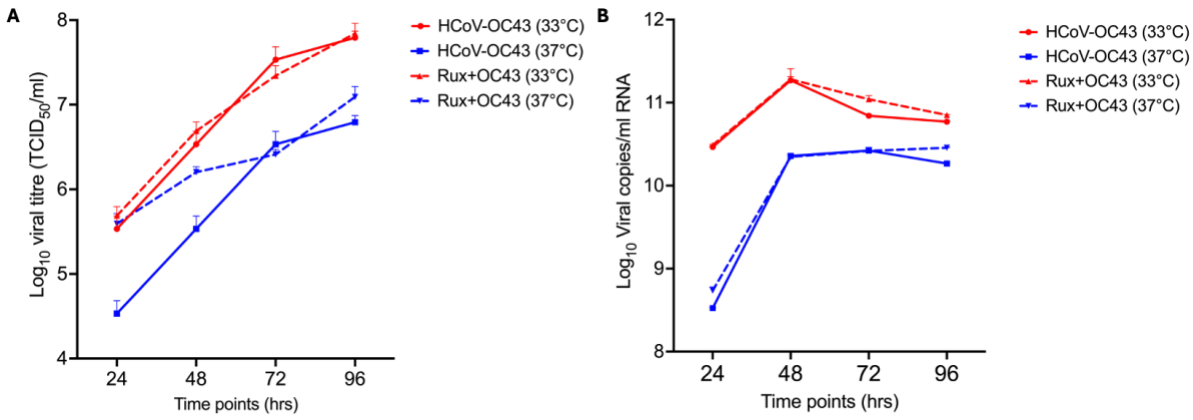

Comparison	24	48	72	96
HCoV-OC43 (33°C) vs. HCoV-OC43 (37°C)	ns	ns	*	***
HCoV-OC43 (33°C) vs. Rux+OC43 (33°C)	ns	ns	ns	ns
HCoV-OC43 (33°C) vs. Rux+OC43 (37°C)	ns	ns	*	***
HCoV-OC43 (37°C) vs. Rux+OC43 (33°C)	ns	ns	ns	****
HCoV-OC43 (37°C) vs. Rux+OC43 (37°C)	ns	ns	ns	ns
Rux+OC43 (33°C) vs. Rux+OC43 (37°C)	ns	ns	ns	****

Comparison	24	48	72	96
HCoV-OC43 (33°C) vs. HCoV-OC43 (37°C)	ns	****	ns	ns
HCoV-OC43 (33°C) vs. Rux+OC43 (33°C)	ns	ns	ns	ns
HCoV-OC43 (33°C) vs. Rux+OC43 (37°C)	ns	****	ns	ns
HCoV-OC43 (37°C) vs. Rux+OC43 (33°C)	ns	****	*	ns
HCoV-OC43 (37°C) vs. Rux+OC43 (37°C)	ns	ns	ns	ns
Rux+OC43 (33°C) vs. Rux+OC43 (37°C)	ns	****	*	ns

Figure 6.10: JAK/STAT inhibition by Ruxolitinib restores HCoV-OC43 replication at 37 °C.

MRC-5 cells were infected with HCoV-OC43 (MOI 0.1) in the absence or presence of Ruxolitinib (2 µM) and incubated at 33 °C or 37 °C. Viral replication was monitored over 96 h by (*A*) infectious virus titres (log_{10} $TCID_{50}$/mL), and (*B*) viral RNA copies (log_{10} copies/mL). Data represent mean ± SEM of three independent experiments. Statistical analysis was performed using two-way ANOVA with Tukey's post hoc test. Significant

differences are indicated: *$p < 0.05$, **$p < 0.01$, ***$p < 0.001$, ****$p < 0.0001$; ns, not significant. Ruxolitinib treatment restored viral replication at 37 °C to levels comparable with 33 °C, demonstrating that JAK/STAT-dependent IFN signalling is the main temperature-sensitive barrier to infection.

6.2.10 JAK/STAT blockade prior to IFN priming reveals residual antiviral restriction of HCoV-OC43

To further investigate the role of JAK/STAT signalling in IFN-mediated restriction of HCoV-OC43, I pretreated MRC-5 cells with Ruxolitinib (2 μM, 1 h), followed by stimulation with recombinant IFNα (1000 IU/mL, for 16–24 h) before infection with HCoV-OC43 (MOI 0.1). Cultures were incubated at either 33 °C or 37 °C, and viral replication was measured by $TCID_{50}$ and viral RNA levels over 96 h (Figure 6.11).

As expected, untreated HCoV-OC43 replicated more efficiently at 33 °C than at 37 °C, with titres diverging significantly at 72 h and 96 h ($p < 0.01$, $p < 0.0001$). Viral RNA showed a similar pattern, peaking at approximately 1×10^{11} copies/mL at 33 °C compared to around 5×10^{10} copies/mL at 37 °C.

Interestingly, adding Ruxolitinib before IFN stimulation did not restore replication to untreated levels but instead led to significantly lower titres compared to virus-only controls. At 72-96 h, titres in Ruxolitinib + IFN + OC43 cultures were reduced by about 1-2 logs at both temperatures ($p < 0.01$ to $p < 0.0001$ compared with HCoV-OC43 alone). Viral RNA levels exhibited similar reductions, with significant differences at 48 h ($p < 0.0001$) that persisted until 96 h ($p < 0.05$). Notably, this restriction occurred regardless of incubation temperature, suggesting that even

with JAK/STAT signalling inhibited, IFN stimulation activates additional antiviral pathways capable of partially controlling HCoV-OC43.

Overall, these findings suggest that while JAK/STAT is the main pathway mediating IFN's antiviral effects, alternative antiviral mechanisms remain active in the presence of Ruxolitinib. These may include PRR-driven IRF3/7 activation or residual ISG induction, consistent with the ISG transcription observed under similar conditions. These findings indicate that JAK/STAT blockade does not fully abolish the IFN-mediated restriction of HCoV-OC43, underscoring the multi-layered nature of the IFN response.

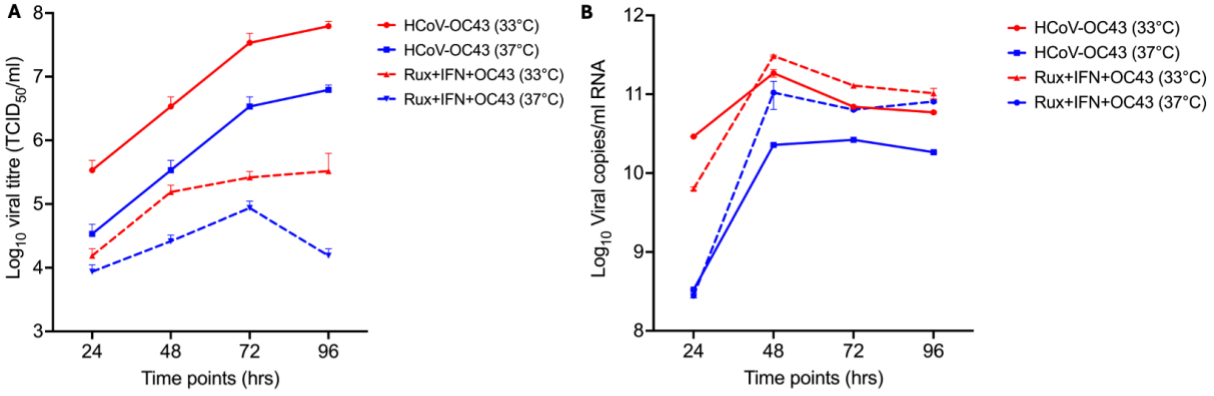

Comparison	24	48	72	96
HCoV-OC43 (33°C) vs. HCoV-OC43 (37°C)	ns	ns	**	****
HCoV-OC43 (33°C) vs. Rux+IFN+OC43 (33°C)	ns	ns	**	****
HCoV-OC43 (33°C) vs. Rux+IFN+OC43 (37°C)	ns	ns	**	****
HCoV-OC43 (37°C) vs. Rux+IFN+OC43 (33°C)	ns	ns	ns	ns
HCoV-OC43 (37°C) vs. Rux+IFN+OC43 (37°C)	ns	ns	ns	ns
Rux+IFN+OC43 (33°C) vs. Rux+IFN+OC43 (37°C)	ns	ns	ns	ns

Comparison	24	48	72	96
HCoV-OC43 (33°C) vs. HCoV-OC43 (37°C)	ns	****	ns	ns
HCoV-OC43 (33°C) vs. Rux+IFN+OC43 (33°C)	ns	****	ns	ns
HCoV-OC43 (33°C) vs. Rux+IFN+OC43 (37°C)	ns	**	ns	ns
HCoV-OC43 (37°C) vs. Rux+IFN+OC43 (33°C)	ns	****	**	**
HCoV-OC43 (37°C) vs. Rux+IFN+OC43 (37°C)	ns	**	ns	*
Rux+IFN+OC43 (33°C) vs. Rux+IFN+OC43 (37°C)	ns	****	*	ns

Figure 6.11: Ruxolitinib pre-treatment prior to IFNα stimulation partially diminishes the antiviral effect against HCoV-OC43.

MRC-5 cells were pretreated with Ruxolitinib (2 µM, 1 h) before stimulation with recombinant IFNα (1000 IU/mL, 16–24 h) and subsequent infection with HCoV-OC43 (MOI 0.1). Cultures were maintained at either 33 or 37 °C, and viral replication was measured by *(A)* infectious titres in supernatants (log_{10} $TCID_{50}$/mL) and *(B)* viral RNA

copies (log_{10} copies/mL) over 96 h. Data represent mean ± SEM from three independent experiments. Statistical analysis was conducted using Two-way ANOVA with Tukey's post hoc test. Significant differences are indicated: *$p < 0.05$, **$p < 0.01$, ***$p < 0.001$, ****$p < 0.0001$; ns, not significant. Rux+IFN+OC43 cultures displayed significantly reduced replication compared with HCoV-OC43 alone, demonstrating residual antiviral restriction even when JAK/STAT signalling is blocked.

6.2.11 Temperature shapes RIG-I and TLR3/MDA5 signalling strength in MRC-5 cells.

Although Ruxolitinib pre-treatment confirmed that JAK/STAT-dependent signalling is the main mediator of IFN-induced restriction, the continued presence of partial antiviral activity in Rux+IFN+OC43 cultures suggested that alternative, JAK/STAT-independent mechanisms also help limit replication. Since viral infection can activate cytosolic and endosomal PRRs such as RIG-I, MDA5, and TLR3, which initiate IRF3/7-dependent ISG transcription independently of IFNAR signalling, I next aimed to explore how temperature affects PRR-driven responses. To assess the temperature dependence at the upstream induction of the type I IFN response, I used a synthetic analogue of double-stranded RNA (which mimics viral RNA), polyinosinic: polycytidylic acid (usually abbreviated poly I:C or poly(I:C)), or 5'-triphosphate dsRNA (5'pppdsRNA) which engages endosomal TLR3/MDA5 and cytosolic RIG-I, respectively, triggering PRR signalling cascades that activates transcriptions of IFN cytokines. In parallel, to isolate the downstream signalling, I added 1000IU/ml of rIFNα directly to the culture medium, allowing IFNAR engagement at the cell surface and subsequent STAT-mediated induction of ISGs. All stimulations were performed at both 33 °C and 37 °C, enabling comparison of IFN induction versus signalling at physiologically relevant temperatures. Unstimulated mock-treated cells were included in these experiments as a negative control.

Poly I:C provoked a broad antiviral transcriptional programme in MRC-5 cells. RNA-seq revealed that most transcripts annotated in the Hallmark "IFN-α response" gene set were

strongly upregulated relative to mock controls, with peak fold-changes approaching 8,000-9,000. Canonical ISGs such as *RSAD2, OASL, CXCL10, CXCL11, IFIT1, IFIT2* and *IFI44L* dominated the left side of the rank-ordered plot, confirming vigorous activation of the RIG-I/MDA5-TLR3 axis. The overall shape of the curves indicates that 37 °C produced slightly higher or comparable induction of the leading ISGs, whereas the tail of lower-ranking genes showed minimal temperature dependence (Figure 6.12).

To validate the sequencing output, six transcripts with distinct positions in the ranked list were quantified by RT-qPCR. The bar graph shows the same direction of change and preserves the temperature effect. *OASL, IFIT1* and *CXCL10* were dramatically more responsive at 37 °C, rising 10- to 15-fold above the levels seen at 33 °C (**** $p < 0.0001$ for OASL and CXCL10; ** $p < 0.01$ for IFIT1). *RSAD2* and *CXCL11* displayed modest induction that did not differ statistically between temperatures, while IFIT2 showed high variability and failed to reach significance. Collectively, the data confirm that Poly I:C is sufficient to trigger the IFN-α signature captured by the MSigDB Hallmark set and that a subset of ISGs, particularly those involved in RNA sensing and chemokine signalling, are preferentially amplified at the core-body temperature of the lower airway (Figure 6.12).

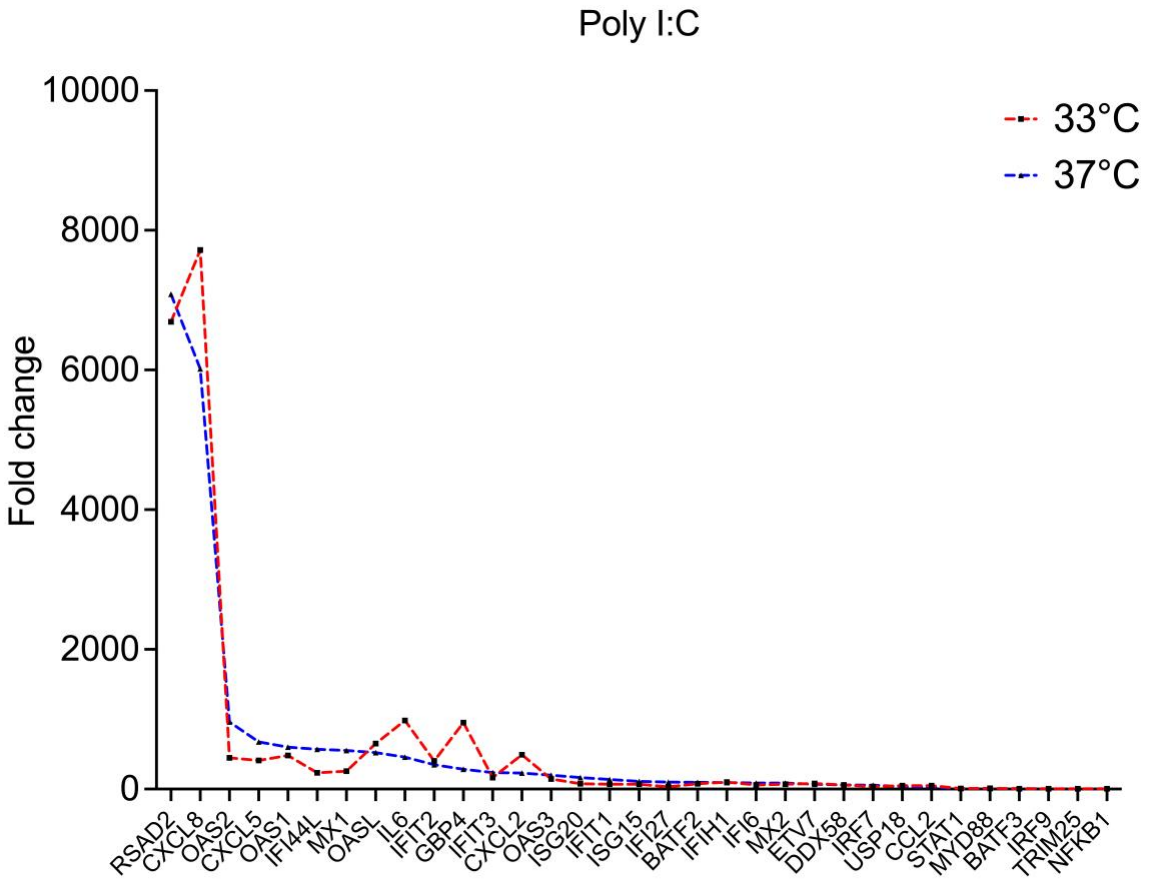
Poly I:C
33°C
37°C
Fold change
10000
8000
6000
4000
2000
0
RSAD2
CXCL8
OAS2
CXCL5
OAS1
IFI44L
MX1
OASL
IL6
IFIT2
GBP4
IFIT3
CXCL2
OAS3
ISG20
IFIT1
ISG15
IFI27
BATF2
IFIH1
IFI6
MX2
ETV7
DDX58
IRF7
USP18
CCL2
STAT1
MYD88
BATF3
IRF9
TRIM25
NFKB1

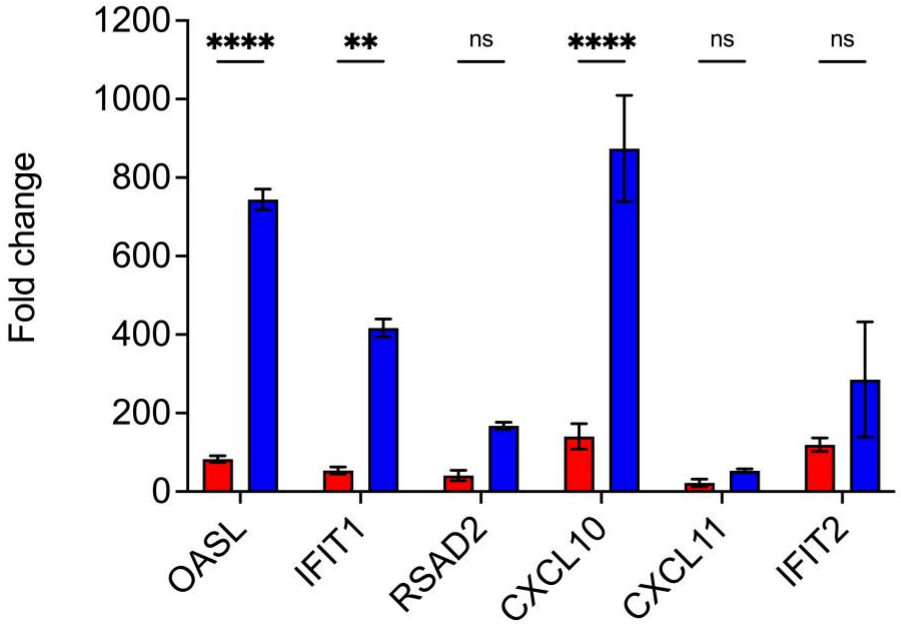
Fold change
1200
1000
800
600
400
200
0
****
**
ns
****
ns
ns
OASL
IFIT1
RSAD2
CXCL10
CXCL11
IFIT2

Figure 6.12: Poly I:C-induced ISG expression in MRC-5 cells at different temperatures: RNA-seq and qPCR validation.

MRC-5 cells were transfected with 1 µg of Poly I:C for 16–24 h at either 33 °C or 37 °C. Total RNA was harvested for high-throughput sequencing and gene expression analysis (top panel) as well as for qPCR validation of selected ISGs (bottom panel). Top panel: RNA-seq data showing fold change of ISGs in response to Poly I:C transfection, with mapped expression profiles plotted for 33 °C and 37 °C. Genes are arranged along the x-axis in descending order of expression. Bottom panel: qPCR validation of selected ISGs (*OASL, IFIT1, RSAD2, CXCL10, CXCL11, IFIT2*) showing significantly higher expression at 37 °C compared to 33 °C for several genes. Bars represent mean ± SEM. Multiple comparison tests were used to determine statistical significance: ****$p < 0.0001$, **$p < 0.01$, ns = not significant. Results confirm that Poly I:C induces robust ISG expression in MRC-5 cells, with temperature exerting a modulatory effect on the magnitude of response, particularly for OASL, IFIT1, and CXCL10.

Stimulation of MRC-5 cells with 5′ppp-dsRNA elicited a strong IFN-α–driven transcriptional response that was generally amplified at 37 °C compared to 33 °C. In the RNA-seq analysis, nearly all genes in the MSigDB Hallmark "IFN-α Response" set were up-regulated by 5′ppp-dsRNA, with the top ISGs (e.g., *RSAD2, GBP4, OAS2, MX1, IFIT1, IFIT2, OAS3, MX2*) showing fold-changes of more than 500-1200 at 37 °C (Figure 6.13). The rank-ordered fold-change curves demonstrate that while 33 °C does induce these same transcripts, the magnitude of induction is consistently lower than at 37 °C, particularly among the highest-expressed ISGs. To confirm these observations by RT-qPCR, I selected four representative genes spanning low- to high-ranking positions in the RNA-seq dataset (*IFIT1, CXCL11*, *IFIT2*, and *IFI44*). *IFIT1* expression increased only modestly at both temperatures and did not differ significantly between 33 and 37 °C. By contrast, *CXCL11* was induced substantially more at 37 than at 33 °C. *IFIT2*, which occupied a mid-range position in the library, exhibited the opposite pattern: the fold-change at 33 °C was significantly higher than at 37 °C. Finally, *IFI44* displayed robust upregulation at both temperatures, but the increase was more pronounced at 37 °C than at 33 °C. Together, these data confirm that 5′ppp-dsRNA engages the RIG-I pathway to activate the same

core IFN-α signature seen with Poly I:C, with a clear enhancement of late-stage ISG induction at normal body temperature (figure 6.13).

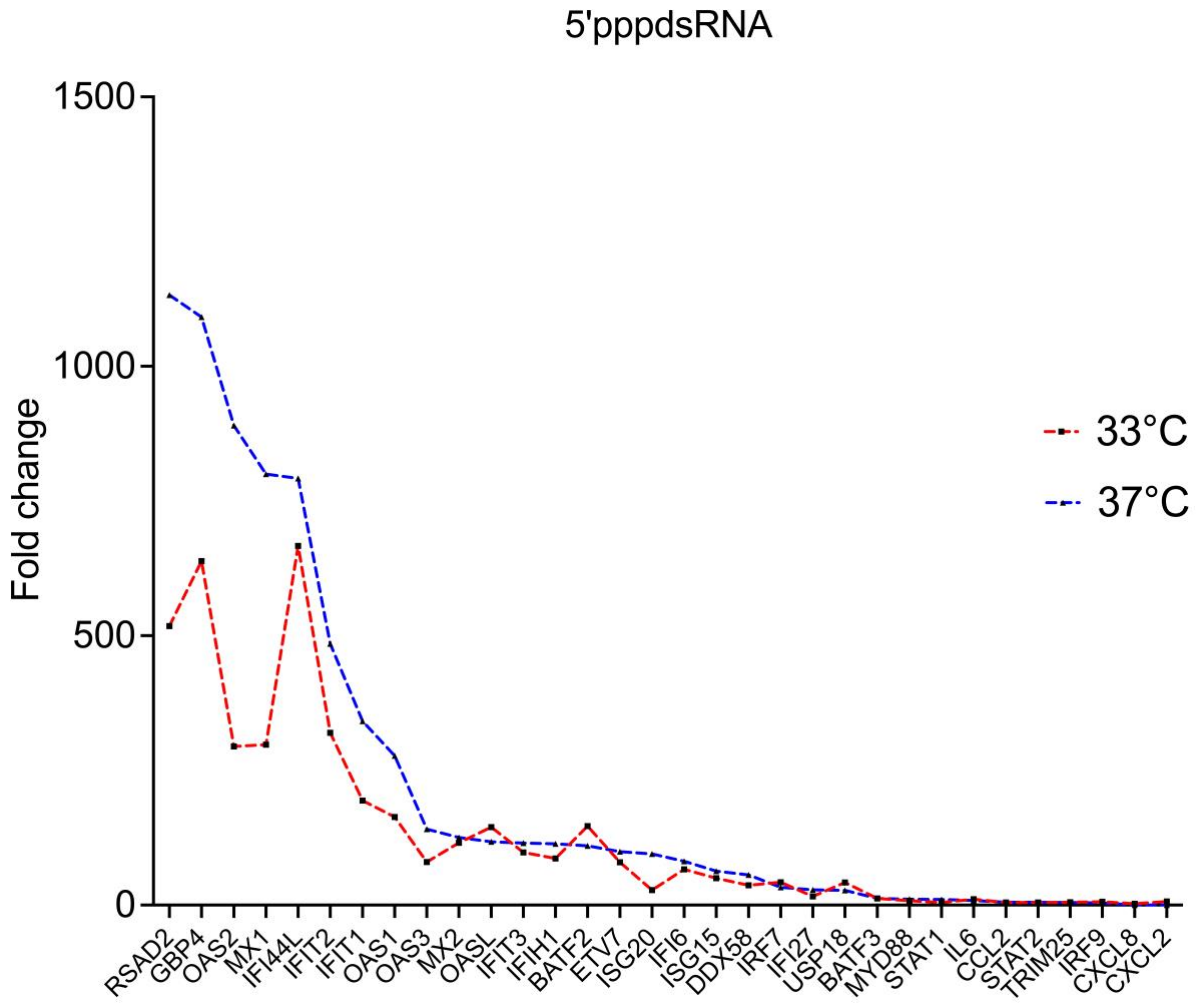

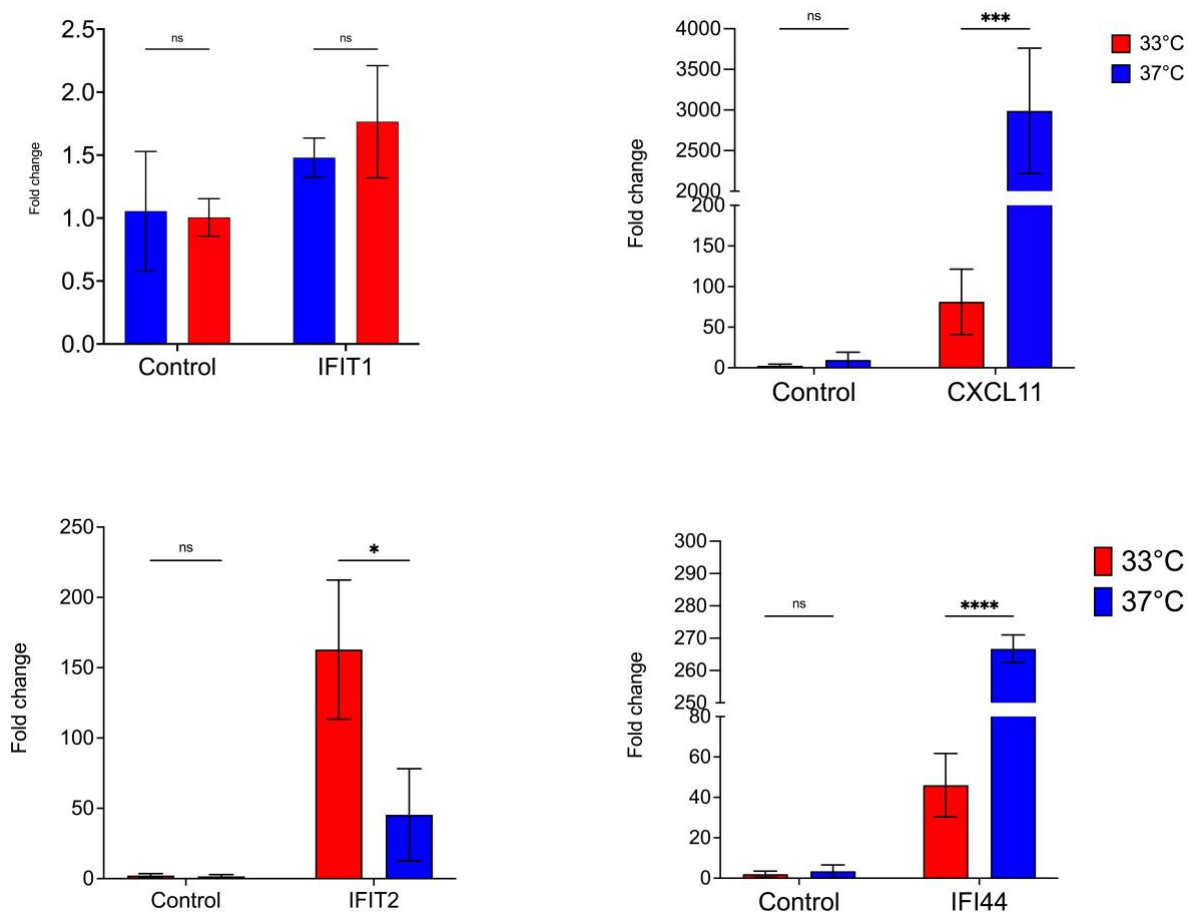

Figure 6.13: Temperature-dependent ISG expression following 5′ppp-dsRNA stimulation in MRC-5 cells: RNA-seq profiling and qPCR validation.

MRC-5 cells were transfected with 5 µg of 5′ppp-dsRNA and incubated for 16–24 h at either 33 °C or 37 °C. Total RNA was extracted for RNA-seq analysis and qPCR validation of selected ISGs. Top panel: RNA-seq analysis showing the fold change of ISG expression following 5′ppp-dsRNA stimulation at 33 °C and 37 °C. Genes are ordered by magnitude of induction. A stronger transcriptional response was observed at 37 °C, with several ISGs, including *RSAD2*, *OASL*, *IFI44*, and *CXCL11*, showing markedly higher induction than at 33 °C. Bottom panel: qPCR validation of selected genes (*IFIT1, CXCL11, IFIT2, IFI44*) confirms the RNA-seq findings. Notably, *CXCL11* and *IFI44* were significantly more induced at 37 °C compared to 33 °C, whereas *IFIT2* showed the opposite trend with higher expression at 33 °C. *IFIT1* expression remained comparable across both temperatures. Data are presented as mean ± SEM. Statistical comparisons were performed using two-way ANOVA with Sidaks multiple comparisons test: ns = not significant, *$p < 0.05$, **$p < 0.01$, ***$p < 0.001$, ****$p < 0.0001$. These findings suggest that while 5′ppp-dsRNA elicits strong ISG responses at both temperatures, temperature modulates the magnitude and profile of gene expression, with certain ISGs displaying distinct temperature preferences.

I also assessed the transcriptional and protein responses following stimulation with synthetic PRR ligands. Western blotting and densitometric quantification demonstrated that 5′ppp-

dsRNA induced strong *RIG-I* and *CXCL11* expression at both 33 °C and 37 °C, with consistently higher responses at 37 °C (Appendix Figure A1A-B). Poly I:C stimulation produced a similar induction of *RIG-I* and *CXCL11*, again more pronounced at 37 °C (Appendix Figure A1C-D). These results confirm that cytosolic (RIG-I) and endosomal (TLR3/MDA5) pathways are functional in MRC-5 cells, and that their activity is influenced by temperature.

Treatment of MRC-5 cells with 1,000 IU/mL rIFN-α for 16–24 h elicited a robust IFN-α transcriptional signature that was broadly comparable at 33 and 37 °C. In the RNA-seq analysis, nearly every gene in the MSigDB Hallmark "IFN-α Response" set was strongly induced relative to unstimulated controls, with top ISGs (e.g., *OAS2, MX1, IFI44L, IFIT2, IFIT1, BST2, OAS3*) showing fold-changes of several hundred to over a thousand at both temperatures (Figure 6.14). The rank-ordered fold-change curves are nearly identical among the highest-expressed ISGs, indicating that recombinant IFN-α drives equivalent up-regulation of its downstream targets regardless of the 4 °C temperature difference. To validate these results by RT-qPCR, I measured the expression of five representative ISGs (*ISG20, OASL, CXCL10, IFI44R*, and *DDX58*) in three independent cultures at each temperature (Figure 6.14). All five transcripts were strongly upregulated compared to untreated controls, and two-way ANOVA with Sidak's multiple comparisons test revealed no statistically significant differences between 33 °C and 37 °C for any gene. Thus, exogenous IFN-α stimulates its classical ISG program in MRC-5 cells without notable temperature dependence under these conditions.

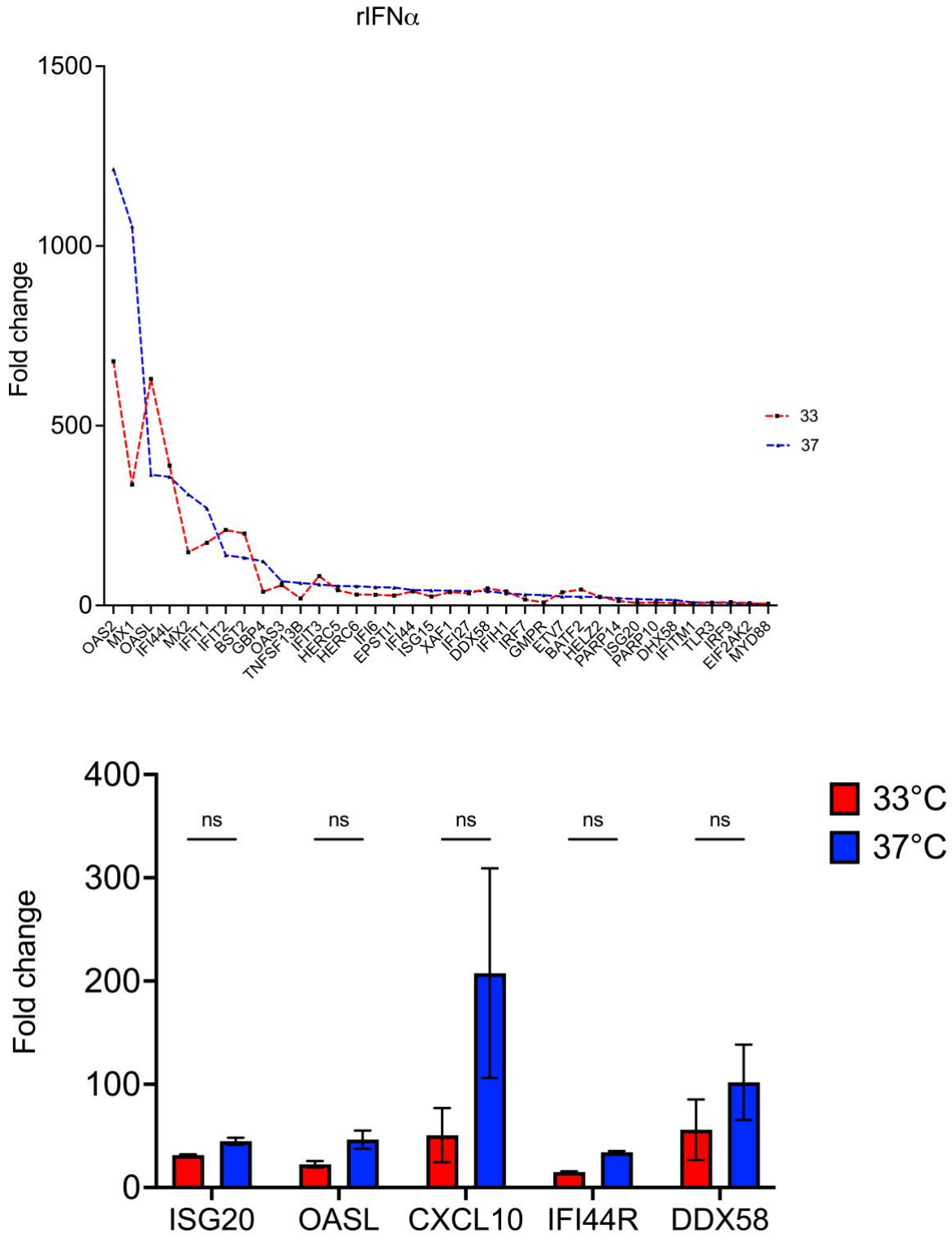

Figure 6.14: ISG expression in MRC-5 cells following stimulation with rIFNα at 33 °C and 37 °C: RNA-seq and qPCR validation.

MRC-5 cells were treated with 1000 IU/ml of rIFNα for 16–24 h at either 33 or 37 °C. Total RNA was collected for transcriptomic profiling and targeted qPCR analysis. Top panel: RNA-seq results showing fold change of ISGs

in response to rIFNα stimulation. Gene expression patterns at 33 and 37 °C are plotted in descending order. Overall, rIFNα induced a strong ISG signature at both temperatures, with largely overlapping profiles and only subtle differences in expression magnitude. Bottom panel: qPCR validation of selected ISGs (*ISG20, OASL, CXCL10, IFI44R, DDX58*) demonstrates comparable expression between 33 °C (red bars) and 37 °C (blue bars). Two-way ANOVA with Sidak's multiple comparisons test revealed no statistically significant differences between 33 °C and 37 °C for any gene, confirming that exogenous IFNα triggers a robust and temperature-independent transcriptional response. Data represent mean ± SEM; ns = not significant. These results indicate that IFNAR-mediated ISG induction remains stable across physiological temperatures, in contrast to the temperature sensitivity observed with PRR agonists such as Poly I:C and 5′ppp-dsRNA.

6.2.12 Comparison of the Pearson correlation between ISG expression at 33 and 37 °C.

I used Pearson correlation analysis to examine how temperature influences the antiviral gene expression landscape. All three treatments elicited similar responses at the two temperatures, but to different extents. rIFN showed the strongest correlation (r = 0.9462) among the three stimuli (Figure 6.15), indicating that direct IFNAR-mediated signalling remains the most stable across temperatures. The ISG expression profile remained essentially unchanged between 33 °C and 37 °C, with minimal variation. This suggests that small temperature shifts driven by exogenous IFN do not significantly impact downstream JAK-STAT activation and ISG transcription. 5'pppdsRNA also displayed a strong correlation (r = 0.9353), slightly lower than that of rIFN, but still indicated a well-preserved transcriptional response (Figure 6. 15). The overall ISG pattern was consistent; however, some genes, such as *IFI27, OASL*, and *IFIT1*, showed higher expression at 33 °C. This points to potentially stronger RIG-I-dependent signalling in cooler conditions, which could be essential for the upper airway. There was a moderate correlation (r = 0.9046) between poly I: C stimulation and the other two (Figure 6. 15). This condition exhibited more variation in ISG expression between the two temperatures compared to the different stimuli. Most genes tended to be more strongly induced at 37 °C, with

only a few (*OASL, IFIT2*) showing greater induction at the lower temperature. This hints that endosomal or cytosolic sensing might be temperature-dependent.

Overall, these results show that ISG induction is largely maintained between 33 and 37 °C; however, the temperature sensitivity varies depending on the stimulus and specific pathways involved. The data illustrate that PRR-driven induction (Poly I: C or 5′pppdsRNA) is modulated by upper-airway temperature, resulting in higher peak ISG expression at 37 °C. Meanwhile, downstream IFNAR signalling remains essentially temperature independent. The high Pearson correlation coefficients in Figure 6. 15 (r = 0.90-0.95) suggest that both 33 °C and 37 °C conditions activate the same core IFN programme, although the amplification levels differ for PRR stimuli. This implies that airway temperature may fine-tune innate sensing pathways without fundamentally changing the ISG response profile.

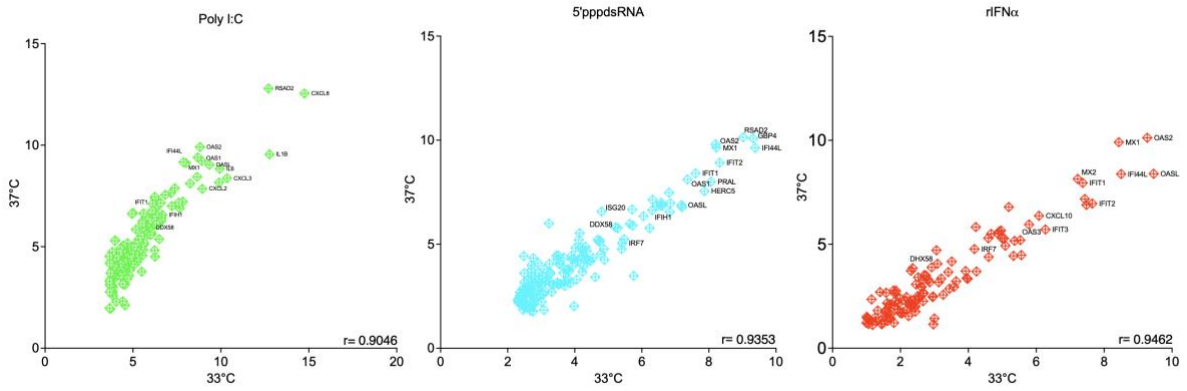

Figure 6.15: Pearson correlation of ISG expression at 33 °C and 37 °C following PRR stimulation and IFN treatment.

Scatter plots show log_2 fold-change values of ISGs measured by RNA-seq following stimulation with Poly I:C (left), 5′ppp-dsRNA (middle), or recombinant IFNα (right) at 33 °C versus 37 °C. Each point represents a single

ISG, with selected genes highlighted. Correlation coefficients (r) were calculated using Pearson correlation. ISG induction correlated strongly between the two temperatures across all conditions, with the highest correlation observed for IFNα treatment (r = 0.9462) and slightly lower correlation for Poly I:C stimulation (r = 0.9046).

6.2.13 HCoV-OC43 infection and innate sensing trigger cytokine responses with different temperature dependencies.

To understand how innate sensing, downstream signalling, and viral infection influence the secreted cytokine environment in a temperature-dependent way, I performed membrane-based cytokine profiling of culture supernatants from MRC-5 cells treated with rIFNα, infected with HCoV-OC43, or stimulated with either Poly I:C or 5′ppp-dsRNA. Each group of cultures was maintained at 33 °C or 37 °C for 48 h before the supernatants were collected. I then used the Human XL Cytokine Array Kit (detecting 109 analytes per membrane) to visualise relative pixel densities for various cytokines, chemokines, and growth factors. Below I report array pixel-density means (arbitrary units, AU; n = 2 per temperature).

To define the downstream outputs of type I IFN signalling, MRC-5 cells were treated with recombinant IFN-α (1000 IU/mL) and profiled by cytokine array at 33 °C and 37 °C (Figure 6.16A). The resulting secretome was the most extensive of all conditions tested, encompassing a wide range of chemokines, growth factors, and acute-phase proteins (n=2; semi-quantitative). Several analytes were produced at maximal levels at both temperatures with minimal temperature dependence: *CXCL8*, *CXCL10*, *CCL2*, and *Serpin E1* all approached the assay saturation limit (~249,000-252,000 AU), indicating that IFNAR engagement potently drives these canonical ISG-linked chemokines regardless of temperature. Similarly, *GDF-15*, *HGF*, and *Dkk-1* were uniformly high (≥220,000 AU) with only marginal differences between 33 °C and 37 °C.

Other analytes showed stronger temperature bias. At 37 °C, MIF (3.1-fold, 59,000-185,000 AU), CHI3L1 (5.8-fold, 33,000-193,000 AU), TSP-1 (4.9-fold, 40,000-195,000 AU), VEGF (5.1-fold, 31,000-158,000 AU), and VCAM-1 (3.9-fold, 41,000-159,000 AU) were all substantially elevated relative to 33 °C. Likewise, BDNF increased from ~42,000 to ~154,000 AU (3.6-fold), and angiogenin from ~94,000 to ~251,000 AU (2.7-fold). Conversely, CXCL1 and CXCL5 were reduced at 37 °C (CXCL1: 141,000 - 101,000 AU; CXCL5: 218,000 - 114,000 AU), suggesting selective attenuation of these NF-κB-linked chemokines at warmer conditions.

Overall, recombinant IFN-α induces a broad chemokine and growth factor-rich secretome in MRC-5 cells, with each analyte consistently exhibiting higher levels at core-body temperature. Nonetheless, the response profile at 33 °C and 37 °C was similar in nature: over 20 detectable analytes were secreted under both conditions, with the main difference being the magnitude of pixel density. This indicates that IFNAR signalling is fully operational at 33 °C but operates more robustly at 37 °C.

MRC-5 cells were infected with HCoV-OC43 (MOI 0.1). As shown in Figure 6.16B, across replicates, several chemokines were abundant at 33 °C and declined at 37 °C. The most pronounced change was *CXCL10*, which fell from ~98,278 AU at 33 °C to ~5,806 AU at 37 °C (0.06-fold). Neutrophil- and monocyte-recruiting chemokines also decreased: *CXCL1* by 0.05-fold (61,502 2,968 AU), *CXCL5* by 0.17-fold (67,152-11,689 AU), *IL-6* by 0.18-fold (15,158-2,741 AU), *CCL2/MCP-1* by 0.77-fold (79,596 - 61,291 AU), and *PTX3* by 0.50-fold (57,976-29,164 AU). *Dkk-1* showed a modest decrease (0.70-fold (88,659-62,429 AU). In contrast, HGF increased by 1.62-fold at 37 °C (68,552-111,006 AU), while *MIF* rose slightly by 1.05-fold (44,874-47,061 AU). Two analytes remained largely stable across

temperatures: *CXCL8* (1.0-fold; 118,606-116,534 AU) and SERPIN E1/PAI-1 (1.0-fold; 122,945-122,927 AU).

To preferentially activate the cytosolic RIG-I pathway, I stimulated cells with 5 µg of 5′ppp-dsRNA and incubated them at either 33 °C or 37 °C for 16 h. The cytokine-array membrane in Figure 6.16C shows a more focused secretome compared to rIFNα or HCoV-OC43 infection. At 37 °C, *CXCL10* was the most strongly induced analyte, averaging ~164,000 AU across replicates compared with ~73,000 AU at 33 °C, a 2.2-fold increase at the higher temperature. *CXCL8* was abundant at both temperatures (132,235 AU at 33 °C vs 132,095 AU at 37 °C), showing little temperature sensitivity. *Dkk-1* decreased modestly at 37 °C (117,264 AU vs 158,127 AU at 33 °C, ~0.74-fold), while *Serpin E1* remained stable (117,561 AU vs 119,157 AU, ~1.0-fold). By contrast, several mediators displayed marked temperature-dependent regulation: *Pentaxin-3* was nearly doubled at 37 °C (41,565 AU at 33 °C vs 78,085 AU), and *IL-6* was only detectable at 37 °C (~86,372 AU). Conversely, *Lipocalin-2* and *Thrombospondin-1* declined at 37 °C (3.5-fold and ~2.5-fold reductions, respectively).

In summary, these findings show that RIG-I stimulation initiates a targeted secretory program that is strongly shaped by temperature, with enhanced induction of *CXCL10* and *IL-6* at 37 °C but reduced abundance of stress-related factors such as *Lipocalin-2* and *Thrombospondin-1*.

In MRC-5 cells stimulated with 1 µg of Poly I:C for 16 h, key leukocyte-recruiting chemokines were readily detected at both 33 °C and 37 °C, and most showed ≤2-fold temperature effects (Figure 6.16D). *CXCL10* was essentially temperature-stable (37 °C/33 °C = 1.02; 168,066 - 165,114 AU), while *RANTES* rose modestly at 37 °C (1.19; 123,102 - 103,721 AU). Several analytes were slightly higher at 33 °C: *CXCL1* (0.63; 41,459 - 65,536 AU), *CXCL8* (0.89; 160,598 - 181,415 AU), *IL-6* (0.86; 122,111 - 142,154 AU), and *CCL2/MCP-1* (0.94; 93,589 - 100,073 AU). By contrast, the fibrinolysis regulator *SERPIN E1/PAI-1* increased at 37 °C (2.28;

52,963 - 23,205 AU), and *HGF* decreased (0.66; 21,091 - 32,185 AU). Overall, poly I:C elicited a mid-breadth, chemokine-rich secretome that was largely preserved at 33 °C, with only modest (~0.6-1.3×) temperature shifts and a notable 37 °C gain for *SERPIN E1*. This contrasts with the sharper temperature skew observed after RIG-I agonism, supporting the view that TLR3/MDA5 signalling remains functionally resilient across the physiological 33-37 °C range.

Across stimuli, the breadth and temperature sensitivity of the secretome vary, but a common pattern emerges. With rIFNα, downstream IFNAR signalling occurs at both temperatures and is stronger at 37 °C. With Poly I:C, several chemokines are maintained or favoured at 33 °C, while others increase at 37 °C, showing that TLR3/MDA5 signalling is relatively resilient to the 4 °C temperature shift. With 5′ppp-dsRNA, *RIG-I*-biased outputs, particularly *CXCL10*, attenuated at 33 °C, indicating RIG-I-MAVS is temperature-sensitive. In HCoV-OC43 infection, however, the main conclusion is that the cytokine profile is mainly driven by viral load rather than a simple, uniform indicator of host immune function.

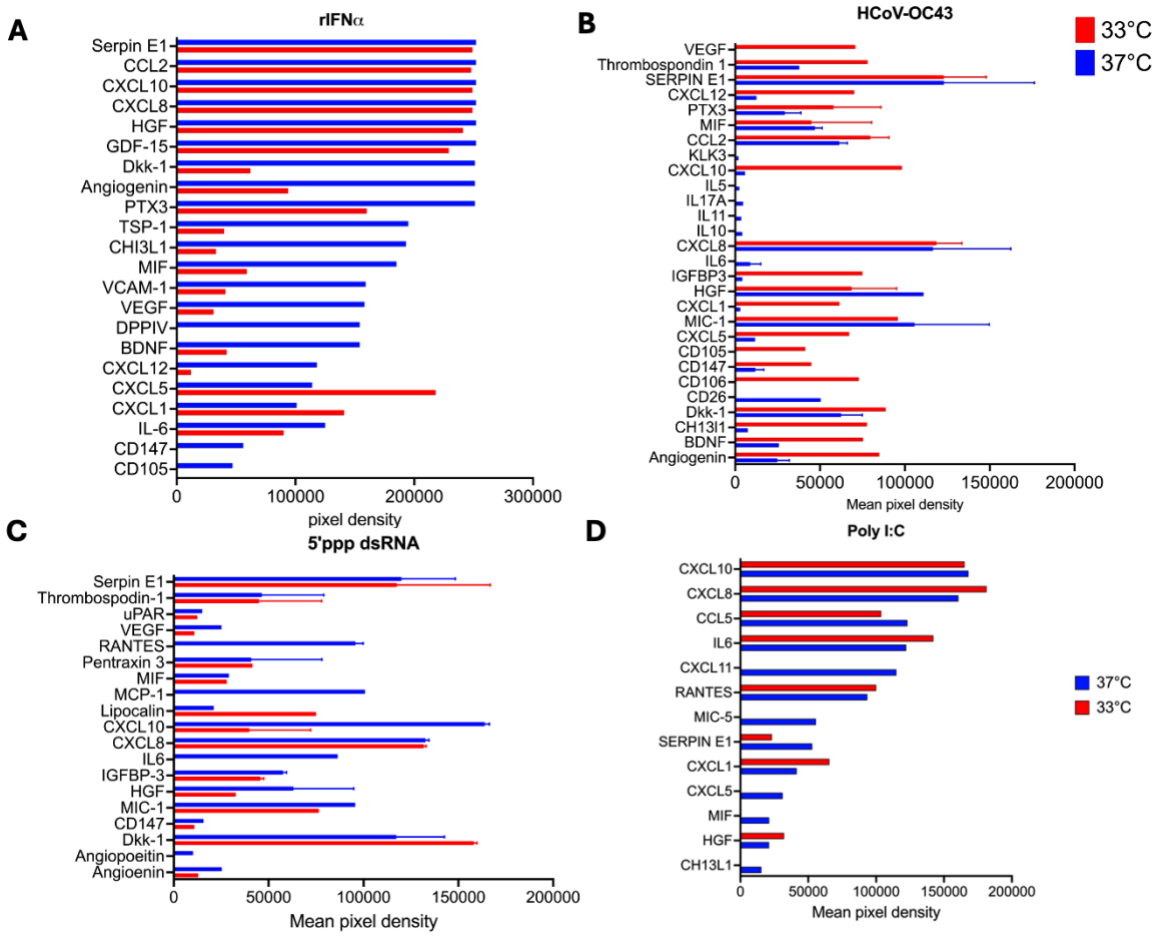

Figure 6.16: Temperature-dependent cytokine and growth-factor secretion profiles in MRC-5 cells upon IFN-α, HCoV-OC43 and PRR stimulation

MRC-5 cells were either treated with recombinant IFNα (1000 IU/mL, 24 h) (A), infected with HCoV-OC43 (MOI 0.1, 24 h) (B), or stimulated with the RIG-I agonist 5′ppp-dsRNA (5 µg/mL, 16 h) (C) or the TLR3/MDA5 agonist poly I:C (1 µg/mL, 16 h) (D). Culture supernatants were collected and analysed using the Human XL Cytokine Array Kit (R&D Systems), and mean pixel densities for key analytes were quantified. Across conditions, chemokines such as *CXCL10*, *CXCL8*, and *CCL2* dominated the secretome, accompanied by acute-phase proteins (e.g., Serpin E1, PTX3) and growth factors (e.g., HGF, MIC-1). In all cases, cytokine secretion was generally higher at 37 °C than at 33 °C, although the degree of temperature sensitivity varied between pathways. Recombinant IFNα induced the broadest secretome, while 5′ppp-dsRNA triggered a focused, strongly temperature-sensitive *RIG-I*-biased response dominated by *CXCL10*. Poly I:C stimulation produced a broader profile, resembling IFNα in scope but with smaller fold differences between 33 °C and 37 °C. HCoV-OC43 infection recapitulated many features of the IFNα-driven secretome, but with infection-specific additions such as MIC-1 and Dkk-1. These results show that airway temperature not only modulates host cytokine signalling

downstream of PRRs but also shapes infection-driven outputs through the combined influence of viral replication and immune pathway activation.

6.2.14 Temperature-dependent phosphokinase signatures in MRC-5 cells.

To complement RNA-seq and cytokine profiling, which capture transcriptional outputs and secreted factors, I next examined the upstream signalling events that drive these responses. Specifically, I profiled phosphoprotein activation using the Proteome Profiler Human Phospho-Kinase Array (39-plex). This approach allows us to link innate sensor engagement and IFNAR signalling with activation of intracellular kinase pathways, providing mechanistic insight into how temperature influences the initiation and propagation of antiviral signalling cascades. In all experiments, cells were incubated at either 33 or 37 °C for 16–24 h before lysate collection, matching the timing of transcriptional and cytokine assays. Below, I describe kinase activation patterns for HCoV-OC43 infection, Poly I:C, 5′ppp-dsRNA, and rIFNα, highlighting how upstream sensing translates into distinct profiles of signalling activity across temperatures.

To define how HCoV-OC43 engages intracellular signalling at airway-relevant temperatures, I infected MRC-5 cells at MOI 0.1 and harvested lysates at 24 hpi for phospho-kinase array analysis. This time point was chosen to capture active host signalling during early replication, before extensive CPE confounds measurements, and to align with the cytokine array window used in parallel. Across the panel, infection triggered a broad phosphorylation programme whose magnitude was generally higher at 37 °C than 33 °C, indicating a temperature-sensitive strengthening of antiviral and stress-responsive pathways at core body temperature.

Within the MAPK module, ERK1/2 (T202/Y204) increased from ~123,000 (33 °C) to ~134,000 (37 °C), a 1.09-fold change, while JNK1/2/3 (T183/Y185) rose from ~21,600 to ~22,900 (1.06-fold). p38α (T180/Y182) showed a more pronounced temperature effect, climbing from ~15,500 to ~25,100 (1.60-fold). These data point to more vigorous stress-activated MAPK

signalling at 37 °C, consistent with the larger chemokine outputs measured in supernatants at that temperature.

Type-I-IFN-linked signalling was also amplified at 37 °C. STAT3 (S727) increased from ~70,000 to ~92,000 (1.31-fold), and STAT2 (Y690), a direct read-out of IFNAR activity, rose from ~15,700 to ~19,700 (1.25-fold). In parallel, the PI3K-Akt axis was clearly temperature sensitive: Akt1/2/3 (T308) increased from ~4.90×10^4 to ~8.31×10^4 (1.70-fold), Akt1/2/3 (S473) from ~18,500 to ~22,000 (1.18-fold), and the downstream effector PRAS40 (T246) from ~ 49,600 to ~76,700 (1.55-fold). Together, these coordinated gains support stronger survival/transcriptional co-activation at 37 °C and align with the higher secretome magnitude observed in the cytokine arrays.

A smaller set of phospho-events showed the opposite trend, cool-biased at 33 °C. GSK-3α/β (S21/S9) decreased from ~159,000 to ~148,000 (0.94-fold) at 37 °C, GSK-3β (S9) from ~123,000 to ~118,000 (0.97-fold), β-catenin from ~111000 to ~84,400 (0.77-fold), Src (Y419) from ~31,000 to ~19,500 (0.63-fold), and Fgr (Y412) from ~158,000 to ~118,000 (0.75-fold). These differences suggest temperature-specific wiring in cytoskeletal/stress-kinase and Wnt/GSK-3 feedback control when cells are maintained at cooler airway conditions.

Other nodes showed either modest enhancement at 37 °C or little change. HSP60 increased by 1.46-fold and c-Jun (S63) nearly doubled (1.98-fold), consistent with a stronger transcriptional stress response at 37 °C. WNK1 (T60) was essentially temperature-neutral (0.99-fold). eNOS (S1177), CREB (S133), and PDGFR-β (Y751) trended lower at 37 °C (approximately 0.64-, 0.77-, and 0.87-fold, respectively), and checkpoint-associated sites (Chk2 T68; p53 S15/S46) varied by ≤~1.2-fold, arguing against wholesale checkpoint activation at this stage.

In aggregate, HCoV-OC43 elicits a temperature-amplified phosphorylation landscape in MRC-5 cells: MAPKs, especially p38, together with STAT2/3 and PI3K-Akt-PRAS40 show ~1.2-1.7-fold higher phosphorylation at 37 °C, while a limited set of Wnt/GSK-3 and Src-family nodes are relatively stronger at 33 °C. These signalling differences dovetail with the cytokine and ISG data, supporting a model in which core temperature permits a more vigorous kinase and secretory response, whereas cooler conditions dampen antiviral kinase activation even as they favour HCoV-OC43 replication.

In MRC-5 cells exposed to 1 μg/mL Poly I:C for 24 h (Figure 6.12B), TLR3/MDA5 engagement led to robust phosphorylation of MAPK family members and stress-response kinases. ERK1/2 (T202/Y204) appeared as the single strongest band at 37 °C (∼180 000 units) compared to ∼150 000 at 33 °C. GSK-3α/β (S21/S9) followed suit, with ∼160 000 units at 37 °C versus ∼140 000 at 33 °C. Akt1/2/3 (T308 and S473) showed moderate but consistent activation (∼70 000 at 37 °C vs. ∼50 000 at 33 °C). PRAS40 (T246) downstream of Akt/mTORC1 was also phosphorylated more at 37 °C (∼100 000 vs. ∼70 000). Remarkably, HSP27 (S78/S82), a known chaperone phosphorylated under stress, was high in both temperatures (∼120 000 at 37 °C, ∼80 000 at 33 °C). *PLCγ1* (Y783) and *WNK1* (T60) were elevated (∼130 000 vs. ∼110 000 and ∼140 000 vs. ∼120 000, respectively), indicating engagement of calcium signalling and osmoregulation. β-Catenin (S552), which links to Wnt and cell-survival pathways, was also more phosphorylated at 37 °C (∼100 000 vs. ∼90 000). In contrast to HCoV-OC43, Poly I:C produced only modest *STAT2* (Y690) activation (∼20 000 at 37 °C vs. ∼10 000 at 33 °C) and minimal *STAT3* (Y705, S727) signals (< 20 000 units in both). This suggests that, although Poly I:C can drive some autocrine IFN production, the dominant signalling cascades are MAPKs and stress kinases. The stronger phosphorylation at 37 °C echoes my observation that Poly I: C-induced cytokine secretion was only mildly

temperature-dependent (1.2-1.5×), indicating that TLR3/MDA5 signalling remains broadly functional at cooler temperatures but is slightly more active at 37 °C.

When MRC-5 cells were stimulated with 5 μg of 5′ppp-dsRNA (Figure 6.12C), RIG-I-mediated sensing a narrow set of kinases, exhibiting pronounced temperature sensitivity. At 37 °C, ERK1/2 phosphorylation was detectable ~60,000 AU at 37 °C but ~15,000 AU at 33 °C, a 4.0-fold increase at 37 °C. HSP27 (S78/S82) rose from ~60,000 AU at 33 °C to ~80,000 AU at 37 °C (1.33-fold), consistent with a general stress response. GSK-3α/β (S21/S9) rose modestly at 37 °C (~20,000 vs. ~10,000 at 33 °C; 2.0-fold), whereas STAT3 (Y705) was only phosphorylated at 37 °C (~12,000); at 33 °C it was essentially zero. No phosphorylation of *STAT2* or *STAT5* was detected, suggesting minimal IFNAR feedback within this 16 h window. Akt and PRAS40 phosphorylation were similarly negligible (< 10,000 units), indicating that PI3K-Akt signalling is not a major early downstream branch of RIG-I in these cells. Overall, the RIG-I agonist engaged HSP27 and ERK1/2 likely through an IRF3/7 → TNF/chemokine axis but these signals were greatly diminished at 33 °C. This agrees with my cytokine data: CXCL10 and CXCL8 secretion were attenuated at 33 °C yet dramatically upregulated at 37 °C, illustrating the tight coupling between RIG-I's kinase-dependent signalling and the extreme temperature sensitivity of the resulting secretome.

In MRC-5 cells treated with 1000 IU/mL rIFN-α (Figure 6.17D), the phospho-array generated a focused signature of JAK/STAT activation, with minimal engagement of MAPK or stress kinases. *STAT1* (Y701) was phosphorylated at ~15 000 units at 37 °C (vs. ~8 000 at 33 °C), *STAT2* (Y690) at ~10 000 vs. ~5 000, and *STAT3* (S727) at ~8 000 vs. ~4 000. *STAT5a/b* (Y694/Y699) saw mild activation (~5 000 vs. ~3 000), whereas STAT6 (Y641) was only modestly phosphorylated at 37 °C (~5 000) and virtually absent at 33 °C. HSP60 (a chaperone associated with IFN signalling) was the only non-STAT protein to show substantial signal

(∼150,000 at 37 °C vs. ∼15,000 at 33 °C), suggesting that prolonged IFNAR engagement up-regulates mitochondrial stress pathways. Interestingly, ERK1/2, AKT, GSK-3, and other MAPKs were at baseline, confirming that exogenous rIFN-α primarily activates JAK/STAT with little crosstalk to MAPK under these conditions. Although STAT phosphorylation was higher at 37 °C, the relative difference was only ∼1.5-2×, much less dramatic than seen with PRR agonists, reinforcing that downstream IFNAR signalling is robust across both temperatures.

Across all four conditions, a consistent hierarchy emerges in both the breadth of kinase activation and the degree of temperature-dependent modulation. HCoV-OC43 infection engaged the broadest set of phospho-kinases, spanning MAPKs (*ERK, JNK, p38*), PI3K/Akt, and JAK/STAT, with peak signals all higher at 37 °C. Poly I:C converged on MAPK and stress kinases (*ERK1/2, GSK-3α/β, HSP27, WNK1, PLCγ1*), again showing greater activation at 37 °C, but with minimal STAT engagement. 5′ppp-dsRNA primarily activated HSP27 and ERK1/2, with near-complete loss of those signals at 33 °C mirroring the almost "all-or-nothing" pattern of IP-10 protein secretion under RIG-I control. rIFN-α, by contrast, restricted its phospho-signal to STAT family members and HSP60, exhibiting only modest temperature shifts (∼1.5×) and no detectable MAPK activation.

These signalling landscapes align closely with the cytokine secretion profiles: HCoV-OC43 and rIFN-α produced a broad chemokine and growth factor-dominated secretome that depended less strictly on temperature; Poly I:C yielded a mid-spectrum chemokine output with modest temperature differences; and 5′ppp-dsRNA induced a narrow, IP-10/IL-8-centric secretome that reduced at 33 °C. In particular, the very high phosphorylation of *ERK1/2, JNK, p38*, and *STAT2* in HCoV-OC43-infected cells at 37 °C matches the broad secreted signature (*CXCL8, CCL2*, *Serpin E1, CXCL10, Dkk-1, CD147*, etc.). Poly I:C's strong phosphorylation of *GSK-3α/β,*

HSP27, and *WNK1* at 37 °C correlates with its ability to secrete *IL-8*, *CXCL10, CCL5, IL-6*, and other inflammatory mediators under both temperatures. For RIG-I, the sharp loss of ERK1/2 and STAT3 phosphorylation at 33 °C corresponds directly to the abrogation of *IP-10* and *IL-8* secretion in that same condition. Finally, the strictly JAK/STAT-driven phospho-pattern of rIFNα, with only small temperature differences, explains why MRC-5 cells secreted *CXCL8, CCL2, CXCL10, HGF*, Serpin E1, and other factors at both 33 °C and 37 °C, with only modest amplification at 37 °C.

Taken together, the phospho-kinase arrays confirm that upstream PRR-sensing pathways (*RIG-I* and *TLR3/MDA5*) and active viral infection engage broad kinase networks, especially MAPKs and PI3K/Akt, which are highly temperature-sensitive. In contrast, direct IFNAR signalling is more narrowly focused on JAK/STAT and only mildly modulated by temperature. Together with the transcriptional and cytokine-secretion data, these phospho-kinase results paint a comprehensive picture: upstream detection of viral PAMPs and active viral replication rely on MAPK-driven signalling that is finely tuned by local temperature, whereas downstream IFNAR signalling and its JAK/STAT effectors remain comparatively robust across the physiologic 33 °C-37 °C range. This dual-axis modulation likely underlies why certain coronaviruses and RIG-I-sensed viruses preferentially infect cooler nasal epithelia, while IFN-based therapies retain their activity throughout the respiratory tract.

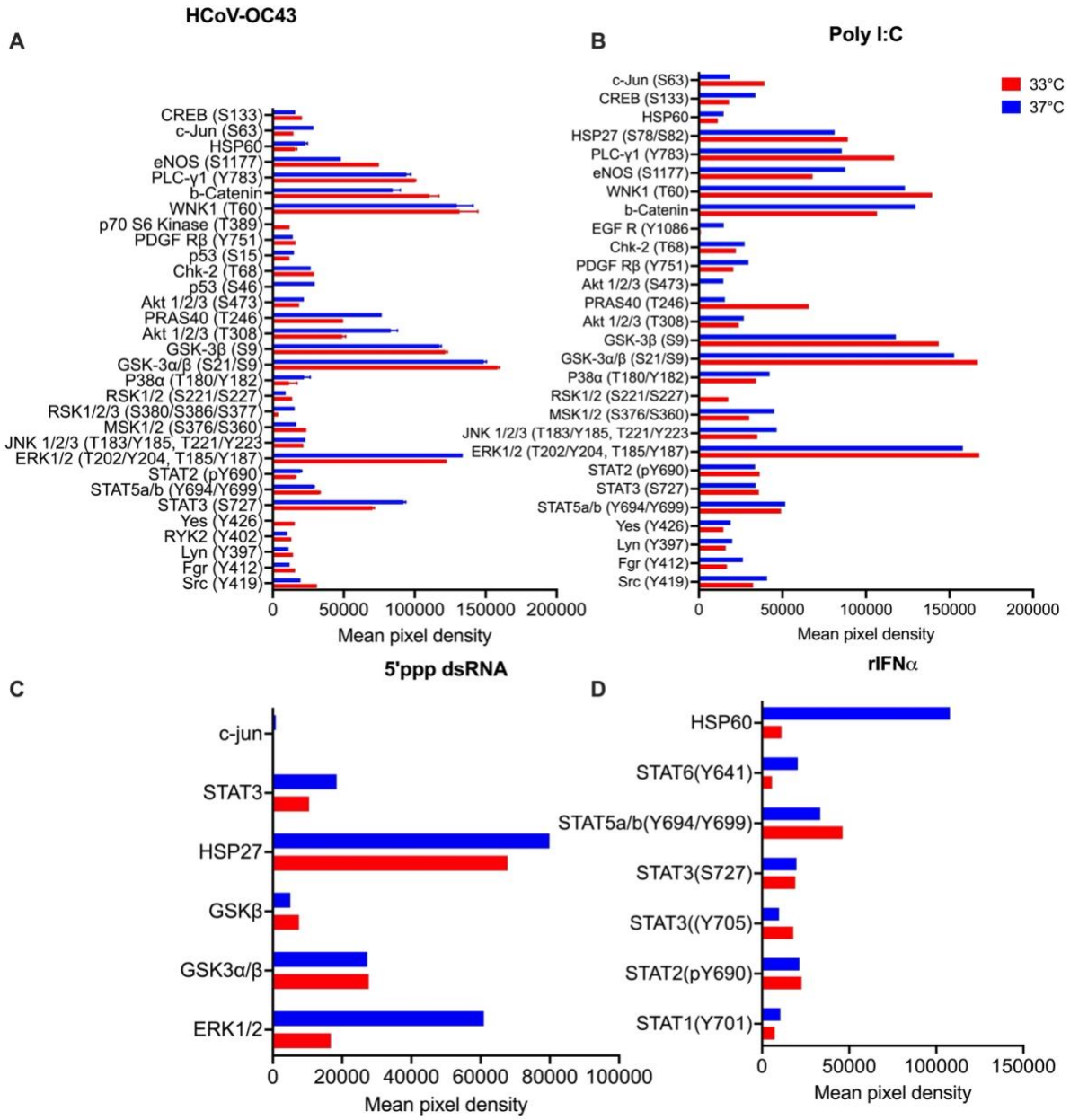

Figure 6.17: Temperature-dependent phosphokinase profiling reveals distinct signalling landscape for HCoV-OC43 infection, PRR agonists and IFN

(A-D) MRC-5 cells were incubated at either 33 °C or 37 °C for 16–24 h and then stimulated with **(A)** HCoV-OC43 (MOI 0.1), **(B)** Poly I:C (1 µg/ml), **(C)** 5′ppp-dsRNA (5 µg), or **(D)** recombinant IFN-α (1000 IU/mL). Cell lysates were applied to a 39-plex phospho-kinase array, and spot intensities were measured as mean pixel density. HCoV-OC43 infection **(A)** caused broad activation of MAPKs (ERK1/2, JNK1/2/3, p38α), PI3K-Akt (Akt T308/S473, PRAS40), GSK-3α/β, and STAT1/2/3, all of which were heightened at 37 °C. Poly I:C **(B)** mainly engaged MAPKs (ERK1/2, p38α, GSK-3α/β) and stress kinases (HSP27), with minimal phosphorylation of STAT2/3. RIG-I agonist 5′ppp-dsRNA **(C)** triggered a narrow response in HSP27 and ERK1/2 that was almost absent at 33 °C.

Direct IFN-α stimulation **(D)** produced a focused JAK/STAT signature (STAT1 Y701, STAT2 Y690, STAT3 Y705/S727, STAT5a/b Y694/Y699, STAT6 Y641) and HSP60, with only modest 1.5-2× increases in phosphorylation at 37 °C.

6.2.15 Functional validation of temperature-sensitive innate pathways using CRISPR knockout cell lines.

Having established temperature effects at the level of transcription, secreted proteins and phosphorylation, my data indicate selective rather than uniform temperature sensitivity across pathways. I next sought to determine whether these innate sensors directly restrict HCoV-OC43 replication at different temperatures. To address this, I compared multi-step growth kinetics of HCoV-OC43 in wild-type (WT) A549 cells and CRISPR/Cas9 knockout derivatives lacking RIG-I, MDA5, or MAVS. Viral replication was quantified by both $TCID_{50}$ assay and qPCR of supernatant RNA over 72 h at 33 °C and 37 °C (Figure 6.13). These A549 knockout lines have been independently validated and used in previous studies to investigate antiviral signalling pathways, providing additional confidence in their suitability for dissecting temperature-dependent restriction of HCoV-OC43 (Teague *et al.*, 2024).

Before adopting the A549 cell line, I attempted to generate knockouts in-house using a CRISPR/Cas9 approach. Guide RNAs targeting *RIG-I, MAVS, IFNAR1, IRF3, TBK1*, and DDX58 were designed and cloned, and transfection efficiency was confirmed in HEK293T cells (Appendix Figure A3). However, attempts in MRC-5 cells were inconclusive: while transient transfections were successful, they did not yield stable knockout colonies, and viral replication assays were inconsistent. This led us to employ pre-validated A549 knockouts (a kind gift from Brian J. Ferguson at the University of Cambridge) to ensure reproducibility. I assessed the functional responsiveness of the knockout lines by stimulating them with IFN-α and measuring ISG induction by qPCR. In WT A549 cells, IFN-α stimulation triggered a robust

upregulation of ISGs, ranging from ~40- to 60-fold relative to mock. By contrast, IFNAR-/- cells showed no measurable induction, confirming the essential role of IFNAR in mediating type I IFN signalling. Both RIG-I-/- and MAVS-/- lines exhibited markedly reduced ISG induction compared with WT, consistent with impaired upstream sensing and signalling (Appendix Figure A6). These results confirm that the engineered knockout cell lines are deficient in the expected pathways and are suitable for dissecting the contribution of individual PRR signalling components to temperature-dependent restriction of HCoV-OC43.

6.2.15.1 RIG-I knockout relieves restriction at 37 °C.

In WT A549 cells, viral titres increased steadily at both temperatures, with replication consistently higher at 33 °C relative to 37 °C. By 72 h, titres at 33 °C reached ~10^7 $TCID_{50}$/ml compared to ~10^6 $TCID_{50}$/ml at 37 °C. Viral RNA copies mirrored this pattern, peaking at ~10^{11} copies/ml at 33 °C versus ~10^{10} at 37 °C (Figure 6.13A-B). In contrast, RIG-I-/- cells displayed elevated titres at 37 °C, effectively abolishing the attenuation seen in WT cells. By 72 h, RIG-I-/- cells at 37 °C produced titres (~10^7 $TCID_{50}$/ml) comparable to WT at 33 °C, while replication at 33 °C was not further enhanced. This indicates that intact RIG-I signalling is required to maintain the restriction observed at 37 °C, consistent with my observation that RIG-I-driven cytokine responses are dampened at cooler temperatures.

6.2.15.2 MDA5 knockout enhances replication across both temperatures.

MDA5-/- A549 cells also exhibited altered replication kinetics (Figure 6.13C-D). At 37 °C, titres rose significantly above WT, reaching ~10^7 $TCID_{50}$/mL by 72 h compared with ~10^6 in WT. At 33 °C, MDA5-/- cells supported even higher viral RNA levels than WT, with genomes exceeding 10^{10} copies/mL by 72 h. Thus, unlike RIG-I, which primarily enforces restriction at

37 °C, MDA5 contributes to viral control at both temperatures, and its loss amplifies the preferential replication at 33 °C that is already evident in WT cells.

6.2.15.3 MAVS knockout abolishes temperature-dependent restriction.

Since RIG-I and MDA5 both signal through the adaptor MAVS, I next tested whether MAVS deletion phenocopied the loss of these sensors. MAVS-/- A549 cells supported rapid HCoV-OC43 replication irrespective of temperature (Figure 6.13E-F). At 72 h, titres at both 33 °C and 37 °C converged at ~10^7 $TCID_{50}$/mL, in sharp contrast to WT cells, where replication was consistently lower at 37 °C. Viral RNA levels followed the same trend: MAVS-/- cells reached ~10^{11} copies/mL at both temperatures, eliminating the preferential replication at 33 °C seen in WT. These results confirm that MAVS is the critical signalling hub linking RIG-I and MDA5 to temperature-dependent restriction.

Together, these findings demonstrate that the attenuation of HCoV-OC43 replication at 37 °C in WT A549 cells is mediated by the RIG-I-MDA5-MAVS axis. RIG-I predominantly contributes to restriction at 37 °C, MDA5 constrains replication across both temperatures, and MAVS integrates both sensors to generate the complete temperature-sensitive antiviral barrier. These data align with my upstream cytokine and phosphokinase assays, which showed reduced RIG-I-driven responses at 33 °C, and provide direct evidence that PRR signalling is responsible for enforcing the differential replication phenotype observed in WT cells.

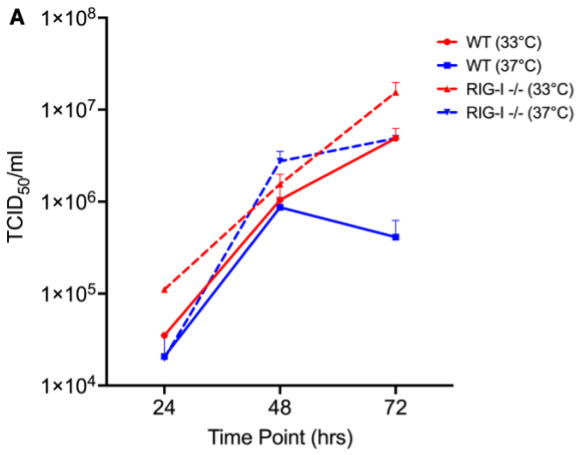

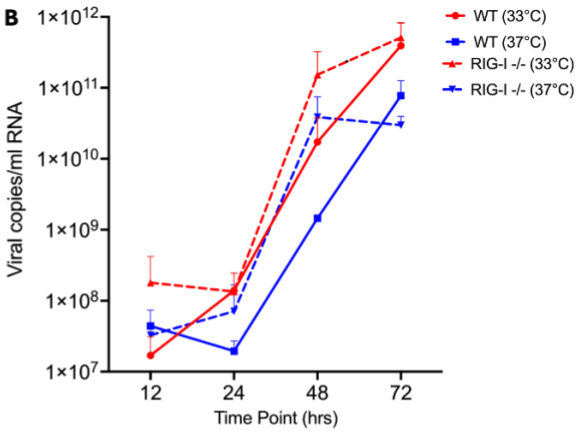

Comparison	24	48	72
WT (33°C) vs. WT (37°C)	ns	ns	ns
WT (33°C) vs. RIG-I -/- (33°C)	ns	ns	**
WT (33°C) vs. RIG-I -/- (37°C)	ns	ns	ns
WT (37°C) vs. RIG-I -/- (33°C)	ns	ns	****
WT (37°C) vs. RIG-I -/- (37°C)	ns	ns	ns
RIG-I -/- (33°C) vs. RIG-I -/- (37°C)	ns	ns	**

Comparison	24	48	72
WT (33°C) vs. WT (37°C)	ns	ns	ns
WT (33°C) vs. RIG-I -/- (33°C)	ns	ns	ns
WT (33°C) vs. RIG-I -/- (37°C)	ns	ns	ns
WT (37°C) vs. RIG-I -/- (33°C)	ns	ns	*
WT (37°C) vs. RIG-I -/- (37°C)	ns	ns	ns
RIG-I -/- (33°C) vs. RIG-I -/- (37°C)	ns	ns	*

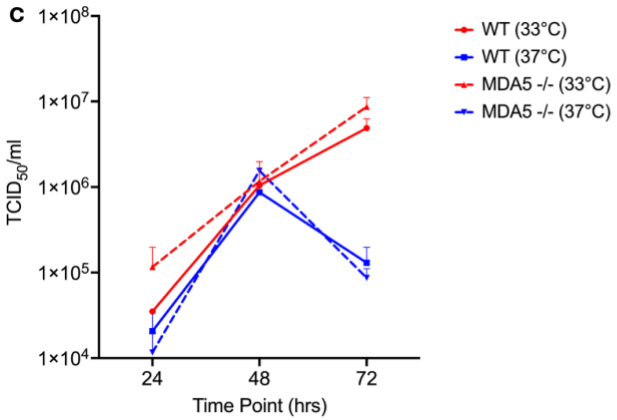

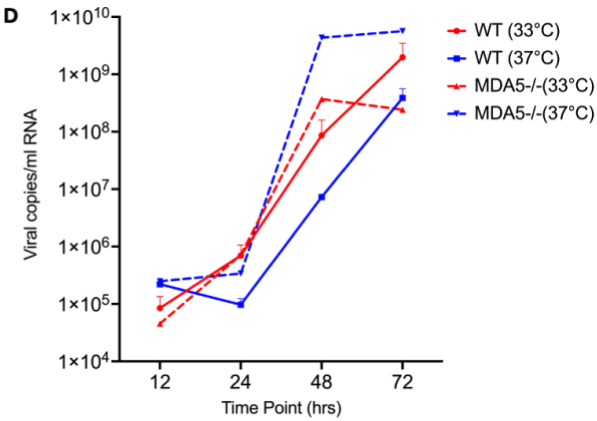

Comparison	24	48	72
WT (33°C) vs. WT (37°C)	ns	ns	*
WT (33°C) vs. MDA5 -/- (33°C)	ns	ns	*
WT (33°C) vs. MDA5-/- (37°C)	ns	ns	*
WT (37°C) vs. MDA5-/- (33°C)	ns	ns	***
WT (37°C) vs. MDA5-/- (37°C)	ns	ns	ns
MDA5 -/- (33°C) vs. MDA5 -/- (37°C)	ns	ns	****

Comparison	24	48	72
WT (33°C) vs. WT (37°C)	ns	ns	ns
WT (33°C) vs. MDA5 -/- (33°C)	ns	ns	ns
WT (33°C) vs. MDA5-/- (37°C)	ns	**	*
WT (37°C) vs. MDA5-/- (33°C)	ns	ns	ns
WT (37°C) vs. MDA5-/- (37°C)	ns	**	**
MDA5 -/- (33°C) vs. MDA5 -/- (37°C)	ns	*	**

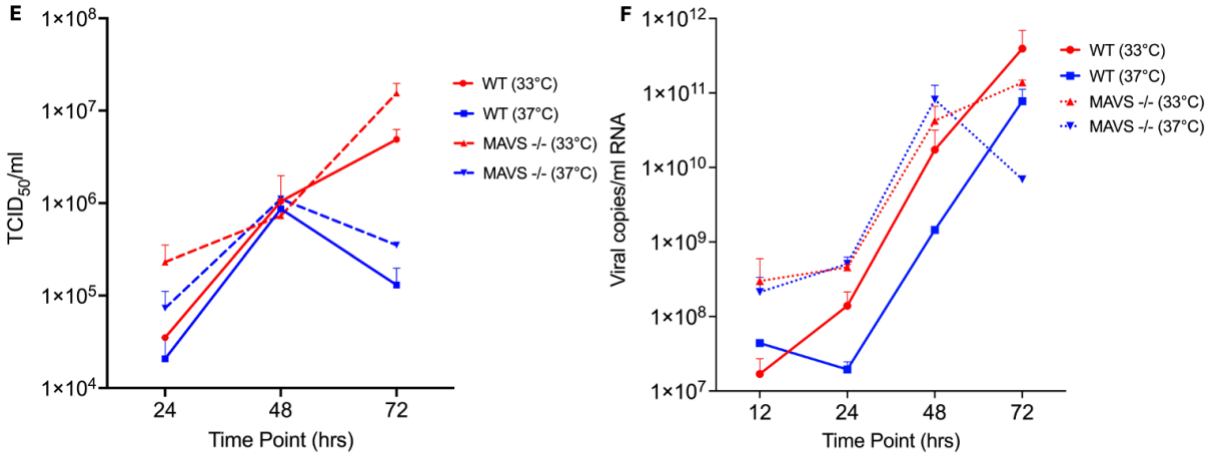

Comparison	24	48	72
WT (33°C) vs. WT (37°C)	ns	ns	ns
WT (33°C) vs. MAVS -/- (33°C)	ns	ns	***
WT (33°C) vs. MAVS-/- (37°C)	ns	ns	ns
WT (37°C) vs. MAVS-/- (33°C)	ns	ns	****
WT (37°C) vs. MAVS-/- (37°C)	ns	ns	ns
MAVS -/- (33°C) vs. MAVS -/- (37°C)	ns	ns	****

Comparison	24	48	72
WT (33°C) vs. WT (37°C)	ns	ns	*
WT (33°C) vs. MAVS -/- (33°C)	ns	ns	ns
WT (33°C) vs. MAVS-/- (37°C)	ns	ns	*
WT (37°C) vs. MAVS-/- (33°C)	ns	ns	ns
WT (37°C) vs. MAVS-/- (37°C)	ns	ns	ns
MAVS -/- (33°C) vs. MAVS -/- (37°C)	ns	ns	ns

Figure 6.18: RIG-I, MDA5, and MAVS contribute to temperature-dependent restriction of HCoV-OC43 in A549 cells.

A549 wild-type (WT) cells or CRISPR/Cas9 knockout derivatives lacking RIG-I **(A-B),** MDA5 **(C-D),** or MAVS (E-F) were infected with HCoV-OC43 at MOI 0.1 and incubated at either 33 °C or 37 °C. Viral replication was quantified over 72 h by **(A, C, E)** $TCID_{50}$ assay and **(B, D, F)** qRT-PCR of viral RNA in culture supernatants. In WT cells, HCoV-OC43 replicated more efficiently at 33 °C than at 37 °C. In contrast, RIG-I-/-, MDA5-/-, and MAVS-/- cells showed elevated replication at 37 °C relative to WT, with MAVS deletion abolishing the temperature-dependent restriction entirely. Data represent mean ± SEM from three biological replicates. Statistical comparisons were conducted by two-way ANOVA with Tukey's post hoc test; *$p < 0.05$, **$p < 0.01$, ***$p < 0.001$, ****$p < 0.0001$, ns = not significant.

6.2.16 Loss of type I IFN signalling removes early restriction at 37 °C but does not abolish enhanced replication at 33 °C

To directly test the contribution of downstream IFN signalling to the temperature-dependent replication phenotype, I compared HCoV-OC43 growth kinetics in A549 WT cells and IFNAR-

/- cells. All cell lines were infected at an MOI of 0.1 and incubated at either 33 or 37 °C, with viral RNA in supernatants quantified by qPCR at 12, 24, 48, and 72 hpi (Figure 6.14).

In WT cells, replication initially lagged at 37 °C compared with 33 °C. At 12-24 hpi, viral RNA levels at 37 °C were more than tenfold lower (~1×10^5–1×10^6 copies/mL) than those at 33 °C (~1×10^6–1×10^7 copies/mL). By 48 hpi, titres at both temperatures increased substantially, with WT 33 °C cultures reaching ~1×10^8 copies/mL compared to ~1×10^7 at 37 °C. By 72 hpi, replication remained higher at 33 °C (~5×10^9 copies/mL) relative to 37 °C (~8×10^8 copies/mL), confirming a sustained temperature-dependent difference.

In contrast, IFNAR-/- cells showed no early restriction at 37 °C: viral loads at 12-24 hpi were already elevated (~1×10^6-1×10^7 copies/mL) and indistinguishable from those at 33 °C. By 48 hpi, both conditions yielded similar titres (~1×10^8 copies/mL), indicating that the absence of IFNAR abolishes the initial temperature gap observed in WT cells. However, by 72 hpi, replication at 33 °C again exceeded that at 37 °C, reaching ~5×10^9 copies/mL compared to ~1×10^9 copies/mL at 37 °C. Importantly, statistical analysis showed no significant differences between WT and IFNAR-/- cells at any time point, indicating that loss of IFNAR did not further enhance replication or abolish the temperature-dependent growth pattern. These findings suggest that although IFNAR signalling contributes to host antiviral defence, it is not the sole determinant of the reduced replication observed at 37 °C. Instead, the persistent temperature effect points to additional IFN-independent mechanisms shaping HCoV-OC43 replication dynamics.

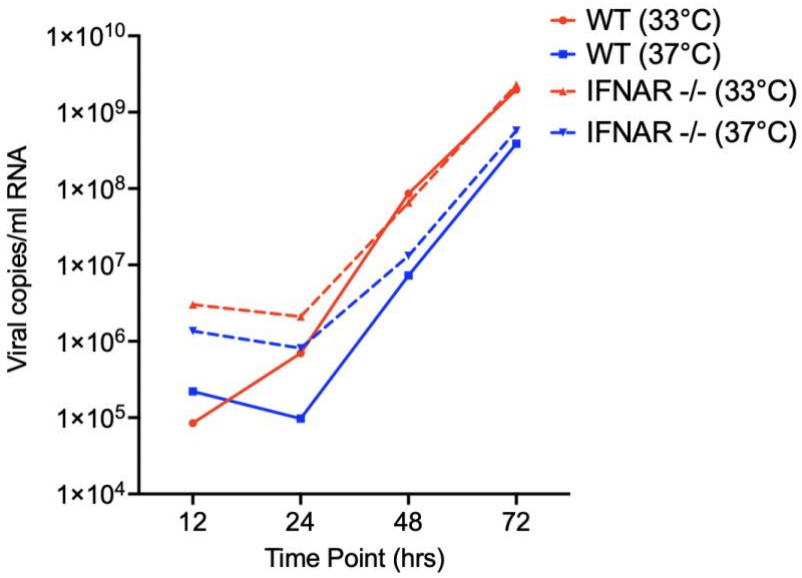

Figure 6.19: Growth kinetics of HCoV-OC43 in WT and IFNAR-/- A549 cells at 33 °C and 37 °C.

WT and IFNAR-/- A549 cells were infected with HCoV-OC43 (MOI 0.1) and cultured at either 33 °C or 37 °C. Viral RNA in supernatants was quantified at 12, 24, 48, and 72 hpi by qPCR. Replication was consistently higher at 33 °C than at 37 °C in both genotypes. Statistical analysis by two-way ANOVA with Tukey's post hoc test revealed no significant differences between WT and IFNAR-/- cells at any time point. Data represent mean ± SEM from biological replicates.

6.3 Discussion

In this study, I tested the hypothesis that the restriction of HCoV-OC43 to the upper respiratory tract is driven by temperature-dependent regulation of type I IFN signalling. Specifically, I proposed that at cooler URT temperatures (33 °C), initiation and amplification of IFN signalling

are attenuated, allowing more efficient viral replication, whereas at core body temperature (37 °C), stronger IFN activation and antiviral gene expression suppress HCoV-OC43 replication and restrict progression to the lower respiratory tract. The findings support the hypothesis and show that HCoV-OC43 replication and innate immunity differ between 33 and 37 °C.

6.3.1 Temperature as a determinant of coronavirus replication and tropism

I tested multiple infection models and found that HCoV-OC43 replicated more efficiently at 33 °C than at 37 °C. This temperature-dependent advantage was observed not only in MRC-5 fibroblasts but also in epithelial-derived A549 and HEK293T cells, as well as in the highly permissive non-human Mv1Lu line. In each case, virus titres rose more rapidly and reached higher peaks at 33 °C. Importantly, the temperature-dependent replication advantage was evident at both low and high multiplicity of infection, which models natural spread and isolates early replication events, respectively. Even at high MOI, viral RNA levels were numerically higher at 33 °C during the first 4 h, suggesting that intrinsic viral processes such as RNA synthesis, uncoating, or polymerase activity may be more efficient at cooler temperatures.

These findings align with studies showing enhanced rhinovirus and influenza replication at 33 °C compared with 37 °C, consistent with URT conditions (Foxman *et al.*, 2015; Mihaylova *et al.*, 2018). SARS-CoV-2 replicates efficiently in differentiated nasal epithelium at 33 °C, whereas SARS-CoV exhibits less sensitivity to this gradient (V'Kovski *et al.*, 2021). My results extend this observation to HCoV-OC43, a coronavirus that has circulated endemically for decades, highlighting that temperature-dependent replication is a general feature shaping coronavirus tropism. This connection is important because it links seasonal coronaviruses with newly emerged pandemic strains: cooler URT temperatures favour viral replication, while warmer LRT temperatures impose stronger host restriction

6.3.2 Intrinsic viral replication advantages at 33 °C

The consistent replication advantage at 33 °C implies that intrinsic steps in the HCoV-OC43 life cycle are optimised for the URT. Coronaviruses replicate in double-membrane vesicles; membrane fluidity, enzymatic rates of the replication-transcription complex, and nucleocapsid dynamics could all be temperature-sensitive (Hartenian *et al.*, 2020). The HCoV-OC43 RNA-dependent RNA polymerase may operate more efficiently at 33 °C, yielding faster genome accumulation. Viral accessory proteins that antagonise innate immunity could also be more stable or active at cooler temperature. Influenza NS1 provides a precedent for temperature-tuned antagonism of host sensing (Foxman *et al.*, 2015). While the work in this chapter focuses on host pathways, the early divergence in high MOI kinetics suggests that viral processes contribute materially to the phenotype.

6.3.3 IFN-α sensitivity and ISG dynamics at different temperatures

Pretreatment with recombinant IFN-α markedly suppressed HCoV-OC43 replication at both 33 and 37 °C, confirming that the virus remains sensitive to IFN-stimulated gene expression. Nonetheless, replication remained higher at 33 than at 37 °C under IFN-α, indicating reduced effectiveness of IFN at the cooler temperature. IFN-α strongly upregulated canonical antiviral genes, including *IFIT1*, *IFIT2*, *ISG20*, *OASL* and *CXCL11*, and these responses tended to be stronger at 37 °C. By contrast, infection alone produced modest ISG induction, consistent with coronavirus strategies that dampen host IFN sensing, induction and signalling (Kindler and Thiel, 2016; Kindler *et al.*, 2016; Banerjee *et al.*, 2019). When cells were pretreated with IFN-α and then infected, ISG expression was reduced compared with IFN-α alone, supporting active antagonism by HCoV-OC43 that is more effective at 33 °C.

My data highlight that temperature does not just affect the virus. It fundamentally alters the effectiveness of the host antiviral response. At 33 °C, IFN pretreatment still suppresses HCoV-OC43, but ISG induction is weaker and more easily countered by viral antagonists. At 37 °C, ISG expression is stronger, cytokine secretion is more robust, and phosphorylation of downstream effectors is amplified. The outcome of infection is therefore set by a shifting balance between viral fitness and host restriction that is tuned by physiological temperature gradients along the airway. This dual mechanism resembles what has been described for arboviruses, where (Lane *et al.*, 2018) showed that IFN efficacy declines at lower temperatures.

6.3.4 Cytokine and chemokine secretion profiles

Cytokine arrays offered a protein-level view of these pathways. Recombinant IFN-α induced secretion of *CXCL8*, *CCL2,* and *CXCL10* alongside growth factors such as HGF and VEGF. HCoV-OC43 infection elicited a broadly similar secretome with additional infection-associated mediators, and nearly all analytes were higher at 37 °C. Poly I:C produced a mid-range chemokine profile that was modestly stronger at 37 °C. In contrast, 5′ppp-dsRNA generated a focused signature dominated by *CXCL10* and *IL-8* that was reduced at 33 °C but was robust at 37 °C. The reduced chemokine release at 33 °C likely reflects temperature-sensitive steps in RIG-I/MAVS signalling and downstream phosphorylation events, together with slower cellular metabolism and vesicle trafficking in fibroblasts. These factors may dampen cytokine output at cooler URT-like temperatures, even when core IFN signalling remains intact.

These findings are consistent with studies of coronaviruses that report secretion of *CXCL10*, *CXCL8*, *CCL2* and *IL-6* as dominant epithelial responses (Majumdar and Murphy, 2021; Rarani *et al.*, 2022; Huang *et al.*, 2025). Poly I:C stimulation of airway epithelium has been shown to elicit the same mediators (Lever *et al.*, 2015). What has been missing is a temperature-resolved view: my data show that these outputs are consistently amplified at 37

°C, extending transcript-level observations in influenza and coronaviruses (Foxman *et al.*, 2015; Laloli *et al.*, 2022).

6.3.5 Phosphokinase signatures as mechanistic correlates

Phospho-kinase profiling 24 h post stimulation revealed temperature-sensitive signalling nodes that align with the secretome. HCoV-OC43 activated ERK1/2, JNK and p38, together with PI3K-Akt and STAT2, with phosphorylation consistently higher at 37 °C. Poly I:C strongly activated ERK1/2, HSP27 and elements of osmoregulatory and calcium signalling, again enhanced at 37 °C. In contrast, 5′ppp-dsRNA induced only weak ERK1/2 and STAT3 phosphorylation that reduced at 33 °C, mirroring the near absence of *CXCL10* in that condition. Recombinant IFN-α primarily activated STAT1/2/3 with modest temperature effects.

These kinase signatures place the temperature effect at specific transducers that connect PRR engagement to IFN production and ISG induction. Weaker phosphorylation at 33 °C undermines the antiviral state, whereas stronger signalling at 37 °C supports restriction. Coronaviruses engage MAPKs, including p38, across models, and modulating p38 alters infection readouts (Mizutani *et al.*, 2004; Jin *et al.*, 2023). Large-scale phosphoproteomics during SARS-CoV-2 infection demonstrates broad kinase network rewiring (Bouhaddou *et al.*, 2020; Kaneko *et al.*, 2024). Together with airway studies showing temperature-contingent antiviral responses at 33 °C versus 37 °C (Foxman *et al.*, 2015; Li *et al.*, 2022) and biophysical evidence that p38 activity shifts with temperature (Deredge *et al.*, 2019), my data support a model where cooler conditions dampen phosphorylation of antiviral nodes, undermining the IFN-driven state, whereas warmer conditions support restriction.

6.3.6 *RIG-I, MDA5,* and *MAVS* are central to the temperature-sensitive restriction of HCoV-OC43

Direct stimulation of PRRs confirmed that Poly I:C and 5′ppp-dsRNA induce robust ISG expression, with responses stronger at 37 °C than at 33 °C. This was further supported by cytokine profiling, which showed a reduction in the secretion of chemokines such as *CXCL10* and *IL-8* at cooler temperatures. These observations suggest that impaired PRR activation at 33 °C contributes to the enhanced replication of HCoV-OC43 in the URT. To test causality, I compared multi-step growth in wild-type A549 cells and CRISPR/Cas9 knockouts. Loss of *RIG-I* or *MDA5* increased replication at both temperatures, and the 33-37 °C difference either persisted or narrowed. In *MAVS*-deficient cells, the temperature effect was no longer detectable within the resolution of my assays: $TCID_{50}$ and supernatant RNA trajectories at 33 °C and 37 °C were indistinguishable across time. This pattern indicates that *MAVS* is a major contributor to the temperature-sensitive antiviral restriction observed in this system. Prior studies show that *RIG-I* and *MDA5* have overlapping roles in coronavirus sensing (Kato *et al.*, 2006; Roth-Cross *et al.*, 2008), and my data extend this by implicating *MAVS* as the upstream adaptor through which these receptors shape temperature-linked control of HCoV-OC43. I did not assay downstream nodes, such as *TBK1*, *IRF3*, or *NF-κB*, directly here, so additional components may also contribute to the phenotype.

6.3.7 Role of *IFNAR1* signalling

Although *IFNAR1-/-* cells supported replication comparable to WT, the early divergence between 33 and 37 °C observed in WT was attenuated. This suggests that early restriction at 37 °C depends on IFNAR1, but the continued replication difference is due to viral features and IFN-independent host defences. This finding resonates with the broader literature on IFN signalling, which emphasises both the complexity and redundancy of the JAK-STAT pathway in antiviral defence (Aaronson and Horvath, 2002). Furthermore, (Otter *et al.*, 2023) recently

demonstrated that IFN signalling in the nasal epithelium is a key determinant of coronavirus clearance and disease outcome. My findings extend this by showing that *IFNAR1* signalling is less effective at cooler temperatures, providing an additional layer of explanation for URT confinement of HCoV-OC43.

6.3.8 Integration with secretome and kinase signalling

My cytokine and phosphokinase profiling experiments provide mechanistic insight into why IFN and PRR signalling are impaired at 33 °C. Cytokine arrays revealed reduced secretion of chemokines and growth factors following HCoV-OC43 infection and PRR stimulation at cooler temperatures, while phosphokinase profiling demonstrated weaker activation of MAPKs, STAT2, and downstream effectors at 33 °C. These results are consistent with recent studies showing that innate defence pathways, including IFN-independent dsRNA-induced strategies, are attenuated at cooler temperatures (Foxman *et al.*, 2015; Foxman *et al.*, 2016). They also compliment earlier findings (Mihaylova *et al.*, 2018), who reported that regional epithelial differences create a trade-off between oxidative stress defence and antiviral capacity. Collectively, my data suggest that reduced kinase signalling and impaired cytokine secretion at 33 °C compromise the establishment of a robust antiviral state, thereby creating conditions that favour HCoV-OC43 replication.

6.3.9 A mechanistic model for temperature-sensitive confinement of HCoV-OC43

Taken together, my findings support a model in which temperature shapes HCoV-OC43 replication and host defence primarily through modulation of host responses. At cooler 33 °C, RIG-I-MDA5-MAVS signalling is blunted, IFNAR1-mediated JAK-STAT activation is less effective, and cytokine secretion is reduced compared to core body temperature. At 37 °C, these pathways synergise to restrict replication, but at 33 °C, HCoV-OC43 can replicate with limited interference. This dual mechanism, enhanced replication in a permissive host environment and

stronger restriction at core body temperature, explains the confinement of HCoV-OC43 to the URT and its inability to establish productive infection in the warmer lower respiratory tract, in contrast to SARS-CoV, MERS-CoV, and SARS-CoV-2, which can replicate efficiently in the LRT where IFN responses are stronger (V'Kovski *et al.*, 2021; Otter *et al.*, 2023). Viral contributions such as polymerase kinetics or structural stability may also influence replication efficiency at different temperatures, but these remain speculative in the absence of direct evidence for HCoV-OC43.

Chapter 7

7.1 General discussion

The overarching aim of this thesis was to determine how physiologically relevant airway temperatures shape the balance between HCoV-OC43 replication and type I IFN responses, potentially explaining its confinement to the upper respiratory tract (URT). Seasonal human coronaviruses (HCoVs) long attracted limited study, owing to their typically mild disease and the technical challenges of propagating them in immortalised cell lines. HCoV-OC43 in particular, remains difficult to culture consistently, with titres varying widely across cell types, overlay systems, and incubation conditions.

A fundamental first step was to establish reproducible systems for the growth and measurement of HCoV-OC43 (Chapter 3). Comparative experiments across multiple cell lines showed that plaque assays, though traditional, were inconsistent in human-derived cells, while $TCID_{50}$ assays offered reproducibility and reliability. MRC-5 fibroblasts emerged as the most suitable model for replication and IFN studies, supported by epithelial cell lines such as A549. This chapter goes beyond just setting up lab methods; it showed which cell types and tests work best, giving us a solid foundation to explore how temperature and the immune system affect the virus.

Once robust systems were in place, I investigated how seasonal coronaviruses differ in their interaction with host defences (Chapter 4). Bulk RNA-seq of primary nasal epithelial cells infected with HCoV-229E or HCoV-OC43 revealed that HCoV-OC43 induces a weaker antiviral programme than HCoV-229E. Genes such as *IFIT1*, *IFIT2*, *IFI44L*, and *CXCL10* were strongly upregulated by HCoV-229E but only modestly induced by HCoV-OC43, particularly at 33 °C. Pathway enrichment confirmed weaker activation of RIG-I-like receptor and JAK-STAT signalling. These findings established that HCoV-OC43 has a reduced ability to trigger host antiviral defences compared to another seasonal coronavirus.

To determine whether HCoV-OC43 is intrinsically resistant to IFN, I performed pretreatment assays with recombinant IFN-α (Chapter 5). Both qPCR and $TCID_{50}$ assays demonstrated that IFN-α strongly inhibited replication at 33 °C and 37 °C, indicating that HCoV-OC43 remains highly sensitive in the presence of exogenous IFNα. Luciferase reporter assays confirmed robust ISG promoter activation following IFN stimulation, while infection alone elicited only modest activity. This clarified a key point: HCoV-OC43 does not resist IFN action but rather avoids triggering sufficient IFN induction during infection.

Finally, I addressed how temperature modifies this balance (Chapter 6). Across fibroblast and epithelial models, viral titres were consistently higher at 33 °C than at 37 °C, independent of multiplicity of infection. Direct PRR stimulation revealed that RIG-I-MDA5 signalling is impaired at cooler temperatures, whereas IFNAR-mediated signalling was unaffected. Cytokine secretion (*CXCL10*, *IL-8*) and phosphorylation of ERK, JNK, and STAT2 were also weaker at 33 °C. Knockout experiments provided mechanistic insight into which innate pathways underpin the temperature sensitivity of HCoV-OC43. Loss of RIG-I or MDA5 increased replication at both 33 and 37 °C, confirming that these RNA sensors contribute to restriction. However, the fold difference between the two temperatures was maintained, suggesting that neither receptor alone explains the temperature effect. In contrast, MAVS knockout largely removed this replication gap, with titres at 33 and 37 °C converging to similarly high levels. This suggests that MAVS is essential for the temperature-dependent restriction observed in wild-type cells and serves as the key adaptor linking upstream sensors to downstream antiviral responses in this context.

It is important to emphasise that my experiments did not assess downstream components of the MAVS pathway, such as TBK1, IRF3/7, or NF-κB. Therefore, while MAVS appears to function as a principal integration point for temperature-dependent restriction in this system, additional signalling nodes may contribute. The interpretation that MAVS-dependent signalling

is inherently weaker at cooler temperatures is consistent with findings from rhinovirus models (Foxman et al., 2015) and with reports that coronaviruses, including SARS-CoV-2, target MAVS to subvert host immunity (Feng et al., 2021). By placing my data in this framework, I conclude that MAVS plays a critical but not exclusive role in shaping the balance between viral replication and host defence across airway temperatures.

Taken together, these results converge on a coherent model: HCoV-OC43 replicates efficiently in the URT because cooler temperatures blunt MAVS-dependent IFN induction. At 37 °C, stronger PRR signalling and more robust ISG induction restrict replication, preventing spread into the LRT. HCoV-OC43 is therefore not intrinsically resistant to IFN-α but exploits a host environment where induction is naturally weaker. The synergy between viral replication capacity and host immune attenuation explains its seasonal behaviour, its URT confinement, and its contrast with epidemic coronaviruses that replicate efficiently at 37 °C through potent IFN antagonism.

7.2 Broader implications

This work builds on and extends recent studies of temperature-dependent immunity. Foxman and colleagues showed that rhinovirus replication is favoured at cooler temperatures due to impaired RIG-I-like receptor signalling in mouse airway epithelial cells (Foxman *et al.*, 2015; Foxman *et al.*, 2016). Similar findings have been reported for arboviruses, where IFN-mediated restriction was less effective at lower temperatures (Lane *et al.*, 2018). More recently, a study reported that SARS-CoV-2 replicates more efficiently at 33 °C in human nasal epithelial cells, while SARS-CoV is favoured at 37 °C, emphasising that temperature is a key determinant of coronavirus tropism (V'Kovski *et al.*, 2021). My findings on HCoV-OC43 provide important confirmation and extension of these principles, showing that temperature sensitivity is not restricted to emerging viruses but is a defining feature of endemic seasonal coronaviruses as well.

7.2.1 Temperature as a determinant of HCoV-OC43 replication

Across all tested infection models, HCoV-OC43 replicated more efficiently at 33 °C than at 37 °C. This was evident in MRC-5, A549, HEK293T cells, and even non-human Mv1Lu cells. Viral titres rose more rapidly and to higher levels at the cooler temperature, regardless of the multiplicity of infection. Early time-course experiments demonstrated that this advantage was not limited to viral entry but persisted through the replication cycle. These observations mirror the clinical reality that HCoV-OC43 is primarily confined to the URT, where local temperature favours its replication.

The mechanisms underlying this replication advantage are not fully resolved. One possibility is that viral enzymes, including the RNA-dependent RNA polymerase (RdRp), function more efficiently at 33 °C, similar to what has been suggested for rhinoviruses (Foxman *et al.*, 2015). Alternatively, structural stability of the viral nucleocapsid or spike proteins may be enhanced at cooler temperatures, facilitating genome protection or entry. Although this thesis did not directly test viral enzymatic activity, the consistent growth advantage at 33 °C across multiple cell lines suggests an intrinsic viral preference for cooler environments.

7.2.2 IFN sensitivity and viral antagonism

Although HCoV-OC43 grew better at cooler temperatures, it remained sensitive to IFNα pretreatment. Both $TCID_{50}$ and qPCR assays showed that IFN-α substantially reduced replication at either temperature. This demonstrates that the virus is not intrinsically resistant to IFN but relies on limiting its induction. Reporter assays confirmed that IFN-α robustly activated ISG promoters, while HCoV-OC43 infection drove only modest responses. Transcriptomic data revealed overlap between ISGs most strongly induced by IFN-α and those least induced during infection, highlighting the virus's selective suppression strategy.

These findings align with work by (Otter *et al.*, 2024), who showed that IFN competence of nasal epithelial cells distinguishes seasonal from lethal coronaviruses. Seasonal strains such as HCoV-OC43 suppress IFN responses and generally trigger a more modest type I IFN program than epidemic strains. Although strong IFN antagonism is a common feature of coronaviruses, disease severity depends on the timing and magnitude of the host response and the virus's countermeasures. My data refine this view by showing that the balance is temperature dependent: cooler conditions blunt innate sensing and shift the equilibrium toward OC43 replication.

7.2.3 Temperature-dependent IFN responses

Equally important was the observation that host IFN responses were profoundly shaped by temperature. ISG induction following infection was consistently higher at 37 °C than at 33 °C. Cytokine profiling revealed that secretion of key chemokines such as *CXCL10* and *IL-8*, which recruit immune cells and amplify antiviral states, was markedly reduced at cooler temperatures. Phosphokinase arrays confirmed that activation of MAPKs and STATs, central mediators of antiviral signalling, was attenuated at 33 °C. Together, these findings show that cooler temperatures not only enhance viral replication but also create a permissive immune environment by weakening host responses.

This dual effect aligns with the concept of "temperature-immunity trade-offs." (Mihaylova *et al.*, 2018) showed that epithelial cells in different airway regions balance stress resistance with antiviral defence, suggesting that the local environment tunes immune capacity. Similarly, (Otter *et al.*, 2024) reported that nasal epithelial cells mount strong IFN responses against lethal coronaviruses but weaker ones against seasonal strains. My results extend this framework by directly linking temperature to IFN competence, demonstrating that even within the same cell type, antiviral capacity is reduced at 33 °C.

7.2.4 PRR stimulation and MAVS as the central adaptor

To identify which pathways were most sensitive to temperature, I stimulated cells with synthetic PRR agonists. Poly I:C, which signals via TLR3 and MDA5, induced robust ISG responses at both temperatures, whereas direct IFNAR stimulation by recombinant IFN-α was largely unaffected by temperature. In contrast, 5′ppp-dsRNA, a RIG-I agonist, provoked strong responses at 37 °C but reduced at 33 °C. This pinpointed RIG-I signalling as the most temperature-sensitive pathway, consistent with reports in rhinovirus(Foxman *et al.*, 2015).

Genetic knockout experiments provided crucial mechanistic validation. Loss of *RIG-I* or *MDA5* enhanced replication, but only *MAVS* knockout abolished the difference between 33 °C and 37 °C. *IFNAR1* knockout reduced early restriction but did not eliminate temperature dependence, confirming that IFN-independent MAVS functions also contribute. These results establish MAVS as a key adaptor that integrates upstream signals and mediates temperature-dependent restriction of HCoV-OC43.

The identification of MAVS as central has broader implications. MAVS acts as the hub for RIG-I-like receptor signalling, linking cytosolic RNA recognition to IFN production (Seth et al., 2005). Its importance in coronavirus infection has been highlighted in studies of SARS-CoV-2, where multiple viral proteins target MAVS for antagonism (Feng *et al.*, 2021). My findings show that even without strong viral antagonism, MAVS signalling is inherently weaker at 33 °C, providing a natural vulnerability that HCoV-OC43 exploits. This reinforces MAVS as both a biological bottleneck and a potential therapeutic target.

7.2.5 A unifying model of coronavirus tropism

Together, the results presented in this thesis support a unifying model: the confinement of HCoV-OC43 to the URT arises from the intersection of viral replication preferences and host immune capacity, each influenced by temperature. At 33 °C, the virus replicates efficiently,

while RIG-I-MAVS signalling is impaired and IFN amplification blunted, resulting in a permissive environment. At 37 °C, replication slows, and MAVS-dependent restriction is strong, curbing viral spread and preventing invasion of the LRT.

This model not only explains the benign nature of HCoV-OC43 but also offers a lens to interpret differences among coronaviruses. Epidemic strains such as SARS-CoV-2 replicate efficiently at 37 °C and encode antagonists targeting MAVS and downstream signalling, enabling LRT infection and severe disease (V'Kovski *et al.*, 2021; Otter *et al.*, 2023). Seasonal strains such as HCoV-OC43 exploit cooler URT niches and persist without causing pneumonia. Thus, airway temperature gradients act as ecological filters, and the ability to overcome MAVS restriction at 37 °C may define whether a coronavirus remains endemic or emerges as a pandemic threat.

7.3 Limitations and future directions

While this thesis provides important new insights into the temperature-dependent replication and IFN response of HCoV-OC43, several limitations must be acknowledged. These limitations relate not only to experimental design and methodology but also to the broader translational interpretation of the findings. Addressing these constraints is critical for placing the results in appropriate context and for guiding the next stages of research.

7.3.1 Constraints of the *in vitro* model systems

Most of the experimental work was performed in immortalised or transformed cell lines, including MRC-5 fibroblasts, A549 lung epithelial cells, and HEK293T cells. These systems are widely used in virology because they are easy to maintain, highly permissive to infection, and allow controlled experimental conditions. However, they cannot fully replicate the complexity of the human respiratory tract epithelium.

Primary human nasal epithelial cells (hNECs) cultured at the ALI better mimic the *in vivo* situation by maintaining multiple differentiated cell types, including ciliated cells, goblet cells, and basal cells. These cells are embedded within mucus and exhibit polarised architecture, all of which strongly influence viral entry, replication, and innate immune sensing. Although Chapter 4 incorporated hNECs, these cultures were limited in number and not fully differentiated at ALI. Consequently, their responses are not directly comparable to those of a physiological URT epithelium.

This limitation is especially important because IFN signalling is highly cell-type specific. Previous work has shown that basal cells and ciliated cells differ in their IFN competence, with basal cells being more responsive to viral dsRNA stimulation (Mihaylova et al., 2018). By relying primarily on fibroblasts and immortalised epithelial cells, this thesis cannot exclude the possibility that some of the observed temperature-dependent differences reflect artefacts of the chosen models rather than actual physiological behaviour. Future work should utilise fully differentiated ALI hNECs, supported by single-cell RNA-seq, to identify which cell types drive temperature-sensitive IFN production.

Functional data rely on pre-generated A549 knockouts. A549 cells differ from MRC-5 and from primary airway cells in basal IFN tone and innate wiring. The absence of matched CRISPR lines in MRC-5, due to low transfection and clonal bottlenecks, limits cross-cell-type generalisation. Advances in lentiviral and electroporation-based delivery systems make this feasible even in slow-growing or diploid cells (Sanjana *et al.*, 2014). Priorities for follow-up include stable CRISPR knockouts in MRC-5 using improved delivery, or CRISPRi for partial, tuneable knockdown in physiologically relevant backgrounds.

7.3.2 Narrow temperature range

Comparisons focused on 33 °C and 37 °C. The airway spans roughly 30-37+ °C and shifts during fever or cold exposure. Replication and IFN induction may exhibit nonlinear behaviour across this gradient, with thresholds rather than a simple scaling relationship. Next steps should test a fuller gradient (for example, 30-39 °C) and include dynamic shifts that model fever or cooling. Sampling began at 4 hpi; early sensing can occur within minutes. Higher temporal resolution, live-cell imaging, or time-resolved phosphoproteomics would capture immediate sensor activation and separate primary temperature effects from downstream cascades.

7.3.3 Lack of *in vivo* validation

A further limitation is the absence of animal models in this study. *In vivo* systems provide critical context for infection dynamics, including systemic responses such as fever, immune cell infiltration, and adaptive immunity, none of which can be captured *in vitro*. During fever, core body temperature can rise to 38-39 °C, while hypothermia or cold air inhalation may lower nasal temperatures further. Fever in particular is an important physiological variable: elevated body temperature (≥38°C) has long been considered an antiviral defence, and recent work has suggested that febrile-range temperatures enhance IFN activity against respiratory viruses (Moriyama et al., 2015). Without *in vivo* studies, it remains uncertain whether the magnitude of the effects observed *in vitro* directly translates to the airway environment of an infected host.

Others have employed mouse-adapted HCoV-OC43 strains and murine coronavirus models to investigate neuroinvasion and disease progression (Jacomy & Talbot, 2003; Kyuwa & Yamaguchi, 1998). While these models differ from human infection, they could nonetheless serve as valuable systems for validating whether MAVS-dependent restriction is also temperature-sensitive *in vivo*. The lack of such validation in this thesis means that the findings, although robust in cell culture, should be extrapolated with caution.

7.3.4 Viral diversity and mechanistic depth

Experiments used a laboratory-adapted ATCC HCoV-OC43 strain. Seasonal coronaviruses differ in tropism and disease; HCoV-NL63, -HKU1, and -229E may not share the same temperature-IFN balance. Multi-strain, multi-species comparisons are needed to learn whether temperature-sensitive MAVS restriction is general or HCoV-OC43-specific.

7.3.5 Viral factor contributions

The data suggest that MAVS signalling is a host target, but viral proteins may also exhibit temperature-dependent activity. The function of HCoV-OC43 polymerase, replication complex stability, nucleocapsid dynamics, and the antagonism of accessory proteins to IFN were not directly tested across different temperatures. Reverse genetics, purified-enzyme kinetics, and temperature-shift assays can define whether viral functions are intrinsically temperature sensitive, clarifying whether upper-airway bias reflects host vulnerability, viral adaptation, or both.

7.3.6 Immune pathway scope

This work centres on type I IFN. Type II and type III IFNs, together with key cytokine networks, also contribute to shaping epithelial antiviral states by modulating antigen presentation, driving immune cell recruitment, and coordinating crosstalk with adaptive immunity. These pathways were not systematically examined here, but future studies incorporating them, ideally in ALI or in vivo systems, will be essential to provide a more complete picture of how temperature influences host defence.

7.4 Conclusion

Together, the findings support a model in which HCoV-OC43 remains confined to the upper airway because type I IFN defences that depend on MAVS are less effective at cooler

temperatures. At the same time, viral replication processes function well in that range. Moving forward, three strands will convert this into a translational framework: (i) validate in fully differentiated ALI and *in vivo* systems, (ii) expand the thermal and temporal resolution, and (iii) dissect viral accessory and polymerase functions across temperatures. These efforts will test whether the capacity to overcome MAVS-linked restriction at 37 °C marks a step toward lower-airway competence that separates seasonal coronaviruses from high-consequence strains.

References

Aaronson, D. and Horvath, C. (2002) 'A road map for those who don't know JAK-STAT', *science,* 296(5573), pp. 1653-1655.

Almazan, F., DeDiego, M. L., Sola, I., Zuniga, S., Nieto-Torres, J. L., Marquez-Jurado, S., Andres, G. and Enjuanes, L. (2013) 'Engineering a Replication-Competent, Propagation-Defective Middle East Respiratory Syndrome Coronavirus as a Vaccine Candidate', *Mbio,* 4(5) e00650-13.

Alspach, E., Lussier, D. M. and Schreiber, R. D. (2019) 'Interferon γ and its important roles in promoting and inhibiting spontaneous and therapeutic cancer immunity', *Cold Spring Harbor perspectives in biology,* 11(3), pp. a028480.

Amini-Bavil-Olyaee, S., Choi, Y. J., Lee, J. H., Shi, M., Huang, I. C., Farzan, M. and Jung, J. U. (2013) 'The Antiviral Effector IFITM3 Disrupts Intracellular Cholesterol Homeostasis to Block Viral Entry', *Cell Host & Microbe,* 13(4), pp. 452-464.

Ank, N., West, H. and Paludan, S. R. (2006a) 'IFN-lambda: Novel antiviral cytokines', *Journal of Interferon and Cytokine Research,* 26(6), pp. 373-379.

Ank, N., West, H. and Paludan, S. R. (2006b) 'IFN-λ: novel antiviral cytokines', *Journal of Interferon & Cytokine Research,* 26(6), pp. 373-379.

Asthana, A., Gaughan, C., Dong, B., Weiss, S. and Silverman, R. (2021) 'Specificity and Mechanism of Coronavirus, Rotavirus, and Mammalian Two-Histidine Phosphoesterases That Antagonize Antiviral Innate Immunity', *Mbio,* 12(4) e01781-21.

Bailey-Elkin, B. A., Knaap, R. C. M., Johnson, G. G., Dalebout, T. J., Ninaber, D. K., van Kasteren, P. B., Bredenbeek, P. J., Snijder, E. J., Kikkert, M. and Mark, B. L. (2014) 'Crystal Structure of the Middle East Respiratory Syndrome Coronavirus (MERS-CoV) Papain-like Protease Bound to Ubiquitin Facilitates Targeted Disruption of Deubiquitinating Activity to Demonstrate Its Role in Innate Immune Suppression', *Journal of Biological Chemistry,* 289(50), pp. 34667-34682.

Bakkers, M., Lang, Y., Feitsma, L., Hulswit, R., de Poot, S., van Vliet, A., Margine, I., de Groot-Mijnes, J., van Kuppeveld, F., Langereis, M., Huizinga, E. and de Groot, R. (2017) 'Betacoronavirus Adaptation to Humans Involved Progressive Loss of Hemagglutinin-Esterase Lectin Activity', *Cell Host & Microbe,* 21(3), pp. 356-366.

Barber, G. N. (2001) 'Host defense, viruses and apoptosis', *Cell Death and Differentiation,* 8(2), pp. 113-126.

Beidas, M. and Chehadeh, W. (2018) 'Effect of Human Coronavirus OC43 Structural and Accessory Proteins on the Transcriptional Activation of Antiviral Response Elements', *Intervirology,* 61(1), pp. 30-35.

Bhardwaj, P. (2020) 'History and Origin of Coronaviruses', *Journal of the Practice of Cardiovascular Sciences,* 6(3), pp. 234-238.

Blanco-Melo, D., Nilsson-Payant, B. E., Liu, W.-C., Uhl, S., Hoagland, D., Moller, R., Jordan, T. X., Oishi, K., Panis, M., Sachs, D., Wang, T. T., Schwartz, R. E., Lim, J. K., Albrecht, R. A. and tenOever, B. R. (2020) 'Imbalanced Host Response to SARS-CoV-2 Drives Development of COVID-19', *Cell,* 181(5), pp. 1036-+.

Bonavita, C., Wells, H. and Anthony, S. (2024) 'Cellular dynamics shape recombination frequency in coronaviruses', *PLOS Pathogens,* 20(9) e1012596.

Bracci, N., Pan, H. C., Lehman, C., Kehn-Hall, K. and Lin, S. C. (2020) 'Improved plaque assay for human coronaviruses 229E and OC43', *Peerj,* 8 e10639.

Bucknall, R., Chanock, R., Kapikian, A. And King, L. 1972. [Studies With Human Coronaviruses .2. Some Properties of Strains 229E and OC43]. *Proceedings of the Society for Experimental Biology and Medicine,* **139**(3): pp. 722-727

Butler, N., Pewe, L., Trandem, K. and Perlman, S. 2006. [Murine encephalitis caused by HCoV-OC43, a human coronavirus with broad species specificity, is partly immune-mediated]. *Virology.*

Cadena, C. and Hur, S. (2019) 'Filament-like Assemblies of Intracellular Nucleic Acid Sensors: Commonalities and Differences', *Molecular Cell,* 76(2), pp. 243-254.

Castaño-Rodriguez, C., Honrubia, J., Gutiérrez-Alvarez, J., DeDiego, M., Nieto-Torres, J., Jimenez-Guardeño, J., Regla-Nava, J., Fernandez-Delgado, R., Verdia-Báguena, C., Queralt-Martín, M., Kochan, G., Perlman, S., Aguilella, V., Sola, I. and Enjuanes, L. (2018) 'Role of Severe Acute Respiratory

Syndrome Coronavirus Viroporins E, 3a, and 8a in Replication and Pathogenesis', *Mbio,* 9(3) e02325-17.
Chang, C., Hsu, Y., Chang, Y., Chao, F., Wu, M., Huang, Y., Hu, C. and Huang, T. (2009) 'Multiple Nucleic Acid Binding Sites and Intrinsic Disorder of Severe Acute Respiratory Syndrome Coronavirus Nucleocapsid Protein: Implications for Ribonucleocapsid Protein Packaging', *Journal Of Virology,* 83(5), pp. 2255-2264.
Chang, C.-Y., Liu, H. M., Chang, M.-F. and Chang, S. C. (2020) 'Middle East Respiratory Syndrome Coronavirus Nucleocapsid Protein Suppresses Type I and Type III Interferon Induction by Targeting RIG-I Signaling', *Journal of Virology,* 94(13) e00099-20.
Chen, Y., Cai, H., Pan, J. a., Xiang, N., Tien, P., Ahola, T. and Guo, D. (2009) 'Functional screen reveals SARS coronavirus nonstructural protein nsp14 as a novel cap N7 methyltransferase', *Proceedings of the National Academy of Sciences of the United States of America,* 106(9), pp. 3484-3489.
Cheng, A. W., Wang, H., Yang, H., Shi, L., Katz, Y., Theunissen, T. W., Rangarajan, S., Shivalila, C. S., Dadon, D. B. and Jaenisch, R. (2013) 'Multiplexed activation of endogenous genes by CRISPR-on, an RNA-guided transcriptional activator system', *Cell Research,* 23(10), pp. 1163-1171.
Chow, E., Casto, A., Rogers, J., Roychoudhury, P., Han, P., Xie, H., Mills, M., Nguyen, T., Pfau, B., Cox, S., Wolf, C., Hughes, J., Uyeki, T., Rolfes, M., Mosites, E., Shim, M., Duchin, J., Sugg, N., Starita, Chow EJ, Casto AM, Rogers JH, Roychoudhury P, Han PD, Xie H, Mills MG, Nguyen TV, Pfau B, Cox SN, Wolf CR, Hughes JP, Uyeki TM, Rolfes MA, Mosites E, Shim MM, Duchin JS, Sugg N, Starita LA, Englund JA and Chu, H. (2022) 'The clinical and genomic epidemiology of seasonal human coronaviruses in congregate homeless shelter settings: A repeated cross-sectional study', *Lancet Regional Health-Americas,* 15: 100348
Clementz, M. A., Chen, Z., Banach, B. S., Wang, Y., Sun, L., Ratia, K., Baez-Santos, Y. M., Wang, J., Takayama, J., Ghosh, A. K., Li, K., Mesecar, A. D. and Baker, S. C. (2010) 'Deubiquitinating and Interferon Antagonism Activities of Coronavirus Papain-Like Proteases', *Journal of Virology,* 84(9), pp. 4619-4629.
Coccia, E. M., Severa, M., Giacomini, E., Monneron, D., Remoli, M. E., Julkunen, I., Cella, M., Lande, R. and Uzé, G. (2004) 'Viral infection and Toll-like receptor agonists induce a differential expression of type I and λ interferons in human plasmacytoid and monocyte-derived dendritic cells', *European journal of immunology,* 34(3), pp. 796-805.
Collins, A. R. (1993) 'HLA Class-I antigen serves as a receptor for human coronavirus-OC43', *Immunological Investigations,* 22(2), pp. 95-103.
Comar, C., Goldstein, S., Li, Y., Yount, B., Baric, R. and Weiss, S. (2019) 'Antagonism of dsRNA-Induced Innate Immune Pathways by NS4a and NS4b Accessory Proteins during MERS Coronavirus Infection', *Mbio,* 10(2): e00319-19
Daffis, S., Szretter, K. J., Schriewer, J., Li, J., Youn, S., Errett, J., Lin, T.-Y., Schneller, S., Zust, R., Dong, H., Thiel, V., Sen, G. C., Fensterl, V., Klimstra, W. B., Pierson, T. C., Buller, R. M., Gale, M., Jr., Shi, P.-Y. and Diamond, M. S. (2010) '2 '-O methylation of the viral mRNA cap evades host restriction by IFIT family members', *Nature,* 468(7322), pp. 452-456.
Darnell, J. E., Kerr, I. M. and Stark, G. R. (1994) 'JAK-STAT pathways and transcriptional activation in response to ifns and other extracellular signaling proteins', *Science,* 264(5164), pp. 1415-1421.
Das, J. and Roy, S. (2021) 'Comparative analysis of human coronaviruses focusing on nucleotide variability and synonymous codon usage patterns', *Genomics,* 113(4), pp. 2177-2188.
de Klerk, A., Swanepoel, P., Lourens, R., Zondo, M., Abodunran, I., Lytras, S., MacLean, O., Robertson, D., Pond, S., Zehr, J., Kumar, V., Stanhope, M., Harkins, G., Murrell, B. and Martin, D. (2022) 'Conserved recombination patterns across coronavirus subgenera', *Virus Evolution,* 8(2): veac054
De Thoisy, A., Woudenberg, T., Pelleau, S., Donnadieu, F., Garcia, L., Pinaud, L., Tondeur, L., Meola, A., Arowas, L., Clement, N., Backovic, M., Ungeheuer, M., Fontanet, A., White, M. and Teams, C. O. S. S. (2023) 'Seroepidemiology of the Seasonal Human Coronaviruses NL63, 229E, OC43 and HKU1 in France', *Open Forum Infectious Diseases,* 10(7): ofad340
de Weerd, N. A. and Thao, N. (2012) 'The interferons and their receptors-distribution and regulation', *Immunology and Cell Biology,* 90(5), pp. 483-491.
de Wilde, A. H., Snijder, E. J., Kikkert, M. and van Hemert, M. J. (2018) 'Host Factors in Coronavirus Replication', in Tripp, R.A. & Tompkins, S.M. (eds.) *Roles of Host Gene and Non-Coding RNA*

Expression in Virus Infection Current Topics in Microbiology and Immunology. Cham: *Springer International Publishing* Ag, pp. 1-42.
Deng, X., Hackbart, M., Mettelman, R. C., O'Brien, A., Mielech, A. M., Yi, G., Kao, C. C. and Baker, S. C. (2017) 'Coronavirus nonstructural protein 15 mediates evasion of dsRNA sensors and limits apoptosis in macrophages', *Proceedings of the National Academy of Sciences of the United States of America,* 114(21), pp. E4251-E4260.
Devaraj, S. G., Wang, N., Chen, Z., Chen, Z., Tseng, M., Barretto, N., Lin, R., Peters, C. J., Tseng, C.-T. K., Baker, S. C. and Li, K. (2007) 'Regulation of IRF-3-dependent innate immunity by the papain-like protease domain of the severe acute respiratory syndrome coronavirus', *Journal of Biological Chemistry,* 282(44), pp. 32208-32221.
Diamond, M. and Farzan, M. (2013) 'The broad-spectrum antiviral functions of IFIT and IFITM proteins', *Nature Reviews Immunology,* 13(1), pp. 46-57.
Ding, S.-W. and Voinnet, O. (2007) 'Antiviral immunity directed by small RNAs', *Cell,* 130(3), pp. 413-426.
Duncan, J. K. S., Xu, D. Y., Licursi, M., Joyce, M. A., Saffran, H. A., Liu, K. W., Gohda, J., Tyrrell, D. L., Kawaguchi, Y. and Hirasawa, K. (2023) 'Interferon regulatory factor 3 mediates effective antiviral responses to human coronavirus 229E and OC43 infection', *Frontiers in Immunology,* 14: 930086
Eccles, R. 2021. [Why is temperature sensitivity important for the success of common respiratory viruses?]. *Reviews In Medical Virology,* **31**(1): pp. 1-8.
Edwards, D., Edwards, A., Li, D., Wang, L., Chung, K., Bhatta, D., Bilstein, A., Hanes, J., Endirisinghe, I., Freeman, B., Gutay, M., Livraghi-Butrico, A. and Button, B. (2025) 'Global warming risks dehydrating and inflaming human airways', *Communications Earth & Environment,* 6(1).
Fausto, A., Otter, C., Bracci, N. and Weiss, S. (2023) 'Improved Culture Methods for Human Coronaviruses HCoV-OC43, HCoV-229E, and HCoV-NL63', *Current Protocols,* 3(10).
Faye, M., Barry, M., Jallow, M., Wade, S., Mendy, M., Sy, S., Fall, A., Kiori, D., Ndiaye, N., Goudiaby, D., Diamanka, A., Niang, M. and Dia, N. (2023) 'Epidemiology of Non-SARS-CoV2 Human Coronaviruses (HCoVs) in People Presenting with Influenza-like Illness (ILI) or Severe Acute Respiratory Infections (SARI) in Senegal from 2012 to 2020', *Viruses-Basel,* 15(1).
Feng, H., Zhang, Y.-B., Gui, J.-F., Lemon, S. M. and Yamane, D. (2021) 'Interferon regulatory factor 1 (IRF1) and anti-pathogen innate immune responses', *Plos Pathogens,* 17(1): 193.
Forni, D., Cagliani, R., Arrigoni, F., Benvenuti, M., Mozzi, A., Pozzoli, U., Clerici, M., De Gioia, L. and Sironi, M. (2021a) 'Adaptation of the endemic coronaviruses HCoV-OC43 and HCoV-229E to the human host', *Virus Evolution,* 7(2): veab048
Forni, D., Cagliani, R., Arrigoni, F., Benvenuti, M., Mozzi, A., Pozzoli, U., Clerici, M., De Gioia, L. and Sironi, M. (2021b) 'Adaptation of the endemic coronaviruses HCoV-OC43 and HCoV-229E to the human host', *Virus Evolution,* 7(2), pp. 11.
Foxman, E. F., Storer, J. A., Fitzgerald, M. E., Wasik, B. R., Hou, L., Zhao, H. Y., Turner, P. E., Pyle, A. M. and Iwasaki, A. (2015) 'Temperature-dependent innate defense against the common cold virus limits viral replication at warm temperature in mouse airway cells', *Proceedings of the National Academy of Sciences of the United States of America,* 112(3), pp. 827-832.
Foxman, E. F., Storer, J. A., Vanaja, K., Levchenko, A. and Iwasaki, A. (2016) 'Two interferon-independent double-stranded RNA-induced host defense strategies suppress the common cold virus at warm temperature', *Proceedings of the National Academy of Sciences of the United States of America,* 113(30), pp. 8496-8501.
Frieman, M., Ratia, K., Johnston, R. E., Mesecar, A. D. and Baric, R. S. (2009) 'Severe Acute Respiratory Syndrome Coronavirus Papain-Like Protease Ubiquitin-Like Domain and Catalytic Domain Regulate Antagonism of IRF3 and NF-kappa B Signaling', *Journal of Virology,* 83(13), pp. 6689-6705.
Fung, T. S. and Liu, D. X. (2019) 'Human Coronavirus: Host-Pathogen Interaction', in Gottesman, S. (ed.) *Annual Review of Microbiology, Vol 73 Annual Review of Microbiology*. Palo Alto: Annual Reviews, pp. 529-557.
Fung, T. S. and Liu, D. X. (2021) 'Similarities and Dissimilarities of COVID-19 and Other Coronavirus Diseases', *Annual Review of Microbiology,* 75(Volume 75, 2021), pp. 19-47.
Funk, C. J., Wang, J. R., Ito, Y., Travanty, E. A., Voelker, D. R., Holmes, K. V. and Mason, R. J. (2012) 'Infection of human alveolar macrophages by human coronavirus strain 229E', *Journal of General Virology,* 93, pp. 494-503.

García, M., Meurs, E. and Esteban, M. (2007) 'The dsRNA protein kinase PKR:: Virus and cell control', *Biochimie,* 89(6-7), pp. 799-811.
Gaunt, E., Hardie, A., Claas, E., Simmonds, P. and Templeton, K. (2010) 'Epidemiology and Clinical Presentations of the Four Human Coronaviruses 229E, HKU1, NL63, and OC43 Detected over 3 Years Using a Novel Multiplex Real-Time PCR Method', *Journal of Clinical Microbiology,* 48(8), pp. 2940-2947.
Gildenhuys, S. (2020) 'Expanding our understanding of the role polyprotein conformation plays in the coronavirus life cycle', *Biochemical Journal,* 477(8), pp. 1479-1482.
Goldstein, S., Thornbrough, J., Zhang, R., Jha, B., Li, Y., Elliott, R., Quiroz-Figueroa, K., Chen, A., Silverman, R. and Weiss, S. (2017) 'Lineage A Betacoronavirus NS2 Proteins and the Homologous Torovirus Berne pp1a Carboxy-Terminal Domain Are Phosphodiesterases That Antagonize Activation of RNase L', *Journal Of Virology,* 91(5): e02201-16.
Greenberg, S. B. (2016) 'Update on Human Rhinovirus and Coronavirus Infections', *Seminars in Respiratory and Critical Care Medicine,* 37(4), pp. 555-571.
Han, S., Xu, B., Feng, Q., Feng, Z., Zhu, Y., Ai, J., Deng, L., Li, C., Cao, L., Sun, Y., Fu, Z., Jin, R., Shang, Y., Chen, Z., Xu, L., Xie, Z. and Shen, K. (2023) 'Multicenter analysis of epidemiological and clinical features of pediatric acute lower respiratory tract infections associated with common human coronaviruses in China, 2014-2019', *Virology Journal,* 20(1): pp. 229.
Harrison, C. M., Doster, J. M., Landwehr, E. H., Kumar, N. P., White, E. J., Beachboard, D. C. and Stobart, C. C. (2023) 'Evaluating the Virology and Evolution of Seasonal Human Coronaviruses Associated with the Common Cold in the COVID-19 Era', *Microorganisms,* 11(2), pp. 445.
Hirose, R., Watanabe, N., Bandou, R., Yoshida, T., Daidoji, T., Naito, Y., Itoh, Y. and Nakaya, T. (2021) 'A Cytopathic Effect-Based Tissue Culture Method for HCoV-OC43 Titration Using TMPRSS2-Expressing VeroE6 Cells', *Msphere,* 6(3): e00159-21.
Hu, B., Guo, H., Zhou, P. and Shi, Z.-L. (2022a) 'Characteristics of SARS-CoV-2 and COVID-19 (vol 19, pg 141, 2021)', *Nature Reviews Microbiology,* 20(5), pp. 315-315.
Hu, Y., Li, W., Gao, T., Cui, Y., Jin, Y., Li, P., Ma, Q., Liu, X. and Cao, C. (2017) 'The Severe Acute Respiratory Syndrome Coronavirus Nucleocapsid Inhibits Type I Interferon Production by Interfering with TRIM25-Mediated RIG-I Ubiquitination', *Journal of Virology,* 91(8): e02143-16.
Hu, Y., Ma, C. and Wang, J. (2022b) 'Cytopathic Effect Assay and Plaque Assay to Evaluate in vitro Activity of Antiviral Compounds Against Human Coronaviruses 229E, OC43, and NL63', *Bio-Protocol,* 12(3): e4314
Hui, D. J., Bhasker, C. R., Merrick, W. C. and Sen, G. C. (2003) 'Viral stress-inducible protein p56 inhibits translation by blocking the interaction of eIF3 with the ternary complex eIF2 center dot GTP center dot Met-tRNA(i)', *Journal of Biological Chemistry,* 278(41), pp. 39477-39482.
Hulswit, R. J. G., Lang, Y., Bakkers, M. J. G., Li, W., Li, Z., Schouten, A., Ophorst, B., van Kuppeveld, F. J. M., Boons, G.-J., Bosch, B.-J., Huizinga, E. G. and de Groot, R. J. (2019) 'Human coronaviruses OC43 and HKU1 bind to 9-O-acetylated sialic acids via a conserved receptor-binding site in spike protein domain A', *Proceedings of the National Academy of Sciences of the United States of America,* 116(7), pp. 2681-2690.
Hurtado-Tamayo, J., Requena-Platek, R., Enjuanes, L., Bello-Perez, M. and Sola, I. (2023) 'Contribution to pathogenesis of accessory proteins of deadly human coronaviruses', *Frontiers in Cellular and Infection Microbiology,* 13: 1090917
Iwasaki, A., Foxman, E. and Molony, R. (2017) 'Early local immune defences in the respiratory tract', *Nature Reviews Immunology,* 17(1), pp. 7-20.
Jacomy, H. and Talbot, P. 2003. [Vacuolating encephalitis in mice infected by human coronavirus OC43]. *Virology,* 315(1): 20-33.
Kakuya, F., Terao, R., Onoda, H., Okubo, H., Fujiyasu, H., Inyaku, F., Fukuura, A., Arai, T. and Kinebuchi, T. (2024) 'Epidemiology of endemic human coronavirus infection during the COVID-19 pandemic', *Journal Of Infection And Chemotherapy,* 30(5), pp. 400-405.
Kato, K., Ahmad, S., Zhu, Z., Young, J. M., Mu, X., Park, S., Malik, H. S. and Hur, S. (2021) 'Structural analysis of RIG-I-like receptors reveals ancient rules of engagement between diverse RNA helicases and TRIM ubiquitin ligases', *Molecular Cell,* 81(3): pp. 599-613.e8.
Kawai, T. and Akira, S. (2006) 'TLR signaling', *Cell Death & Differentiation,* 13(5), pp. 816-825.

Kesheh, M. M., Hosseini, P., Soltani, S. and Zandi, M. (2022) 'An overview on the seven pathogenic human coronaviruses', *Reviews in Medical Virology,* 32(2), pp. 13.
Killip, M., Fodor, E. and Randall, R. (2015) 'Influenza virus activation of the interferon system', *Virus Research,* 209, pp. 11-22.
Kim, D. E., Min, J. S., Jang, M. S., Lee, J. Y., Shin, Y. S., Park, C. M., Song, J. H., Kim, H. R., Kim, S., Jin, Y. H. and Kwon, S. (2019) 'Natural Bis-Benzylisoquinoline Alkaloids-Tetrandrine, Fangchinoline, and Cepharanthine, Inhibit Human Coronavirus OC43 Infection of MRC-5 Human Lung Cells', *Biomolecules,* 9(11): pp. 758
Kim, M. I. and Lee, C. (2023) 'Human Coronavirus OC43 as a Low-Risk Model to Study COVID-19', *Viruses,* 15(2), pp. 578.
Kim, Y.-M. and Shin, E.-C. (2021) 'Type I and III interferon responses in SARS-CoV-2 infection', *Experimental & Molecular Medicine,* 53(5), pp. 750-760.
Kindler, E., Thiel, V. and Weber, F. 2016. Interaction of SARS and MERS Coronaviruses with the Antiviral Interferon Response. *Advances In Virus Research, Vol 96: pp. 219-243 Coronaviruses.*
Klemm, T., Ebert, G., Calleja, D. J., Allison, C. C., Richardson, L. W., Bernardini, J. P., Lu, B. G. C., Kuchel, N. W., Grohmann, C., Shibata, Y., Gan, Z. Y., Cooney, J. P., Doerflinger, M., Au, A. E., Blackmore, T. R., van der Heden van Noort, G. J., Geurink, P. P., Ovaa, H., Newman, J., ... and Komander, D. (2020) 'Mechanism and inhibition of the papain-like protease, PLpro, of SARS-CoV-2', *Embo Journal,* 39(18): e106275.
Knoops, K., Kikkert, M., van den Worm, S. H. E., Zevenhoven-Dobbe, J. C., van der Meer, Y., Koster, A. J., Mommaas, A. M. and Snijder, E. J. (2008) 'SARS-coronavirus replication is supported by a reticulovesicular network of modified endoplasmic reticulum', *Plos Biology,* 6(9), pp. 1957-1974.
Kopecky-Bromberg, S. A., Martinez-Sobrido, L., Frieman, M., Baric, R. A. and Palese, P. (2007) 'Severe acute respiratory syndrome coronavirus open reading frame (ORF) 3b, ORF 6, and nucleocapsid proteins function as interferon antagonists', *Journal of Virology,* 81(2), pp. 548-557.
Kovacs, D., Mambule, I., Read, J., Kiran, A., Chilombe, M., Bvumbwe, T., Aston, S., Menyere, M., Masina, M., Kamzati, M., Ganiza, T., Iuliano, D., Mcmorrow, M., Bar-Zeev, N., Everett, D., French, N. and Ho, A. (2024) 'Epidemiology of Human Seasonal Coronaviruses Among People With Mild and Severe Acute Respiratory Illness in Blantyre, Malawi, 2011-2017', *Journal Of Infectious Diseases,* 230(2), pp. e363-e373.
Kristiansen, H., Gad, H., Eskildsen-Larsen, S., Despres, P. and Hartmann, R. (2011) 'The Oligoadenylate Synthetase Family: An Ancient Protein Family with Multiple Antiviral Activities', *Journal of Interferon and Cytokine Research,* 31(1), pp. 41-47.
Kume, Y., Hashimoto, K., Shirato, K., Norito, S., Suwa, R., Chishiki, M., Ono, T., Mashiyama, F., Mochizuki, I., Sato, M., Ishibashi, N., Suzuki, S., Sakuma, H., Takahashi, H., Takeda, M. and Hosoya, M. (2022) 'Epidemiological and clinical characteristics of infections with seasonal human coronavirus and respiratory syncytial virus in hospitalized children immediately before the coronavirus disease 2019 pandemic', *Journal of Infection and Chemotherapy,* 28(7), pp. 859-865.
Kutter, J., Spronken, M., Fraaij, P., Fouchier, R. and Herfst, S. 2018. [Transmission routes of respiratory viruses among humans]. *Current Opinion in Virology,* 28: pp. 142-151.
Lambert F, Jacomy H, Marceau G & Talbot PJ. (2008) *Titration of human coronaviruses using an immunoperoxidase assay*. *Journal of Visualized Experiments*, (vol 14, 751, 2008)', *Jove-Journal of Visualized Experiments,* (14): e751.
Lane, W. C., Dunn, M. D., Gardner, C. L., Lam, L. K. M., Watson, A. M., Hartman, A. L., Ryman, K. D. and Klimstra, W. B. (2018) 'The Efficacy of the Interferon Alpha/Beta Response versus Arboviruses Is Temperature Dependent', *Mbio,* 9(2): e00535-18
Laporte, M., Raeymaekers, V., Van Berwaer, R., Vandeput, J., Marchand-Casas, I., Thibaut, H., Van Looveren, D., Martens, K., Hoffmann, M., Maes, P., Pöhlmann, S., Naesens, L. and Stevaert, A. 2021. [The SARS-CoV-2 and other human coronavirus spike proteins are fine-tuned towards temperature and proteases of the human airways]. *Plos Pathogens,* 17(4): e1009500.
Lazear, H. M., Schoggins, J. W. and Diamond, M. S. (2019) 'Shared and Distinct Functions of Type I and Type III Interferons', *Immunity,* 50(4), pp. 907-923.
Lei, X., Dong, X., Ma, R., Wang, W., Xiao, X., Tian, Z., Wang, C., Wang, Y., Li, L., Ren, L., Guo, F., Zhao, Z., Zhou, Z., Xiang, Z. and Wang, J. (2020) 'Activation and evasion of type I interferon responses by SARS-CoV-2', *Nature Communications,* 11(1): 3810.

Levy, D. E., Marié, I. J. and Durbin, J. E. (2011) 'Induction and function of type I and III interferon in response to viral infection', *Current opinion in virology,* 1(6), pp. 476-486.
Li, G., Fan, Y., Lai, Y., Han, T., Li, Z., Zhou, P., Pan, P., Wang, W., Hu, D., Liu, X., Zhang, Q. and Wu, J. (2020) 'Coronavirus infections and immune responses', *J Med Virol,* 92(4), pp. 424-432.
Li, K., Markosyan, R. M., Zheng, Y.-M., Golfetto, O., Bungart, B., Li, M., Ding, S., He, Y., Liang, C., Lee, J. C., Gratton, E., Cohen, F. S. and Liu, S.-L. (2013) 'IFITM Proteins Restrict Viral Membrane Hemifusion', *Plos Pathogens,* 9(1): e1003124.
Li, Y., Banerjee, S., Wang, Y., Goldstein, S. A., Dong, B., Gaughan, C., Silverman, R. H. and Weiss, S. R. (2016) 'Activation of RNase L is dependent on OAS3 expression during infection with diverse human viruses', *Proceedings of the National Academy of Sciences of the United States of America,* 113(8), pp. 2241-2246.
Li, Y., Surya, W., Claudine, S. and Torres, J. (2014) 'Structure of a Conserved Golgi Complex-targeting Signal in Coronavirus Envelope Proteins', *Journal of Biological Chemistry,* 289(18), pp. 12535-12549.
Lim, Y. X., Ng, Y. L., Tam, J. P. and Liu, D. X. (2016) 'Human Coronaviruses: A Review of Virus-Host Interactions', *Diseases (Basel, Switzerland),* 4(3): 26
Ling, Z., Tran, K. and Teng, M. (2009) 'Human Respiratory Syncytial Virus Nonstructural Protein NS2 Antagonizes the Activation of Beta Interferon Transcription by Interacting with RIG-I', *Journal of Virology,* 83(8), pp. 3734-3742.
LIU, D. and INGLIS, S. (1991) 'Association of the Infectious-Bronchitis Virus-3c Protein with the Virion Envelope', *Virology,* 185(2), pp. 911-917.
Liu, D. X., Liang, J. Q. and Fung, T. S. (2021a) 'Human coronavirus-229E,-OC43,-NL63, and-HKU1 (Coronaviridae)', *Encyclopedia of virology*, pp. 428.
Liu, G., Lee, J.-H., Parker, Z. M., Acharya, D., Chiang, J. J., van Gent, M., Riedl, W., Davis-Gardner, M. E., Wies, E., Chiang, C. and Gack, M. U. (2021b) 'ISG15-dependent activation of the sensor MDA5 is antagonized by the SARS-CoV-2 papain-like protease to evade host innate immunity', *Nature Microbiology,* 6(4), pp. 467-+.
Loo, S.-L., Wark, P. A. B., Esneau, C., Nichol, K. S., Hsu, A. C.-Y. and Bartlett, N. W. (2020a) 'Human coronaviruses 229E and OC43 replicate and induce distinct antiviral responses in differentiated primary human bronchial epithelial cells', *American Journal of Physiology-Lung Cellular and Molecular Physiology,* 319(6), pp. L926-L931.
Loo, S.-L., Wark, P. A. B., Esneau, C., Nichol, K. S., Hsu, A. C. Y. and Bartlett, N. W. (2020b) 'Human coronaviruses 229E and OC43 replicate and induce distinct antiviral responses in differentiated primary human bronchial epithelial cells', *American Journal of Physiology-Lung Cellular and Molecular Physiology,* 319(6), pp. L926-L931.
Loo, S. L., Wark, P. A. B., Esneau, C., Nichol, K. S., Hsu, A. C. Y. and Bartlett, N. W. (2020c) 'Human coronaviruses 229E and OC43 replicate and induce distinct antiviral responses in differentiated primary human bronchial epithelial cells', *American Journal of Physiology-Lung Cellular and Molecular Physiology,* 319(6), pp. L926-L931.
Loske, J., Roehmel, J., Lukassen, S., Stricker, S., Magalhaes, V., Liebig, J., Chua, R., Thurmann, L., Messingschlager, M., Seegebarth, A., Timmermann, B., Klages, S., Ralser, M., Sawitzki, B., Sander, L., Corman, V., Conrad, C., Laudi, S., Binder, M., ... and Lehmann, I. (2022) 'Pre-activated antiviral innate immunity in the upper airways controls early SARS-CoV-2 infection in children', *Nature Biotechnology,* 40(3), pp. 319-+.
Lu, R., Zhao, X., Li, J., Niu, P., Yang, B., Wu, H., Wang, W., Song, H., Huang, B., Zhu, N., Bi, Y., Ma, X., Zhan, F., Wang, L., Hu, T., Zhou, H., Hu, Z., Zhou, W., Zhao, L., ... and Tan, W. 2020. [Genomic characterisation and epidemiology of 2019 novel coronavirus: implications for virus origins and receptor binding]. *Lancet,* 395(10224): pp. 565–574.
Lu, X., Pan, J. a., Tao, J. and Guo, D. (2011) 'SARS-CoV nucleocapsid protein antagonizes IFN-beta response by targeting initial step of IFN-beta induction pathway, and its C-terminal region is critical for the antagonism', *Virus Genes,* 42(1), pp. 37-45.
Lu, Y., Lu, X. and Denison, M. R. (1995) 'Identification and characterization of a serine-like proteinase of the murine coronavirus MHV-A59', *Journal of virology,* 69(6), pp. 3554-3559.
Luo, Y., Lv, H., Zhao, S., Sun, Y., Liu, C., Chen, C., Liang, W., Kwok, K., Teo, Q., So, R., Lin, Y., Deng, Y., Li, B., Dai, Z., Zhu, J., Zhang, D., Fernando, J., Wu, N., Tun, H., ... and Mu, X. (2023) 'Age-

related seroprevalence trajectories of seasonal coronaviruses in children including neonates in Guangzhou, China', *International Journal of Infectious Diseases,* 127, pp. 26-32.
Mahony, R., Gargan, S., Roberts, K. L., Bourke, N., Keating, S. E., Bowie, A. G., O'Farrelly, C. and Stevenson, N. J. (2017) 'A novel anti-viral role for STAT3 in IFN-alpha signalling responses', *Cellular and Molecular Life Sciences,* 74(9), pp. 1755-1764.
Mantlo, E., Bukreyeva, N., Maruyama, J., Paessler, S. and Huang, C. (2020) 'Antiviral activities of type I interferons to SARS-CoV-2 infection', *Antiviral Research,* 179: 104811
Marra, M. A., Jones, S. J., Astell, C. R., Holt, R. A., Brooks-Wilson, A., Butterfield, Y. S., Khattra, J., Asano, J. K., Barber, S. A., Chan, S. Y., Cloutier, A., Coughlin, S. M., Freeman, D., Girn, N., Griffith, O. L., Leach, S. R., Mayo, M., McDonald, H., Montgomery, S. B., ... and Roper, R. L. (2003) 'The Genome sequence of the SARS-associated coronavirus', *Science,* 300(5624), pp. 1399-404.
Masters, P. S. (2006) 'The Molecular Biology of Coronaviruses', *Advances in Virus Research*: Academic Press, pp. 193-292.
Menachery, V. D., Gralinski, L. E., Mitchell, H. D., Dinnon, K. H., III, Leist, S. R., Yount, B. L., Jr., Graham, R. L., McAnarney, E. T., Stratton, K. G., Cockrell, A. S., Debbink, K., Sims, A. C., Waters, K. M. and Baric, R. S. (2017) 'Middle East Respiratory Syndrome Coronavirus Nonstructural Protein 16 Is Necessary for Interferon Resistance and Viral Pathogenesis', *Msphere,* 2(6): e00346-17
Menachery, V. D., Yount, B. L., Jr., Josset, L., Gralinski, L. E., Scobey, T., Agnihothram, S., Katze, M. G. and Baric, R. S. (2014) 'Attenuation and Restoration of Severe Acute Respiratory Syndrome Coronavirus Mutant Lacking 2 '-O- Methyltransferase Activity', *Journal of Virology,* 88(8), pp. 4251-4264.
Mesel-Lemoine, M., Millet, J., Vidalain, P.-O., Law, H., Vabret, A., Lorin, V., Escriou, N., Albert, M. L., Nal, B. and Tangy, F. (2012) 'A Human Coronavirus Responsible for the Common Cold Massively Kills Dendritic Cells but Not Monocytes', *Journal of Virology,* 86(14), pp. 7577-7587.
Mihaylova, V., Kong, Y., Fedorova, O., Sharma, L., Dela Cruz, C., Pyle, A., Iwasaki, A. and Foxman, E. (2018) 'Regional Differences in Airway Epithelial Cells Reveal Tradeoff between Defense against Oxidative Stress and Defense against Rhinovirus', *Cell Reports,* 24(11), pp. 3000-+.
Morales, D. J. and Lenschow, D. J. (2013) 'The Antiviral Activities of ISG15', *Journal of Molecular Biology,* 425(24), pp. 4995-5008.
Mordstein, M., Neugebauer, E., Ditt, V., Jessen, B., Rieger, T., Falcone, V., Sorgeloos, F., Ehl, S., Mayer, D., Kochs, G., Schwemmle, M., Guenther, S., Drosten, C., Michiels, T. and Staeheli, P. (2010) 'Lambda Interferon Renders Epithelial Cells of the Respiratory and Gastrointestinal Tracts Resistant to Viral Infections', *Journal of Virology,* 84(11), pp. 5670-5677.
Mu, J., Xu, J., Zhang, L., Shu, T., Wu, D., Huang, M., Ren, Y., Li, X., Geng, Q., Xu, Y., Qiu, Y. and Zhou, X. (2020) 'SARS-CoV-2-encoded nucleocapsid protein acts as a viral suppressor of RNA interference in cells', *Science China-Life Sciences,* 63(9), pp. 1413-1416.
Neil, S. J. D., Zang, T. and Bieniasz, P. D. (2008) 'Tetherin inhibits retrovirus release and is antagonized by HIV-1 Vpu', *Nature,* 451(7177), pp. 425-U1.
Nickbakhsh, S., Ho, A., Marques, D., McMenamin, J., Gunson, R. and Murcia, P. (2020) 'Epidemiology of Seasonal Coronaviruses: Establishing the Context for the Emergence of Coronavirus Disease 2019', *Journal of Infectious Diseases,* 222(1), pp. 17-25.
Odendall, C., Dixit, E., Stavru, F., Bierne, H., Franz, K. M., Durbin, A. F., Boulant, S., Gehrke, L., Cossart, P. and Kagan, J. C. (2014) 'Diverse intracellular pathogens activate type III interferon expression from peroxisomes', *Nat Immunol,* 15(8), pp. 717-26.
Ogimi, C., Kim, Y. J., Martin, E. T., Huh, H. J., Chiu, C.-H. and Englund, J. A. (2020) 'What's New With the Old Coronaviruses?', *Journal of the Pediatric Infectious Diseases Society,* 9(2), pp. 210-217.
Ogunjinmi, O., Abdullahi, T., Somji, R., Bevan, C., Barclay, W., Temperton, N., Brooke, G. and Giotis, E. (2024) 'The antiviral potential of the antiandrogen enzalutamide and the viral-androgen signaling interplay in seasonal coronaviruses', *Journal of Medical Virology,* 96(3): e29540
Orzalli, M., DeLuca, N. and Knipe, D. (2012) 'Nuclear IFI16 induction of IRF-3 signaling during herpesviral infection and degradation of IFI16 by the viral ICP0 protein', *Proceedings of the National Academy of Sciences of The United States of America,* 109(44), pp. E3008-E3017.
Otter, C., Fausto, A., Tan, L., Khosla, A., Cohen, N. and Weiss, S. 2023. [Infection of primary nasal epithelial cells differentiates among lethal and seasonal human coronaviruses]. *Proceedings of the National Academy of Sciences of the United States of America,* 120(15): e2218083120.

Otter, C., Renner, D., Fausto, A., Tan, L., Cohen, N. and Weiss, S. (2024) 'Interferon signaling in the nasal epithelium distinguishes among lethal and common cold coronaviruses and mediates viral clearance', *Proceedings of the National Academy of Sciences Of the United States of America,* 121(21).
Park, A. and Iwasaki, A. (2020) 'Type I and Type III Interferons - Induction, Signaling, Evasion, and Application to Combat COVID-19', *Cell Host & Microbe,* 27(6), pp. 870-878.
Paul, D. and Bartenschlager, R. (2013) 'Architecture and biogenesis of plus-strand RNA virus replication factories', *World journal of virology,* 2(2), pp. 32-48.
Perlman, S. and Netland, J. (2009) 'Coronaviruses post-SARS: update on replication and pathogenesis', *Nature Reviews Microbiology,* 7(6), pp. 439-450.
Pfaffl, M. W. (2001) 'A new mathematical model for relative quantification in real-time RT-PCR', *Nucleic Acids Research,* 29(9): e45
Pindel, A. and Sadler, A. (2011) 'The Role of Protein Kinase R in the Interferon Response', *Journal of Interferon and Cytokine Research,* 31(1), pp. 59-70.
Platanias, L. C. (2005a) 'Mechanisms of type-I- and type-II-interferon-mediated signalling', *Nature Reviews Immunology,* 5(5), pp. 375-386.
Platanias, L. C. (2005b) 'Mechanisms of type-I-and type-II-interferon-mediated signalling', *Nature Reviews Immunology,* 5(5), pp. 375-386.
Ramakrishnan, M. A. (2016) 'Determination of 50% endpoint titer using a simple formula', *World journal of virology,* 5(2), pp. 85-6.
Reikine, S., Nguyen, J. B. and Modis, Y. (2014) 'Pattern recognition and signaling mechanisms of RIG-I and MDA5', *Frontiers in immunology,* 5, pp. 82715.
Rio, D. C., Ares, M., Jr., Hannon, G. J. and Nilsen, T. W. (2010) 'Purification of RNA using TRIzol (TRI reagent)', *Cold Spring Harbor protocols,* 2010(6), pp. pdb.prot5439-pdb.prot5439.
Savoie, C. and Lippe, R. (2022) 'Optimizing human coronavirus OC43 growth and titration', *Peerj,* 10.
Schindler, C., Levy, D. E. and Decker, T. (2007) 'JAK-STAT signaling: From interferons to cytokines', *Journal of Biological Chemistry,* 282(28), pp. 20059-20063.
Schirtzinger, E., Kim, Y. and Davis, A. 2022. [Improving human coronavirus OC43 (HCoV-OC43) research comparability in studies using HCoV-OC43 as a surrogate for SARS-CoV-2]. *Journal of Virological Methods,* 299: 114317.
Schmidt, O., Cooney, M. and Kenny, G. (1979) 'Plaque-Assay and Improved Yield of Human Coronaviruses In A Human Rhabdomyosarcoma Cell-Line', *Journal of Clinical Microbiology,* 9(6), pp. 722-728.
Shabani, E., Dowlatshahi, S. and Abdekhodaie, M. (2021) 'Laboratory detection methods for the human coronaviruses', *European Journal of Clinical Microbiology & Infectious Diseases,* 40(2), pp. 225-246.
Shah, M., Winn, A., Dahl, R., Kniss, K., Silk, B. and Killerby, M. (2022) 'Seasonality of Common Human Coronaviruses, United States, 2014-2021', *EMERGING INFECTIOUS DISEASES,* 28(10), pp. 1970-1976.
Shereen, M. A., Khan, S., Kazmi, A., Bashir, N. and Siddique, R. (2020) 'COVID-19 infection: Emergence, transmission, and characteristics of human coronaviruses', *Journal of Advanced Research,* 24, pp. 91-98.
Shin, D., Mukherjee, R., Grewe, D., Bojkova, D., Baek, K., Bhattacharya, A., Schulz, L., Widera, M., Mehdipour, A. R., Tascher, G., Geurink, P. P., Wilhelm, A., van der Heden van Noort, G. J., Ovaa, H., Mueller, S., Knobeloch, K.-P., Rajalingam, K., Schulman, B. A., Cinatl, J., ... and Dikic, I. (2020) 'Papain-like protease regulates SARS-CoV-2 viral spread and innate immunity', *Nature,* 587(7835), pp. 657-+.
Siu, K.-L., Kok, K.-H., Ng, M.-H. J., Poon, V. K. M., Yuen, K.-Y., Zheng, B.-J. and Jin, D.-Y. (2009) 'Severe Acute Respiratory Syndrome Coronavirus M Protein Inhibits Type I Interferon Production by Impeding the Formation of TRAF3 center dot TANK center dot TBK1/IKK epsilon Complex', *Journal of Biological Chemistry,* 284(24), pp. 16202-16209.
Siu, K.-L., Yeung, M. L., Kok, K.-H., Yuen, K.-S., Kew, C., Lui, P.-Y., Chan, C.-P., Tse, H., Woo, P. C. Y., Yuen, K.-Y. and Jin, D.-Y. (2014) 'Middle East Respiratory Syndrome Coronavirus 4a Protein Is a Double-Stranded RNA-Binding Protein That Suppresses PACT-Induced Activation of RIG-I and MDA5 in the Innate Antiviral Response', *Journal of Virology,* 88(9), pp. 4866-4876.
Snijder, E. J., Limpens, R. W. A. L., de Wilde, A. H., de Jong, A. W. M., Zevenhoven-Dobbe, J. C., Maier, H. J., Faas, F. F. G. A., Koster, A. J. and Barcena, M. (2020) 'A unifying structural and functional

model of the coronavirus replication organelle: Tracking down RNA synthesis', *Plos Biology,* 18(6): e3000715.
Sommereyns, C., Paul, S., Staeheli, P. and Michiels, T. (2008) 'IFN-lambda (IFN-lambda) is expressed in a tissue-dependent fashion and primarily acts on epithelial cells in vivo', *Plos Pathogens,* 4(3): e1000017
Spann, K., Tran, K., Chi, B., Rabin, R. and Collins, P. (2004) 'Suppression of the induction of alpha, beta, and gamma interferons by the NS1 and NS2 proteins of human respiratory syncytial virus in human epithelial cells and macrophages', *Journal of Virology,* 78(8), pp. 4363-4369.
Spence, J. S., He, R., Hoffmann, H.-H., Das, T., Thinon, E., Rice, C. M., Peng, T., Chandran, K. and Hang, H. C. (2019) 'IFITM3 directly engages and shuttles incoming virus particles to lysosomes', *Nature Chemical Biology,* 15(3), pp. 259-+.
Sposito, B., Broggi, A., Pandolfi, L., Crotta, S., Clementi, N., Ferrarese, R., Sisti, S., Criscuolo, E., Spreafico, R., Long, J., Ambrosi, A., Liu, E., Frangipane, V., Saracino, L., Bozzini, S., Marongiu, L., Facchini, F., Bottazzi, A., Fossali, T., ... and Zanoni, I. (2021) 'The interferon landscape along the respiratory tract impacts the severity of COVID-19', *Cell,* 184(19), pp. 4953-+.
Stertz, S., Reichelt, M., Spiegel, M., Kuri, T., Martinez-Sobrido, L., Garcia-Sastre, A., Weber, F. and Kochs, G. (2007) 'The intracellular sites of early replication and budding of SARS-coronavirus', *Virology,* 361(2), pp. 304-315.
Stodola, J., Dubois, G., Le Coupanec, A., Desforges, M. and Talbot, P. (2018) 'The OC43 human coronavirus envelope protein is critical for infectious virus production and propagation in neuronal cells and is a determinant of neurovirulence and CNS pathology', *Virology,* 515, pp. 134-149.
Takahashi, T., Heaton, S. M. and Parrish, N. F. (2021) 'Mammalian antiviral systems directed by small RNA', *Plos Pathogens,* 17(12): e1010091
Takeuchi, O. and Akira, S. (2009) 'Innate immunity to virus infection', *Immunological Reviews,* 227, pp. 75-86.
Tan, Y. J., Lim, S. G. and Hong, W. (2006) 'Understanding the accessory viral proteins unique to the severe acute respiratory syndrome (SARS) coronavirus', *Antiviral Res,* 72(2), pp. 78-88.
Tang, G., Liu, Z. and Chen, D. (2022) 'Human coronaviruses: Origin, host and receptor', *Journal of Clinical Virology,* 155: 105246.
Teague, H., Lefevre, C., Rieser, E., Wolfram, L., de Miguel, D., de Oliveira, D., Oliveira, M., Mansur, D., Irigoyen, N., Walczak, H. and Ferguson, B. (2024) 'LUBAC is required for RIG-I sensing of RNA viruses', *Cell Death and Differentiation,* 31(1), pp. 28-39.
Trinchieri, G. (2010) 'Type I interferon: friend or foe?', *The Journal of experimental medicine,* 207(10), pp. 2053.
Ujike, M. and Taguchi, F. (2015) 'Incorporation of Spike and Membrane Glycoproteins into Coronavirus Virions', *Viruses-Basel,* 7(4), pp. 1700-1725.
Unterholzner, L., Keating, S., Baran, M., Horan, K., Jensen, S., Sharma, S., Sirois, C., Jin, T., Latz, E., Xiao, T., Fitzgerald, K., Paludan, S. and Bowie, A. (2010) 'IFI16 is an innate immune sensor for intracellular DNA', *Nature Immunology,* 11(11), pp. 997-U42.
V'Kovski, P., Gultom, M., Kelly, J. N., Steiner, S., Russeil, J., Mangeat, B., Cora, E., Pezoldt, J., Holwerda, M., Kratzel, A., Laloli, L., Wider, M., Portmann, J., Tran, T., Ebert, N., Stalder, H., Hartmann, R., Gardeux, V., Alpern, D., ... and Dijkman, R. (2021) 'Disparate temperature-dependent virus-host dynamics for SARS-CoV-2 and SARS-CoV in the human respiratory epithelium', *Plos Biology,* 19(3): e3001158.
Wallace, L., de Vries, E., van Kuppeveld, F. and de Haan, C. (2023) 'Neuraminidase-dependent entry of influenza A virus is determined by hemagglutinin receptor-binding specificity', *Journal of Virology,* 97(10): e00078-23
Wan, Z., Zhang, Y., He, Z., Liu, J., Lan, K., Hu, Y. and Zhang, C. (2016) 'A Melting Curve-Based Multiplex RT-qPCR Assay for Simultaneous Detection of Four Human Coronaviruses', *International Journal of Molecular Sciences,* 17(11): 1880.
Wang, C., Hesketh, E., Shamorkina, T., Li, W., Franken, P., Drabek, D., van Haperen, R., Townend, S., van Kuppeveld, F., Grosveld, F., Ranson, N., Snijder, J., de Groot, R., Hurdiss, D. and Bosch, B. (2022) 'Antigenic structure of the human coronavirus OC43 spike reveals exposed and occluded neutralizing epitopes', *Nature Communications,* 13(1): 2921.

Wang, W., Lin, X.-D., Guo, W.-P., Zhou, R.-H., Wang, M.-R., Wang, C.-Q., Ge, S., Mei, S.-H., Li, M.-H., Shi, M., Holmes, E. C. and Zhang, Y.-Z. (2015) 'Discovery, diversity and evolution of novel coronaviruses sampled from rodents in China', *Virology,* 474, pp. 19-27.
Warnes, S. L., Little, Z. R. and Keevil, C. W. (2015) 'Human Coronavirus 229E Remains Infectious on Common Touch Surface Materials', *Mbio,* 6(6): e01697-15
Wathelet, M. G., Lin, C. H., Parekh, B. S., Ronco, L. V., Howley, P. M. and Maniatis, T. (1998) 'Virus infection induces the assembly of coordinately activated transcription factors on the IFN-beta enhancer in vivo', *Molecular Cell,* 1(4), pp. 507-518.
Weiss, S. and Leibowitz, J. 2011. [Coronavirus Pathogenesis]. *Advances In Virus Research, Vol 81.*
Wells, A. I. and Coyne, C. B. (2018) 'Type III Interferons in Antiviral Defenses at Barrier Surfaces', *Trends in Immunology,* 39(10), pp. 848-858.
Wickenhagen, A., Sugrue, E., Lytras, S., Kuchi, S., Noerenberg, M., Turnbull, M., Loney, C., Herder, V., Allan, J., Jarmson, I., Cameron-Ruiz, N., Varjak, M., Pinto, R., Lee, J., Iselin, L., Palmalux, N., Stewart, D., Swingler, S., Greenwood, E., ... and Investigators, I. C. (2021) 'A prenylated dsRNA sensor protects against severe COVID-19', *Science,* 374(6567).
Wilson, R., Kovacs, D., Crosby, M. and Ho, A. (2024) 'Global Epidemiology and Seasonality of Human Seasonal Coronaviruses: A Systematic Review', *Open Forum Infectious Diseases,* 11(8): ofae418.
Wolff, G., Melia, C. E., Snijder, E. J. and Barcena, M. (2020) 'Double-Membrane Vesicles as Platforms for Viral Replication', *Trends in Microbiology,* 28(12), pp. 1022-1033.
Woo, P. C., Huang, Y., Lau, S. K. and Yuen, K.-Y. (2010) 'Coronavirus genomics and bioinformatics analysis', *viruses,* 2(8), pp. 1804-1820.
Woo, P. C. Y., Lau, S. K. P., Chu, C. M., Chan, K. H., Tsoi, H. W., Huang, Y., Wong, B. H. L., Wong, H. L., Poon, R. W. S., Cai, J. J., Luk, W. K., Poon, L. L. M., Wong, S. S. Y., Guan, Y., Peiris, J. S. M. and Yuen, K. Y. (2005) 'Characterization and complete genome sequence of a novel coronavirus, coronavirus HKU1, from patients with pneumonia', *Journal of Virology,* 79(2), pp. 884-895.
Wölfel, R., Corman, V. M., Guggemos, W., Seilmaier, M., Zange, S., Müller, M. A., Niemeyer, D., Jones, T. C., Vollmar, P., Rothe, C., Hoelscher, M., Bleicker, T., Brünink, S., Schneider, J., Ehmann, R., Zwirglmaier, K., Drosten, C. and Wendtner, C. (2020) 'Virological assessment of hospitalized patients with COVID-2019', *Nature,* 581(7809), pp. 465-469.
Yang, Y., Zhang, L., Geng, H., Deng, Y., Huang, B., Guo, Y., Zhao, Z. and Tan, W. (2013) 'The structural and accessory proteins M, ORF 4a, ORF 4b, and ORF 5 of Middle East respiratory syndrome coronavirus (MERS-CoV) are potent interferon antagonists', *Protein & Cell,* 4(12), pp. 951-961.
Ye, R., Gong, C., Cui, X., Liu, J., Fan, H., Xie, H., Wang, Q., Ren, Z., Zhang, Y., Xia, L., Zhang, M., Li, Y., Li, Z., Du, L., Zhang, J., Cheng, N., Shi, W., Li, M., Zhao, L., ... and Cao, W. (2023) 'Continuous evolution and emerging lineage of seasonal human coronaviruses: A multicenter surveillance study', *Journal of Medical Virology,* 95(6): e28861
Yuen, C.-K., Lam, J.-Y., Wong, W.-M., Mak, L.-F., Wang, X., Chu, H., Cai, J.-P., Jin, D.-Y., To, K. K.-W., Chan, J. F.-W., Yuen, K.-Y. and Kok, K.-H. (2020) 'SARS-CoV-2 nsp13, nsp14, nsp15 and orf6 function as potent interferon antagonists', *Emerging Microbes & Infections,* 9(1), pp. 1418-1428.
Zeng, Q., Langereis, M., van Vliet, A., Huizinga, E. and de Groot, R. (2008) 'Structure of coronavirus hemagglutinin-esterase offers insight into corona and influenza virus evolution', *Proceedings of the National Academy of Sciences of the United States of America,* 105(26), pp. 9065-9069.
Zhang, R., Wang, K., Ping, X., Yu, W., Qian, Z., Xiong, S. and Sun, B. (2015) 'The ns12.9 Accessory Protein of Human Coronavirus OC43 Is a Viroporin Involved in Virion Morphogenesis and Pathogenesis', *Journal Of Virology,* 89(22), pp. 11383-11395.
Zhang, Y., Gargan, S., Lu, Y. and Stevenson, N. J. (2021) 'An overview of current knowledge of deadly CoVs and their interface with innate immunity', *Viruses,* 13(4), pp. 560.
Zhao, L., Jha, B., Wu, A., Elliott, R., Ziebuhr, J., Gorbalenya, A., Silverman, R. and Weiss, S. (2012) 'Antagonism of the Interferon-Induced OAS-RNase L Pathway by Murine Coronavirus ns2 Protein Is Required for Virus Replication and Liver Pathology', *Cell Host & Microbe,* 11(6), pp. 607-616.
Zhao, X. S., Guo, F., Liu, F., Cuconati, A., Chang, J. H., Block, T. M. and Guo, J. T. (2014) 'Interferon induction of IFITM proteins promotes infection by human coronavirus OC43', *Proceedings of the National Academy of Sciences of the United States of America,* 111(18), pp. 6756-6761.

Appendix

Supplemental material

Appendix table 1: List of donors used to generate the study's nasal epithelial airway cells (Data were provided by Epithelix, Geneva, Switzerland).

Batch number	Age	Gender
AB0870	77	F
AB0866	54	M
AB0863	57	F
AB0825	65	F
AB0824	69	M
AB080901	24	M
AB080701	61	M
AB079401	53	M
AB077401	38	M
AB077101	23	M
AB076700	71	M
AB076001	45	N/A
AB074501	45	M
AB050701	29	M

Appendix Table 1.2: List of all the primers used in these studies

Gene name	Forward primer 5'-3'	Reverse primer 5'-3'
hGAPDH	ATTCCACCCATGGCAAATTC	CGCTCCTGGAAGATGGTGAT
hOASL	GCACGAGACATCCACTTGACA	GGGAGAAGATCCCATATTTGGCT
hRSAD2	TGGGTGCTTACACCTGCTG	TGAAGTGATAGTTGACGCTGGT
hIFIT1	CAGAACGGCTGCCTAATTTACA	CAGACTATCCTTGACCTGATGATCA
hIFT2	CAGCTGAGAATTGCACTGCAA	CGTAGGCTGCTCTCCAAGGA
hIFIT3	CTCCGATCTCGCTGAGTTCC	GGAACTCAGCGAGATCGGAG

hIRF3	AGGACCCTCACGACCCACAT	CATGACTCCCCCACACAGAA
hIRF7	AGCTGCACGTTCCTATACGG	CCGTATAGGAACGTGCAGCT
hISG15	GGACAAATGCGACGAACCTC	GAGGTTCGTCGCATTTGTCC
hISG20	CGCCTCCTACACAAGAGCAT	ATGCTCTTGTGTAGGAGGCG
hRIG-I	AGGAAAACTGGCCCAAAACT	TTTCCCCTTTTGTCCTTGTG
hMAVS	TGCCGTTTGCTGAAGACAAGAC	TCAGTGCCGCAATGAAGTACTC
hIFNAR	TGTTATGTGGGCTTTGGATGGT	GGAGCCACTGAACTTGAAAGGT
hTBK1	ACCTGGAAGCGGCAGAGTTAG	GCGTCATAGCTTTTGTGGCATG
hCXCL8	TTTCTGCAGCTCTGTGTGAAGG	AAACTTCTCCACAACCCTCTGC
hCXCL10	CTGCTTTGGGGTTTATCAGA	CCACTGAAAGAATTTGGGC
hCXCL11	AGCAGTGAAAGTGGCAGAT	TTGGGATTTAGGCATCGT
hTBP	GGGCACCACTCCACTGTATC	TTTGCAGCTGCGGTACAATC
hB2M	GCTCGCGCTACTCTCTCTTT	CTCTGCTGGATGACGTGAGT
hHPRT1	CCTGGCGTCGTGATTAGTGA	CGAGCAAGACGTTCAGTCCT
hRPLP0	GAACACCATGATGCGCAAGG	CATTCCCCCGGATATGAGGC
SOCS1	GACTGCCTCTTCGAGCTGC	TCTGGAAGGGGAAGGAGCTC
hNFKB1	GCACCCTGACCTTGCCTATT	TTTCCTCCCCTCCAGTCACA
hSTAT1	ACACGAGACCAATGGTGTGG	AACTTGCTGCAGACTCTCCG

Appendix Table 1.3: List of antibodies used for western blotting

Primary antibody	Supplier	Reactivity	Dilution (ul)
RSAD2	Invitrogen	Rabbit	1:1000
CXCl11	Invitrogen	Mouse	1:500
Beta-Actin	Invitrogen	Rabbit	1:20000
Anti-RIG-I	Invitrogen	Rabbit	1:1000
OC43 N	Invitrogen	Rabbit	1:1000
OC43 anti-N	Invitrogen	Mouse	1:1000

Appendix table 1.4: Full QC Metrics for MRC-5 HCoV-229E and HCoV-OC43 from the hNEC dataset

Sample	Condition	Time	Total Reads (millions)	% Aligned Reads	Unique Paired (%)	Non-unique Paired (%)	Coverage (%)	Avg. Depth	Mean Aligned Phred Score	% GC
Mock_A	Uninfected	0h	41.6	97.25 %	93.14 %	4.11 %	55.77 %	74.34	35.17	51.85 %
Mock_B	Uninfected	0h	35.5	97.08 %	92.85 %	4.23 %	50.50 %	55.77	35.20	51.81 %
E229_24A	229E	24h	31.7	97.80 %	92.44 %	5.36 %	4.46%	74.34	35.90	51.85 %
E229_24B	229E	24h	23.8	97.90 %	93.76 %	4.13 %	4.77%	50.78	35.96	51.90 %
E229_72A	229E	72h	24.4	97.25 %	87.16 %	10.09 %	5.25%	52.18	35.95	54.54 %

E229_72B	229E	72h	27.5	96.93%	88.07%	8.86%	4.21%	71.55	35.88	54.41%
OC43_24A	OC43	24h	25.0	97.91%	93.96%	3.96%	5.20%	48.94	35.95	50.98%
OC43_24B	OC43	24h	25.3	97.94%	93.66%	4.28%	49.44%	49.44	35.86	50.93%
OC43_72A	OC43	72h	24.5	97.21%	90.36%	6.85%	28.85%	28.85	35.91	52.95%
OC43_72B	OC43	72h	30.6	97.93%	94.06%	3.87%	52.61%	52.61	35.97	50.90%

Appendix table 1.5: Full QC Metrics for MRC-5 HCoV-229E dataset

Sample ID	Time (hpi)	Replicate	Total Reads (M)	Total Alignments	Aligned (%)	Unique (%)	Non-unique (%)	Coverage (%)	Avg. Depth	Avg. Read Length (bp)	Mean Quality	%GC
GSM4718629	0	A	24.37	31.73	99.01	84.52	14.49	2.81	18.37	50.72	35.69	50.88%
GSM4718630	0	B	23.68	30.87	99.10	84.54	14.56	2.72	18.47	50.72	35.70	51.19%

GSM4718631	0	C	24.11	29.50	99.12	87.59	11.53	2.96	16.25	50.72	35.72	50.68%
GSM4718632	6	A	27.32	33.43	99.11	87.59	11.52	3.12	17.48	50.73	35.72	50.82%
GSM4718633	6	B	23.35	28.82	98.08	86.03	12.05	2.69	17.47	50.74	35.77	51.98%
GSM4718634	6	C	26.48	20.38	62.89	56.07	6.82	2.51	13.25	50.74	35.78	50.64%
GSM4718635	24	A	24.90	19.67	64.89	57.96	6.94	2.50	12.83	50.75	35.79	50.67%
GSM4718636	24	B	25.22	19.81	64.01	56.98	7.02	2.47	13.06	50.74	35.77	51.10%
GSM4718637	24	C	27.70	26.14	77.59	67.44	10.15	2.69	15.86	50.74	35.78	50.64%
GSM4718638	48	A	23.22	22.03	78.02	67.84	10.18	2.51	14.30	50.74	35.77	50.55%
GSM4718639	48	B	24.44	23.36	78.92	68.87	10.05	2.55	14.92	50.74	35.76	50.32%
GSM4718640	48	C	23.44	21.08	75.16	67.29	7.87	2.61	13.15	50.74	35.78	50.61%
GSM4718641	72	A	25.14	22.59	74.85	66.90	7.96	2.65	13.90	50.74	35.78	50.42%
GSM4718642	72	B	25.14	22.59	74.85	66.90	7.96	2.65	13.90	50.74	35.78	50.42%
GSM4718643	72	C	25.14	22.59	74.85	66.90	7.96	2.65	13.90	50.74	35.78	50.42%

Appendix Table 1.5: Full QC Metrics for MRC-5 HCoV-OC43 dataset

Sample ID	Time (hpi)	Replicate	Total Reads (M)	Mean Phred Score	% N	% GC	Aligned (%)	Unique Paired (%)	Non-unique Paired (%)	Coverage (%)	Avg. Depth
GSM8005236	–1	A	73.21	30.00	0.08%	51.03%	96.96%	83.29%	13.67%	21.61%	13.63
GSM8005244	–1	B	63.05	30.00	0.08%	49.63%	98.05%	84.88%	12.22%	22.26%	13.66
GSM8005252	–1	C	47.28	30.00	0.06%	47.20%	97.12%	82.14%	14.98%	19.75%	11.45
GSM8005245	1.5	A	69.69	30.00	0.08%	51.33%	97.69%	86.44%	11.25%	22.05%	12.80
GSM8005265	1.5	B	51.11	30.00	0.08%	51.26%	96.68%	86.12%	12.56%	19.70%	11.45

GSM8005253	1.5	C	49.21	30.00	0.08%	51.00%	97.50%	87.08%	10.42%	21.83%	11.90
GSM8005237	3	A	78.70	30.00	0.08%	49.63%	98.05%	87.13%	10.92%	22.26%	13.66
GSM8005246	3	B	73.58	30.00	0.08%	49.18%	98.12%	86.74%	11.38%	22.01%	13.39
GSM8005266	3	C	41.43	30.00	0.08%	46.08%	97.21%	85.02%	12.19%	20.08%	11.21
GSM8005238	6	A	65.53	30.00	0.08%	49.63%	97.30%	85.96%	11.34%	22.01%	11.39
GSM8005255	6	B	51.50	30.00	0.08%	50.12%	92.19%	81.07%	11.12%	19.70%	10.18
GSM8005267	6	C	55.38	30.00	0.08%	50.35%	96.35%	84.22%	12.13%	20.01%	10.80
GSM8005239	9	A	61.43	30.00	0.08%	47.59%	79.54%	72.01%	7.53%	20.08%	9.63
GSM8005247	9	B	70.80	30.00	0.08%	48.63%	82.91%	75.21%	7.70%	22.26%	11.02
GSM8005256	9	C	53.51	30.00	0.08%	47.12%	70.55%	66.12%	4.43%	20.08%	9.27
GSM8005240	12	A	71.35	30.00	0.08%	49.08%	51.96%	46.88%	5.08%	22.26%	9.27

GSM8005248	12	B	67.66	30.00	0.08%	49.36%	53.83%	49.12%	4.71%	22.01%	9.63
GSM8005257	12	C	45.38	30.00	0.08%	48.31%	45.55%	41.22%	4.33%	20.08%	9.27
GSM8005241	18	A	71.94	30.00	0.08%	47.86%	35.30%	31.74%	3.56%	22.26%	11.02
GSM8005249	18	B	74.09	30.00	0.08%	48.31%	35.38%	32.14%	3.24%	22.01%	9.63
GSM8005258	18	C	47.24	30.00	0.08%	48.52%	35.86%	32.66%	3.20%	20.08%	9.27
GSM8005242	24	A	69.26	30.00	0.08%	50.08%	34.27%	31.48%	2.79%	21.61%	13.63
GSM8005250	24	B	65.77	30.00	0.08%	49.99%	32.97%	30.47%	2.50%	22.26%	13.66
GSM8005269	24	C	59.46	30.00	0.08%	48.12%	46.39%	42.12%	4.27%	20.08%	9.27
GSM8005243	30	A	81.19	30.00	0.08%	48.63%	35.24%	32.98%	2.26%	22.26%	11.02
GSM8005251	30	B	71.14	30.00	0.08%	47.85%	36.45%	34.12%	2.33%	20.08%	9.27
GSM8005272	30	C	83.71	30.00	0.08%	48.74%	37.79%	35.12%	2.67%	22.26%	11.02

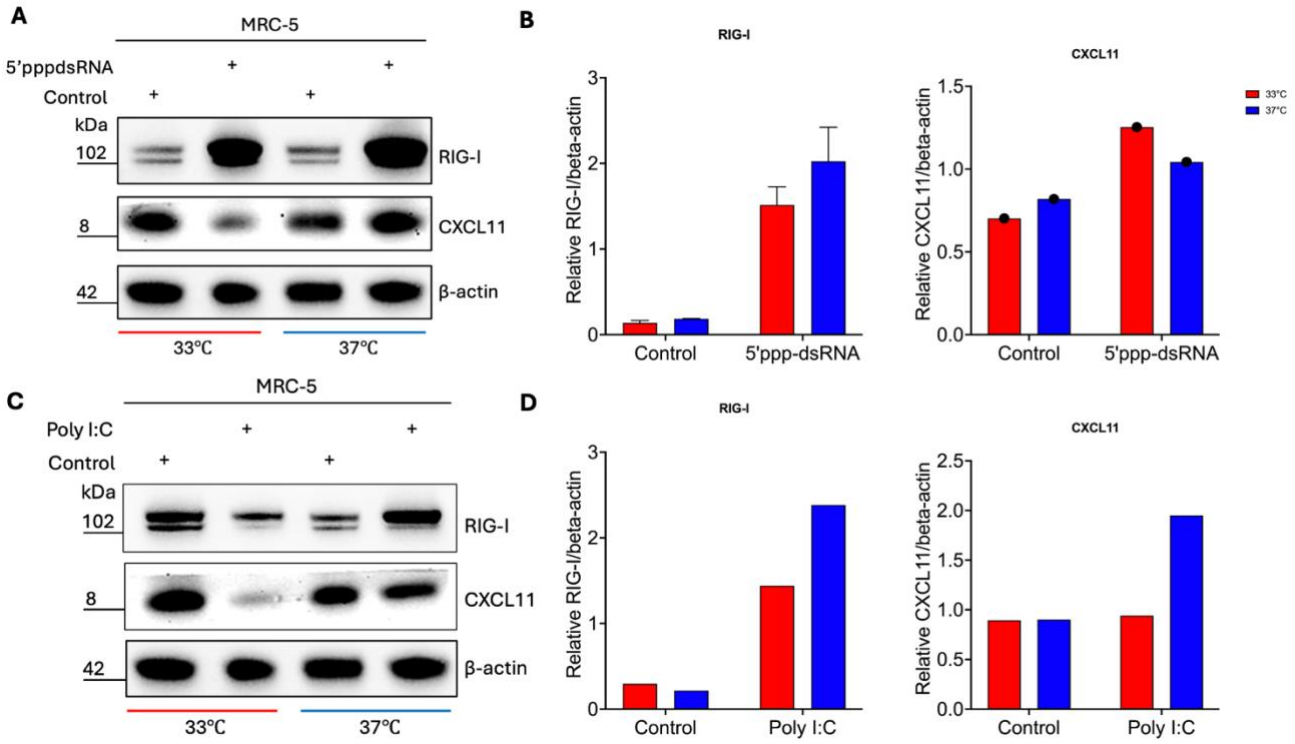

Appendix Figure A1: Temperature-dependent induction of RIG-I and CXCL11 in MRC-5 cells following stimulation with RIG-I and MDA5 agonists.

MRC-5 fibroblasts were stimulated with either 5′ppp-dsRNA (RIG-I agonist; panels A-B) or Poly I:C (MDA5/TLR3 agonist; panels C–D) at 33 °C or 37 °C for 24 h. (A, C) Western blotting analysis of RIG-I and CXCL11 protein expression, with β-actin used as a loading control. (B, D) Densitometric quantification of RIG-I and CXCL11 bands normalised to β-actin and expressed relative to unstimulated controls. Data show increased RIG-I induction and CXCL11 expression at 37 °C compared with 33 °C, with a stronger temperature sensitivity observed for 5′ppp-dsRNA stimulation than Poly I:C. Representative of two independent experiments.

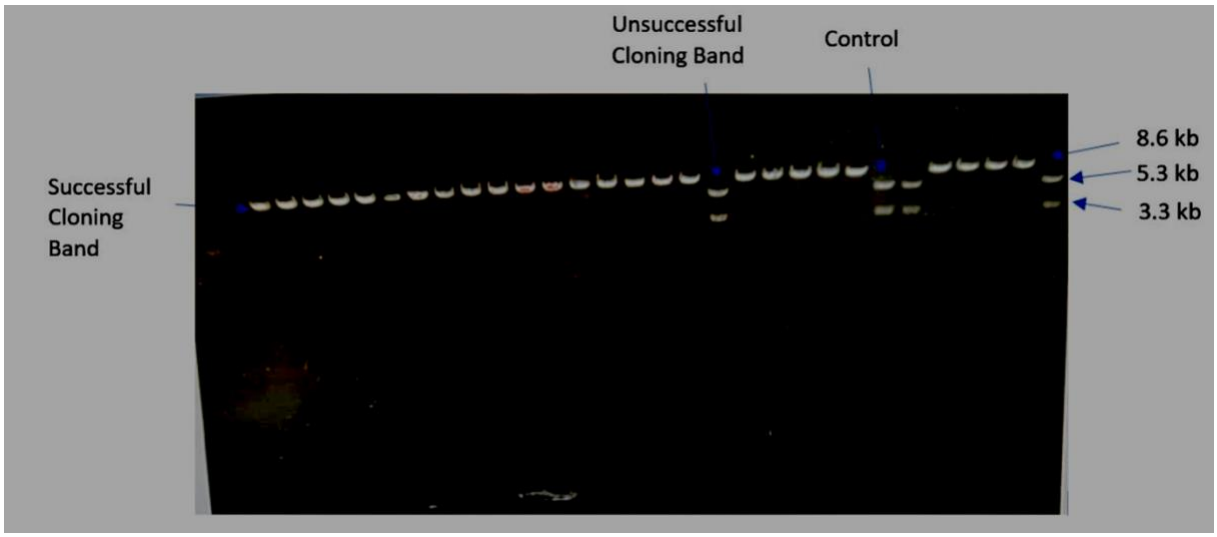

Appendix Figure A2: Agarose gel electrophoresis showing the results of CRISPR/Cas9 cloning attempts.

Successful cloning is indicated by the expected recombinant plasmid band (~8.6 kb), while unsuccessful cloning produced a lower band (~5.3 kb). A control plasmid band (~3.3 kb) was included for comparison. The presence of both successful and unsuccessful bands demonstrates variable cloning efficiency across colonies. DNA was visualised with ethidium bromide under UV illumination.

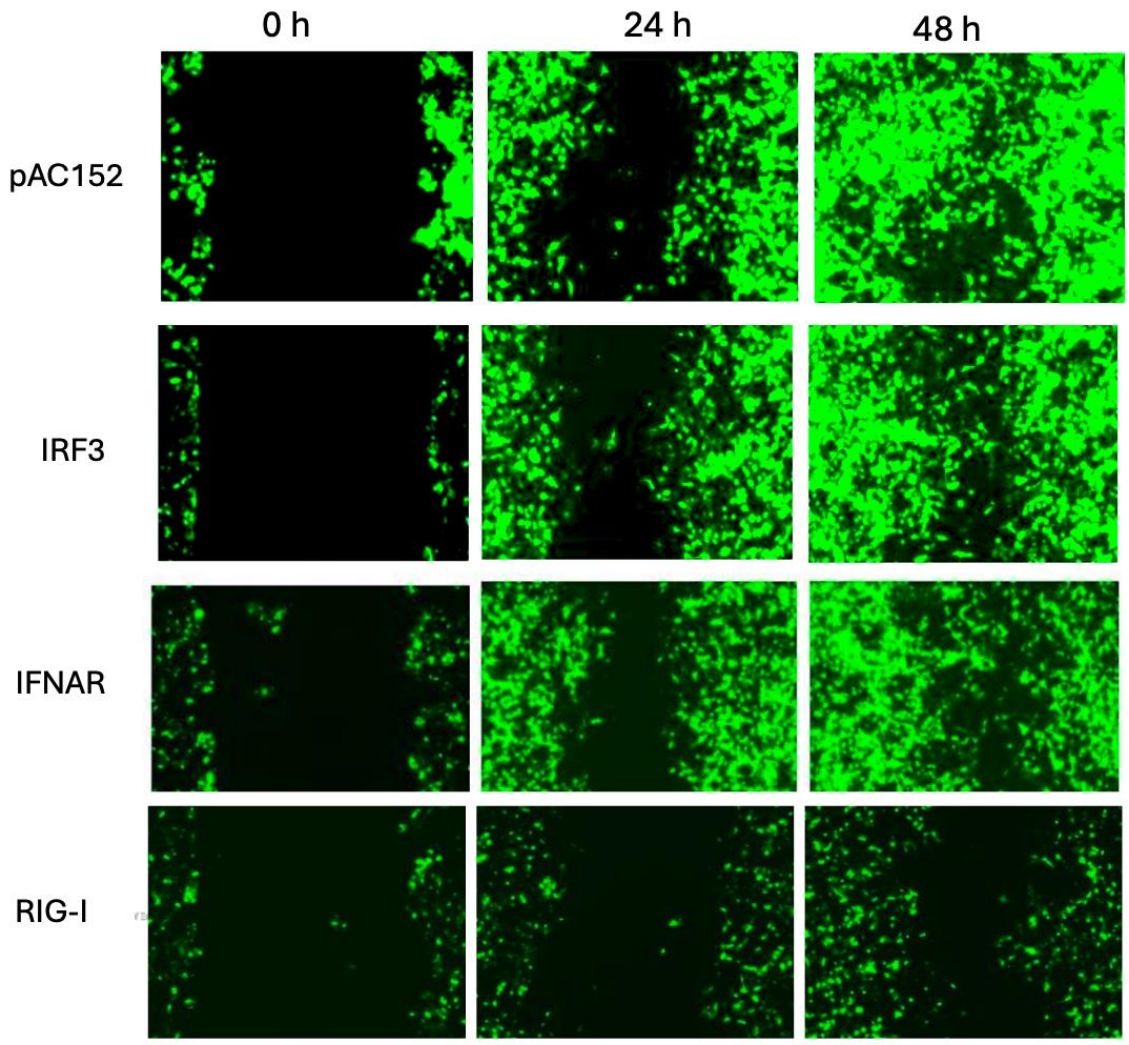

Appendix Figure A3: Wound-healing (scratch) assay shows that CRISPR editing does not impair basal migration.

Wound healing assay of A549 wild-type and CRISPR knockout cell lines (IRF3, IFNAR, and RIG-I) following transfection with the pAC152 vector. Confluent monolayers were scratched with a pipette tip (0 h) and imaged at 24 h and 48 h post-scratch. Green fluorescence indicates GFP-expressing cells, allowing visualisation of migration into the wound gap. Across all knockout lines, the rate of wound closure was comparable to control (pAC152), suggesting that disruption of IFN signalling pathways did not significantly alter basal cell migration dynamics under these conditions.

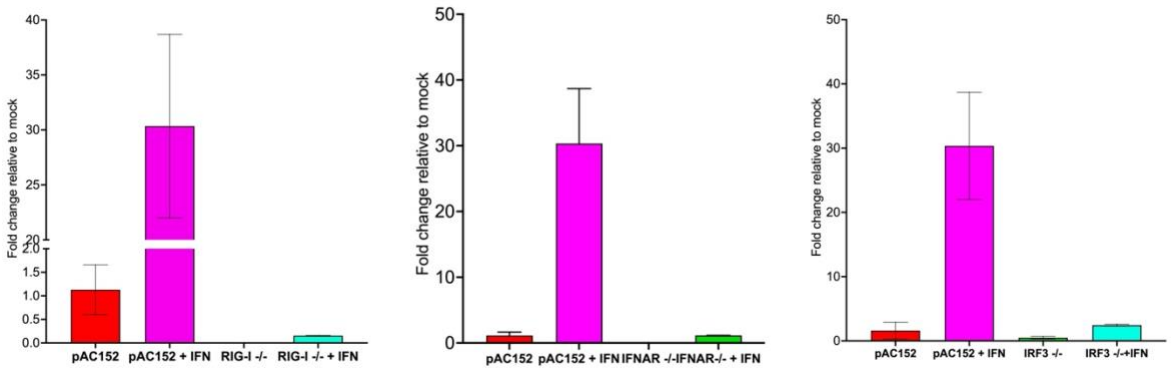

Appendix Figure A4: qPCR validation: IFN-α driven ISG induction is lost in knockout lines

Quantification of ISG induction following IFN-α stimulation in CRISPR/Cas9 knockout A549 cell lines. Cells transfected with the pAC152 control vector or knockout derivatives (IRF3, IFNAR, or RIG-I) were treated with IFN-α (1000 IU/mL, 24 h), and relative ISG expression was assessed by qPCR. (Left) pAC152 control and IRF3 knockout with or without IFN-α treatment. (Middle) IFNAR knockout response compared to pAC152 control. (Right) RIG-I knockout response compared to pAC152 control. Data are presented as fold change relative to mock (mean ± SD, n = 2 biological replicates). Results show that IFN-α stimulation induced robust ISG expression in control cells but not in IRF3, IFNAR, or RIG-I knockouts, validating the functional disruption of these signalling pathways.

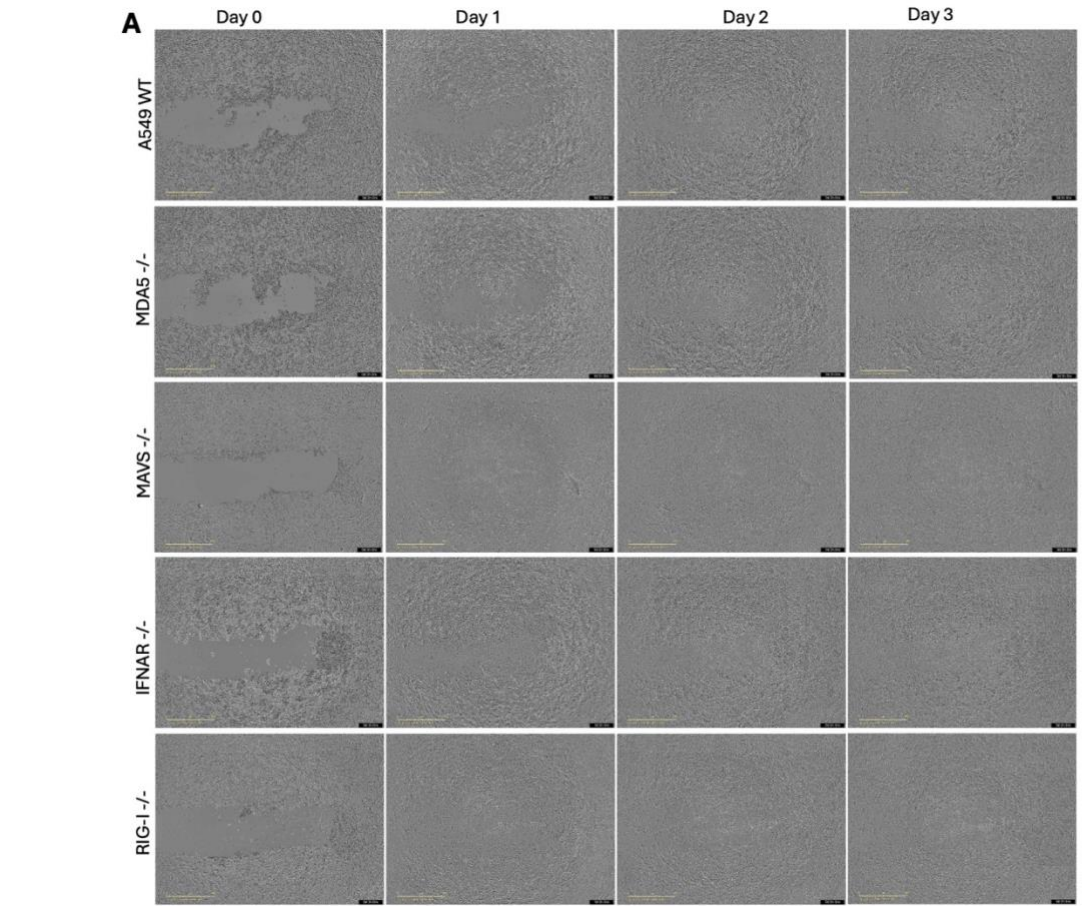
A
Day 0
Day 1
Day 2
Day 3
A549 WT
MDA5 -/-
MAVS -/-
IFNAR -/-
RIG-I -/-

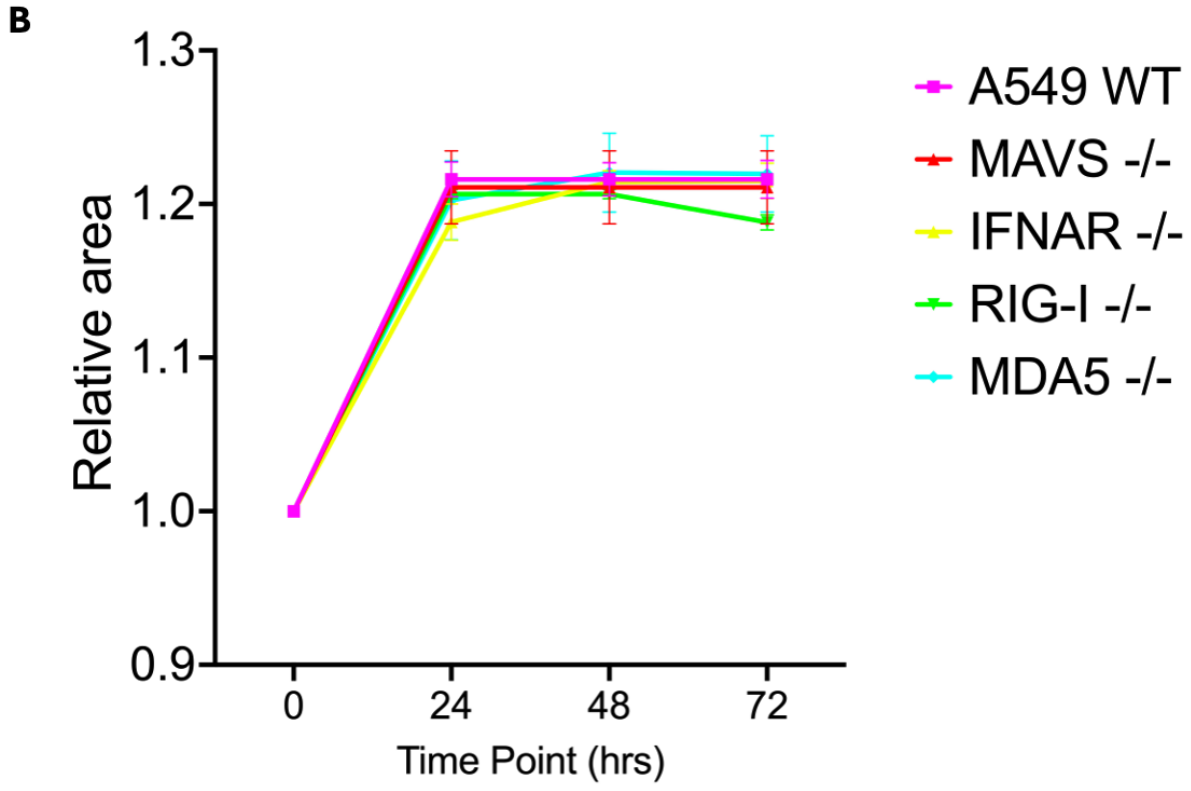
B
Relative area
1.3
1.2
1.1
1.0
0.9
0
24
48
72
Time Point (hrs)
A549 WT
MAVS -/-
IFNAR -/-
RIG-I -/-
MDA5 -/-

Appendix Figure A5: Wound healing assay in A549 wild-type and CRISPR knockout lines (RIG-I-/-, MDA5-/-, MAVS-/-, IFNAR-/-).

(A) Confluent monolayers of A549 WT and knockout derivatives were scratched and imaged over 3 days to assess wound closure. Representative phase-contrast images are shown at day 0, day 1, day 2, and day 3 for each genotype. Scale bars: 200 µm. (B) Quantification of wound closure expressed as relative area over time. All cell lines, including WT, RIG-I-/-, MDA5-/-, MAVS-/-, and IFNAR-/-, demonstrated comparable wound closure dynamics, with no significant differences in migration rate between WT and knockout lines. Data represent the mean ± SEM of two independent biological replicates.

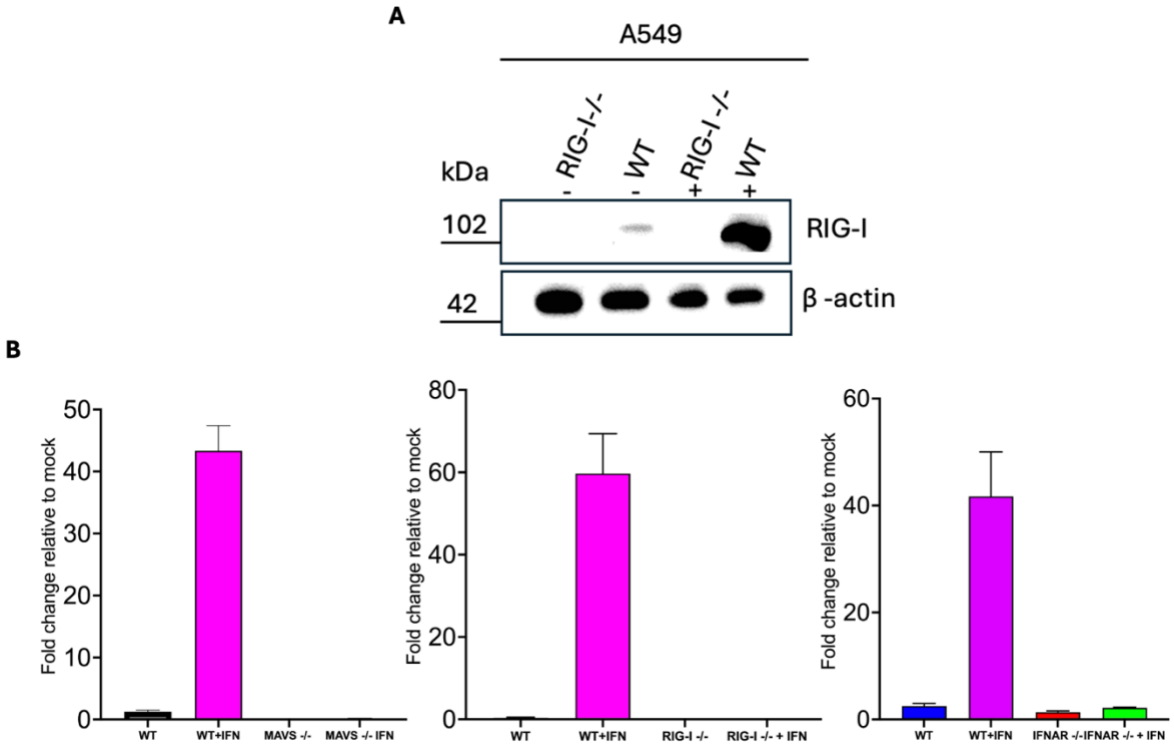

Appendix Figure A6. Validation of CRISPR knockout A549 cell lines by western blotting and qPCR.

(A) Western blotting analysis confirming loss of RIG-I protein expression in RIG-I knockout (RIG-I-/-) A549 cells compared with wild-type (WT). β-actin was used as a loading control. Bands at ~102 kDa correspond to RIG-I, and bands at ~42 kDa correspond to β-actin. (B) qPCR analysis of IFN-stimulated gene expression following IFN-α treatment in A549 WT, MAVS-/-, RIG-I-/-, and IFNAR-/- cell lines. In WT cells, IFN-α stimulation induced robust ISG expression (40-60-fold increase relative to mock), whereas this induction was abrogated in IFNAR-/- and strongly reduced in MAVS-/- and RIG-I-/- lines. Data represent mean ± SEM of two independent experiments, normalised to mock-treated controls.

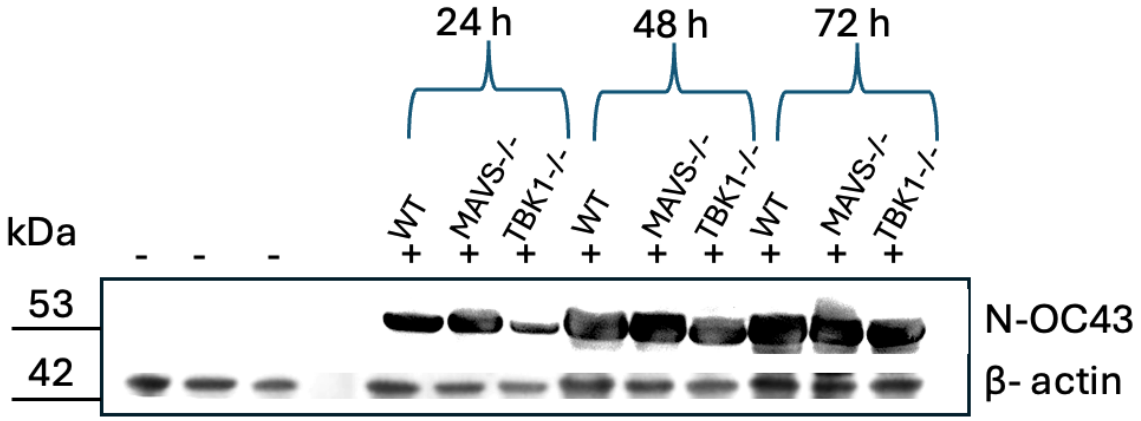

Appendix Figure A8: Validation of MAVS and TBK1 contributions to HCoV-OC43 replication in A549 cells.

A549 WT, MAVS-/-, and TBK1-/- cells were infected with HCoV-OC43 (MOI 0.1) and lysates were collected at 24, 48, and 72 hpi. Western blotting was performed using an anti-OC43 nucleocapsid (N) antibody. β-actin was used as a loading control. Strong accumulation of N protein was observed over time in all three cell types.